



**UNIVERSITY OF LEEDS**

# The Ultra-Compact H II Region Population of the Galaxy

**Ivayla Emilova Kalcheva**

School of Physics and Astronomy

University of Leeds

Submitted in accordance with  
the requirements for the degree of

*Doctor of Philosophy*

December 2018



*To my family*



## Declaration

The candidate confirms that the work submitted is her own, except where work which has formed part of jointly authored publications has been included. The contribution of the candidate and the other authors to this work has been explicitly indicated. The candidate confirms that appropriate credit has been given within the thesis where reference has been made to the work of others.

This copy has been supplied on the understanding that it is copyright material and that no quotation from the thesis may be published without proper acknowledgement.

Ivayla Emilova Kalcheva

December 2018

## Preface

The basis of Chapter 2 is the work published in the paper titled *The Coordinated Radio and Infrared Survey for High-Mass Star Formation III. A catalogue of northern ultra-compact H II regions* – I. E. Kalcheva, M. G. Hoare, J. S. Urquhart, S. Kurtz, S. L. Lumsden, C. R. Purcell and A. A. Zijlstra, 2018, A&A, 615, A103.

The survey data reduction and the initial visual classification of the candidate UCHII regions were performed by the co-authors. M. G. Hoare led the CORNISH survey observations. All data analysis and writing was carried out by the primary author, I. E. Kalcheva. The co-authors provided comments on various drafts.

## Acknowledgements

I would like to express my gratitude to my supervisor Melvin Hoare for entrusting me with this project, for all the helpful advice, for taking the time to read countless drafts, and for always putting the tea kettle on during AstroLab observing breaks. Working with you on this project and demonstrating alongside you has been a privilege and a pleasure.

I would like to extend my thanks to the rest of the staff at the School of Physics and Astronomy at Leeds, for the friendliness, guidance, and assistance, which helped make my PhD a rewarding experience.

And of course, warm thanks to all my fellow PhD students and postdocs, for sharing discussions, coffee, movies, trips, and a multitude of other adventures. The roundabout of old and new faces made every year different in a lovely way. May we have many pleasant occasions to reassemble! Special thanks to Tonye for being my CORNISH sis who has been there for me to discuss work and life. I am in awe of your dedication. Thank you, Jingyao, Alice Pérez, Evgenia, for your friendship and for your encouragement. In every conversation you make me smile and feel more hopeful. I am better for knowing you all.

Thanks are also due to my teachers back home at the Rozhen Observatory, where I started my astronomy journey as a wide-eyed high schooler looking out for bears in the night sky and on the way to the domes.

Above all, thank you, Grandma, Mom, Dad.



## Abstract

This thesis focuses on one of the key phases of massive star formation – ultra-compact H II regions. It is now possible to build up on the existing census of these sources by exploring the dense photo-ionised gas in unprecedented resolution and at higher frequency than previously available. Such data are delivered by the CORNISH survey. A catalogue of 239 ultra-compact H II regions (UCHIIs) found in the CORNISH survey at 5 GHz and 1.5'' resolution in the region  $10^\circ < l < 65^\circ, |b| < 1^\circ$  is presented. This is the largest complete and well-selected sample of UCHIIs to date and provides the opportunity to explore the global and individual properties of this key state in massive star formation at multiple wavelengths. The nature of the candidates was validated, based on observational properties and calculated spectral indices, and the analysis is presented in this work. The physical sizes, luminosities, and other physical properties were computed by utilising literature distances or calculating the distances whenever a value was not available. The near- and mid-infrared extended source fluxes were measured and the extinctions towards the UCHIIs were computed. The new results were combined with available data at longer wavelengths and the spectral energy distributions (SEDs) were reconstructed for 177 UCHIIs. The bolometric luminosities obtained from SED fitting are presented. By comparing the radio flux densities to previous observational epochs, it was found that about 5% of the sources appear to be time variable. Follow-up higher-resolution observations of unresolved CORNISH

sources increased the number of UCHIIs with morphological information in the sample to 213. The UCHII region morphologies were classified with a new, multi-wavelength morphological classification scheme. Cometary UCHIIs make up 71% of the sample. This fraction is significantly higher than those found in previous, radio-based classifications. As many as 10-15% of the CORNISH UCHII regions have point-like or extended hard X-ray emission counterparts. This first high-resolution area survey of the Galactic plane shows that the total number of UCHIIs in the Galaxy is  $\sim 750$  – a factor of 3-4 fewer than found in previous large area radio surveys. It will form the basis for future tests of models of massive star formation.

# Table of contents

<b>List of figures</b>	<b>xv</b>
<b>List of tables</b>	<b>xix</b>
<b>Abbreviations</b>	<b>xxi</b>
<b>1 Introduction</b>	<b>1</b>
1.1 Massive star formation . . . . .	1
1.1.1 The cradles of stars . . . . .	2
1.1.2 Sites of massive star formation . . . . .	4
1.1.3 Theoretical models . . . . .	8
1.2 UCHII regions . . . . .	10
1.2.1 Surveying the birthplaces of massive stars . . . . .	10
1.2.2 Morphological studies . . . . .	14
1.2.3 Distances to Galactic UCHIIs . . . . .	22
1.2.4 Infrared signatures . . . . .	25
1.2.5 Use of X-ray data in UCHII studies . . . . .	26
1.3 Radio interferometry – brief overview . . . . .	29
1.4 Thesis motivation and outline . . . . .	33
<b>2 A catalogue of northern UCHII regions</b>	<b>35</b>
2.1 Introduction . . . . .	35

2.2	Identification of the CORNISH UCHII sample . . . . .	36
2.3	Radio properties of the CORNISH UCHIIs . . . . .	40
2.3.1	Lower-resolution radio counterparts . . . . .	43
2.3.2	5GHz–1.4GHz spectral indices . . . . .	48
2.4	Evidence for short-timescale UCHII variability? . . . . .	52
2.5	Distances . . . . .	60
2.5.1	Distances from ATLASGAL and RMS . . . . .	61
2.5.2	Distance estimates for remaining sources using CO data . . . . .	61
2.5.3	Resolving the KDA . . . . .	62
2.6	Derived physical properties . . . . .	68
2.7	Infrared properties . . . . .	73
2.7.1	Associations with mid-infrared data . . . . .	73
2.7.2	Associations with near-infrared data and extinctions . . . . .	75
2.8	Spectral energy distributions and bolometric luminosities . . . . .	81
2.9	Comparison of UCHII search methods in blind surveys . . . . .	87
2.9.1	Sub-mm – ATLASGAL . . . . .	89
2.9.2	Mid-IR – RMS . . . . .	89
2.9.3	Previous radio surveys of the Galactic plane . . . . .	90
2.10	Conclusions . . . . .	90
<b>3</b>	<b>Higher-resolution follow-up of point-like CORNISH UCHII re-</b>	
	<b>gions</b>	<b>95</b>
3.1	Introduction . . . . .	95
3.2	The JVLA A-configuration targeted survey of CORNISH UCHIIs . . . . .	96
3.2.1	Target selection . . . . .	96
3.2.2	JVLA observational set-up . . . . .	97
3.3	Data reduction . . . . .	98
3.3.1	Quality check – calibrator fluxes . . . . .	98

3.3.2	Pipeline processing and flagging . . . . .	100
3.3.3	Imaging . . . . .	102
3.4	Target detection statistics . . . . .	107
3.5	Target maps . . . . .	108
3.5.1	Two target non-detections? . . . . .	119
3.6	Neighbour maps . . . . .	121
3.7	Flux densities and source sizes . . . . .	126
3.8	Observed and derived properties . . . . .	127
3.8.1	10 GHz sample properties . . . . .	127
3.8.2	10GHz–1.4GHz spectral indices . . . . .	131
3.9	Conclusions . . . . .	138
<b>4</b>	<b>UCHII region morphology</b>	<b>141</b>
4.1	Introduction . . . . .	141
4.2	Radio and mid-IR morphological classification of UCHIIs . . . . .	142
4.2.1	Radio classification . . . . .	144
4.2.2	Infrared classification . . . . .	144
4.2.3	Joint radio-IR classification . . . . .	149
4.3	Morphology statistics . . . . .	153
4.3.1	Dependence on resolution and wavelength . . . . .	155
4.3.2	Comparison to previous classifications . . . . .	158
4.4	Physical properties and morphologies . . . . .	160
4.4.1	Sizes and electron densities . . . . .	160
4.4.2	Luminosities and spectral types . . . . .	162
4.5	Gallery of morphological types . . . . .	168
4.5.1	Spherical UCHIIs . . . . .	168
4.5.2	Bipolar UCHIIs . . . . .	169
4.5.3	Shell-like UCHIIs . . . . .	170

4.5.4	Irregular UCHIIs . . . . .	173
4.5.5	Cometary UCHIIs with ionising star candidates . . . . .	178
4.6	Findings of the extended joint classification . . . . .	187
4.6.1	Cometary morphologies at all studied scales . . . . .	187
4.6.2	Environment and multiplicity . . . . .	189
4.6.3	Signposts of younger MSF stages . . . . .	192
4.7	Conclusions . . . . .	193
<b>5</b>	<b>X-ray view of UCHIIs</b>	<b>195</b>
5.1	Introduction . . . . .	195
5.2	The new <i>Chandra</i> Source Catalog 2.0 . . . . .	196
5.3	18 X-ray associations to 14 CORNISH UCHII regions . . . . .	201
5.3.1	Summary of X-ray properties . . . . .	201
5.3.2	Location and extent of the X-ray associations . . . . .	203
5.3.3	X-ray to bolometric luminosity ratios . . . . .	206
5.4	<i>XMM-Newton</i> counterparts – spectral fits . . . . .	214
5.5	Conclusions . . . . .	221
<b>6</b>	<b>Conclusions and outlook</b>	<b>223</b>
6.1	Conclusions . . . . .	224
6.2	Outlook . . . . .	227
	<b>References</b>	<b>233</b>
	<b>Appendix A Radio fluxes and spectral indices</b>	<b>253</b>
	<b>Appendix B Distances, physical properties, morphologies</b>	<b>261</b>
	<b>Appendix C Extended IR source fluxes</b>	<b>275</b>
	<b>Appendix D JVLA follow-up – photometric results</b>	<b>295</b>

# List of figures

1.1	The famous H II region M16 . . . . .	2
1.2	Hierarchical structures inside a molecular cloud . . . . .	3
1.3	Evolutionary diagram for the formation of massive stars . . . . .	5
1.4	The radio spectrum of an idealised H II region . . . . .	6
1.5	Velocity fields in cometary H II regions . . . . .	20
1.6	Simulated cometary UCHII region viewed at different projection angles . . . . .	20
1.7	Morphological classes of UCHII regions . . . . .	21
1.8	The origin of the kinematic distance ambiguity . . . . .	23
1.9	Central region of the Orion Nebula Cluster . . . . .	27
1.10	Visibility $(u, v)$ coverage of a source . . . . .	30
2.1	Images of the cometary UCHII G028.6869+00.1770 . . . . .	37
2.2	CORNISH and GLIMPSE images of G010.6223–00.3788 . . . . .	39
2.3	Observational properties of the candidate sample . . . . .	41
2.4	Ratio of integrated to peak flux vs. angular size . . . . .	43
2.5	Comparison of the MAGPIS 6 cm and CORNISH integrated fluxes	44
2.6	Spectral indices against brightness temperature . . . . .	49
2.7	Continuum-subtracted VGPS spectra . . . . .	66
2.8	Continuum-subtracted VGPS spectra – contd. . . . .	67
2.9	Parameter distributions of the CORNISH UCHIIs . . . . .	69

2.10	Mid-IR colour-colour diagram of the CORNISH UCHIIIs . . . . .	74
2.11	Near-IR colour-colour diagram of near-IR nebulae associated with the CORNISH UCHIIIs . . . . .	76
2.12	Visual extinctions of the UCHIIIs . . . . .	78
2.13	Average SED for all UCHIIIs with available multi-wavelength data	82
2.14	Bolometric luminosity distribution for the UCHIIIs with fitted SEDs . . . . .	83
2.15	5 GHz radio luminosity against bolometric luminosity . . . . .	84
3.1	Phase calibrators and flux calibrator used in the JVLA follow-up	99
3.2	Standard cleaning vs. multi-scale clean – central portion of W49A104	
3.3	Standard cleaning vs. multi-scale clean – off-centre portion of W49A . . . . .	105
3.4	JVLA angular sizes against distance . . . . .	108
3.5	Target maps . . . . .	112
3.6	Target maps, continued . . . . .	113
3.7	Target maps, continued . . . . .	114
3.8	Target maps, continued . . . . .	115
3.9	Target maps, continued . . . . .	116
3.10	Target maps, continued . . . . .	117
3.11	Target maps, continued . . . . .	118
3.12	Three-colour Spitzer image of G18.67+0.03 . . . . .	120
3.13	Neighbour maps . . . . .	123
3.14	Neighbour maps, continued . . . . .	124
3.15	G032.7441–00.0755 at higher resolution . . . . .	125
3.16	Ratio of integrated to peak flux against angular size of the JVLA targets . . . . .	128
3.17	Histograms of the JVLA sample properties . . . . .	129

3.18	10 GHz over 5 GHz integrated flux against angular size at 10 GHz	130
3.19	Spectral indices from fits to the 10 GHz, 5 GHz and 1.4 GHz integrated flux of the target UCHIIs . . . . .	130
3.20	Radio SEDs of JVLA targets . . . . .	135
3.21	Radio SEDs of JVLA targets, continued . . . . .	136
3.22	Radio SEDs of JVLA targets, continued . . . . .	137
4.1	Example CORNISH images used in the radio-only morphological classification . . . . .	145
4.2	Example images used in the mid-IR-only morphological classifi- cation . . . . .	146
4.3	Example images of W49A used in the joint morphological classi- fication . . . . .	148
4.4	Results from different morphological classification methods . . .	154
4.5	Comparison of morphology distributions . . . . .	158
4.6	Electron density vs physical diameter for the different morpho- logical classes . . . . .	163
4.7	Lyman continuum flux vs distance for the different morphological classes . . . . .	164
4.8	Distribution of spectral types and morphological classes . . . . .	165
4.9	Possible origins of the observed spherical and shell-like morpholo- gies . . . . .	166
4.10	Gallery of spherical UCHIIIs . . . . .	168
4.11	Gallery of bipolar UCHIIIs . . . . .	171
4.11	Gallery of bipolar UCHIIIs – continued . . . . .	172
4.12	Gallery of shell-like UCHIIIs . . . . .	174
4.12	Gallery of shell-like UCHIIIs – continued . . . . .	175
4.13	Gallery of irregular UCHIIIs . . . . .	176

---

4.14	CORNISH and GLIMPSE images of an over-resolved irregular UCHII . . . . .	177
4.15	Gallery of cometary UCHIIs with candidate ionising stars . . . .	182
4.15	Gallery of cometary UCHIIs with candidate ionising stars – continued . . . . .	183
4.15	Gallery of cometary UCHIIs with candidate ionising stars – continued . . . . .	184
4.16	Intersections of commonly observed categories associated with the cometary CORNISH UCHIIs . . . . .	188
4.17	Candidate triggered sources . . . . .	190
5.1	<i>Chandra</i> sky coverage of the GLIMPSE region . . . . .	197
5.2	Comparison between the <i>Chandra</i> and <i>XMM-Newton</i> X-ray detection of G043.1651–00.0283 . . . . .	197
5.3	CORNISH UCHII regions with point-like <i>Chandra</i> associations .	207
5.3	CORNISH UCHII regions with point-like <i>Chandra</i> counterparts – continued . . . . .	208
5.3	CORNISH UCHII regions with point-like <i>Chandra</i> counterparts – continued . . . . .	209
5.4	CORNISH UCHII regions with extended <i>Chandra</i> associations .	210
5.4	CORNISH UCHII regions with extended <i>Chandra</i> associations – continued . . . . .	211
5.5	X-ray vs. bolometric luminosity of UCHII region X-ray associations	212
5.6	CORNISH UCHII regions with overlaid 3XMM-DR5 sources .	216
5.7	Fitted UCHII X-ray spectra . . . . .	217
6.1	Temperature map of a simulated UCHII region . . . . .	230

# List of tables

1.1	Observed types of star-forming objects and their properties . . .	8
1.2	Details for the MAGPIS and CORNISH surveys . . . . .	11
2.1	Catalogue vs measured MAGPIS 6 cm integrated fluxes . . . . .	47
2.2	Ratio of CORNISH to MAGPIS 5 GHz fluxes for candidate variable UCHII regions . . . . .	53
2.3	Comparison between velocities measured in this work and by Anderson et al. [2009] . . . . .	63
2.4	KDA-resolved UCHII distances . . . . .	64
2.5	Comparison between extinction values . . . . .	80
3.1	Summary of observational parameters . . . . .	97
3.2	Comparison of tabulated and newly measured JVLA calibrator fluxes . . . . .	98
3.3	Properties of candidate MYSO-jet components . . . . .	108
3.4	Properties of a dark H II region . . . . .	125
4.1	Extended classification – categories . . . . .	151
4.2	Morphological classification – summary of results . . . . .	153
4.3	Slopes and correlation coefficients – electron densities vs. physi- cal diameter . . . . .	160
4.4	Stand-off distances to candidate ionising stars . . . . .	179

---

4.5	Spectral types of candidate ionising stars . . . . .	186
4.6	Results of the extended classification . . . . .	191
5.1	<i>Chandra</i> X-ray counterparts – summary . . . . .	200
5.2	Parameters obtained from X-ray spectral fits . . . . .	218
6.1	CORNISH and CORNISH-South . . . . .	227
A.1	Remeasured fluxes of the MAGPIS counterparts to CORNISH UCHIIs; CORNISH – MAGPIS 20 cm spectral indices . . . . .	253
B.1	Distances, physical properties and morphologies of the 239 COR- NISH UCHIIs . . . . .	262
C.1	GLIMPSE counterparts – fluxes and magnitudes . . . . .	276
C.2	UKIDSS counterparts – fluxes and magnitudes . . . . .	286
C.3	Extinctions towards UCHII with near-IR nebulae . . . . .	290
D.1	Photometric results for the higher-resolution data targets . . . . .	296
D.2	Photometric results for the higher-resolution data – neighbour set	300

# Abbreviations

ATLASGAL	APEX Telescope Large Area Survey of the Galaxy
CORNISH	Co-Ordinated Radio ‘N’ Infrared Survey for High-mass star formation
CSC	<i>Chandra</i> Source Catalog
FOV	field of view
GLIMPSE	the Galactic Legacy Infrared Mid-Plane Survey Extraordinaire
HCHII	hyper-compact HII region
IRDC	infrared dark clouds
ISM	interstellar medium
JVLA	Karl G. Jansky Very Large Array
MSF	massive star formation
MYSO	massive young stellar object
PSF	point spread function

UCHII	ultra-compact HII region
UKIDSS	UKIRT Infrared Deep Sky Survey
UV	ultraviolet
VLA	Very Large Array
YSO	young stellar object



# Chapter 1

## Introduction

### 1.1 Massive star formation

The puzzle of the birth and early life of stars exceeding  $8 M_{\odot}$  is not yet fully assembled. Some of the obstacles towards building a complete evolutionary sequence for massive stars include their rarity due to their brief lifetime and the rapid evolution of each observable stage. The main sequence is reached while the young star is still embedded within a dense core and as a result the early phases of its development are hidden behind a heavy veil of dust. A well-founded distinction between global and individual properties of sources in each evolutionary stage is hampered by the strong influence of other objects within the multiple systems where massive stars typically form.

It is a vital task for modern astronomy to overcome these challenges. Massive stars affect not only their immediate surroundings, but also shape their parent galaxy. Their formation controls phase changes in the interstellar medium (ISM) via the profuse emission of ionising UV photons [Molinari et al., 2014]. Processes associated with their evolution, such as winds, outflows, expanding H II regions and supernovae, stir the ISM and enrich it with heavy elements [Zinnecker and Yorke, 2007]. This makes their understanding a stepping stone



Fig. 1.1 The famous H II region M16, re-imaged recently by the *Hubble Space Telescope*. Left: optical image of dense gas not yet dissipated by UV emission. The ionisation fronts are glowing. Right: IR image of the same region<sup>2</sup>.

towards a more detailed picture of the Milky Way, as well as the extent to which galaxy formation and evolution in general is driven by stellar populations.

This introduction briefly summarises the observed sites, evolutionary stages, and current competing theoretical models of massive star formation (MSF). It focuses on ultra-compact H II (UCHII) regions as an important part of the evolutionary sequence and the surveys which are key to studying these objects, with focus on the CORNISH survey<sup>1</sup>. The survey provides a representative and unbiased sample, conveniently available across other wavelengths within related surveys, to study the properties of this deeply embedded phase.

### 1.1.1 The cradles of stars

In the past several decades, dense molecular clouds in the ISM have been identified as the birthplaces of stars [Shu et al., 1987]. They are known as giant molecular clouds (GMCs) and trace the spiral arms of the Milky Way (and of spiral galaxies in general). They are among the largest and most massive

<sup>1</sup><http://cornish.leeds.ac.uk/public/index.php>

<sup>2</sup>From <http://hubblesite.org/newscenter/archive/releases/2015/01/image/c/>.

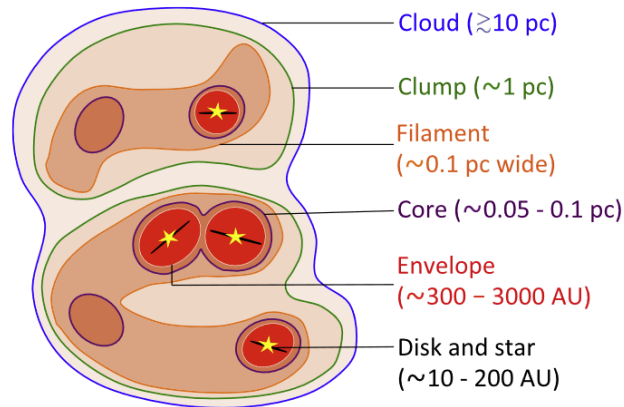


Fig. 1.2 Schematic of the hierarchical structures inside a molecular cloud forming low-mass stars (Fig. 1 from Pokhrel et al. 2018) – the cloud, clumps, filaments, cores, envelopes, and protostellar systems are shown.

objects in the Galaxy ( $M \sim 10^4 - 10^6 M_{\odot}$ ), reaching hundreds of parsecs in size [Lada and Shu, 1990] and holding over 80% of the molecular hydrogen (with column densities  $N_{\text{H}} = 10^{23} - 10^{24} \text{ cm}^{-2}$  and temperatures  $T = 10 - 15 \text{ K}$  [Larson, 1985]).

Molecular clouds are hierarchically structured, as illustrated in Figure 1.2. A hierarchy of nested ‘fragments’, ranging from larger filaments and clumps to dense cores and disks, is seen in observational and theoretical studies of  $\sim 10 \text{ pc}$  clouds, produced through sequential fragmentation (see e.g. Dobbs et al. 2014, Pokhrel et al. 2018).

The formation mechanism from a dense core to a low-mass star is understood through the classical theory by Larson [1969] and Shu et al. [1987]. Compressive turbulent motions in the ISM trigger the formation of rotating, bounded dense cores in a molecular cloud. Young stellar objects (YSOs) form from the gravitational collapse of such a dense core, after it has lost its thermal and magnetic support. Material is channelled onto the YSO through an accretion disk formed as a consequence of the rotation of the collapsing cloud fragment. The excess angular momentum is transferred away via the accretion disk, as

well as bipolar outflows and high-velocity jets which clear openings in the rotating envelope. This allows accumulation of material onto the YSO.

Initially, stars are hidden in an embedded state within their parent dense molecular core. The high column densities of gas and dust in molecular clouds absorb the optical and UV emission of these young stars, turning the clouds opaque to optical and shorter wavelengths. Figure 1.1 shows how imaging at longer wavelengths unveils the sites of newborn stars, otherwise hidden from view in optical emission.

### 1.1.2 Sites of massive star formation

There is no observationally established analogue to the evolutionary sequence of low-mass stars in the case of massive star formation, due to the obstacles described in §1.1. One of the main differences to low-mass stars is the substantial quantity of ionising radiation emitted by massive stars. It plays an important role during their lives and as early as their formation phase. The strong radiation field is capable of dissipating their accretion disc and protostellar envelope, thus limiting further accretion and the final mass they reach [Zinnecker, 2004]. Recent theoretical and observational efforts have shown that jets and outflows from the massive young stellar object (MYSO) could provide a getaway for the radiation by carving cavities into the surrounding material, and MSF could thus proceed similarly to the low-mass case (see e.g. Banerjee and Pudritz 2007; Manoj et al. 2016; Purser et al. 2016).

The embedded phase likely comprises several groups of objects, as indicated by mid-IR to radio observations [Menten et al., 2005]. A theoretical nomenclature exists to categorise the likely massive star precursors, borrowing from the low-mass star-formation sequence, as illustrated in Figure 1.3. Infrared dark clouds (IRDCs, first identified by Perault et al. 1996), are thought to

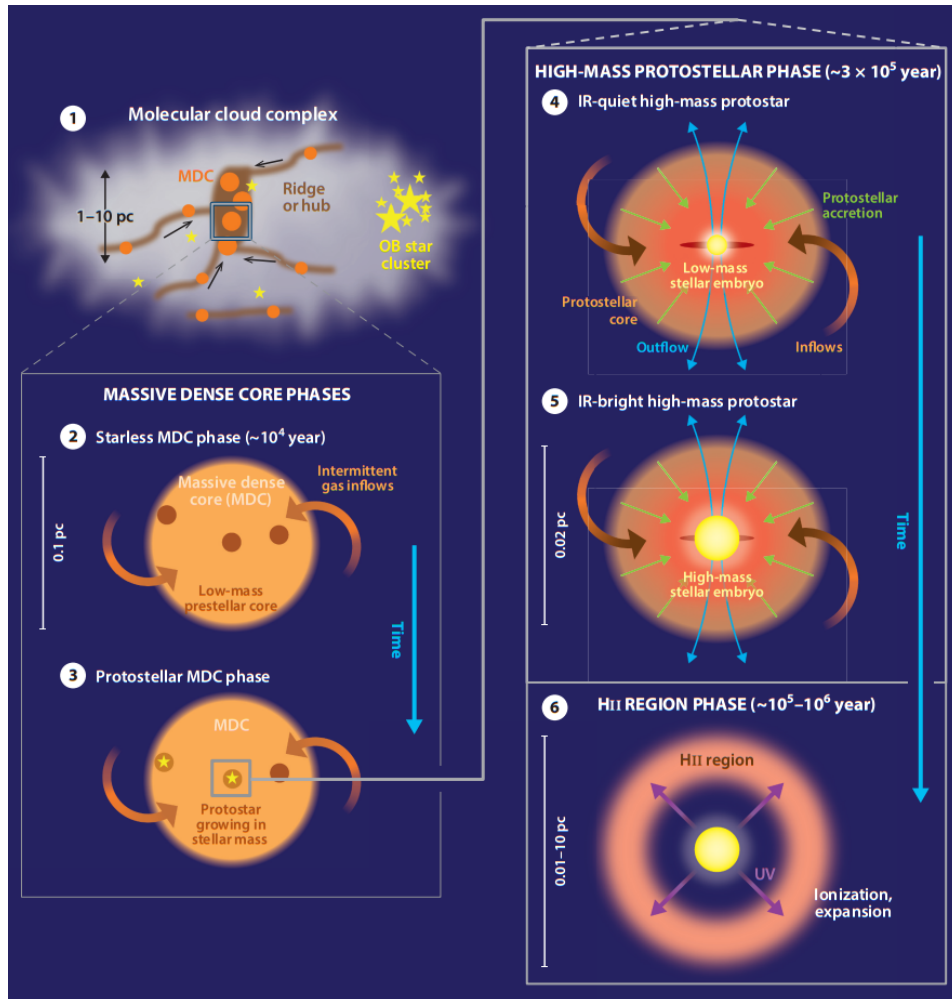


Fig. 1.3 Proposed evolutionary diagram for the formation of massive stars – Figure 8 from the recent review by Motte et al. [2017]. (1) Massive stars form in molecular dense cores hosted by massive filaments and spherical clumps, called here ridges and hubs. (2) and (3): In this scenario, low-mass prestellar cores become protostars with growing mass, rather than high-mass prestellar cores [Tigé et al., 2017]. (4), (5), and (6): Protostellar envelopes gather matter from gravitationally-driven inflows, leading to the formation of a massive protostar, which stays IR-quiet if/until it reaches  $8 M_{\odot}$ . The main accretion phase ends when the UV field from the star ionises the protostellar envelope to produce an H II region.

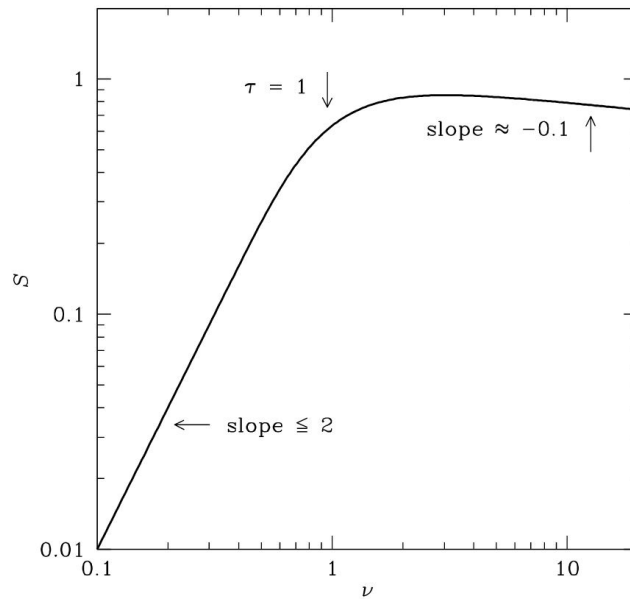


Fig. 1.4 The radio spectrum of an idealised H II region is a black body at low frequencies  $\nu$ . The slope equals 2 in the case of a uniform cylinder (optically thick case) and is less than 2 otherwise ( $\approx -0.1$  for the optically thin case) [Stahler and Palla, 2008].

provide the initial conditions for massive star formation and to contain dozens of massive starless clumps [Williams et al., 2000]. The earliest phase of massive star formation has also been called high-mass prestellar cores or massive cold molecular cores (see the recent review by Motte et al. 2017). From such gravitationally bound cores, individual massive stars or massive binaries would eventually form. The nature of, and relationship to, surrounding larger-scale cloud structures is uncertain.

The next phase is that of collapsing cloud fragments, which are named high-mass protostellar objects, massive protostars, protostellar massive dense cores, or hot molecular cores, provided they have the capacity to form a massive binary (but not a cluster) [Beuther et al., 2002]. Such hot molecular cores contain large amounts of warm, dense gas, heated by the loss of potential energy from the formation of protostars. The gas is mixed with dust and complex organic molecules. Hot cores are also associated with methanol maser emission [Kurtz et al., 2000].

Massive young stellar objects are late hot cores, when the ionising radiation of the star has not yet started to dissipate its surroundings. MYSOs are radio-quiet and unresolved in the mid-IR at 1'' resolution [Mottram et al., 2011]. These sources have lower effective temperatures than their zero age main sequence (ZAMS) counterparts, which is the likely cause for the lack of ionising radiation considering their luminosity [Hoare et al., 2007].

After a massive star has formed, it ionises a pocket of hydrogen gas which remains confined in its vicinity while expanding – thus forming an H II region. H II regions are highly convenient tracers of massive star formation, as they are clearly visible across the Galactic plane in the cm-regime [Anderson and Bania, 2008]. Since only the most massive stars are capable of emitting considerable amounts of radiation exceeding the Lyman limit, the radio continuum free-free emission of the H II region around the star provides one of the earliest observable clues to understanding massive star formation [Hoare et al., 2007]. The free-free emission arises from the ionised gas from the freed electrons being decelerated when deflected by ions, the excess energy being carried away by photons with a typical spectrum as shown in Figure 1.4. The dense heated dust within the ionised gas reprocesses the UV radiation into submillimetre and infrared wavelengths.

Churchwell [2002] proposed an empirical evolutionary sequence of H II regions, based on ionization expansion – from ultra-compact to compact H II regions, followed by classical/evolved H II regions. An even earlier phase was subsequently added to this scenario – hyper-compact H II regions (HCHII) [Kurtz et al., 2000]. HCHII and UCHII regions are associated with the youngest massive stars and reveal the most information about massive star formation. HCHII regions are likely to still be accreting [Keto, 2007]. They are thought to be distinct from UCHII regions primarily because they have extremely broad radio recombination line profiles ( $\Delta v \sim 40 - 50 \text{ km s}^{-1}$  and sometimes exceeding

Object	$M$ ( $M_{\odot}$ )	$L$ (pc)	$T$ (K)	$n_{\text{tot}}$ ( $\text{cm}^{-3}$ )
GMC	$10^4 - 10^6$	$\sim 50$	$10 - 15$	$\sim 10^2$
Clump	$10^2 - 10^4$	$0.5 - 20$	$10 - 25$	$\sim 10^3$
Cold Core	$10^3 - 10^4$	$< 0.5$	$10 - 50$	$\sim 10^4$
Hot Core	$10^2 - 10^3$	$\sim 0.1$	$\gtrsim 10^2$	$10^5 - 10^7$
HCHII region	-	$< 0.05$	$> 10^4$	$> 10^6$
UCHII region	-	$< 0.1$	$\sim 10^4$	$> 10^4$

Table 1.1 Observed types of star-forming objects and some of their properties [Charbonnel et al., 2011; Churchwell, 2002; Hoare et al., 2007; Zinnecker and Yorke, 2007].

$100 \text{ km s}^{-1}$ , whereas for UCHII this value is  $\sim 30 - 40 \text{ km s}^{-1}$ ) [Afferbach et al., 1996; Keto et al., 1995]. These stages are followed by the compact and classical region phase, where the gas is ionised globally, expands and disrupts its cloud, thus enabling observations in the visible and near-IR wavelengths [Churchwell, 2002; Zinnecker and Yorke, 2007]. Details about each observed stage are included in Table 1.1.

### 1.1.3 Theoretical models

The exact manner in which a protostar is born from the dense molecular material is an outstanding question in massive star formation. The observable stages listed above physically overlap and the transition between them is not understood in detail. The evolutionary phases are not found in isolation, complicating the task of the observer given the limited angular resolution and vast distances to massive star formation sites. Three primary models are still competing to explain massive star formation. Each of these models requires different initial and environmental conditions. The controversy arises from inconclusive, so far, observational data [Stahler and Palla, 2008; Zinnecker and Yorke, 2007]. The scenarios are, respectively:

- Monolithic collapse (also known as turbulent core model) [McKee and Tan, 2002], where large-scale turbulence in the parent GMC driven by

supernovae aids the formation of prestellar cores which are static and isolated on the verge of their collapse. This model is, in its essence, scaled-up low-mass star formation. Once the supplementary turbulent and magnetic support of a massive prestellar cores is lost, core collapse leads to the formation of a protostellar core, which accretes through a disk, at a rate set by the ambient gas pressure. Early in the accretion stage, a massive outflow emerges. Most of the high-energy radiation pours out via the so-formed cavity of optically thin material, thus relieving the radiation pressure. Simulations which include feedback and magnetic fields expect formation of isolated massive stars that can reach  $M \lesssim 140 M_{\odot}$  [Kuiper et al., 2010]. The monolithic collapse model suffers from problems such as the inability to explain fragmentation into small stars and the statistics of observed protostellar accretion disks [Tan et al., 2014]. The process that leads from runaway global collapse to a quasi-static configuration at the prestellar core scale is unknown [Motte et al., 2017].

- Competitive accretion and runaway growth [Bonnell et al., 2001; Murray and Chang, 2012] – in this model, massive prestellar cores do not exist as small ( $\sim 0.02$  pc) condensations isolated from their environment. The high-mass equivalent of prestellar cores could be low-mass cores within massive infalling clumps [Tigé et al., 2017]. The location and environment of a protostar determines the final stellar mass. Thus, competitive accretion differs from the low-mass star formation model, without the two falling into contradiction – low-mass stars can form, following the classical scheme, in the less dense cloud regions. The most massive stars form in the centres of clumps, where the large gravitational potential allows the protostar to keep accreting increasingly more material from neighbouring regions of the clump. The high accretion rates and disk

accretion solve both the radiation problem and the timescale problem. Filaments in the clumps could aid the transfer of gas from outer to inner regions of the clump (e.g. Smith et al. 2014). The competitive accretion model does not seem to work in a medium with high turbulence [Krumholz and McKee, 2005].

- Protostar collisions and coalescence (e.g. Bonnell and Bate 2005; Bonnell et al. 1998) – the model is based on stellar collisions and mergers which result in the formation of the most massive stars residing in very dense systems. This could be relevant in the rare case of close stellar encounters, or for rapidly-rotating massive stars – the progenitors of long-duration  $\gamma$ -ray bursts [Fryer and Heger, 2005; Zinnecker, 2006]. Computational simulations do not reproduce the stellar densities required for stellar mergers to be frequent, hence coalescence is unlikely to be a prevalent MSF mechanism (e.g. Bontemps et al. 2010).

## 1.2 UCHII regions

### 1.2.1 Surveying the birthplaces of massive stars

#### A family of Galactic plane surveys

The bounds of current understanding of massive star formation are widened by the modern family of Galactic plane surveys, covering the dust (from hot to cold), the molecular, the atomic, and the ionised gas. These include the GLIMPSE programme [Benjamin et al., 2003; Churchwell et al., 2009] and its companion MIPS GAL survey (mid-IR) [Carey et al., 2009], the UKIDSS GPS survey (near-IR) [Lucas et al., 2008], the BU-FCRAO Galactic Ring Survey (CO) [Jackson et al., 2005], the ATLASGAL survey (sub-mm) [Schuller et al., 2009], the VGPS survey ( $\text{H I}$ ) [Stil et al., 2006], the CORNISH survey (radio)

Survey	$\nu$ (GHz)	$\theta$ (")	Coverage	VLA-config.
MAGPIS 6 cm	5	4×9	$-10^\circ \leq l \leq 42^\circ$ $ b  < 0.4^\circ$	C
MAGPIS 20 cm	1.4	5	$5^\circ \leq l \leq 48.5^\circ$ $ b  < 0.8^\circ$	B,C,D
CORNISH	5	1.5	$10^\circ \leq l \leq 65^\circ$ $ b  < 1^\circ$	B/BnA

Table 1.2 Details for the MAGPIS and CORNISH surveys.

[Hoare et al., 2012; Purcell et al., 2013]. These legacy surveys provide resolution and sensitivity apposite to the detection and discerning of sources occupying angular scales down to  $\sim 1''$ . At the same time, they cover wide areas on the sky and overcome the high extinction of the plane. In this way, a multi-wavelength treasure trove of unbiased, high-resolution and statistically representative data are available to aid the studies of the earliest phases of massive star formation.

### The CORNISH survey and its context

The CORNISH survey, the first Galactic plane survey that is comparable in resolution and coverage with the GLIMPSE data, maps the compact ionised gas within the ISM. At present, the CORNISH catalogue of the northern Galactic plane, imaged with the VLA, is the most uniformly sensitive, homogeneous and complete list of northern compact radio sources at 5 GHz.

Among the key scientific goals of the CORNISH survey is massive star formation. In particular, it aims to fully characterize the population of the most compact H II regions. Distinguished as a separate observational class by Wood and Churchwell [1989b], ultra-compact H II (UCHII) regions link the accretion phase when a massive protostar is formed, and the development of a more diffuse and less obscured H II region. UCHII regions are defined as embedded photoionised regions  $\lesssim 0.1$  pc in diameter, with emission measures  $\gtrsim 10^7$  pc cm<sup>-6</sup> and electron densities  $n_e \gtrsim 10^4$  cm<sup>-3</sup> [Wood and Churchwell,

1989b]. They are the most luminous objects in the Milky Way in the far-IR, and are observable in the radio part of the spectrum if their luminosities are equivalent or higher than a B3 main-sequence star with  $L_{\text{bol}} \sim 10^3 L_{\odot}$  (Bohm-Vitense 1981, Meynet and Maeder 2003). The Lyman continuum ionising flux corresponding to zero-age main-sequence stars with spectral class from B2 to O5 is in the range  $10^{44} - 10^{49}$  photons  $\text{s}^{-1}$ . Estimating the distances to UCHII regions, together with their density distributions, luminosities, morphologies, kinematics and relationship to the parent molecular clouds is essential. These properties can be used to help understand not only the effect of UCHII regions on their environment, but also test the existing evolutionary models of massive star formation and the structure of the Milky Way [Hoare et al., 2007].

The CORNISH team identified 240 ultra-compact H II region candidates. The sample provides the largest unbiased and uniform collection of these objects to date and can be used to help answer questions such as the feedback process in high mass star formation regions and the Milky Way structure traced by them, the evolution of H II regions and their effect on their environment, the star formation efficiency in the Galaxy, the upper Initial Mass Function (IMF) for different environments, among many others. Another important aspect to be explored is the morphology of UCHII regions.

The lifetime of the UCHII phase can be estimated from comparing the numbers of field OB stars in the Milky Way from the latest IR surveys to the relative numbers of UCHII regions [Mottram et al., 2011; Wood and Churchwell, 1989a,b]. Such an estimate, together with knowledge of the stellar content of representative UCHII samples and with current theoretical models, can be used to address the ‘lifetime problem’ of UCHII regions [Wood and Churchwell, 1989b]. It arose because simple H II region models (i.e. monotonic, pressure-driven expansion) suggest a brief dynamical lifetime of the UCHII phase, which would result in low UCHII numbers. At a typical expansion speed of

$\sim 10 \text{ km s}^{-1}$ , an H II region would exceed a size of 0.1 pc in about  $10^4$  years – just one percent of the lifetime of its ionising star (see e.g. Kahn et al. 1954, Roth et al. 2013). Observed UCHII numbers did not seem to match these estimates, as around 10% of O stars are associated with UCHII regions. This indicated a confining mechanism at work, prolonging the UCHII lifetime by a factor of ten or more (see e.g. Dyson et al. 1995; Hollenbach et al. 1994; Roth et al. 2013; Van Buren et al. 1990).

Previous radio UCHII samples comprise predominantly IR-targeted surveys based on IRAS point sources with far-IR colours similar to well-known UCHIIIs. Wood and Churchwell [1989a,b] selected a sample of 75 UCHIIIs (out of  $\sim 1600$  candidates in the Galaxy) to observe at 6 cm and 2 cm with the VLA using this method and classified them morphologically. Similarly, Miralles et al. [1994] selected and observed 12 sources at 6 and 2 cm with the VLA. Garay et al. [1993] also based their selection on strong IRAS point sources associated with compact H II regions and produced multi-frequency observations with the VLA (resolved and morphologically classified). Kurtz et al. [1994] performed radio-continuum observations on 59 UCHIIIs, again IRAS-selected. De Pree et al. [2005] located and resolved a hundred objects within the massive star forming regions W49A and Sgr B2 from VLA radio continuum and radio recombination line emission observations (and revisited the Wood and Churchwell 1989b morphological classification).

The RMS survey [Lumsden et al., 2013; Urquhart et al., 2009, 2007] marked a new era of massive star formation studies. Colour-selected sources from MSX [Price et al., 2001] and 2MASS [Skrutskie et al., 2006] were followed up by arcsecond-resolution IR, as well as mm and radio observations. These, together with archival data, were used to identify for the first time a Galaxy-wide sample of  $\sim 900$  candidate massive young stellar objects (MYSOs) and as many H II regions [Lumsden et al., 2013]. Mottram et al. [2011] used the RMS

survey to determine a lifetime of 300 kyr for the compact H II region phase (about 3-10% of the MS lifetime). Davies et al. [2011] simulated the RMS survey for different accretion models and compared the model results to the observed luminosity distribution. H II regions were assumed to be forming through simple Strömgen expansion (a uniform density medium and no stellar wind).

The biggest disadvantage of IR-selection in UCHII studies is the discrimination against the most deeply-embedded sources. The issue is resolved by unbiased radio surveys. The first larger-scale unbiased survey at 1.4 GHz (inner Galaxy, VLA B and A/B configuration) was conducted by Zoonematkermani et al. [1990] and was followed by (VLA C configuration) 5 GHz observations [Becker et al., 1994] covering about a fourth of the GLIMPSE region. The survey (now contained within a larger collection of re-reduced archival radio data known as MAGPIS, see Helfand et al. 2006) is useful for the study of extended thermal sources such as evolved H II regions, bubbles, etc. However, UCHII regions are unresolved or marginally resolved, and even in some instances missed altogether due to insufficient sensitivity. The CORNISH survey covers the entire GLIMPSE region and its noise level of 0.4 mJy ensures the detection of virtually all UCHIIs within the covered area. More details are included in Table 1.2.

### 1.2.2 Morphological studies

Strömgen [1939] derived that an H II region embedded in a uniform medium of neutral hydrogen has a size equal to its Strömgen radius  $R_S$ . This is the radius at which the recombination rate density ( $\alpha n^2$ ) and the total rate of

ionizing photons  $N^*$  are in balance within the volume of the sphere:

$$R_S = \left( \frac{3N^*}{4\pi\alpha n^2} \right)^{\frac{1}{3}}. \quad (1.1)$$

For typical values,  $100 \text{ pc} > R_S > 10 \text{ pc}$ .

### Observed UCHII region morphologies

Evidence for departures from spherical morphology of the compact H II region components located within extended H II regions was reported shortly after the advent of aperture synthesis radio observations. An early such example are the observations of bright ‘compact’ and ‘sub-compact’ H II regions carried out by Israel [1977]; Israel et al. [1973] at 21 cm (24.6'' synthesized beam) and at 6 cm (7.2'' synthesized beam)<sup>3</sup>. Benson and Johnston [1984] observed compact H II regions at arcsecond resolution in Sgr B2 and G34.3+0.2 with clearly distinguishable cometary morphologies. Wood and Churchwell [1989b] were the first to define five morphological classes of UCHII regions, using VLA radio continuum snapshots and recombination line data with 0.4'' resolution at 2 and 6 cm. They observed 75 UCHIIs, out of which  $\sim 43\%$  were classified as spherical or unresolved,  $\sim 20\%$  – cometary,  $\sim 17\%$  – irregular or multiply peaked,  $\sim 16\%$  – core-halo, and  $\sim 4\%$  – shell. In a follow-up study, Kurtz et al. [1994] used similar techniques to identify and classify 59 UCHII regions. They found a similar distribution of morphological classes. Walsh et al. [1998] reported that the resolved UCHIIs (at arcsecond resolution) in their southern UCHII sample<sup>4</sup> were either cometary (43%) or irregular (40%). The observed recurring morphology of UCHII regions is evidence for ordered underlying physical processes. Studying these morphologies provides information about

<sup>3</sup>The observations were carried out with the Westerbork Synthesis Radio Telescope (WSRT)

<sup>4</sup>Observed with the Australia Telescope Compact Array (ATCA).

the state of the surrounding medium soon after the formation of massive stars [Hoare et al., 2007].

De Pree et al. [2005] revised the Wood and Churchwell [1989b] classification scheme through the addition of a bipolar class (UCHIIs elongated along one axis, with broad radio recombination lines) and the removal of the core-halo class. The latter was deemed obsolete, as through the use of multi-configuration imaging (which provides more spatial dynamic range) it was revealed that UCHII regions cannot be treated as isolated entities – virtually all are associated with large-scale diffuse emission that is distinguishable from the compact core. In their VLA-D-configuration radio-continuum survey, Kurtz et al. [1999] found 12 UCHIIs associated with extended emission out of 15 observed fields. The authors concluded that for about half of these sources, the ultra-compact and extended (typically 1' in diameter) emission are likely directly connected, and highlighted the need for models where this interconnectedness is addressed. In the multi-configuration 21 cm radio continuum survey and follow-up molecular line observations of 16 UCHIIs by Kim and Koo [2001, 2003], the authors found that in 15 cases, the compact and extended components were likely ionised by the same source, as their molecular line velocities were the same. Ellingsen et al. [2005] observed eight southern UCHIIs, selected through their association with class II methanol masers, and also concluded that the extended and compact radio continuum emission coexists within H II regions for a long time, and that H II regions evolve within hierarchically structured molecular clouds. The main difference between the results by De Pree et al. [2005] and previous classification statistics is that 28% of the sources were classified as shell-like. As discussed in the review of existing morphological surveys by Hoare et al. [2007], almost half of the shell-like sources classified by De Pree et al. [2005] could also be classified as cometary, as they are highly asymmetric.

Higher-sensitivity observations of cometary UCHII regions can reveal cavities evacuated by the wind from the ionising star, which are not seen in less sensitive observations, and cause them to appear more shell-like/limb-brightened. Other classifications can also change, depending on the resolution, type, and sensitivity of the radio observations used. At higher resolution, spherical regions typically reveal further structure (see e.g. the discussions by Hoare et al. 2007; Wood and Churchwell 1989b).

The original morphological classification by Wood and Churchwell [1989b] and the updated classification by De Pree et al. [2005] are presented in Fig. 1.7. These classifications rely only on radio maps – the sources were selected using the IRAS catalogue, but at poorer than arcmin resolution<sup>5</sup>, it contained no morphological information for UCHIIIs. Using radio data alone to explore their spatial structure clearly comes with dynamic range limitations due to the nature of high-resolution radio interferometric observations, as discussed by De Pree et al. [2005]; Hoare et al. [2007]; Wood and Churchwell [1989b]. Addressing these limitations through the use of deep, multi-configuration observations is, with current up and running radio-interferometric arrays, time-consuming and thus an impractical approach for conducting large surveys. The next generation of instruments, notably the Square Kilometre Array (SKA), will alleviate this issue [Manoj et al., 2016]. At present, existing classification schemes can be updated by expanding them into more complete, multi-wavelength classifications.

### **Theoretical models of UCHIIIs**

Various physical mechanisms have been proposed to explain the origin of the observed morphological types, but linking the observational results with models is made difficult by the fact that all morphological classifications are limited by the resolution, sensitivity, and dynamic range of the observations. Other pitfalls

---

<sup>5</sup> <https://irsa.ipac.caltech.edu/IRASdocs/exp.sup/ch7/J.html#2>

are due to the subjective nature of visual classifications, and the complexity of processes shaping young H II regions.

The cometary class, with its highly regular structure and its ubiquity, has been used to test past theoretical models. Notably, those are the champagne flow/blister model [Israel, 1978; Tenorio-Tagle, 1979], the bow shock model [Reid and Ho, 1985; Van Buren et al., 1990], the mass-loading/clumpy models [Dyson et al., 1995]. The work by Lumsden and Hoare [1996] highlighted where the first two models fell short, through observing IR lines to analytically model the density and velocity structure of the well-studied cometary UCHII G29.96–0.02. The bow shock model fails to explain the large velocity gradient across the tail of the UCHII, which can be explained by the champagne model predictions. The authors noted that the effects of stellar winds should be included in the champagne model to match more features of the observational data.

This was supported also by more recent observational findings, in particular the kinematic study by Cyganowski et al. [2003], (and the follow-up by Immer et al. 2014), of the DR 21 massive star-forming region containing two cometary H II regions, aligned nearly perpendicular to each other. Based on the observed gas velocities, which could not be explained by champagne flow or bow shock alone, Cyganowski et al. [2003] proposed a hybrid model. Figure 1.5 (corresponding to Fig. 4 in Cyganowski et al. 2003) illustrates the velocity field vectors for each main category of theoretical models.

In recent theoretical efforts, the mixed scenario has been put forward to help investigate the main physical processes shaping UCHII regions. Key in coming closer to agreement with observations was the addition of stellar winds, to reproduce swept-up ionised shells. A cohort of hybrid hydrodynamical models were investigated by Arthur and Hoare [2006], such as champagne flow plus stellar wind models, and combined bow shock and champagne flow

models with varied density gradients, stellar wind strengths, and stellar motion. Arthur and Hoare [2006] combined observational and computational efforts and demonstrated that the commonly observed limb-brightened morphologies can be explained with the inclusion of stellar winds in the champagne flow model. Steggle et al. [2017] took this a step further to simulate cometary H II regions with strong stellar winds and ionising stars born off-centre from power-law density gas clouds for a wide range of densities and stellar masses. Observed features such as cavities and limb-brightening were successfully reproduced.

With these models, the observed spherical and shell morphological classes can be explained to arise due to different viewing angles, luminosities, and distances of the cometary H II region (see Fig. 1.6). For example, morphologies are more shell-like at smaller angles between the viewing direction and the axis of symmetry of the UCHII, as well as when the source is better resolved – in particular, for nearby, lower-luminosity UCHIIs. More spherical morphologies would arise for higher-luminosity, more distant UCHIIs, and/or for UCHIIs whose expansion is limited by a denser immediate environment.

A number of theoretical works predict time-variable radio flux densities (Franco-Hernández and Rodríguez 2004, Rodríguez et al. 2007, Gómez et al. 2008, Galván-Madrid et al. 2008, Peters et al. 2010a,b,c, Galván-Madrid et al. 2011, Klassen et al. 2012a). Such models predict e.g. optically thick clumps in the stellar wind blocking the radiation [Galván-Madrid et al., 2008; Peters et al., 2010a], or surface temperature fluctuations of the forming star [Franco-Hernández and Rodríguez, 2004]. The flux changes could be associated with morphological changes across observational epochs. In the Keto [2007], Peters et al. [2010a], and Galván-Madrid et al. [2011] models, accretion has not ceased during the early H II region phases and can lead to their gravitational ‘trapping’ within the accretion flow. A bipolar morphology of the H II region is expected in the case of an ionised accretion flow (e.g. Keto 2007).

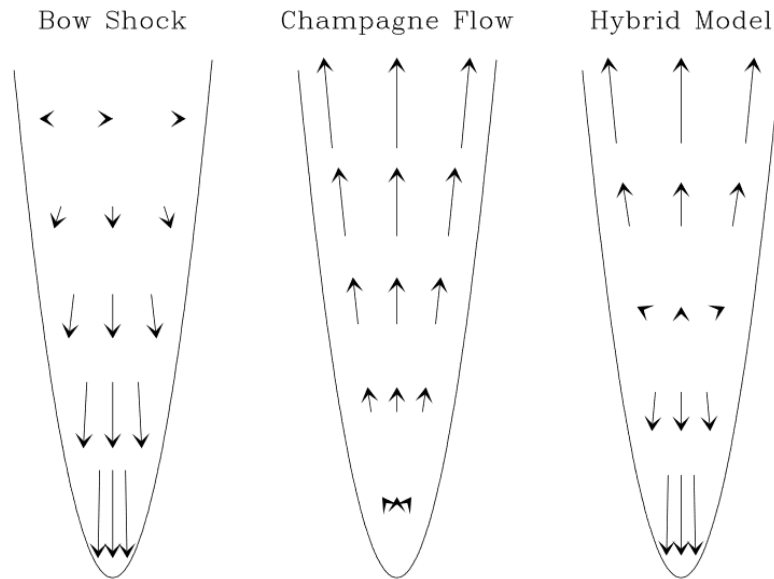


Fig. 1.5 This is Figure 4 in Cyganowski et al. 2003, presenting the velocity fields in cometary H II regions for three models. From left to right, these are the bow shock model, the champagne flow model, a hybrid model. The ambient molecular gas surrounding the regions serves as the velocity reference for all these models.

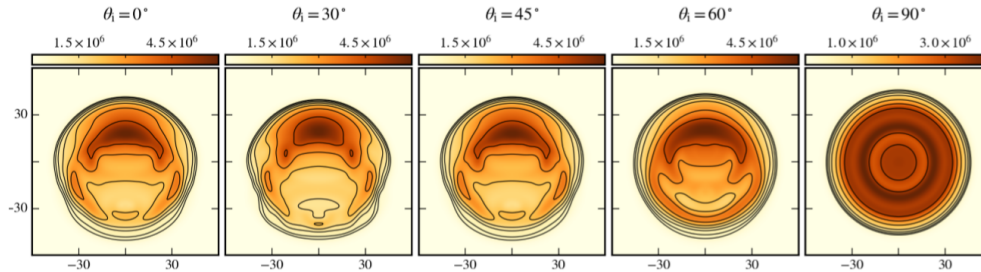


Fig. 1.6 This is Figure 7 in Steggle et al. 2017, presenting emission measure maps of a simulated cometary UCHII region viewed at different projection angles.

### Molecular masers

Masers indicate the presence of warm (IR pumped) as well as shocked (collisionally pumped) gas. The 6.7 GHz transition of methanol produces the brightest, most widespread masers. Such masers are expected to be associated with the hot molecular core phase, as well as with younger H II regions (HCHIIs), and their presence in the vicinity of UCHIIs is thus possible evidence

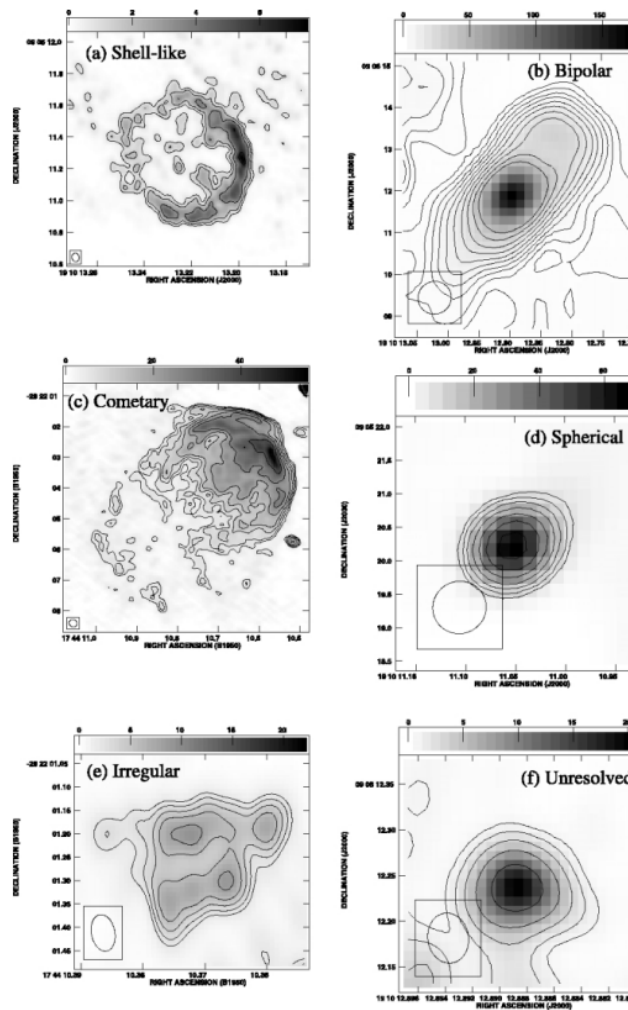
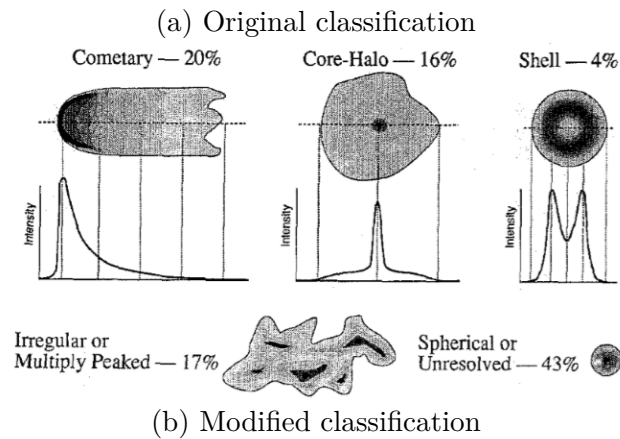


Fig. 1.7 *Panel a*: The five original morphological classes of UCHII regions, with their respective definitions, as they appear in the review by Churchwell 1990. The 75 UCHIs were observed at 2 cm and 6 cm with the VLA, at  $0.4''$  resolution. *Panel b*: Revised morphologies from De Pree et al. [2005]: (a) Shell-like source, W49A/D (7 mm; De Pree et al. 2004); (b) bipolar source, W49A/A (3.6 cm; De Pree et al. 1997a); (c) cometary source, Sgr B2 Main/I (1.3 cm; Gaume et al. 1995); (d) spherical source, W49A/R (3.6 cm; De Pree et al. 1997a); (e) irregular source, Sgr B2 Main/F2 (7 mm; De Pree et al. 1998); and (f) unresolved source, W49A/A2 (7 mm; De Pree et al. 2004).

for sequential/triggered massive star formation (e.g. Hu et al. 2016). Walsh et al. [1998] found a significant difference between the general proximity of methanol and water masers to their cometary and irregular UCHIIIs, which is indicative of different environments stimulating the masing. The Arecibo Galactic plane methanol maser survey uniformly sampled 18.2 square degrees in the region  $32.5^\circ < l < 53.7^\circ$ ,  $|b| < 0.41^\circ$  [Pandian et al., 2007]<sup>6</sup>. Other notable maser surveys are the HOPS survey [Walsh et al., 2011], which supplies a catalogue of water masers in the Southern plane, and the Methanol Multibeam (MMB) survey, covering over 60% of the Galactic plane between  $|b| < 0.41^\circ$  [Green et al., 2008]. These provide an opportunity to look for maser associations of UCHIIIs and thus compare the immediate environments of different morphological classes.

### 1.2.3 Distances to Galactic UCHIIIs

A crucial step towards characterising UCHII regions is to determine the distance to these sources. One can then convert measured parameters (e.g. fluxes and angular sizes) into physical quantities (e.g. luminosities and physical sizes). Accurately derived distances to UCHII regions are used to test the current models of the face-on Galactic structure [see e.g. Urquhart et al., 2013]. As the heavy obscuration hinders the use of any optical distance determination techniques, the distances to most UCHII regions are kinematically derived. The kinematic distance is found by fitting the radial velocity of the source to a Galactic rotation curve (e.g. Brand and Blitz 1993; Reid et al. 2009), using radio or mm spectral line data. Errors in the calculated distance arise when the source radial velocity differs from the one assumed by the model (e.g. velocity

---

<sup>6</sup>For reference, CORNISH covers  $10^\circ < l < 65^\circ$ ,  $|b| < 1^\circ$ , and the scale height of UCHIIIs is  $|b| < 0.6^\circ$ .

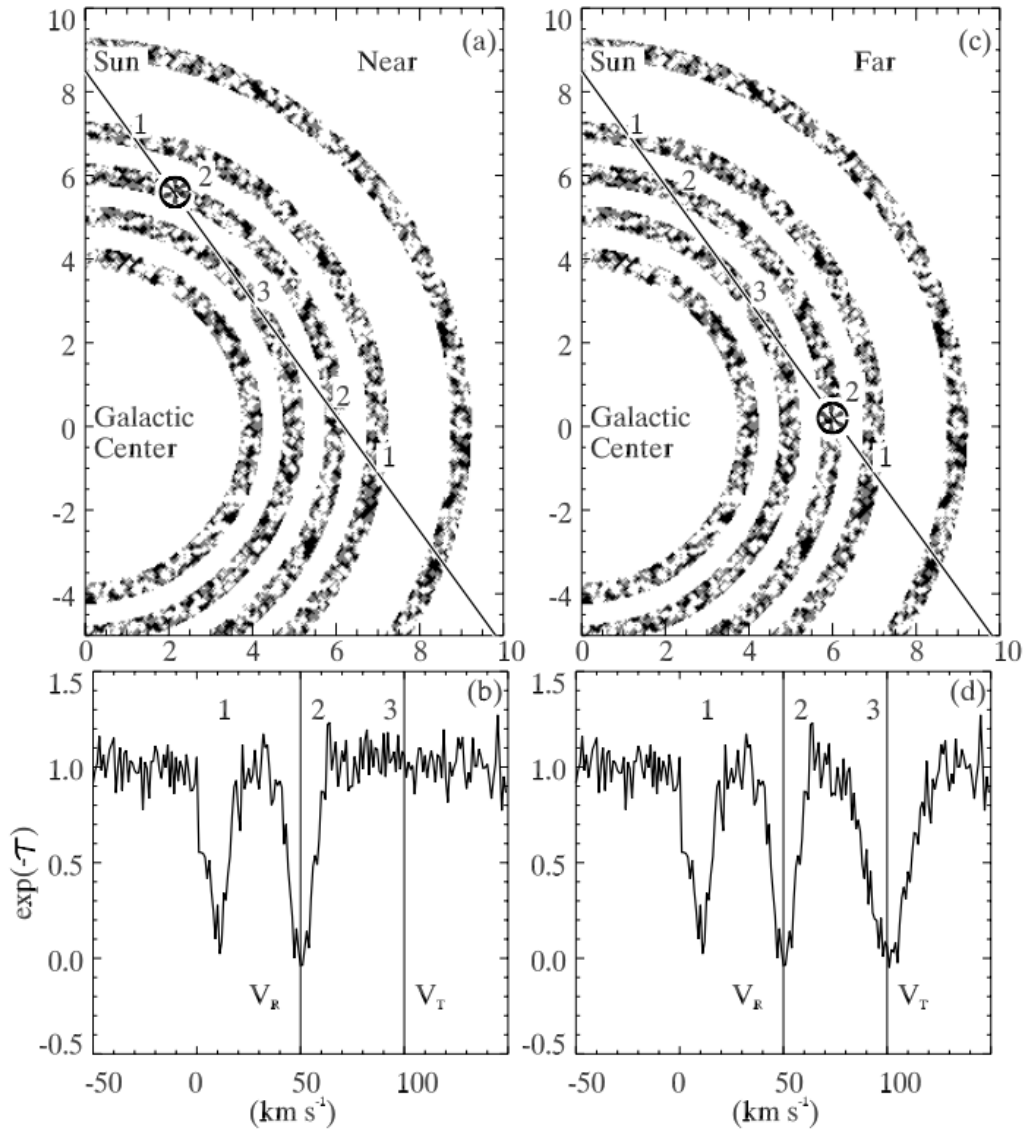


Fig. 1.8 Image illustrating the origin of the kinematic distance ambiguity (from Kolpak et al. [2003]). The view is from the north Galactic pole, i.e. the rotation is clockwise. The solid straight line traces the line of sight to the H II region through cold and clumpy H I. The radial velocity is the same at the near (a) and far (c) distance of the source's orbit. The tangent point (3) is a velocity maximum, and there is no kinematic distance ambiguity at the tangent velocity. Absorption spectra (line-to-continuum intensity ratio vs. H I radial velocity) are included for each case – near (b) and far (d), with the source recombination line velocity and the tangent point velocity marked on top of the absorption.

errors of about  $10 \text{ km s}^{-1}$  due to the velocities departing from circular rotation as a result of streaming motions) [Anderson and Bania, 2008].

Distance estimates for the outer Galaxy are relatively straightforward. However, a major obstacle arises when one seeks the kinematic distance for objects within the Solar circle. At Galactic radii smaller than that of the Sun, two possible distances exist for each radial velocity. These distances, known as near and far, are situated at equal intervals from the tangent point distance. The kinematic distance ambiguity (KDA) is not present only for the tangent point velocity, which is the maximum radial velocity. This is illustrated in Figure 1.8. Different methods exist to assign the correct kinematic distance to the sources of interest – for example, H I Emission/Absorption (H I E/A), H I Self-Absorption (H I SA), or using absorption lines from other molecules, for example formaldehyde (H<sub>2</sub>CO) (as discussed by Anderson and Bania 2008). This is made possible by the fact that H II regions are associated with strong radio continuum emission and that interstellar lines or H I absorb the continuum free-free emission. This is particularly true for deeply embedded sources such as UCHII regions, where the free-free radio continuum emission dominates the Galactic background emission at 21 cm. More significantly, UCHII regions are exclusive to massive stars, which are the only ones that produce significant radiation exceeding the Lyman limit [Hoare et al., 2007]. As the maximum radial velocity along the line of sight is always the tangent velocity, lack of absorption between the source and tangent velocity reveals that the source is located at the near distance. Otherwise, the far distance is assigned (or the tangent distance, in the cases when the source velocity equals the tangent velocity).

### 1.2.4 Infrared signatures

#### The mid-infrared

As discussed by Watson et al. [2008], the emission detected in the vicinity of hot stars is dominated by a different emission process in each of the four mid-IR GLIMPSE-IRAC bands. This emission is excited by the far-UV stellar flux and is therefore particularly bright in H II regions and reflection nebulae illuminated by massive stars (e.g. Draine and Li 2007; Peeters et al. 2004). The mid-IR images of UCHII regions have a structure similar to larger IR bubbles. The hot dust component within the ionised region is seen in 24  $\mu\text{m}$  thermal continuum emission. The surrounding photo-dissociation region (PDR) contains large polycyclic aromatic hydrocarbon (PAH) molecules, dust, and swept-up interstellar gas.

The presence of PAH emission is based on observing mid-IR shells around the H II region. These shells are dominated by strong PAH features in the IRAC bands at 3.6, 5.8, and 8  $\mu\text{m}$ , and are not seen at 4.5  $\mu\text{m}$ . The inner surface of each shell is located at a distance from the ionising star that is equal to the PAH destruction radius. The 3.6  $\mu\text{m}$  band is dominated by stars, with contributions from the diffuse PAH feature at 3.3  $\mu\text{m}$  and perhaps from scattered starlight. The 4.5  $\mu\text{m}$  band exhibits no PAH features; the brightest contributors are stars and the diffuse emission is due to the shared contribution of lines from H II regions ( $\text{Br}\alpha$  and  $\text{Pf}\beta$ ) and from shocked molecular gas (from  $\text{H}_2$  and CO). CO gas shocked by protostellar outflows is observed at 4.5  $\mu\text{m}$  in the form of extended green objects (EGOs) in the colour *Spitzer* images [Cyganowski et al., 2011, 2008] and thus serves as a signpost of early star formation stages. The diffuse emission in the 5.8  $\mu\text{m}$  band is dominated by the 6.2  $\mu\text{m}$  PAH feature, apart from the immediate vicinity of O stars, where PAHs are destroyed and the contribution is from thermally emitting dust and

stochastically heated small grains [Watson et al., 2008]. The innermost shell is seen at 8  $\mu\text{m}$ . The diffuse emission in the 8  $\mu\text{m}$  band is dominated by the strong 7.7 and 8.6  $\mu\text{m}$  PAH features, or by thermal emission of dust heated by the hot stars and Lyman- $\alpha$  photons [Hoare et al., 1991; Roelfsema et al., 1996; Watson et al., 2008].

### **The near-infrared**

At near-IR wavelengths, the continuum emission from UCHII regions is mainly from bound-free and free-free emission from the nebular gas. Emission from hot grains, non-thermal equilibrium emission from small grains, and scattered light also contribute. The visual extinction in the line of sight to UCHIIs can be estimated from their J, H and K fluxes, assuming the diffuse emission is due to purely nebular gas emission. Several methods can be utilised to achieve this, such as the use of near-IR colours, or ratios of the near-IR flux to the radio flux [Willner et al., 1972]. When using the colour-dependent methods, provided sufficiently reliable magnitude measurements of the embedded sources, one's choice comes down to a compromise between scattering effects and infrared excess. Dust excess (typically pronounced in the K-band) causes the  $H - K$  colours to appear redder, and scattered light (due to dust grains) at shorter wavelengths results in bluer  $J - H$  colours [Porter et al., 1998]. It is useful to compare the results from the different methods and in this way weigh the severity of systematic issues while providing an extinction range for the studied sources.

### **1.2.5 Use of X-ray data in UCHII studies**

Knowledge of the multi-wavelength properties of massive stars is key to the better understanding of the H II regions they ionise. Extinction associated

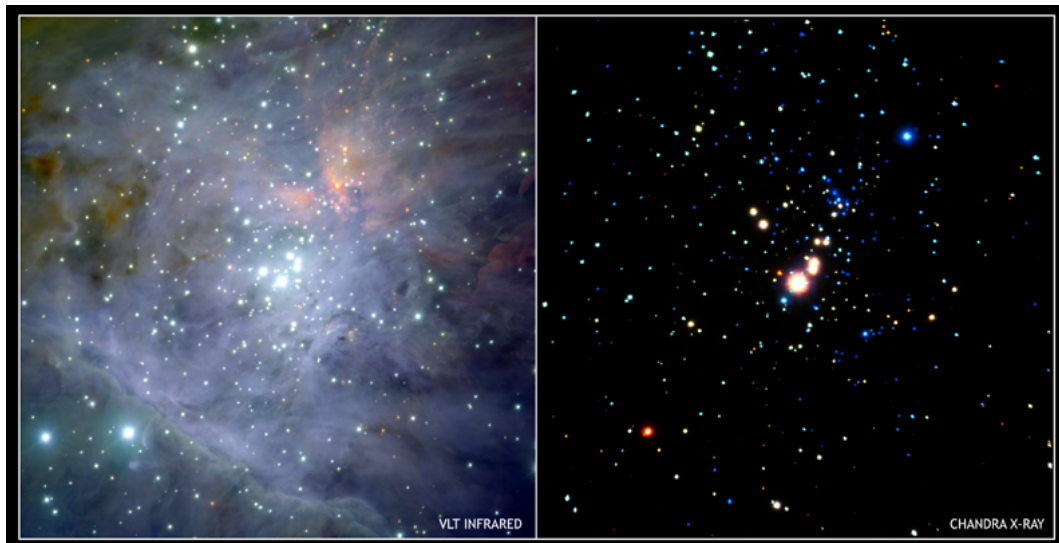


Fig. 1.9 Image of the central region (field of view 5.5 square arcmin) of the Orion Nebula Cluster: left panel – IR image (ESO Very Large Telescope, McCaughrean et al. 2002); right: comparison with *Chandra* data for the same field of view (FOV) [Getman et al., 2005]. All five Trapezium cluster stars (seen in the centre) are bright in X-rays.

with massive star forming regions (MSFRs) is an obstacle that optical and UV spectroscopy cannot overcome. Near-IR spectroscopic studies are likely to detect the strong nebular continuum emission as it dominates over the emission from the central sources [Hoare et al., 2007]. X-rays can overcome the cocoon of gas and dust around these sources, and there is very little source confusion and contamination by unrelated sources [Anderson et al., 2011; Feigelson et al., 2007]. The low source confusion is particularly valuable for uncovering the young stellar populations in massive star forming regions. A side-by-side comparison of IR [McCaughrean et al., 2002] and X-ray [Getman et al., 2005] images of the Trapezium cluster in the Orion Nebula is shown in Figure 1.9, with the Trapezium cluster stars dominating the field centre (see e.g. Schulz et al. 2001, Flaccomio et al. 2003, Feigelson et al. 2003, Stelzer et al. 2005, for X-ray studies of the region).

Thermal X-ray emission arises from optically thin plasma ( $T > 10^6 - 10^7 \text{K}$ ) in the form of bremsstrahlung or line emission<sup>7</sup>. Until relatively recently, X-rays have been rarely detected from MSFRs. This has been due to technological limitations and observational problems such as the high visual extinction within MSFRs, which absorbs the line-of-sight soft X-ray emission. As well as this, observations have mostly been of evolved massive star formation sites and not the youngest embedded stages. Modern X-ray satellite observatories are capable of detecting sources obscured by  $A_V \approx 10 - 100$  mag, and sometimes up to 1000 mag, allowing the rapid growth of this niche field [Feigelson et al., 2007]. X-ray counterparts to near-IR sources in SFRs provide two independent methods of measuring the extinction to the region (e.g. Grosso et al. 2000, Law and Yusef-Zadeh 2004, Stelzer et al. 2005). In particular, the absorption column density at  $\sim 3$  keV derived from spectral fitting provides a valuable comparison to the near-IR/optical extinction [Law and Yusef-Zadeh, 2004].

There are some notable differences between the X-ray imprint of low and high mass star forming regions, which can provide vital observational clues about the underlying physical mechanism in each case. For instance, diffuse X-ray emission is observed in high-mass regions. Diffuse X-ray emission in the soft band has been detected in some young massive clusters and the nebulae around Wolf-Rayet (WR) stars. The emission is consistent with a region of a size about 5 – 10 pc with thermal plasma of  $T \sim 10^6$  K and  $L_{\text{tot}} \approx 10^{33} - 10^{34}$  erg s<sup>-1</sup> [Tsujimoto et al., 2006]. Both types of objects are believed to be too young to host SN remnants, and the predictions of the wind-blown bubble model (see e.g. Castor et al. 1975, Weaver et al. 1977) matches the observed emission well. In this model, mass lost via stellar winds and eruptions interacts

---

<sup>7</sup>X-ray point sources that require non-thermal models are not discussed here as they are typically associated with X-ray binaries, where the X-ray emission is synchrotron radiation or inverse Compton scattering from the accretion disc around a compact degenerate object such as a white dwarf, neutron star or black hole.

with the surrounding material and forms cavities surrounded by a dense shell, thus creating a wind-blown bubble.

The origin of hard ( $k_B T > 2 \text{ keV}$ ) extended emission is not well-understood. It is typically associated with smaller regions (0.1 – 1 pc) and plasma temperatures exceeding  $10^7 \text{ K}$ . The spectra can be non-thermal and can exhibit fluorescent Fe lines (6.4 keV), which are evidence for the presence of cold matter [Tsujiimoto et al., 2006]. Suggested explanations include unresolved point sources (low-mass and high-mass) [Takagi et al., 2002], colliding winds (rather than a wind colliding with cold matter at rest) [Cantó et al., 2000], magnetic activity of young O stars [Stelzer et al., 2005], magnetic flares from (low-mass) YSOs [Feigelson and Montmerle, 1999], or even a special case of wind-blown bubble. Spectral modelling of available X-ray data can uncover the mechanism of X-ray production coincident with H II regions.

### 1.3 Radio interferometry – brief overview

Radio interferometry provides the high resolution needed for the study of massive star-forming regions through combining signals from a radio telescope array and producing high quality synthesis images. The independent measurements from the radio antennas are combined into an image of resolution  $\theta$  according to

$$\theta \sim \frac{\lambda}{B}, \quad (1.2)$$

where  $B$  (the ‘baseline’) is the maximal spacing between each pair of dishes, and  $\lambda$  is the observed wavelength. The resolution increases for increasing baseline. The brightness distribution of the observational target is not directly measured. Instead, what is mapped is a quantity known as the ‘complex visibility’ between antennas,  $V_\nu(u, v)$ , which is a unique function of the source brightness. An

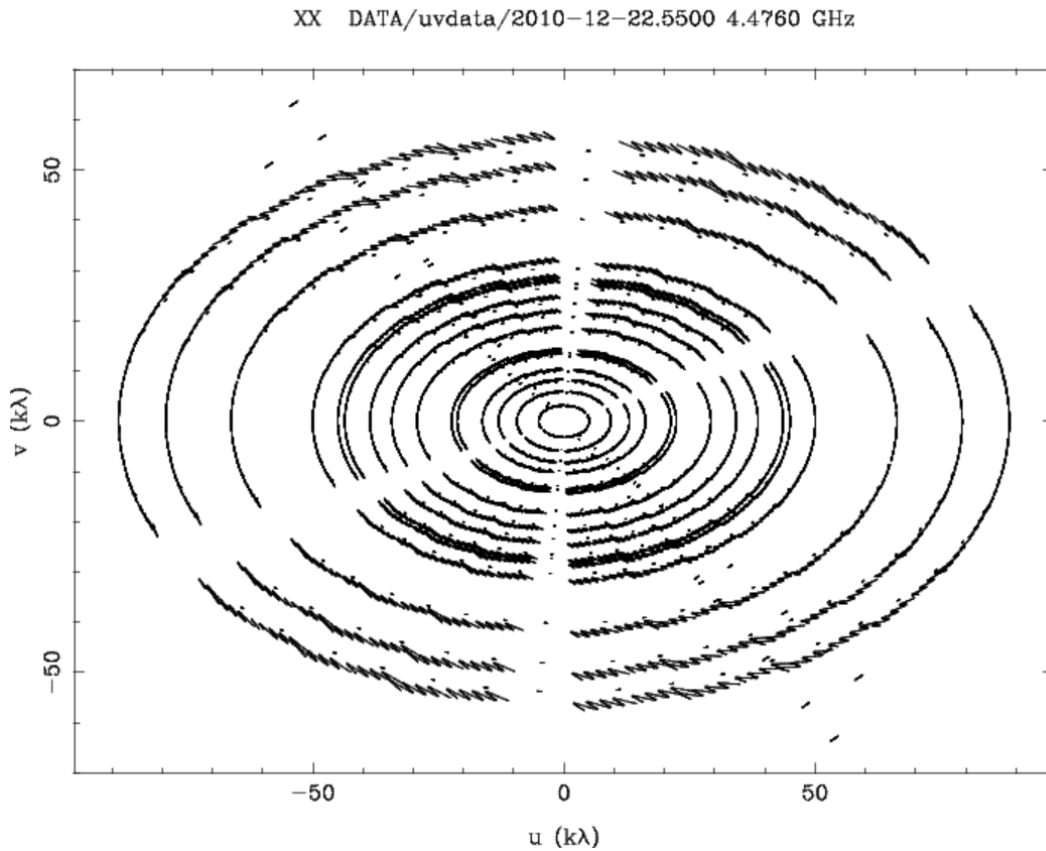


Fig. 1.10 Visibility  $(u, v)$  coverage of a source from one day of observations (example ATCA data from the CORNISH-South survey). The concentric curves represent different sampled regions of  $(u, v)$  space.

interferometer makes one measure of the visibility at a time, at a baseline coordinate  $(u, v)$  [Wilson et al., 2009]. The definition for the visibility function (in 2D) is:

$$V_\nu(u, v) = \iint I_\nu(l, m) e^{-2\pi i(ul+vm)} dl dm, \quad (1.3)$$

where  $(l, m)$  are the sky coordinates (the direction cosines of a point on the source) and  $(u, v)$  are the baseline coordinates. The latter define the  $u - v$  plane – the Fourier-transform plane of the angular distribution of the target on the sky. This can (roughly) be compared to the plane of the surface of a single equivalent dish. Via the methods of aperture synthesis, the intensity distribution  $I_\nu$  is derived from the measured visibility function for a part of the

sky. Inverting the integral through a Fourier transform gives the real intensity

$$I_\nu(l, m) = \int \int V_\nu(u, v) e^{2\pi i(ul+vm)} dudv \quad (1.4)$$

by the Van Cittert-Zernike theorem [Wilson et al., 2009]. This, however, represents an ideal case, in which the interferometer and Earth’s rotation are employed to obtain the source visibilities very densely over the  $u - v$  plane. A Fourier transform of such a densely sampled  $V_\nu$  would produce an image which is equivalent to an observation from a single dish of diameter equal to the array diameter. In practice, radio interferometry observations leave gaps in the  $u - v$  plane coverage. A two-dish interferometer would gather data over two elliptical arcs in the  $u - v$  plane due to the rotation of the Earth. More antennas add more such arcs, but there would always be missing data due to the unavoidable spacing between the individual antennas (Fig. 1.10). The missing data cause side-lobes in the synthesised antenna beam. The result is known as a ‘dirty’ image,

$$I_{\nu,D} = \int \int V_\nu(u, v) S(u, v) e^{2\pi i(ul+vm)} dudv , \quad (1.5)$$

where  $S(u, v)$  is the  $u - v$  plane sampling function ( $S(u, v) = 1$  for a measurement and 0 otherwise). The dirty image is the convolution of the true distribution and the point spread function (PSF):

$$I_{\nu,D}(l, m) = I(l, m) * \int \int S(u, v) e^{2\pi i(ul+vm)} dudv = I(l, m) * B(l, m) . \quad (1.6)$$

$B(l, m)$  is known as the ‘dirty’ beam and can differ significantly from an ideal PSF for poor sampling of  $S(u, v)$ . Even when the field that is being imaged contains only unresolved sources, the superposition of the dirty beams associated with each source makes the image hard to interpret. A standard

approach is to apply a CLEAN algorithm [Högbom, 1974] to reduce the dirty beam artefacts. This consists of:

- approximating the image as a field of point sources;
- finding the brightest point in the dirty map;
- subtracting the (appropriately scaled) dirty beam from this position;
- storing the location and subtracted intensity (as a ‘clean component’);
- finding the brightest point in the thus modified dirty map;
- repeating the previous three steps until no further subtraction can occur without creating negative values in the dirty map.

In this process, many parameters can be adjusted to affect the final image, depending on the specific scientific goal and on the best compromise to obtain a CLEANed (but not over-CLEANed) image. Other improvements can be made, for example ‘tapering’, i.e. convolving  $V_\nu$  with a Gaussian to reduce the terms at the largest baselines. This is analogous to apodization, so the image artefacts are suppressed but the synthesized beam diameter is increased [Wilson et al., 2009].

Aperture synthesis is also associated with some reduction problems. For one, very small baselines are not achievable, which reduces the interferometer sensitivity dramatically at small spatial frequencies. This leads to lost flux for extended features of low surface brightness. Another issue is caused by very strong sources, as they may not appear in the high-quality part of the map while their dirty artefacts do. In such case, the brightest point of the dirty map may not be one and the same with the source position and the CLEAN algorithm will not work. Earth’s atmosphere may cause phase errors. Turbulence, charged particles in the ionosphere, variations in the refractive index due to water vapour, all have their negative effect in different radio frequency ranges. Common methods applied to reduce these effects on the

phase include gathering data over short time intervals or observing calibrator sources. Closure phases and amplitude information in the array can be modelled in order to deduce the structure of the target independent of the phase errors. Self-calibration can be performed by ensuring that there is a bright point source within the primary beam that is detected at all baselines.

## 1.4 Thesis motivation and outline

As highlighted in this introduction, a better understanding of the dominant processes involved in massive star formation is required. Studying UCHII regions is, with present observational capabilities, the most reliable way to obtain the global properties of the sites where newborn Galactic OB stars form. UCHII regions are readily seen throughout the Galactic disk due to their brightness in IR and radio emission, resulting in much better number statistics of confirmed sources in comparison to representatives of earlier MSF phases.

This work explores the sample of ultra-compact H II regions from the CORNISH survey, the majority of which are also conveniently available within the related surveys, to study the properties of this deeply embedded phase. The CORNISH survey supplies the largest complete, well-selected, and coordinated at multiple wavelengths 5 GHz sample of candidate UCHII regions to date. At the observed frequency and high resolution, the survey was tailored to detect the optically-thin ionised gas and to reveal the UCHII structure at high sensitivity. In this work, the nature of 239 CORNISH UCHII regions is confirmed, with the goal to measure and compute their main observational and physical properties. Among those properties are the Galactic UCHII region count, multiplicity, extended IR fluxes, and predominant morphology and relationship to the immediate surroundings. Patterns characteristic to the birthplaces of massive stars are identified. Future theoretical models can thus

be guided to better reflect the global properties of the Galactic population of young massive stars.

In Chapter 2, the nature of the CORNISH UCHII sample is verified and the UCHII observational and physical properties are computed and analysed. In Chapter 3, the processing and analysis of a higher-resolution follow-up to CORNISH is presented, and the structure of the formerly unresolved UCHIIs is successfully revealed. In Chapter 4, a new, multi-wavelength morphological classification is proposed and the available high-quality, high-resolution coordinated and unbiased radio and infrared data are explored through this new classification. Results from a search for X-ray counterparts to CORNISH UCHIIs are presented in Chapter 5. This work is summarised in Chapter 6.

# Chapter 2

## A catalogue of northern UCHII regions

### 2.1 Introduction

The CORNISH catalogue provides a complete and unbiased sample of UCHII regions found in the CORNISH survey at 5 GHz and 1.5'' resolution in the region  $10^\circ < l < 65^\circ$ ,  $|b| < 1^\circ$ , as introduced in §1.2.1. The preliminary work, such as the CORNISH survey observations and data reduction, as well as the initial visual classification of 240 candidate UCHII regions, was performed by the CORNISH team (lead by M. G. Hoare). The observations and data processing methodology are described in the CORNISH survey papers I [Hoare et al., 2012] and II [Purcell et al., 2013]<sup>1</sup>.

A catalogue of 239 confirmed UCHII regions in the imaged region of the Galactic plane is presented in this chapter, and the observational and physical properties of the UCHIIs are explored. All radio, near- and mid-IR photometric measurements are new, except for those of the original CORNISH 5 GHz data,

---

<sup>1</sup>See also the survey pages at <http://cornish.leeds.ac.uk/public/index.php> for a detailed list of all participants in the CORNISH project.

where the results from papers I and II (included in the CORNISH survey database<sup>2</sup>) are adopted. The data analysis in this chapter was carried out in full by the author of this thesis. The work presented here has been the basis of Kalcheva et al. [2018] (see also the Preface page).

The initial UCHII sample selection procedure (as previously carried out by the CORNISH team) is presented and discussed in §2.2. The nature of the identified sources is verified in this work through their observational properties (§2.3) and spectral indices (§2.3.2). Candidate short-timescale variable sources are presented in §2.4. The methodology of obtaining the distance information and the computed distances are presented in §2.5. The derived physical properties are discussed in §2.6. Results from performing automated polygon-based aperture photometry on UKIDSS and GLIMPSE infrared associations are discussed in §2.7 and presented in an extended source catalogue table. The spectral energy distributions of the sample sources from near-IR to sub-mm wavelengths were explored and utilized via SED fitting to obtain the UCHII bolometric luminosities (§2.8). In §2.9, different UCHII search methods in blind surveys are compared. The chapter is summarised in §2.10.

## 2.2 Identification of the CORNISH UCHII sample

In this section, the methodology previously utilised by the CORNISH team for the UCHII candidate sample selection is described and discussed. The CORNISH catalogue comprises 3062 sources above a  $7\sigma$  detection limit. Above this limit, less than one spurious source is expected [Purcell et al., 2013]. The 240 UCHII regions were selected from this high-reliability catalogue. All

---

<sup>2</sup>See <http://cornish.leeds.ac.uk/public/catalogue.php>.

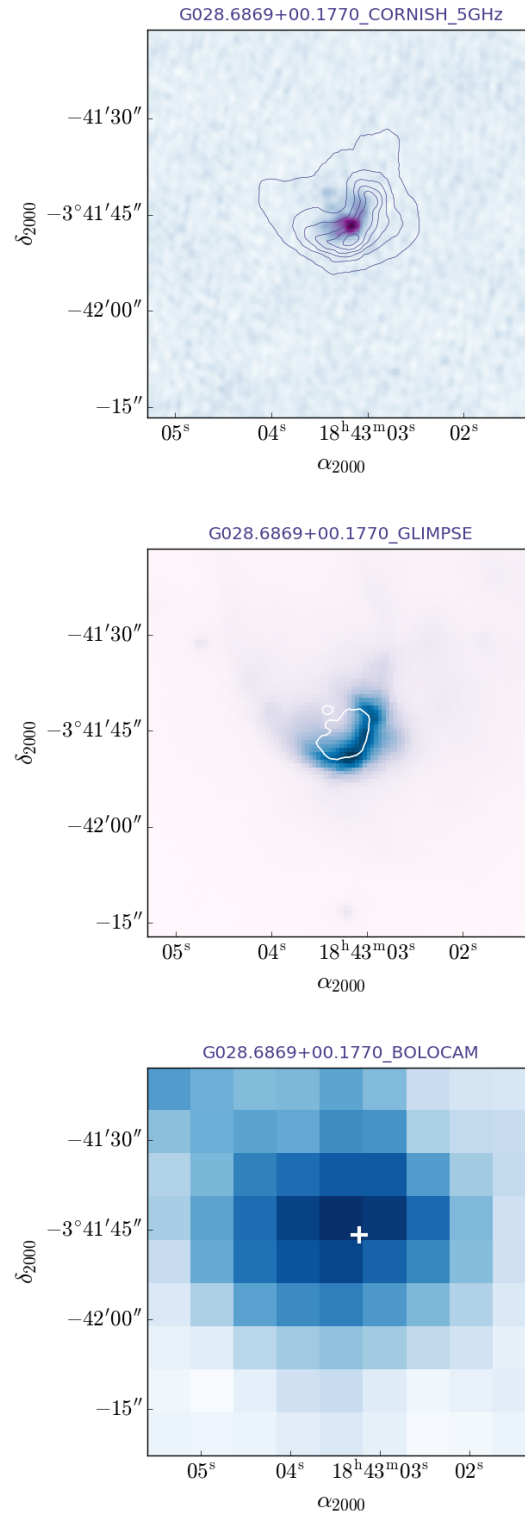


Fig. 2.1 Images of the cometary UCHII G028.6869+00.1770. Top: CORNISH 6 cm image with overlotted GLIMPSE 8 micron contours, with the corresponding GLIMPSE image shown below, with overlotted radio contours. The morphology at both wavelengths is in very good agreement, and there is excellent positional coincidence between the two catalogues, allowing reliable source identification. The BOLOCAM image (bottom panel) shows a bright unresolved source at 1.1 mm coincident with G028.6869+00.1770 (the source coordinates are marked by a white cross).

UCHIIs were visually identified, following criteria similar to the RMS survey, where millimetre, infrared and radio data were used for source classification [see Lumsden et al., 2013]. It should be noted that the CORNISH team also identified 48 diffuse H II regions (as judged by comparison to the MAGPIS and GLIMPSE surveys), which are a part of the larger sample of CORNISH H II regions.

The full UCHII radio sample has counterparts in GLIMPSE, in all four bands (namely, IRAC 3.6, 4.5, 5.8, and 8.0  $\mu\text{m}$ ), with excellent positional accuracy in both surveys. This was utilised for the source identification. In the case of UCHIIs, there is overall a good agreement between the mid-IR and the 5 GHz source morphology, which ensures that the same source was captured by both surveys. A particularly good check for this are the 8  $\mu\text{m}$  images. They show the morphology produced by a combination of warm Lyman- $\alpha$  heated dust inside the ionised zone [Hoare et al., 1991] and PAH emission from just outside the ionisation front [Watson et al., 2008] (see also §1.2.4). This can be seen in Fig. 2.1. Comparison between both wavelengths was therefore used for the distinction of adjacent unrelated sources and over-resolved emission [see Purcell et al., 2013]. An inspection of the radio and 8  $\mu\text{m}$  images can also reveal the most heavily obscured objects (those deeply embedded in infrared-dark clouds or hidden behind dust lanes), as shown in Fig. 2.2.

MYSOs, unlike UCHIIs, do not have strong 8.0  $\mu\text{m}$  PAH emission, which is consistent with the lack of a strong UV continuum [e.g. Gibb et al., 2004]. They are also generally undetected at 5 GHz, even though there are a few known MYSOs observed at radio wavelengths, with radio luminosities ( $S_\nu D^2$ ) always below  $\sim 30$  mJy kpc<sup>2</sup> (discussed in Hoare et al. 2007, Lumsden et al. 2013, and seen from the recent sample by Purser et al. 2016). Sources above this limit are thus H II regions or planetary nebulae (PNe). Intermediate- and low-mass protostars in massive star-forming regions have even lower radio luminosities.

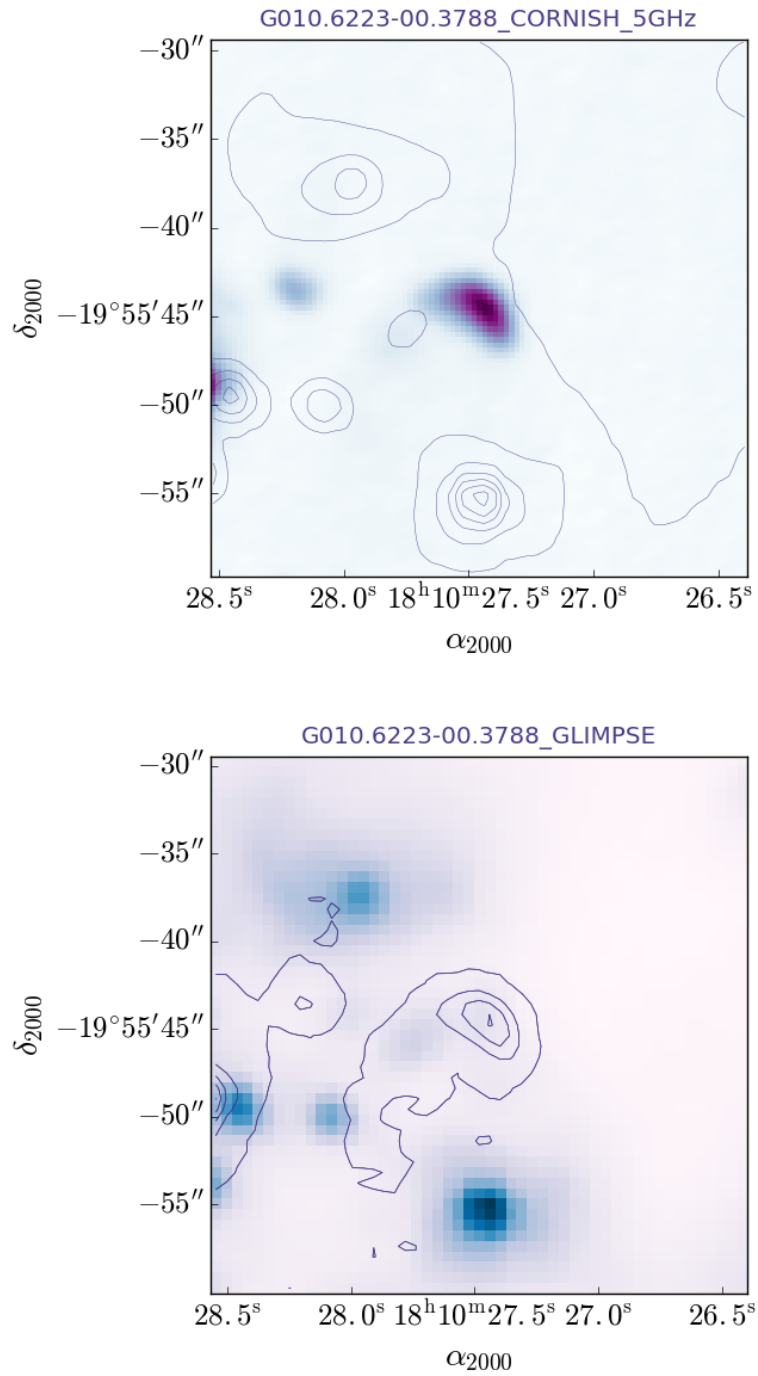


Fig. 2.2 CORNISH (top panel) and GLIMPSE (bottom panel) images of G010.6223–00.3788, presented as in Fig. 2.1, with overplotted 8 micron and 6 cm contours, respectively. A dust lane is hiding the UCHII in the 8 micron image.

For  $10 L_{\odot} < L_{\text{bol}} < 10^2 L_{\odot}$ , their luminosity is  $S_{\nu} D^2 \sim 0.03\text{-}0.13$  mJy kpc<sup>2</sup> at 5-14 GHz (e.g. Osorio et al. 2015). Detection requires a sensitivity of  $\sim 0.5$   $\mu$ Jy, much lower than the CORNISH sensitivity limit ( $5\sigma$  flux sensitivity of 2 mJy, see Hoare et al. 2012).

This leaves PNe as possible contaminants of the selected sample. Unlike PNe, UCHIIs are found within molecular clouds, often in close proximity to IR clusters and dust lanes, which aids the visual classification. A lower but significant fraction of sources are found near other radio sources. About 33% of the CORNISH UCHIIs are situated in a radio cluster (within 12'' of another source), with 30% in a sky region containing more than seven detections of  $7\sigma$  sources. The outlines of 24% of the UCHIIs overlap one or more  $7\sigma$  sources (see §2.3). H II regions are expected to be strong sources in 1 mm continuum (which maps the cool dust), whereas planetary nebulae are not. BOLOCAM 1.1 mm images [see Rosolowsky et al., 2010] centred at the radio source position were visually inspected in conjunction with the IR images to verify that the UCHII sample is not contaminated by PNe.

It is easier to sift out other classes of sources such as radio stars and radio galaxies. Radio stars can be distinguished by their lack of mid- and far-IR emission, whereas radio galaxies have no infrared counterparts.

## 2.3 Radio properties of the CORNISH UCHIIs

The distribution of the Galactic latitudes, angular sizes, and integrated fluxes of the sample of candidate UCHIIs are shown in Fig. 2.3. The sources are closely confined to the Galactic plane, as expected for very young massive star forming regions. Using the CORNISH survey, Urquhart et al. [2013] fit a scale-height of  $20.7 \pm 1.7$  pc for compact and ultra-compact H II regions.

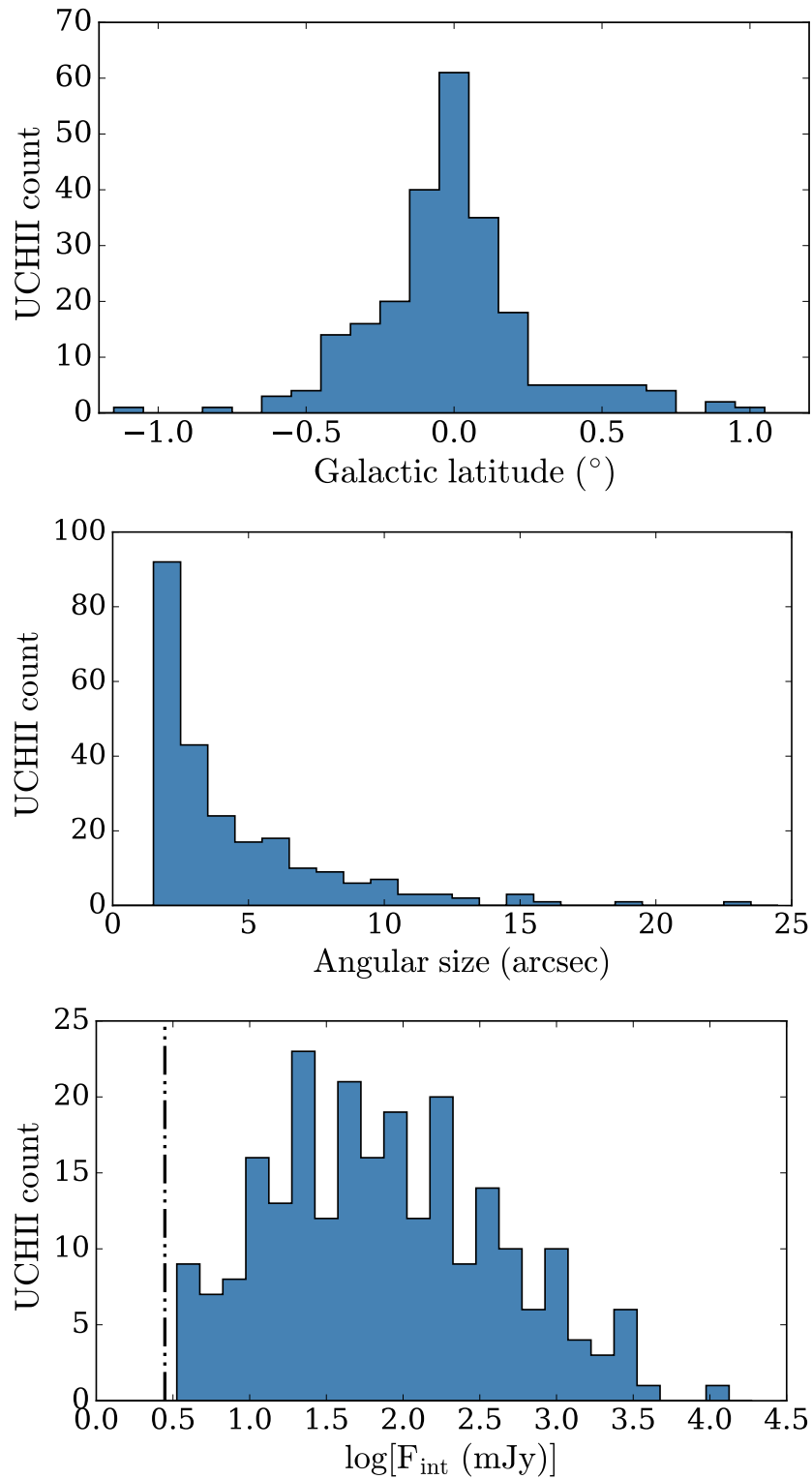


Fig. 2.3 Observational properties of the candidate sample – the confinement to the Galactic plane (top panel), small angular sizes (middle panel), and total radio fluxes (bottom panel) are consistent with UCHII regions. The dot-dashed line in the bottom panel marks the  $7\sigma$  (2.8 mJy) sensitivity limit of CORNISH.

As discussed by Purcell et al. [2013], the 90% completeness limit is 3.9 mJy for unresolved sources, and at the VLA configuration used for CORNISH, sources begin to suffer from significant over-resolution above angular sizes of  $14''$  (in which case the completeness limit significantly decreases). The majority of the ultra-compact H II regions have angular sizes below  $5''$ , with the histogram peaking towards unresolved sources. Most CORNISH UCHIIs have integrated fluxes above 10 mJy, and the brightest one has a flux density of 12.6 Jy. Purcell et al. [2013] identified over-resolved radio emission broken up by the source finder by visually inspecting the  $8\ \mu\text{m}$  GLIMPSE images and re-integrated it by utilising hand-drawn polygons for the CORNISH survey photometry. Cases where a dust lane is obscuring the UCHII in the mid-IR pose a limitation to this method of identification of over-resolved radio flux (Fig. 2.2), but only  $\sim 7\%$  of mid-IR UCHII counterparts are affected (see Chapter 4).

Taking the above into account, the clear downturn towards the lowest values in the integrated flux histogram indicates that the UCHII sample is close to complete. The CORNISH survey is not complete towards more diffuse/evolved H II region phases (comprising the separate, diffuse H II region sample, see §2.2), for which over-resolution effects become severe. CORNISH is also incomplete towards HCHII, due to the inherent bias of 5 GHz observations towards the discovery of sources with flat or falling spectral indices – HCHII have rising radio spectra and typical  $\alpha \sim 1$  (see e.g. the discussion by Yang et al. 2018 and §2.6).

The CORNISH beam size is  $1.5''$  and all sources with  $\theta < 1.8''$  are marked as unresolved in the catalogue table (detailed checks for the entire CORNISH catalogue are discussed in Purcell et al. 2013). Within the CORNISH UCHII candidate sample, the flux was measured by fitting a Gaussian in 90 out of the 239 cases (angular size range  $1.5''$  to  $6.2''$ ), and for the remaining 149 sources, a hand-drawn polygon was used instead (angular size range from  $1.8''$  to  $23.4''$ ).

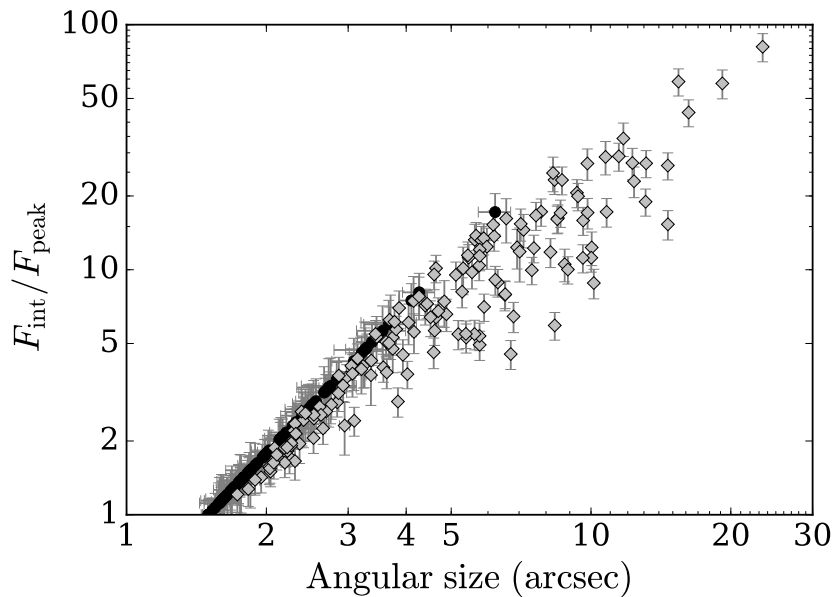


Fig. 2.4 Ratio of integrated to peak flux vs. angular size of the 239 CORNISH UCHIIs. Fluxes estimated from Gaussian fits and from polygon apertures are shown as black circles and grey diamonds, respectively.

The integrated and peak fluxes were compared as a function of angular size of each source, as shown in Fig. 2.4. Naturally, those sources whose fluxes were measured from a Gaussian fit show a clear trend of the flux ratio with increasing angular size, whereas the remaining sources with manually drawn contours show more variation.

### 2.3.1 Lower-resolution radio counterparts

The Multi-Array Galactic Plane Imaging Survey (MAGPIS) [Helfand et al., 2006] is useful for the study of evolved H II regions and other extended, optically thin thermal emitters. However, it is not well-suited to explore dense, thermal sources, as those are unresolved or only marginally resolved. Catalogues at 20 cm (VLA B,C,D configuration) and at 6 cm (VLA C configuration) are available [White et al., 2005]. The 6 cm catalogue covers  $\sim 23\%$  of the northern-GLIMPSE region, and at the survey resolution most of the detected CORNISH counterparts are unresolved, i.e. no morphological information is available.

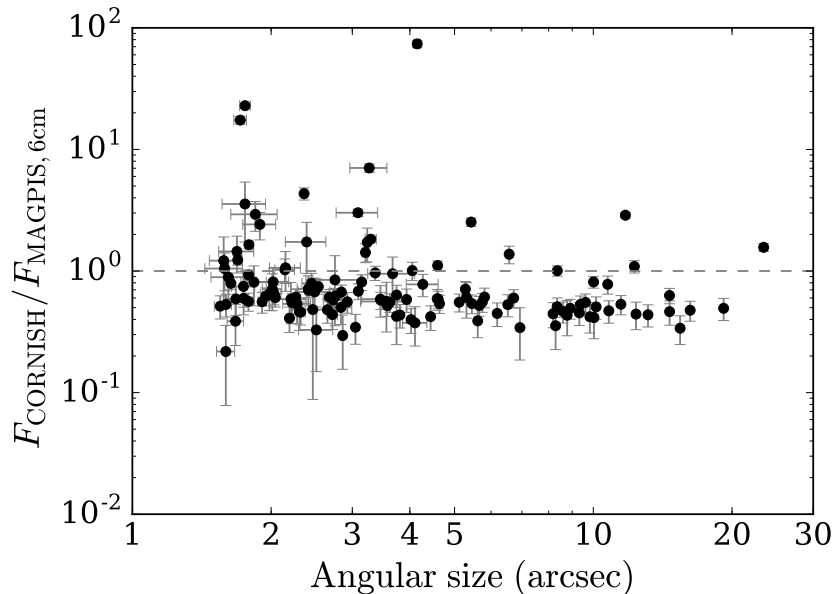


Fig. 2.5 Comparison of the MAGPIS 6 cm and CORNISH integrated fluxes (black circles) with plotted line of equality, plotted against the corresponding CORNISH angular size.

The benefits of a comparison between CORNISH and MAGPIS are explained in detail in Purcell et al. [2013] (see Figs. 20, 21). In brief, for extended sources in the CORNISH sample, the measured flux density could be a lower limit in cases where some of the extended emission was filtered out due to gaps in  $uv$  coverage, and the measured angular sizes could be underestimated by as much as 50% for non-Gaussian sources in interferometric measurements [see e.g. Panagia and Walmsley, 1978]. To test for such instances, a comparison to the MAGPIS 6 cm data is useful, as the survey configuration allowed the recovery of more diffuse emission at the cost of lower resolution.

It is important to note that there are instances of repeats in the combined 6cm/20cm MAGPIS catalogue. This is due to the fact that sources matching more than once are listed multiple times, e.g. a 6 cm source listed with each 20 cm counterpart and vice versa [White et al., 2005]. Since the structure of the MAGPIS catalogue leads to repeats even within a small cross-matching radius, to obtain a sufficiently reliable cross-match with the MAGPIS catalogue

table, the matched sample had to be limited to only 47 associations. Visual identification of the associations was therefore preferred. The CORNISH team visually identified 216 20 cm matches (out of which 162 have both a 6 cm and 20 cm MAGPIS detection). These matches were adopted from the CORNISH database.

In this work, the corresponding MAGPIS images were visually inspected and aperture photometry of the counterparts to the CORNISH UCHIIs was performed<sup>3</sup>. Thus, the fluxes of the 20 cm and 6 cm MAGPIS UCHII associations were measured independently of the MAGPIS catalogue table values. Median absolute deviation from the median (MADFM) background estimation was utilised (for all photometry in this chapter), as it is insensitive to the presence of outliers and is a reliable estimate of the noise [Purcell et al., 2013]. Using this method, errors are computed following Masci [2009] and include prior (noise-model) and derived uncertainties.

The radio outlines from the CORNISH database – hand-drawn polygons in the case of extended radio sources, and Gaussian outlines in the case of compact radio sources, were utilised (§2.3). In order to use these outlines as apertures for the lower-resolution MAPGIS data, they were expanded accordingly. The necessary ‘padding’ value (i.e. the required radial expansion) was determined after multiple runs with different aperture sizes and visual inspection of the images with the overplotted apertures. Based on the curve of growth and the visual inspection, a padding value of 4'' (i.e. total expansion of 8'') was chosen for the flux measurement.

Fig. 2.5 shows that the majority of the flux ratio values occupy the range between  $\sim 0.2$  and 1.1, which indicates that some flux was not recovered at the higher resolution (around 65% of the flux was detected for these sources). The slightly negative slope of the flux ratio is due to worsening over-resolution

---

<sup>3</sup>Automated aperture photometry scripts courtesy of C. Purcell.

with increasing angular size. Sources overlapping with one or more  $5\sigma$  or  $7\sigma$  CORNISH neighbours were excluded, as these sources are unresolved and merged in the MAGPIS 6 cm images and their flux measurements are unreliable. The outliers above the equality line, i.e. with CORNISH fluxes significantly higher than their MAGPIS 6 cm counterpart, are investigated for potential short-timescale variability in §2.4.

The reliability of the measured 216 20-cm and 162 6-cm flux values was judged on the basis of their median brightness level of the sky. For all sources with abnormal (i.e. outside the range of the majority of sources) median level in the sky-annuli, upper flux limits are included in the presented flux table (Table A.1 in Appendix A). Sources with consistent sky values that are also not overlapping with a  $5\sigma$  or  $7\sigma$  source are here considered to be the highly-reliable MAGPIS flux measurement subset. These were used to compute the spectral indices of the CORNISH UCHIIs – see §2.3.2.

A comparison of some of the MAGPIS flux values in the published catalogue table with the highly-reliable measured flux values presented in this work is shown in Table 2.1. These are also compared to flux results obtained with *CASA*, by Gaussian fits in unresolved cases or computing the flux for the extended source region otherwise (the same method was tested on the CORNISH images, in good agreement with the catalogued values). Clearly, neither the photometry performed with the automated script or with *CASA* reproduced the catalogued 6 cm MAGPIS values to a reasonable degree, with a much better agreement between our two photometric measurements. This also appears to be true for extended 20 cm sources. This is why the fluxes of all available lower-resolution counterparts were remeasured in this work. The results obtained for unresolved 20 cm sources appear to be overall in better agreement with the catalogue.

Table 2.1 Comparison of a few MAGPIS flux values in the published 6cm-20cm catalogue table (5th and 8th columns) with the measured flux values presented in this work – as from the automated script (3rd and 6th columns) and individual measurements with **CASA** (4th and 6th columns). Only highly-reliable values (based on median sky values and no overlapping sources) are compared in the table. All values are in mJy. The second column includes the corresponding CORNISH fluxes. The source denoted by ‡ could be intrinsically variable at 6 cm.

CORNISH name	$F_C$ (cat.)	$F_{M6cm}$ (ap.)	$F_{M6cm}$ (CASA)	$F_{M6cm}$ (cat.)	$F_{M20cm}$ (ap.)	$F_{M20cm}$ (CASA)	$F_{M20cm}$ (cat.)
G011.1104–00.3985	$305 \pm 29$	$304 \pm 9$	320	112	$327 \pm 4$	371	187
G012.1988–00.0345	$63 \pm 6$	$103 \pm 1$	110	60	$42 \pm 1$	48	62
G016.3913–00.1383‡	$124 \pm 15$	$43 \pm 4$	43	20	$57 \pm 5$	67	58
G018.7106+00.0002	$107 \pm 11$	$178 \pm 2$	189	103	$37 \pm 1$	42	35
G021.8751+00.0075	$567 \pm 54$	$1065 \pm 9$	1073	264	$686 \pm 8$	719	600
G037.8731–00.3996	$2561 \pm 234$	$5189 \pm 23$	5219	1518	$1770 \pm 7$	1800	1279

### 2.3.2 5GHz–1.4GHz spectral indices

The spectral indices ( $\alpha$ ) were computed from the relation

$$\alpha = \frac{\ln(S_{5\text{GHz}}/S_{1.4\text{GHz}})}{\ln(5/1.4)}, \quad (2.1)$$

where  $S_{5\text{GHz}}$  and  $S_{1.4\text{GHz}}$  are the integrated fluxes at 6 cm and 20 cm, respectively.

The uncertainty was found from

$$\Delta\alpha = \frac{\sqrt{(\sigma_{5\text{GHz}}/S_{5\text{GHz}})^2 + (\sigma_{1.4\text{GHz}}/S_{1.4\text{GHz}})^2}}{\ln(5/1.4)}. \quad (2.2)$$

The indices were calculated for the CORNISH 6 cm flux and using the newly measured 20 cm fluxes. As discussed in the previous section, for the purpose of obtaining reliable spectral indices, all overlapping sources were excluded, thus making it possible to compute 93 spectral indices. This should be sufficiently representative of the sample as a whole, as the selection is in this way based on image quality alone.

The brightness temperatures of the sources in the UCHII sample at 6 cm were also calculated. This was done for all CORNISH UCHII regions (see Fig. 2.9e), using the equation

$$T_{\text{b}} = \frac{1.36\lambda^2 S_{\nu}}{\theta^2}, \quad (2.3)$$

where the flux density  $S_{\nu}$  is in mJy, the brightness temperature  $T_{\text{b}}$  is in K, the wavelength  $\lambda$  is in cm and the HPBW (half-power beam width)  $\theta$  for a Gaussian beam is in arcseconds. For all unresolved sources, this provides a lower limit.  $T_{\text{b}}$  serves as a measure of optical thickness – increasing with larger optical depth and reaching the electron temperature ( $T_{\text{e}}$ ) of the ionised region in the optically thick limit [Siódmiak and Tyłenda, 2001]. The optical depths

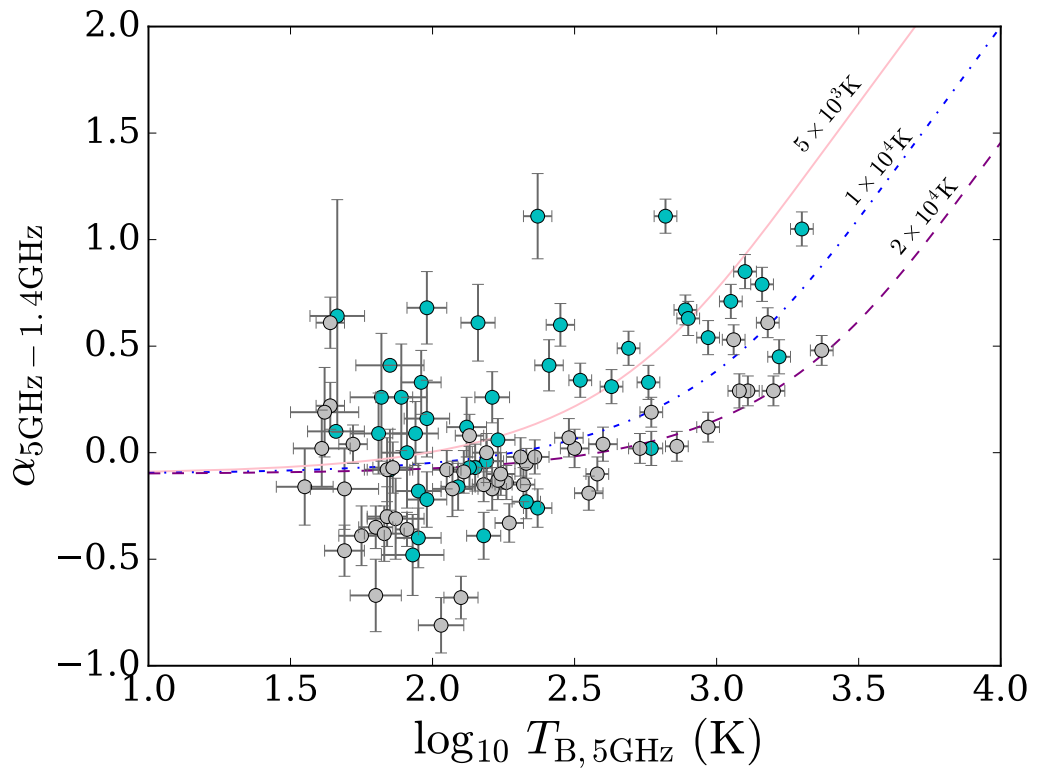


Fig. 2.6 Spectral indices between 1.4 GHz and 5 GHz against brightness temperature of the corresponding CORNISH source at 5 GHz. The model lines signify different  $T_e$ . All CORNISH sources with an overlapping  $5\sigma$  or  $7\sigma$  source were excluded, as they are not resolved in MAGPIS. UCHIIIs resolved in CORNISH are marked in grey, whereas unresolved sources are in cyan.

$\tau_\nu$  at 5 GHz were found from

$$T_b = T_e \left(1 - e^{-\tau_\nu}\right), \quad (2.4)$$

for  $T_e = 10^4$  K (Eqn. 4 in Siódmiak and Tyłenda 2001). Note that the optical depth results (Fig. 2.9f) are lower limits in the case of unresolved sources (due to the angular size dependence of  $T_b$ ), as well as for the most extended sources (due to the possible underestimation of the 5 GHz flux, see Fig. 2.5).

The spectral index analysis was performed by plotting the UCHII spectral indices (Fig. 2.6) as a function of their corresponding 6 cm brightness temperatures and comparing the result to the theoretical model developed by Bojičić et al. [2011] (see Eqn. 6 in their paper), who followed up on the work by Siódmiak and Tyłenda [2001]. The focus of these works were planetary nebulae, however the model is general and should be applicable to all ionised nebulae. It assumes a uniform nebula characterized by its electron temperature and optical thickness at a corresponding reference frequency. The individual spectral index values (along with the measured fluxes at 6 cm and 20 cm) can be found in Table A.1.

The majority of UCHII candidates were found to be within the expected theoretical limits for free-free emission ( $-0.1 \lesssim \alpha \lesssim 2$ ) – that is, between sources with optically thin or optically thick radio continuum emission at both frequencies. None of the sources have a spectral index above 1.5. However,  $\sim 18\%$  of the sources are found below the lower limit (taking errors into account), which is inconsistent with thermal emission. The reason for the apparently non-thermal spectral indices is likely to be the difference in the VLA configuration at 1.4 GHz and 5 GHz (i.e. the  $uv$  coverage at higher resolution resulting in filtering out of some of the flux, as seen in Fig. 2.5). If the 6 cm fluxes were  $\sim 1.6$  times higher (as high as the measured 6 cm MAPGIS fluxes,

Fig. 2.5), all but two sources (G010.6297–00.3380 and G023.8985+00.0647) would be shifted within the thermal bounds. These negative spectral indices ( $\alpha \lesssim -0.5$ ) are associated with UCHIIs that are resolved in CORNISH (angular sizes  $\sim 4''$ ), which supports this possibility (Fig. 2.6).

The optimal method to compute the spectral indices would be from UCHIIs unresolved at both 6 cm and 20 cm, as the flux measured from an unresolved radio source is closest to its ‘true’ flux (see §1.3). Despite this, the CORNISH 6 cm data was preferred over the MAGPIS 6 cm images, as the latter show significantly greater image-to-image variations in median sky levels and thus provide fewer 6 cm frames that are viable for the spectral index calculation (only 71/162 MAGPIS 6 cm sources when overlapping sources are excluded). The 20 cm images appear overall of higher quality than the MAGPIS 6 cm data. Therefore, by utilising the CORNISH 6 cm images and the (reduced sample of 93) MAGPIS 20 cm images, the spectral index analysis was limited to the best available data. Due to the time difference between the 20 cm observations and (both sets of) the 6 cm observations, source variability, as discussed in §2.4, is another possible explanation for some instances of non-thermal (appearing) UCHIIs. Unfortunately, it is not possible at this time to quantify this effect without more 20 cm observations.

The location of each UCHII in Fig. 2.6 is determined by both its optical thickness and its electron temperature. The model lines in the diagram correspond to applying Eqn. 6 of Bojičić et al. [2011] for electron temperatures  $T_e = 5 \times 10^3$  K,  $T_e = 1 \times 10^4$  K and  $T_e = 2 \times 10^4$  K. For reference, the mean value for the electron temperature of Galactic H II regions has been estimated to be 8000 K [Quireza et al., 2006]. At lower brightness temperatures, the UCHIIs scatter around the optically thin limit, where the majority of the sample is found. The much larger associated uncertainties of the sources with lower  $T_b$  (i.e. of lower opacity at 6 cm) should be noted in this case.

With increasing  $T_b$ ,  $\alpha$  increases in agreement with the model, corresponding to  $5 \times 10^3 \text{ K} \lesssim T_e \lesssim 2 \times 10^4 \text{ K}$ , revealing sources that appear optically thick. Lower electron temperatures would be a better fit to the sample if the possible under-estimation of the 6 cm flux is taken into account.

The presented spectral index results are a validation of the UCHII region nature of our sample.

## 2.4 Evidence for short-timescale UCHII variability?

All sources with available MAGPIS and CORNISH 6 cm images were revisited to look for significant flux changes between the two epochs that cannot be attributed to image quality or other individual reasons. Such sources could be variable over short timescales comparable with the difference in time between the MAGPIS 6 cm survey (obs. 1989–1991) and the CORNISH survey (obs. 2006–2008). The flux ratio lower limits were taken into account to quantify this. The higher flux at the earlier epoch (due to the detection of more extended emission) prevents a reliable investigation of instances of intrinsic flux decrease, particularly for sources larger than  $5''$ . A further hindrance is that any hypothetical UCHII regions that are completely invisible at the later epoch due to a significant flux decrease over time cannot be reliably differentiated from more extended H II region phases due to the lower resolution at the earlier epoch.

Due to these limitations imposed by the different VLA configurations used at the two epochs, in the context of this work, the term variability is used here to refer to increase in flux in the  $\sim 15$  years separating the two surveys. The

Table 2.2 Ratio of CORNISH to MAGPIS 5 GHz fluxes for candidate variable UCHII regions (observed 15 years apart). Note that in cases where the source was not detected at 6 cm in MAGPIS, the upper flux limit was used for the comparison.

CORNISH name	$F_C/F_{M,6\text{cm}}$
G011.0328+00.0274	$>2 \pm 1$
G011.9786−00.0973	$>4 \pm 2$
G014.5988+00.0198	$>3 \pm 1$
G016.3913−00.1383	$3 \pm 0$
G023.4553−00.2010	$>17 \pm 1$
G025.7157+00.0487	$>4 \pm 1$
G030.7579+00.2042	$>74 \pm 4$
G030.7661−00.0348	$>7 \pm 1$
G037.7347−00.1128	$>23 \pm 1$

sources which appear to be intrinsically variable all have a flux increase greater than  $\sim 50\%$  (see §2.3.1 and Fig. 2.5). These are listed in Table 2.2.

#### **G011.0328+00.0274**

This is a CORNISH source ( $F_C = 5.69 \pm 1.06$  mJy) that is not discernible in the MAGPIS 6 cm image and was not listed as a detection in the MAGPIS 6 and 20 cm catalogues or in the RMS survey. The source is clearly visible in the mid-IR, far-IR and at  $1.1 \mu\text{m}$ . Weaker nebulae can be seen close by, all on a filament. The object is just resolved and appears to have cometary morphology. Its distance is 2.6 kpc [Urquhart et al., 2013] and its physical size is  $\sim 0.015$  pc.

#### **G011.9786−00.0973**

This is a weak, unresolved CORNISH source that is not detected in the MAGPIS 6 and 20 cm catalogue or in the RMS survey. It is visible only in the 20 cm image, about 4 times above the background. It appears to be a dense knot of a larger H II complex, as seen in GLIMPSE. The source is clearly seen also in the far-IR, but is dim at  $1.1$  mm and not listed as a BOLOCAM detection. No distance is known for this source, hence no size upper limit could be computed.

**G014.5988+00.0198**

This source is just resolved in CORNISH and not seen in either MAGPIS image, but is included in RMS. It was detected by Walsh et al. [1998] at 8.6 GHz (2.1 mJy). Its distance is 2.8 kpc [Urquhart et al., 2013] (2.7 kpc in RMS) and its size is  $\sim 0.015$  pc. Data at 21, 22 and 70  $\mu\text{m}$  are available from the RMS database. The 70 $\mu\text{m}$ /22 $\mu\text{m}$  flux ratio is  $\sim 15$ , and the 70 $\mu\text{m}$ /21 $\mu\text{m}$  flux ratio is  $\sim 30$ .

**G016.3913–00.1383**

Counterparts for this extended CORNISH source are found in both MAPGIS images but not in RMS. The 6 cm source appears to be more extended and  $\sim 2.7$  times brighter at the later epoch. The corresponding GLIMPSE image at 8  $\mu\text{m}$  shows a bubble of comparable size and the source is clearly seen in the far-IR. The BOLOCAM image reveals a weak mm continuum source. The source far distance – 12.2 kpc – was available from Cesaroni et al. [2015], giving an upper limit on the physical size of 0.48 pc.

**G023.4553–00.2010**

This is an unresolved source ( $< 0.048$  pc) with a mid-IR (and far-IR) counterpart, not in RMS. It is isolated in the CORNISH image and not seen at either MAGPIS wavelength, but the mid-IR and the lower-resolution radio data reveal diffuse emission  $\sim 1'$  away. The 1.1 mm counterpart is very dim and was not listed as a detection in BOLOCAM. The source is also in Wood and Churchwell [1989b] and in SCUBA (submm-continuum) [Di Francesco et al., 2008]. It is 5.8 kpc away [Urquhart et al., 2013].

**G025.7157+00.0487**

This is a small, just resolved UCHII region, with a diameter of  $\sim 0.083$  pc. It is 9.5 - 9.8 kpc away (from Urquhart et al. [2013] and the RMS database, respectively). The source is seen clearly at 20 cm but is quite dim in the MAGPIS 6 cm image ( $\sim 4.3$  times weaker than the CORNISH detection, which is 20.79 mJy). It should be noted that the CORNISH image rms noise is slightly higher –  $\sim 0.4$  mJy, compared to  $\sim 0.3$  mJy in the MAPGIS image. From the data on the RMS database, the  $70\mu\text{m}/22\mu\text{m}$  flux ratio is  $\sim 9$ , whereas the  $70\mu\text{m}/21\mu\text{m}$  ratio is  $\sim 13$ . Walsh et al. [1998] measured 6.3 mJy at 8.6 GHz. The source was classified as an UCHII by Wood and Churchwell [1989b] (G25.72+0.05), with a measured flux of 15.8 mJy at 4.8 GHz (observations were conducted between 1986 and 1988 with the VLA in A and B configuration). Assuming one ionising star, Wood and Churchwell [1989b] found the lower limit of the spectral type to be B0 (based on the radio data, where dust absorption of the UV flux can be significant), and the upper limit to be O5 (based on IRAS data, where the  $2'$  beam can include surrounding sources). The radio recombination line (RRL) velocity is  $52 \text{ km s}^{-1}$  [Garay et al., 1985], which is broader than the typical velocities for UCHII regions of  $30\text{-}40 \text{ km s}^{-1}$  (Hoare et al. [2007] and references therein). Based on the RRL velocity, the source is more consistent with a hyper-compact H II region.

**G030.7579+00.2042**

G030.7579+00.2042 appears to be a new detection at 6 cm. No counterpart is seen in the MAGPIS 6 cm image, but the 20 cm counterpart is as bright as the CORNISH source. The source is small but resolved, with a distance of  $\sim 7.22$  kpc (this work) and a physical size of  $\sim 0.14$  pc. There are no other radio sources in the immediate vicinity (within  $1'$ ), but the GLIMPSE

images, particularly at 8  $\mu\text{m}$ , reveal about 5 sources of comparable sizes huddled together within diffuse emission. These are not associated with catalogued GLIMPSE point sources. At least one of the sources has been identified as a YSO (G030.7578+0.2049 in Veneziani et al. [2013]).

### **G030.7661–00.0348**

G030.7661–00.0348 has much busier surroundings than the other 6 cm variables. It is 7.22 kpc away (this work), with a size of 0.1 pc. The source coincides with the W43 star cluster, with a dark cloud to its west. The carbon-rich binary Wolf-Rayet star WR 121 [Luque-Escamilla et al., 2011] is 3.23'' away from the source position and the supernova remnant (SNR) RRF 207 [Langston et al., 2000] is 6.03'' away, among a multitude of other sources. The source is hard to discern from the background in both MAGPIS images, particularly at 6 cm, among the abundant diffuse radio emission picked up at the lower resolution. Its 5 GHz emission appears to be  $\sim 9$  times weaker at the earlier epoch, although the noisy MAGPIS images lead to the exclusion of the flux measurements at both 6 and 20 cm from the final radio flux table presented in this work. Using either combination of 6 cm and 20 cm fluxes (catalogued or measured anew) for this source results in a negative spectral index with an upper limit of  $\alpha \simeq -0.55$ . Luque-Escamilla et al. [2011] found that the extended radio emission of the W43 central cluster has a negative spectral index and a high brightness temperature ( $7.1 \times 10^4$  K), based on the pre-existing sets of VLA observations for this source (Table 2 and the associated references) and on the integrated radio luminosity from 0.1 to 100 GHz, respectively. They concluded that the W43 radio emission is likely to be of non-thermal synchrotron nature, the strength of which suggests that it is driven by the collective effect of the stellar winds of the WR and O stars in the cluster. Interestingly, Luque-Escamilla et al. [2011] also found that one of the WR 121 components (W43 1b, the O

star companion of the WR star) coincides with the *Chandra* X-ray source CXO J184736.6–015633 (at the  $10.8\sigma$  confidence level). The available *XMM-Newton* spectrum for the W43 cluster was modelled, which indicated extended hard thermal X-ray emission (§5.4). This is likely associated with the same WR 121 binary source reported by Luque-Escamilla et al. [2011], as there are no other nearby X-ray sources in the higher-resolution *Chandra* image. The cluster is also associated with  $\gamma$ -ray emission, as reported by Lemoine-Goumard et al. [2011]. This is clearly an extremely complex environment influencing G030.7661–00.0348, which could explain the difference in flux between the two epochs.

### **G037.7347–00.1128**

This is an unresolved source in CORNISH ( $< 0.088$  pc), 10.3 kpc away [Urquhart et al., 2013], which was not detected in the MAGPIS 6 cm image and has no RMS data, but is clearly seen at 20 cm (and is particularly bright at 1.1 mm). It is found on the edge of a bubble, which is visible in the lower resolution radio data and the mid-IR images. There are three more sources beaded around the edge, all of which are near-IR and radio-dark and outshine the CORNISH source in the GLIMPSE images.

The 6-cm variables appear to have several properties in common:

1. They exist in relative isolation (no overlapping sources, no other radio sources within  $\gtrsim 1'$ , no busy complexes). An exception to this is G030.7661–00.0348, which is likely experiencing substantially different effects than the rest in the bustling environment of W43;
2. They are all near-IR dark (apart from G030.7661–00.0348);
3. Most are particularly compact ( $\lesssim 0.1$  pc), with the exception of G016.3913–00.1383.

4. Their 5GHz–1.4GHz spectral indices are not anomalous with respect to the rest of the sample.

The potentially variable sources comprise  $\sim 5\%$  of the CORNISH UCHII sample. In four cases (G011.9786–00.0973, G014.5988+00.0198, G023.4553–00.2010, and G030.7661–00.0348), the CORNISH source was not detected at both 6 and 20 cm at the earlier observational epoch. Three sources (G025.7157+00.0487, G030.7579+00.2042, and G037.7347–00.1128) all have only a 20 cm detection at the earlier epoch (and there is a dim 20 cm counterpart for G011.0328+00.0274). The extended G016.3913–00.1383 has 6 and 20 cm counterparts, but these appear smaller and dimmer at the earlier epoch. Although there are some suggestive correlations, this group of candidate variable sources is clearly statistically insufficient to establish any common pattern linking the (presence or lack of) emission at 6 and 20 cm at the same epoch. Unfortunately, the 6 cm variability cannot be linked in any way to variability at 20 cm, due to the lack of other available 20 cm data of comparable quality for the 6-cm variables.

For another portion of the CORNISH UCHII sample, a total of 57 1.5 GHz counterparts are available from the Garwood et al. [1988] VLA-B continuum survey of the Galactic plane ( $4''$  resolution,  $0^\circ < l < 90^\circ$ , with snapshots taken every  $0.5^\circ$  along  $b = 0^\circ$ ). There are several sources with flux increase between the two epochs (observations were conducted in December 1983, whereas the MAGPIS 1.4 GHz data were collected from 1990). However, any instances of non-detections would not be in the Garwood et al. [1988] source list and the catalogue cross-match would miss such variable sources - the images are needed for inspection. For the available matched sources, the fluxes of  $\sim 77\%$  of the Garwood et al. [1988] sources are lower than their MAGPIS counterparts,

as would be expected when comparing the B-configuration-only data to the multi-configuration MAGPIS data.

Therefore, variability could not be reliably addressed in terms of 20 cm flux decrease. The majority of the remaining sources in common have fluxes in agreement, with  $1.6 \lesssim F_G/F_{M,20\text{cm}} \lesssim 3$ . These are the CORNISH sources G023.8618–00.1250, G010.9584+00.0221, G020.0809–00.1362, and G043.2371–00.045.

Time-variable radio flux densities of several ultra-compact and hyper-compact (HC) H II regions have been reported previously (Acord et al. 1998, Franco-Hernández and Rodríguez 2004, Rodríguez et al. 2007, Gómez et al. 2008, Galván-Madrid et al. 2008). The flux changes have been associated with morphological changes across observational epochs, on timescales of a few years. The UC and HC H II regions have been caught expanding [Acord et al., 1998]. Galván-Madrid et al. [2008] discuss contracting UC and HC H II regions; however their sources are unresolved. Variability over observable timescales could be caused by factors that are either external or internal to the forming star. The former could be the result of chaotic motions of the material surrounding the ionising star. In this scenario, optically thick gas (e.g. clumps in the stellar wind) would occasionally block the outgoing radiation, shielding the outer ionised gas layers and thus neutralising them [Peters et al., 2010a]. In the latter scenario, the forming star itself is undergoing changes [Franco-Hernández and Rodríguez, 2004] – surface temperature fluctuations affect the UV flux and thus the H II region size.

Theoretical studies have reproduced this behaviour, referred to as flickering. The three-dimensional collapse simulations of massive star formation of Peters et al. [2010a,b,c] and Klassen et al. [2012b] include feedback by ionising radiation and show time variability leading to changes in H II region appearance and flux comparable to observations. The Peters et al. [2010a] model produces flickering

on scales of  $\sim 10$  years. In this model, accretion has not ceased prior to the UCHII stage. The infalling neutral flow becomes ionised when in close proximity to the star. The H II region is gravitationally trapped early on, which is followed by a fluctuation between trapped and extended states, and thus changes in flux, size and morphology are seen over time. Galván-Madrid et al. [2011] performed statistical analysis of simulated radio-continuum observations separated by 10 year steps, using the Peters et al. [2010a,b,c] models to form H II regions. They found that 7% of the simulated HC and UC H II regions have a detectable flux increase (larger than 10%) and 3% have a detectable flux decrease, but expect only  $\sim 0.3\%$  of their H II regions to have a flux increase of over 50%. The observations discussed in this work show that  $\sim 5\%$  of the CORNISH UCHII regions have become brighter by 50% or more over a comparable time scale ( $\sim 15$  years), based on the 6 cm data. In practice, any similar statistic of observed sources with flux increase  $\lesssim 10\%$  would be unreliable, given the associated flux uncertainties. In any case, assuming that all of our candidate variable sources truly undergo intrinsic changes, variable HC and UC H II regions could be significantly more common and their brightness could fluctuate more than predicted. If this is the case, invoking ongoing accretion cannot account for the observed dramatic change in flux. The Peters et al. [2010a] model does not include radiation pressure, magnetic fields, winds and outflows, all of which are components of the star formation process and might be related to variability.

## 2.5 Distances

In this work, the H I E/A method was adopted to determine the distance to each UCHII [see e.g. Urquhart et al., 2012]. This method makes use of CO emission line data and H I absorption to obtain the near and far kinematic distances and to attempt to resolve the KDA (see §1.2.3).

### 2.5.1 Distances from ATLASGAL and RMS

The work by Urquhart et al. [2013] presents an unbiased and complete sample of 170 molecular clumps with 213 embedded compact and ultra-compact H II regions over the common GLIMPSE, ATLASGAL and CORNISH survey region. Table 3 from Urquhart et al. [2013] contains distances to all CHII- and UCHII-hosting clumps and Table 4 contains Lyman continuum fluxes ( $F_{Ly}$ ) and source physical sizes. Out of the associated 213 H II regions, 203 also belong to the CORNISH UCHII sample (10 were classified as more extended). Of the remaining 36 UCHII candidates without ATLASGAL distances, 8 were found to have a distance estimate in the Red MSX source survey (RMS) database<sup>4</sup> [Lumsden et al., 2013]. These are the distances for G010.6297–00.3380, G030.6881–00.0718, G032.0297+00.0491, G035.0524–00.5177, G038.5493+00.1646, G048.6099+00.0270, G060.8842–00.1286, and G061.7207+00.8630.

### 2.5.2 Distance estimates for remaining sources using CO data

Anderson et al. [2009] describe a large-scale study of the molecular properties of H II regions of different sizes and morphologies using fully sampled CO maps. This is the BU-FCRAO Galactic Ring Survey [Jackson et al., 2005], which uses  $^{13}\text{CO } J = 1 \rightarrow 0$  emission. This has advantages over the commonly used  $^{12}\text{CO}$  isotopologue, as  $^{13}\text{CO}$  is  $\sim 50$  times less abundant and thus provides a smaller optical depth, and consequently smaller line widths and better separation of velocity components along the line of sight.

<sup>4</sup>[http://rms.leeds.ac.uk/cgi-bin/public/RMS\\_DATABASE.cgi](http://rms.leeds.ac.uk/cgi-bin/public/RMS_DATABASE.cgi)

CO data-cubes from the Galactic Ring Survey<sup>5</sup> were used to obtain radial velocities for the remaining sources without ATLASGAL or RMS distances. The positional accuracy of the GRS is  $\sim 2.3''$ , which is equivalent to 1/10 of the spacing between grid points on the map. Data cubes for the available sources were obtained, and the radial velocities were measured for the sources coinciding with the CORNISH coordinates. The emission line structure of the data is very complex, often with multiple emission lines. This reflects the complexity of the  $(l, b, v_{\text{LSR}})$  structure of the molecular gas in the line of sight of the H II region. The sources were located within the 15' data cubes by going manually through the cube channels and then mapping the cube once the source was found at or close to the precise CORNISH coordinates. A source's velocity was taken to be equal to the velocity of the most prominent emission line in the map at the exact source position. The final CO source velocity results were compared to Table 3 in Anderson et al. [2009] for the sources in common. The code by Reid et al. [2009] was used to obtain near and far kinematic distances corresponding to each radial velocity estimate (see §2.5.3).

### 2.5.3 Resolving the KDA

The H I Emission/Absorption (H I E/A) method was implemented as a standard way to choose between the calculated near and far distances [see e.g. Anderson and Bania, 2008; Urquhart et al., 2012]. The method has proven to be very successful for KDA resolution [Anderson and Bania, 2008].

Out of the 28 CORNISH UCHIIs with missing CO distances, CO and VGPS H I data were found for 21 (CO data were not available within the range  $10^\circ \leq l \leq 17^\circ$ ). In the VGPS spectra, the H I brightness temperature at the source location is overall  $\lesssim 100$  K, as expected for optically thin H I gas. Therefore,

<sup>5</sup><http://www.bu.edu/galacticring/>

Table 2.3 Comparison between velocities (in  $\text{km s}^{-1}$ ) measured in this work and by Anderson et al. [2009], Table 3 for the sources in common. As the peak channel was used to calculate the velocities, the associated errors are given by the channel width. This equals  $0.21 \text{ km s}^{-1}$  for each BU-FCRAO Galactic Ring Survey cube. In practice this error is outweighed by the error due to peculiar motions, which is  $\sim 10 \text{ km s}^{-1}$ .

CORNISH	$v$	Anderson	$v$
G024.4698+00.4954	103	C24.47+0.49	102.67
G024.4721+00.4877	102.8	C24.47+0.49	102.67
G024.4736+00.4950	102.6	C24.47+0.49	102.67
G024.8497+00.0881	109.3	C24.81+0.10	108.31
G030.7661−00.0348	96.1	C30.78−0.03	94.76
G030.7661−00.0348	96.1	U30.84−0.11b	96.89
G031.2420−00.1106	21.1	U31.24−0.11a	21.07
G034.2544+00.1460	57.7	U34.26+0.15	57.1
G034.2571+00.1466	57.7	U34.26+0.15	57.1
G037.9723−00.0965	54.7	C38.05−0.04	54.1
G049.4640−00.3511	59.5	U49.49−0.37	60.08
G049.4891−00.3763	60.9	U49.49−0.37	60.08
G050.3157+00.6747	26.5	U50.32+0.68	26.31

a background source of higher temperature should be seen in H I absorption. The presence of a H II region would provide a sufficiently strong continuum to detect a line in absorption. It should be noted, however, that the VGPS synthesized beam size is  $\sim 45''$  (FWHM) at 21 cm (see Stil et al. 2006 for the VGPS survey paper). The H II region may not be detected at all if the source size is not comparable to the survey beam size [Urquhart et al., 2012]. The extent of the effects of this on our distance estimates are hard to quantify. Moreover, neighbouring CORNISH UCHIIs found within the beam cannot be distinguished. This is the case, for instance, for G024.4721+00.4877, G024.4736+00.4950 and G024.4698+00.4954, whose H I spectra are practically identical. The latter issue is alleviated by the fact that spatially close UCHIIs are likely to belong to the same star-forming region, and hence to be situated at the same distance.

Table 2.4 KDA-resolved UCHII distances. The distances and errors were derived with the Reid et al. [2009] code and the H I E/A method was used to resolve the KDA. The sources that are found at the near, far, and tangent distance, are labelled with n, f, and t, correspondingly. The third column indicates whether the H I spectra used for the KDA resolution were of good quality (i.e. mostly in absorption, marked with ✓) or poor (i.e. mostly in emission, indicated with ✗).

CORNISH name	KDA	Strong H I abs.	$d$ (kpc)
G024.4698+00.4954	n	✓	$5.5 \pm 0.3$
G024.4721+00.4877	n	✓	$5.5 \pm 0.3$
G024.4736+00.4950	n	✓	$5.5 \pm 0.3$
G024.8497+00.0881	n	✓	$5.8 \pm 0.3$
G026.0083+00.1369	f	✗	$13.8 \pm 0.5$
G026.8304−00.2067	f	✗	$11.9 \pm 0.3$
G029.7704+00.2189	f	✗	$9.8 \pm 0.3$
G030.7579+00.2042	t	✗	$7.2 \pm 0.6$
G030.7661−00.0348	t	✓	$7.2 \pm 0.6$
G031.2420−00.1106	f	✗	$12.7 \pm 0.4$
G034.2544+00.1460	n	✓	$3.6 \pm 0.4$
G034.2571+00.1466	n	✓	$3.6 \pm 0.4$
G035.4570−00.1791	f	✗	$9.7 \pm 0.4$
G037.7562+00.5605	f	✗	$12.2 \pm 0.5$
G037.9723−00.0965	f	✗	$9.7 \pm 0.4$
G045.5431−00.0073	t	✗	$5.9 \pm 0.9$
G049.4640−00.3511	t	✓	$5.5 \pm 2.2$
G049.4891−00.3763	t	✓	$5.5 \pm 2.2$
G050.3157+00.6747	f	✗	$8.6 \pm 0.5$
G061.4763+00.0892	t	✓	$4.0 \pm 1.5$
G061.4770+00.0891	t	✓	$4.0 \pm 1.5$

To assign a near or a far distance, the H I data were plotted, together with a line marking the assigned CO radial velocity and its associated error ( $\pm 10 \text{ km s}^{-1}$  due to peculiar motions) and the calculated tangent velocity was included as well (see Figs. 2.7 and 2.8). All sources with CO velocity within  $10 \text{ km s}^{-1}$  of the tangent point velocity were assigned the tangent point distance, in order to limit wrong assignments to the near distance (as suggested by Anderson and Bania 2008). Additional uncertainty arises due to half of the H I spectra being dominated by emission instead of absorption at the UCHII source position. The presence or lack of convincingly strong absorption is indicated in Table 2.4 for each H II region. An example of a reliable H I spectrum is that coinciding with G049.4891–00.3763, as it clearly shows very strong absorption lines. Emission-dominated spectra appear similar to the one coincident with G029.7704+00.2189 (Fig. 2.7).

All 21 UCHIIs with available GRS CO and VGPS H I data were assigned a distance, and 4 more distances were adopted from the paper by Cesaroni et al. [2015]. These are the distances for G010.3204–00.2328, G011.1712–00.0662, G014.1741+00.0245, and G016.3913–00.1383. It should be noted that for these four sources, as for all sources without data to resolve the ambiguity, Cesaroni et al. [2015] assigned the far distance. Placing sources without a distance solution at the near distance is preferable (see the discussion by Urquhart et al. 2012). Only 3 sources (G010.8519–00.4407, G011.9786–00.0973 and G014.1046+00.0918) with no known distance and no available emission and absorption data remain in our sample. From the group of 21 UCHIIs, 6 were assigned the near distance, 8 – the far, and the remaining 7 sources were assigned the tangent point distance.

Fig. 2.7 Continuum-subtracted VGPS spectra (black line) towards sources from the CORNISH UCHII region sample were used to solve their KDA. The red dashed line indicates the tangent point velocity. The blue spectrum shows the measured CO spectrum, with its corresponding y-axis also in blue. The green dot-dashed line represents the CO source velocity, with the region marked in grey on each side showing the expected uncertainty of  $\pm 10 \text{ km s}^{-1}$  due to streaming motions. The H I spectrum of G024.4721+00.4877 is practically identical to G024.4698+00.4954 (top row, left); and therefore was omitted. Continues on next page.

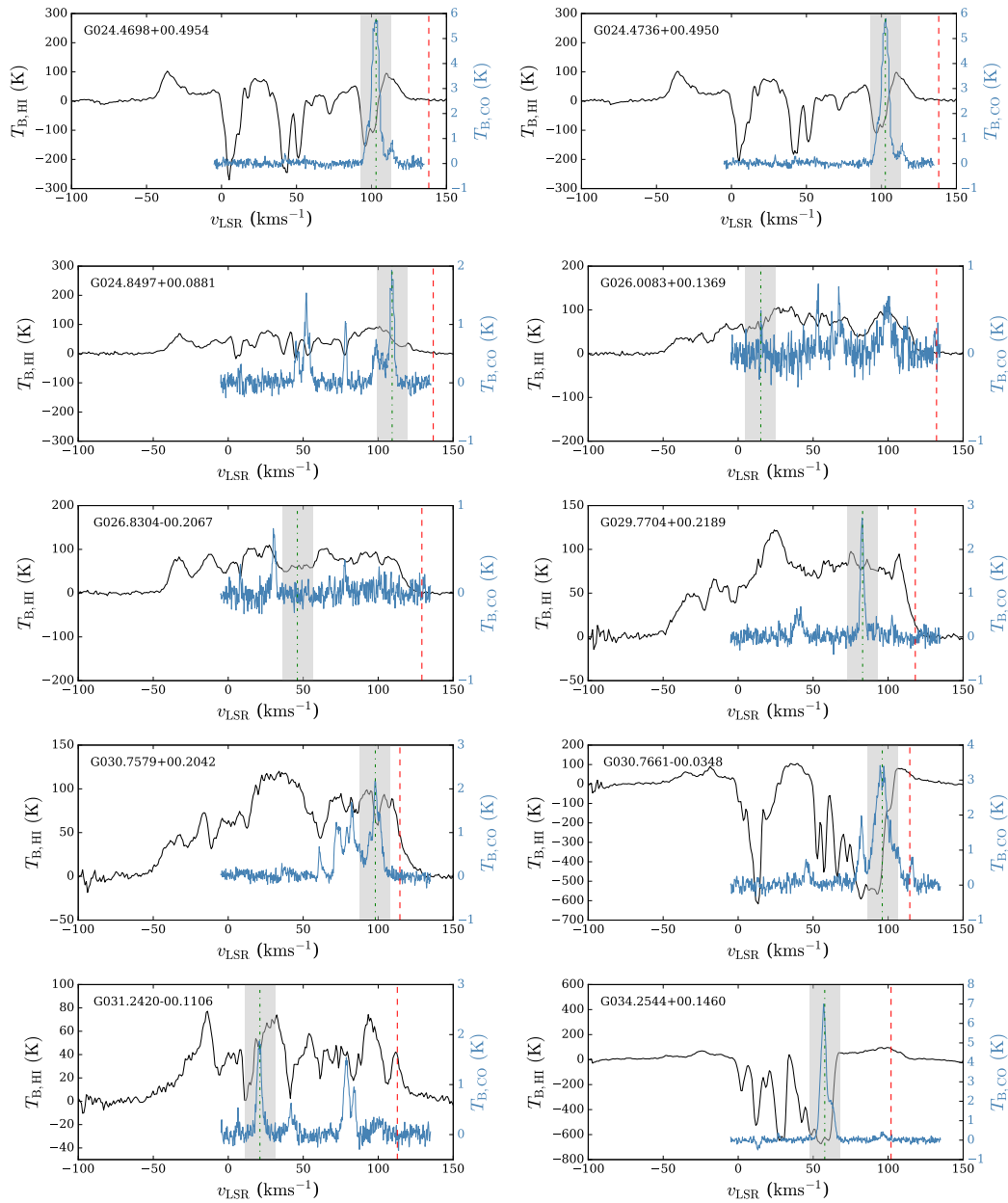
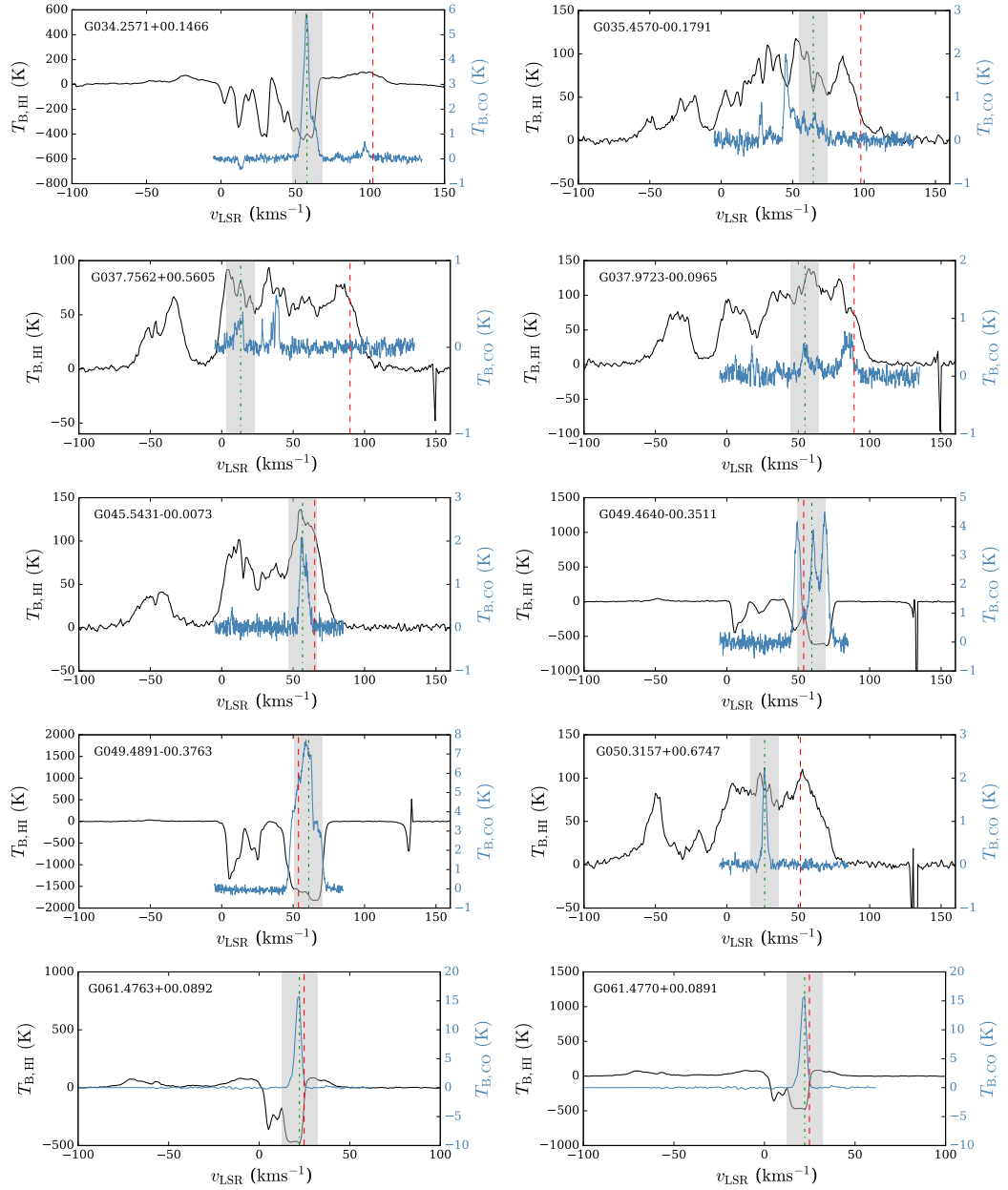


Fig. 2.8 Continuum-subtracted VGPS spectra towards sources from the UCHII region sample, used to solve their KDA (continued).



## 2.6 Derived physical properties

A summary of the physical properties of the sample is presented in Fig. 2.9. The distributions of heliocentric and galactocentric distances, physical sizes, optical depths, brightness temperatures, Lyman continuum fluxes, emission measures, and electron densities are shown. The computed values corresponding to each CORNISH UCHII can be found in Appendix B.

Fig. 2.9a shows the distribution of the UCHII regions with heliocentric distance. The five peaks are at 2, 4, 11, 13, and 17 kpc. As noted by Urquhart et al. [2013] (who also find five similarly situated peaks at 2, 5, 10, 12, and 16 kpc), they likely correspond, in turn, to the near side of the Sagittarius arm, the end of the bar and Scutum-Centaurus arm, the far sides of the Sagittarius and Perseus arms, and the Norma arm. Urquhart et al. [2013] studied the associated clumps to the CORNISH compact H II regions and found that the most prominent peak in the heliocentric distance histogram at  $\sim 11$  kpc corresponds to the W49A complex (as this peak is not seen for clumps).

The galactocentric distances were also estimated (Fig. 2.9b). The galactocentric distance distribution depends only on the choice of Galactic rotation curve [Urquhart et al., 2010]. The peaks are located at  $\sim 4.5$ , 6, and 7.5 kpc, similarly to the findings of Urquhart et al. [2010] (peaks at  $\sim 4$ , 6, and 8 kpc) for the young massive star sample in the RMS survey. Urquhart et al. [2010] identify the peak at approximately 4 kpc to be at the intersection of the Long Bar and the Scutum-Centaurus arm, also coinciding with the W43 complex. The 6 kpc peak is coincident with the Sagittarius arm, and the 7.5 kpc peak corresponds to the Perseus arm (the bin is dominated by the W49A complex – the most active star-forming region in the Galaxy).

The distribution of the physical sizes is shown in Fig. 2.9c. All sources with available deconvolved angular sizes [see Purcell et al., 2013] are presented in

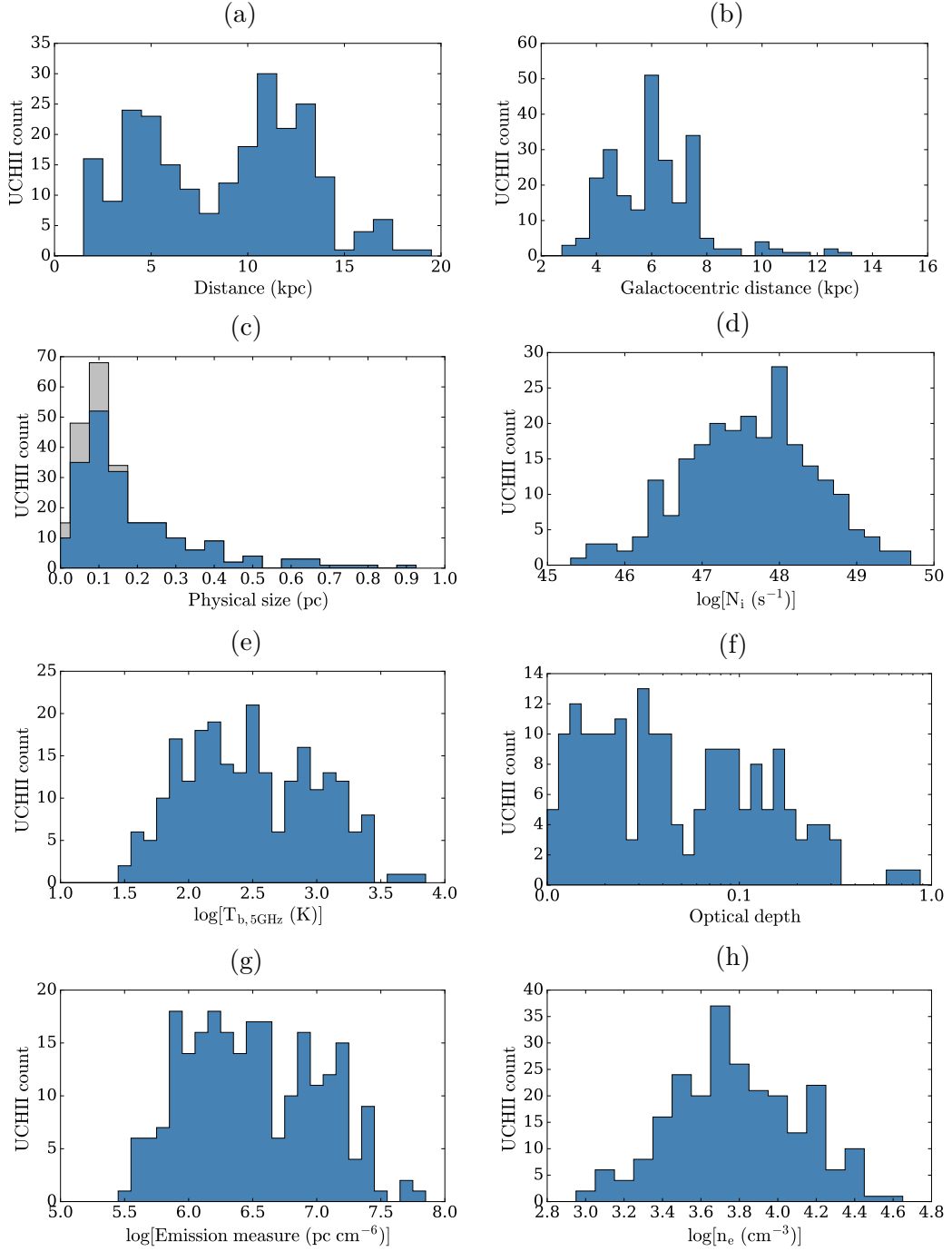


Fig. 2.9 Parameter distributions of the CORNISH UCHIIs. The distance histogram (a) includes values from Urquhart et al. [2012] and Urquhart et al. [2013], as well as the distances computed in this work. The grey area in panel (c) shows upper limits for sizes of unresolved sources. The Lyman continuum flux histogram (d) includes results from Urquhart et al. [2013], as well as results from this work, with  $\pm 10\%$  associated error. There are  $\pm 30\%$  errors on the emission measures (g) and  $\pm 20\%$  errors on the electron densities (h).

the histogram in blue. The physical sizes of 36 UCHII regions could not be obtained because the corresponding sources were unresolved and hence their true sizes are unknown (and three more sources do not have a computed distance). Upper limits on the physical sizes were computed for these unresolved sources with available distances (grey region in the histogram). Most sources ( $\sim 66\%$ ) are larger than 0.05 pc and smaller than 0.2 pc in diameter, and the distribution peaks at 0.1 pc, which is consistent with the typical sizes of UCHII regions. About 12.5% are with sizes between 0.01 pc and 0.05 pc, and the remaining  $\sim 21.5\%$  sources are between 0.2 pc and 0.9 pc. The investigated properties of these sources are in accord with the rest of the sample and therefore likely exhibit the natural variation in size one would expect for a continuum of spectral subtypes and ages, and for different ambient densities.

Lyman continuum fluxes from Urquhart et al. [2013] were available for 203 out of the 239 sources in the CORNISH sample. The Lyman continuum fluxes  $N_i$  for 33 of the remaining sources were computed from

$$\left[ \frac{N_i}{\text{photons s}^{-1}} \right] = 9 \times 10^{43} \left[ \frac{S_\nu}{\text{mJy}} \right] \left[ \frac{d^2}{\text{kpc}} \right] \left[ \frac{\nu^{0.1}}{5 \text{ GHz}} \right], \quad (2.5)$$

where  $S_\nu$  is the flux at a frequency  $\nu$  and  $d$  is the distance (Eqn. 6 from Urquhart et al. 2013). The associated error on  $N_i$  is 10%, which is dominated by the distance error. As for the emission measures and electron densities, a dust-free, optically thin emitter is assumed here. The Lyman continuum flux distribution (Fig. 2.9d) of the CORNISH UCHII sample peaks between  $47.2 < \log(N_i) < 48.5$  photons  $\text{s}^{-1}$ , which is also consistent with the Lyman continuum ionising flux from zero-age main-sequence stars with spectral class from B0 to O7. The computed Lyman continuum fluxes should be treated as lower limits.

The brightness temperature distribution at 6 cm and the corresponding optical depth distribution, as calculated in §2.3.2 (Eqns. 2.3 and 2.4), are shown in Figs. 2.9e and 2.9f, respectively. The optical depth histogram, as well as Fig. 2.6, confirm that assuming optically thin sources at 5 GHz is justified for the majority of UCHIIs in our sample.

The emission measures ( $EM$ , Fig. 2.9g) and the electron densities ( $n_e$ , Fig. 2.9h) of the UCHII regions were computed from the equations

$$\left[ \frac{EM}{\text{pc cm}^{-6}} \right] = 1.7 \times 10^7 \left[ \frac{S_\nu}{\text{Jy}} \right] \left[ \frac{\nu}{\text{GHz}} \right]^{0.1} \left[ \frac{T_e}{\text{K}} \right]^{0.35} \left[ \frac{\theta_S}{''} \right]^{-2} \quad (2.6)$$

and

$$\left[ \frac{n_e}{\text{cm}^{-3}} \right] = 2.3 \times 10^6 \left[ \frac{S_\nu}{\text{Jy}} \right]^{0.5} \left[ \frac{\nu}{\text{GHz}} \right]^{0.05} \left[ \frac{T_e}{\text{K}} \right]^{0.175} \left[ \frac{\theta_S}{''} \right]^{-1.5} \times \left[ \frac{d}{\text{pc}} \right]^{-0.5}, \quad (2.7)$$

where  $T_e = 10^4$  K is the electron temperature and  $\theta_S$  is the source angular size. Both equations were adopted from Sánchez-Monge et al. [2013], who followed the formalism of Mezger and Henderson [1967] and Rubin [1968]. It is assumed that the cm continuum flux is emitted from homogeneous optically thin H II regions. As can be seen from the optical depth results shown in Fig. 2.9f, this is a good description for the sample. The typical uncertainties on the flux density and angular diameter imply an uncertainty on the emission measure of 30% and uncertainty on the electron density of 20%. Taking the  $5\sigma$  flux sensitivity of CORNISH (2 mJy, see Hoare et al. 2012) and the  $1.5''$  resolution, the CORNISH sensitivity to  $\log(EM)$  was estimated to be  $\sim 5.5$  pc cm $^{-6}$ .

The computed UCHII emission measures and electron densities are generally consistent with the results by Kurtz et al. [1994]. No sources in the sample have computed electron densities and emission measures that would exceed

$10^5 \text{ cm}^{-3}$  and  $10^8 \text{ pc cm}^{-6}$ , respectively, even when taking into account the associated uncertainties. Hyper-compact regions have electron densities in excess of  $10^6 \text{ cm}^{-3}$  and emission measures in excess of  $10^{10} \text{ pc cm}^{-6}$  [Hoare et al., 2007]. Thus, the CORNISH survey has identified only UCHIIIs; no HCHIIIs are reported. This is not surprising, because the high density of HCHIIIs implies high turnover frequencies,  $\sim 30 \text{ GHz}$ . For an optically thick free-free spectrum with  $S_\nu \propto \nu^2$ , the flux density at the CORNISH observing frequency of  $5 \text{ GHz}$  will be of the order of  $40\times$  lower than the flux density near the turnover frequency.

The computed optical depths at  $5 \text{ GHz}$  were used to quantify how much of the  $5 \text{ GHz}$  flux density would be missed in (the few) potential cases of optically thick H II regions (as well as how much this effect varies from source to source). In  $80\%$  of all the H II regions observed at  $5 \text{ GHz}$ , the difference between the measured and the theoretical unattenuated flux is below  $10\%$ . The bright UCHII G049.4905–00.3688 has the highest computed difference ( $\sim 56.4\%$ ). The distribution of the flux difference due to attenuation tapers off above differences greater than  $\sim 20\%$ , indicating that there is most likely no significant fraction of sources that have been missed altogether. The same should be true even if the electron temperature varies from region to region (within the expected physical bounds). It should also be noted that the computed Lyman continuum flux in this case is not significantly underestimated due to optically thick free-free emission, but could still be affected by loss of ionising photons (e.g. via dust absorption), or for radio flux that was not recovered.

## 2.7 Infrared properties

### 2.7.1 Associations with mid-infrared data

The CORNISH survey was designed to cover the GLIMPSE region of the Galactic plane [Hoare et al., 2012], ensuring that all sources have mid-infrared counterparts to the radio continuum sources (§1.2.4). Photometry of all GLIMPSE UCHII sources in the four IRAC bands was performed. Selecting the correct size of the IR source would not have been straightforward without knowledge of the position and size of the ultra-compact radio source, as the IR environment is more complex than in the radio view due to the different contributions to the emission. It is also difficult to disentangle individual sources in busy neighbourhoods.

In order to use the hand-drawn polygons (in the case of extended radio sources), and Gaussian outlines (in the case of compact radio sources) as apertures for the IR data, they were expanded accordingly. The exact ‘padding’ value necessary for each of the four GLIMPSE bands was chosen after measuring (for each band) the counts at different aperture sizes and examining where the curve of growth begins to plateau before starting to increase again with the inclusion of unrelated sources. This was done for a small sub-sample of sources with a range of sizes representative of the UCHII sample, in all four bands. The ‘padding’ radii used for the 3.6, 4.5, 5.8, and 8  $\mu\text{m}$  images were 2'', 2.4'', 3.4'', and 4.3'', respectively. The measured fluxes are included in Table C.1 in Appendix C<sup>6</sup>. The background was measured with the MADFM method described in §2.3.1. After visually inspecting all 956 GLIMPSE images (all four bands), 36 8.0  $\mu\text{m}$  images were found to be saturated at the source location after visual inspection, as well as two 5.8  $\mu\text{m}$  images and one 4.5  $\mu\text{m}$  image. These, together with non-detections, were excluded from the final results. The

---

<sup>6</sup>All sources were detected at at least 9 times the median background value.

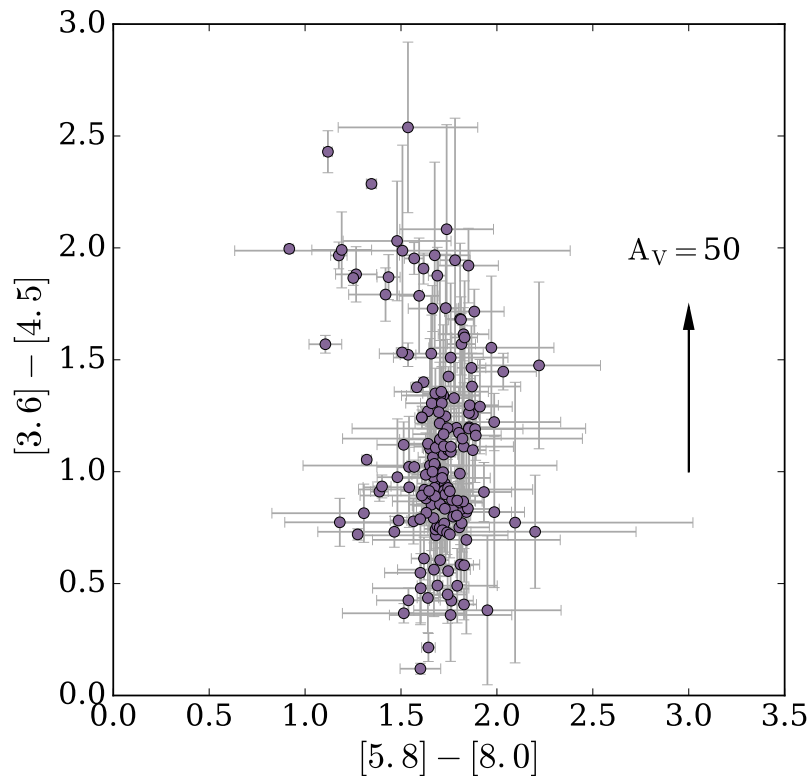


Fig. 2.10 Mid-IR colour-colour diagram of the CORNISH UCHIIs (excluding all sources with one or more saturated GLIMPSE images or otherwise unreliable GLIMPSE fluxes). The arrow shows the reddening vector, based on the extinction law of Indebetouw et al. [2005]. The plot is in the Vega magnitude system.

photometric results for G031.2801+00.0632 were also excluded, as diagnostic diagrams showed them to be dominated by a neighbouring YSO (seen in all GLIMPSE bands) rather than the UCHII region. This left 180 sources with 3.6  $\mu\text{m}$  fluxes, 191 – with 4.5  $\mu\text{m}$  fluxes, 190 – with 5.8  $\mu\text{m}$  fluxes, and 184 – with 8.0  $\mu\text{m}$  fluxes.

A colour-colour plot is shown in Fig. 2.10. Only sources for which it was possible to compute both the  $[3.6] - [4.5]$  and  $[5.8] - [8.0]$  colours were included (and no upper or lower limits for the remaining sources), to avoid overcrowding the plot. This was not found to affect the exhibited trends for the mid-IR colours. From the 174 sources with reliable flux values in all bands,  $\sim 85\%$  occupy the zone  $1.5 < [5.8] - [8.0] < 2$ . The  $[3.6] - [4.5]$  colour ranges between

0.1 and 2.1. This is similar to the results reported by de La Fuente et al. [2009] for 19 ultra-compact H II regions. They find that about 75% of the UCHIIs are grouped around  $[5.8] - [8.0] \simeq 1.7$  and  $0.5 \lesssim [3.6] - [4.5] \lesssim 2.0$ .

### 2.7.2 Associations with near-infrared data and extinctions

The visual extinction in the line of sight to UCHII regions can be estimated from their near-IR fluxes, as discussed in §1.2.4. The UKIDSS Galactic plane survey [Lucas et al., 2008] covered the northern and equatorial Galactic plane at  $|b| < 5^\circ$  in the J (1.17–1.33  $\mu\text{m}$ ), H (1.49–1.78  $\mu\text{m}$ ), K (2.03–2.37  $\mu\text{m}$ ) bands and provides an opportunity to investigate the near-IR properties of the CORNISH UCHII sample, such as fluxes and detection statistics. Only a point-source UKIDSS catalogue is available at present. Therefore automated photometry was performed in the same manner as described in §2.7.1 on all CORNISH sources with available UKIDSS data. In total, 230 sources had available UKIDSS images in the J band, 228 – in H, 227 – in K. The visual inspection revealed that out of all sources, 83 have a visible nebula in K, out of which 31 also have an H-band nebula. Out of these, 14 nebulae are visible in J<sup>7</sup>. Aperture photometry (with median background subtraction) of all contaminant bright stars found within the expanded polygon aperture used for the automated J, H, and K flux measurements was also performed. This was done for all images with a visible near-IR nebula coinciding with an UCHII. The measured stellar fluxes were subtracted from the total photometric fluxes in order to obtain the nebular fluxes. Some of the near-IR UCHII fluxes and corresponding AB magnitudes are presented in Table C.2 in Appendix C.

---

<sup>7</sup>G023.9564+00.1493 has a visible nebula in the near-IR, but photometric issues due to image quality lead to unreliable flux values, and the source is not included in the final results table.

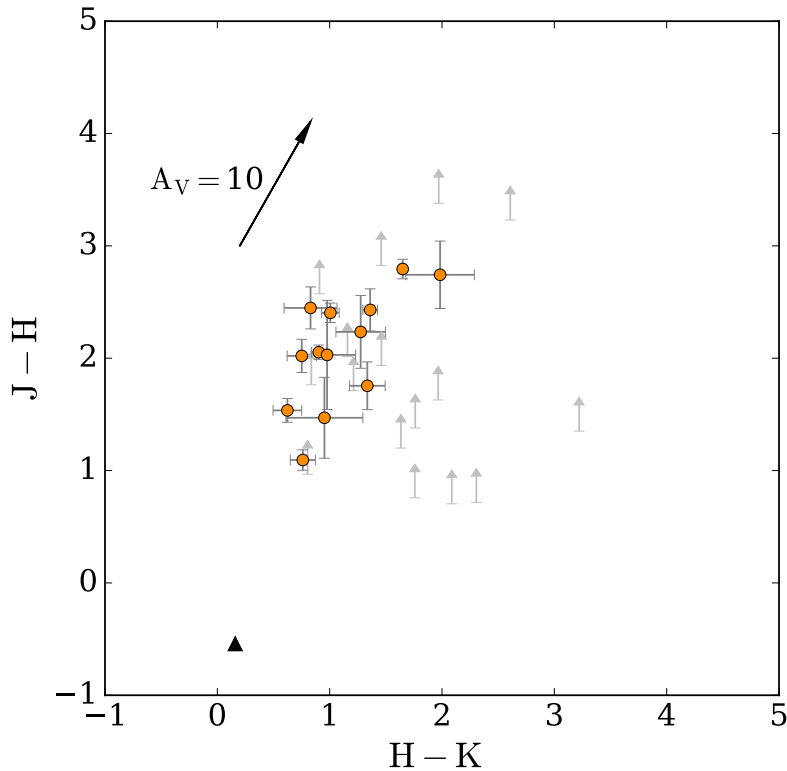


Fig. 2.11 Near-IR colour-colour diagram of near-IR nebulae associated with the CORNISH UCHIIs. The stellar contamination has been removed. Lower limits for sources visible only in H and K are also shown. The arrow shows the extinction vector, calculated using the extinction law from Stead and Hoare [2009]. The predicted intrinsic colours of an ionised nebula are shown with a black triangle. The observed data and the intrinsic colours are shown in the AB magnitude system.

Figure 2.11 shows a diagram of the  $J - H$  against  $H - K$  nebular colours. The mean colour of the nebulae visible in all three bands is 2.1 for  $J - H$ , and 1.1 for  $H - K$ .

Figure 2.12 presents a comparison between the computed visual extinctions for the UCHII sample obtained from four methods:  $F_H/F_{5\text{GHz}}$  and  $F_K/F_{5\text{GHz}}$  (top panel);  $J - H$  and  $H - K$  (bottom panel). The empirically-derived  $R_V$ -dependent extinction law  $A_\lambda/A_V$  from Cardelli et al. [1989] (Eqns. 1-3b) was used to convert from near-IR to visual extinction. The (standard for the ISM) optical total-to-selective extinction ratio  $R_V = 3.1$  was assumed. This has been

found to reach values of 5-6 towards dense clouds [e.g. Cardelli et al., 1989] but using  $R_V = 5$  did not affect the results within error.

The near-IR extinction was computed from the difference between the measured and expected near-IR magnitudes. For the flux-ratio methods, the expected H- and K-band fluxes were obtained by utilising the intrinsic ratios between IR and radio flux found by Willner et al. [1972],  $F_H/F_{5\text{GHz}} = 0.26$  and  $F_K/F_{5\text{GHz}} = 0.3$ . Using the Willner ratios, a value of 0.68 for  $H - K$  was computed in this work. In order to obtain the  $J - H$  extinction,  $F_J/F_{5\text{GHz}} = 0.43$  was computed, using Equation 1 and Table 2 in Brusaard and Van de Hulst [1962], taking into account the significant Paschen- $\beta$  line contribution to the J band [Hummer and Storey, 1987]. This resulted in a value of  $-0.1$  for  $J - H$ . These predicted intrinsic  $J - H$  and  $H - K$  colours of ionised nebulae agree well with those from near-IR photometry of planetary nebulae (with 2MASS data) studied by Larios and Phillips [2005]:  $H - K = 0.65$  and  $J - H \sim -0.1$ . Weidmann et al. [2013] also found comparable values, using PNe in the VVV survey<sup>8</sup>:  $H - K = 0.62$  and  $J - H = 0.0$ . This comparison is in the Vega system, taking into account the 2MASS (Vega system) and UKIDSS (AB system) magnitude offsets for each band. Our computed intrinsic AB colours,  $J - H = -0.54$  and  $H - K = 0.15$ , were converted to the Vega system using Table 7 in Hewett et al. [2006]: the AB offsets for the  $J$ ,  $H$ , and  $K$  bands are 0.938, 1.379, and 1.9, respectively.

The presented results from the four different extinction methods are consistent with previous estimates of visual extinctions towards UCHIIs, which are  $\sim 0-50$  mags [see e.g. Hanson et al., 2002]. Moore et al. [2005] calculated the extinction for a number of compact and ultra-compact H II regions, using observed hydrogen recombination lines. A comparison between extinction

---

<sup>8</sup><https://vvvsurvey.org/>

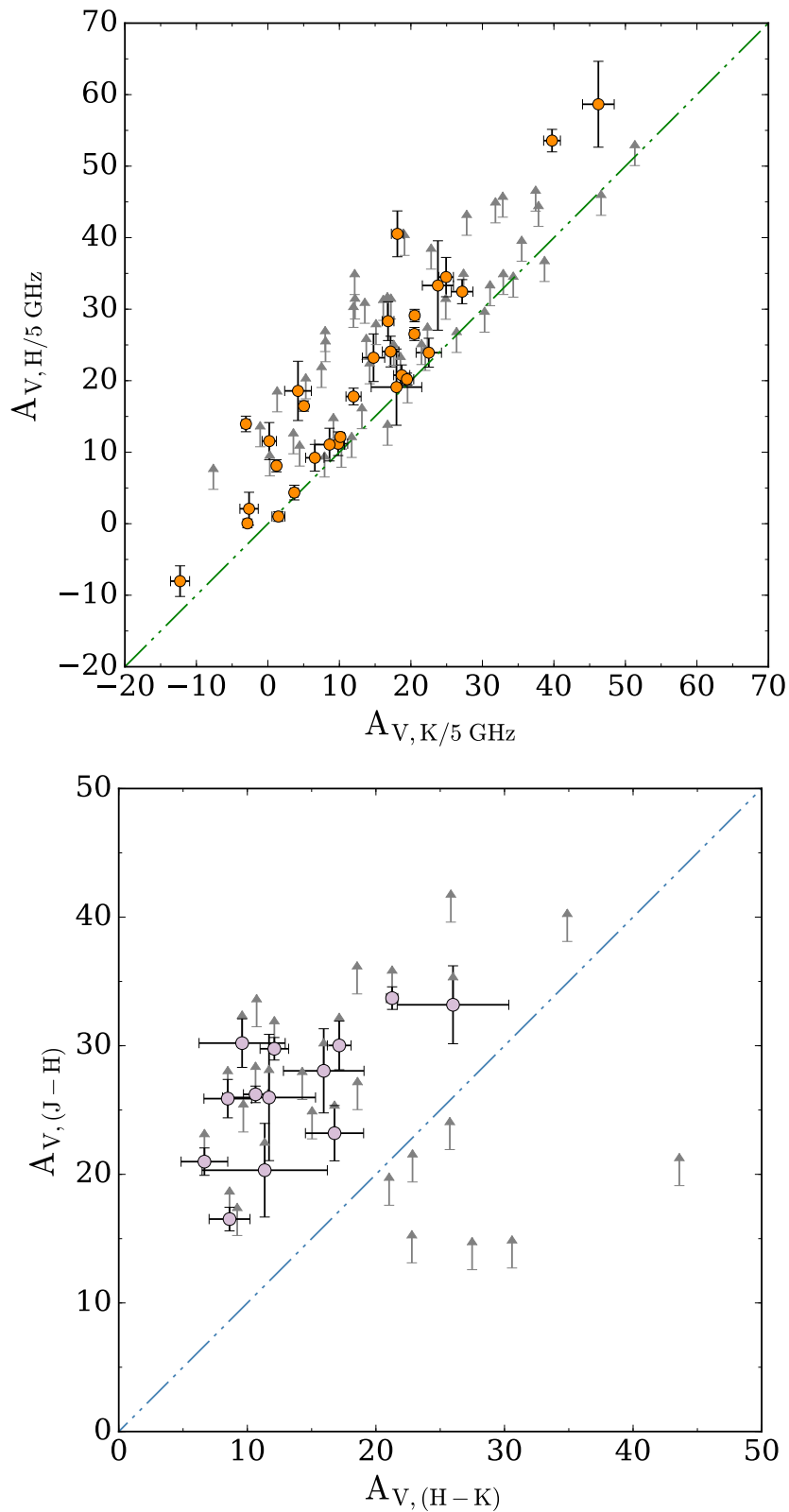


Fig. 2.12 Visual extinctions of the UCHIIs, computed from their near-IR fluxes from four methods –  $F_H/F_{5\text{GHz}}$ ,  $F_K/F_{5\text{GHz}}$ ,  $J-H$ , and  $H-K$ . The top panel compares the H- and K-band derived  $A_V$ . In the bottom panel, the comparison is shown for the  $J-H$  against the  $H-K$  derived  $A_V$ . Lower limits on the extinction are shown in the cases where the UCHII is seen only in H and K (grey arrows). Lines of equality are also plotted.

results from this work and from literature is presented in Table 2.5, showing good agreement.

As can be seen in Fig. 2.12, the offsets between the extinctions obtained from the different methods are clearly systematic. Values derived using the K band are  $\sim 10$  magnitudes lower (i.e. brighter) than those using H (and J). An addition of  $\sim 10$  magnitudes to the K band would bring the  $F_{\text{H}}/F_{5\text{GHz}}$  and  $F_{\text{K}}/F_{5\text{GHz}}$  methods to agreement and eliminate most of the unphysical negative values. Such an addition would mimic eliminating the expected boost to the K band from the contribution of very hot dust in the vicinity of the ionising star. However, a  $\sim 10$ -magnitude addition to  $K$  in the  $A_{\text{V},(\text{J-H})}$  vs.  $A_{\text{V},(\text{H-K})}$  diagram to exclude potential hot dust contribution would actually result in a  $\sim 20$ -magnitude systematic offset between these two methods. Such a discrepancy likely stems from the general nature of each pair of utilised methods and highlights the need for in-depth investigation, preferably on a case-to-case basis (beyond the scope of this work).

Table 2.5 Comparison between some extinction values in this work and in the literature, derived from comparison to 6 cm, Brackett- $\gamma$  line (‘Br $\gamma$ ’), or multi-configuration radio observations (‘radio’). Our results and the referenced literature values are in good agreement with extinction-law fits to H II recombination-line data [Moore et al., 2005].

CORNISH name	$x$	$A_x$ (mag)	Literature name	$x$	$A_x$ (mag)	Reference
G029.9559–00.0168	K/6cm	$2.33 \pm 0.07$	G29.96–0.02	K/radio	$2.14 \pm 0.08$	Watson et al. [1997]
				Br $\gamma$	$2.20 \pm 0.25$	
				Br $\gamma$	$2.16 \pm 0.07$	Moore et al. [2005]
G043.8894–00.7840	K/6cm	$2.83 \pm 0.12$	G43.89–0.78	Br $\gamma$	$3.32 \pm 0.21$	Moore et al. [2005]
G045.4545+00.0591	K/6cm	$2.21 \pm 0.11$	G45.45+0.06	K/6cm	2.5	Feldt et al. [1998]
G049.4905–00.3688	K/6cm	$2.33 \pm 0.07$	W51d	K/6cm	$2.6 \pm 0.3$	Goldader and Wynn-Williams [1994]
				Br $\gamma$	$1.59 \pm 0.07$	Moore et al. [2005]

## 2.8 Spectral energy distributions and bolometric luminosities

The computed UKIDSS and GLIMPSE fluxes were combined with multi-wavelength data from MSX (21  $\mu\text{m}$ ), WISE (22  $\mu\text{m}$ ), Hi-GAL (70, 160, 250, 350, and 500  $\mu\text{m}$ ), and ATLASGAL (870  $\mu\text{m}$ ). These data were available for 177 CORNISH UCHIIIs from Table A.1 in Cesaroni et al. [2015], and the SEDs were reconstructed for these sources. Cesaroni et al. [2015] adopted all sources classified as candidate ultra-compact and diffuse H II regions in the CORNISH catalogue (see §2.2) exactly as those were initially identified by the CORNISH team — i.e. an independent search within the entire CORNISH survey was not conducted. The authors built a summary table of the Hi-GAL and longer-wavelength counterparts to the CORNISH H II region candidates within the shared  $10^\circ$ – $65^\circ$  Galactic longitude range. Here, the multi-wavelength data were adopted only for the sub-sample of confirmed in this work CORNISH UCHIIIs. Not all 239 UCHIIIs have matches due to the lower angular resolution of *Herschel* ( $\gtrsim 9''$ ) – all unresolved Hi-GAL counterparts to close or overlapping UCHIIIs were excluded by Cesaroni et al. [2015].

The majority of the SEDs have very reasonable shapes and exhibit the same average shape. There are a few SEDs with irregularities, typically the flux at 350  $\mu\text{m}$  and 22  $\mu\text{m}$ . There are many SEDs (90/177) where the 4.5  $\mu\text{m}$  flux is low (comparable to the 3.6  $\mu\text{m}$  flux), which is most likely caused by the gap in PAH emission at this wavelength. The average SED for the sample (when all sources are placed at the median distance of 9.8 kpc) is presented in Fig. 2.13.

The bolometric luminosities of the CORNISH UCHIIIs were calculated from fitting the SEDs of the sources with available data across multiple wavelengths. The SED Fitter from Robitaille et al. [2007] was utilised, following the procedure

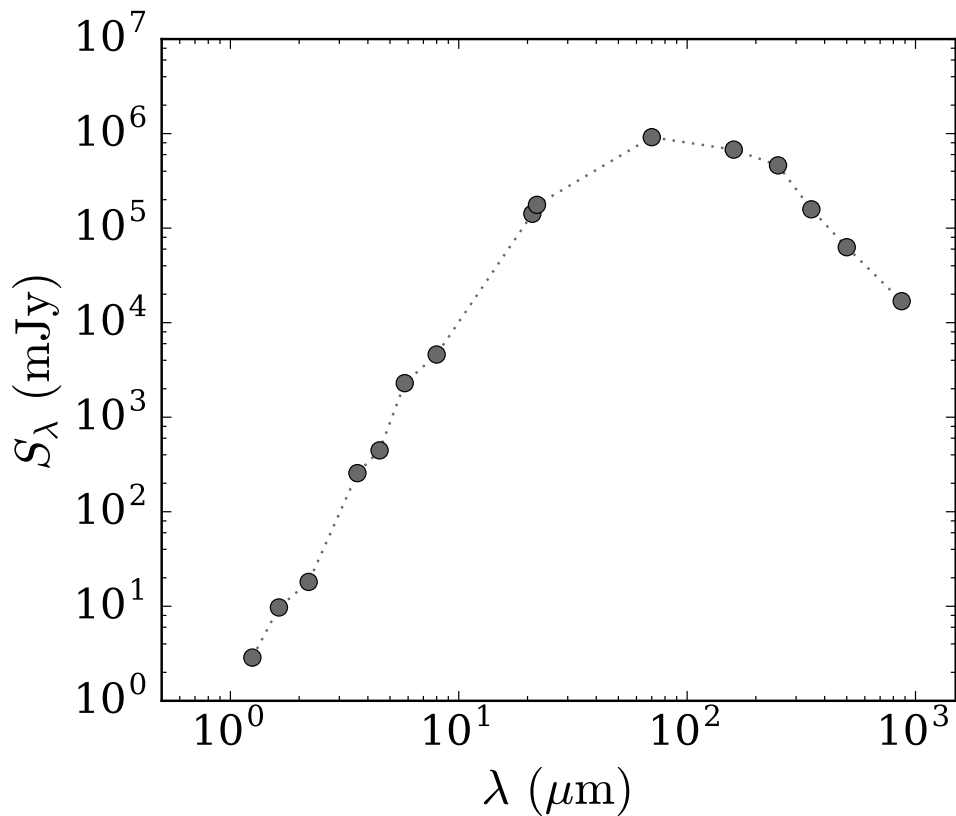


Fig. 2.13 Average SED for all UCHII regions with available multi-wavelength data, normalised to the sample median distance of 9.8 kpc. The plot includes the  $J$ ,  $H$ , and  $K$  UKIDSS fluxes and the 3.6, 4.5, 5.8, and 8.0  $\mu\text{m}$  GLIMPSE fluxes from this work, together with fluxes from MSX (21  $\mu\text{m}$ ), WISE (22  $\mu\text{m}$ ), Hi-GAL (70, 160, 250, 350, and 500  $\mu\text{m}$ ), and ATLASGAL (870  $\mu\text{m}$ ) (see Table A.1 in Cesaroni et al. 2015).

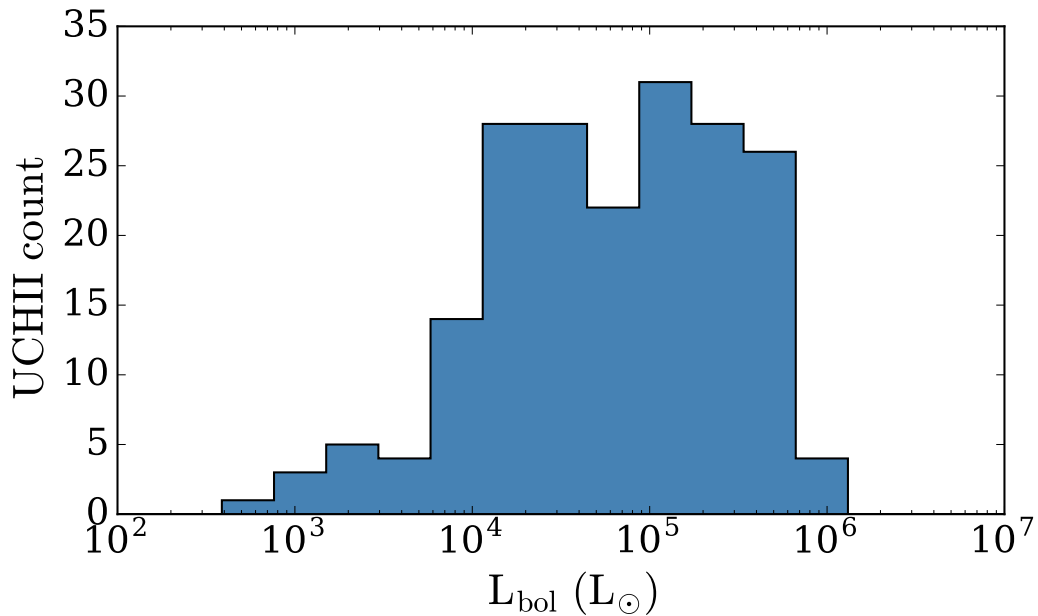


Fig. 2.14 Bolometric luminosity distribution for the UCHII regions with fitted SEDs.

prescribed by Mottram et al. [2011]. The complete sample was split into subsamples according to their distance (as computed in this work) to limit the distance range when running the fits. The fitted bolometric luminosities were then converted to the final bolometric luminosity values by replacing the automatically fitted distances with the distances presented in this work. The results are shown in Fig. 2.14. These are in good agreement with Fig. 19 in Urquhart et al. [2013], which summarises the RMS bolometric luminosities of 135 associated clumps. Note that the models used in the SED fitting are tailored to YSOs and do not take into account additional sources of dust heating in the ionised region, such as Lyman- $\alpha$  [Hoare et al., 1991]. However, the SEDs of UCHII regions and YSOs are sufficiently similar up to radio wavelengths (which are not included in the models) and the fits are useful for computing the bolometric luminosities.

Possible contamination by MYSO jet emission was investigated with a plot of radio luminosity at 5 GHz against bolometric luminosity of the UCHII regions and comparing to a sample of confirmed MYSO jets by Purser [2017].

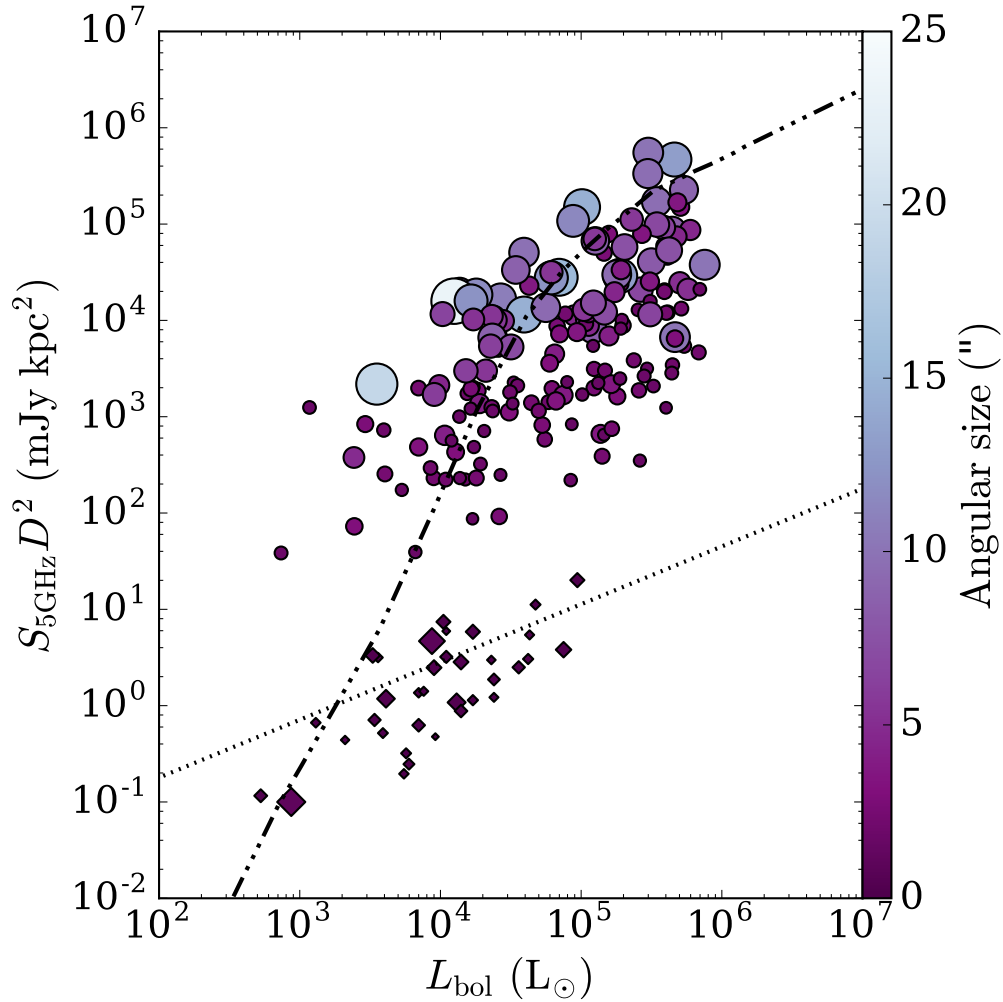


Fig. 2.15 5 GHz radio luminosity against bolometric luminosity for the UCHIIIs with fitted SEDs, shown with circles. A sample of confirmed ionised MYSO jets by Purser [2017] is also included (indicated by diamonds). The dash-dotted line marks the expected radio luminosity from Lyman continuum emission. The dotted line shows the empirical relation extrapolated for low-mass YSO jets [Anglada, 1995]. The angular size of all sources is colour-coded and emphasized through the marker sizes (the jet sample marker sizes are exaggerated, as their resolution is higher).

This is presented in Fig. 2.15. The UCHII regions are brighter, as expected, and the two populations clearly separate. The predicted optically-thin 5 GHz radio luminosities corresponding to a range of bolometric luminosities, from the stellar models by Thompson [1984] for  $L_{\text{bol}} \leq 10^3 L_{\odot}$  and from the models summarised in Table 1 of Davies et al. 2011 for  $L_{\text{bol}} > 10^3 L_{\odot}$ , are shown with a dash-dotted line in the plot. The radio continuum flux can be inferred from the Lyman continuum flux, as the latter determines the amount of ionised material and thus the number of free electrons participating in the thermal bremsstrahlung process.

The majority of CORNISH UCHIIs have radio luminosity that is between 1% and 100% of the theoretical value at the corresponding H II region bolometric luminosity (i.e. below the model line). A mixture of UCHII angular sizes are found at equal fractions of the model luminosity, ruling out angular size as the culprit behind the large variation in observed luminosity. It is to be expected that a large portion of UCHIIs would be dimmer than predicted, as the stellar models do not account for the portion of Lyman continuum flux that is absorbed by dust.

A significant number of sources (about a third) can be found above the line, with radio luminosities up to ten times or more than those predicted. The presence of H II regions in the ‘forbidden’ area above the model line is attributed to a Lyman excess. There are different explanations for such H II regions, as discussed, for example, by Sánchez-Monge et al. [2013], Cesaroni et al. [2015, 2016], and in the references therein. One explanation is the assumption of spherical symmetry, whereas in reality Lyman photons could be leaking in directions tracing lower gas density, which could be away from the line of sight. It is unlikely for the contribution to be from overlapping  $5\sigma$  or  $7\sigma$  UCHIIs, as no systematic trends were found in their distribution in the plot. Cesaroni et al. [2016] used molecular tracers to look for outflows and accretion shocks in

the vicinity of 200 CORNISH H II regions, and found no evidence to support any outflow-related phenomenon. Instead, they found that Lyman-excess sources are more associated with infall than non-excess sources, and propose ongoing accretion and accretion shocks as an explanation, but their HCO<sup>+</sup> measurements are only sensitive to large-scale infall ( $\lesssim 1$  pc), which is not direct evidence of accretion.

Two sources, G065.2462+00.3505 and G011.0328+00.0274, were found to have computed bolometric luminosities below the lower limit for H II region formation – that is, for a B3 type star with  $L_{\text{bol}} \sim 10^3 L_{\odot}$  (Bohm-Vitense 1981, Meynet and Maeder 2003). In the case of G011.0328+00.0274, this is likely due to an individual issue with the distance determination or the bolometric flux determination, as the radio-to-bolometric flux ratio is not extreme. G065.2462+00.3505, originally in the UCHII catalogue, was reclassified as a radio star. Although this unresolved radio source is embedded within an IR nebula  $\sim 50''$  in diameter, there is only a near-IR stellar counterpart but no trace of a compact counterpart at 8  $\mu\text{m}$  or 70  $\mu\text{m}$ .

It should be noted that 6 sources (G011.9786–00.0973, G014.5988+00.0198, G018.6654+00.0294, G031.1590+00.0465, G036.4062+00.0221, and G043.7960–00.1286) could not be shown in the plot. No bolometric luminosity was computed for them as the available supplementary data was not sufficient to build a good portion of their SEDs for a fit. Their  $S_{5\text{GHz}}D^2$  values range from  $\sim 34$  to  $\sim 828$  mJy kpc<sup>2</sup>, and would thus still separate from the MYSO sample in the plot.

The CORNISH sample is close to complete for UCHIIIs with flat or falling spectral indices, but incomplete for younger sources with rising spectra, such as HCHIIIs (§2.3). As discussed in §2.6, as well as by Yang et al. [2018], who searched the CORNISH survey for HCHIIIs, none of the CORNISH sources match the canonical definition of an HCHII region at 5 GHz (as proposed by

Kurtz et al. 2005). Yang et al. [2018] suggested an adjustment to the definition, because many of the 16 confirmed in literature HCHII regions have electron densities, emission measures, and/or physical sizes within the ranges more appropriate to UCHII regions. The gap seen in Fig. 2.15 could thus be the effect of incompleteness towards positive spectral index radio sources – HCHII regions could be located in the region between the MYSO jets and the CORNISH UCHII regions. Future large unbiased samples of HCHII regions, such as from the MeerGAL survey at 14 GHz [Thompson et al., 2016], which will reveal steep spectrum, optically thick sources, could be included in the plot to investigate this.

## 2.9 Comparison of UCHII search methods in blind surveys

In this work it is argued that high resolution blind radio surveys are the most reliable way to obtain the UCHII population census of the Milky Way.

To obtain a Galactic census of UCHII regions using the CORNISH sample of genuine UCHII regions, the CORNISH area needs to be scaled up to the area of the whole Galaxy. It is not possible to simply use the ratio of the longitude ranges of the Milky Way and CORNISH to obtain a total estimate, as massive star formation is more concentrated in the inner Galaxy than the outer Galaxy (see e.g. Price et al. 2001). The RMS survey encompasses  $10^\circ < l < 350^\circ$  and  $|b| < 5^\circ$  and provides the best current map of the non-uniform distribution of massive star formation throughout the Galaxy. Colour-selected RMS sources with detectable radio emission were classified as UCHII regions due to their mid-IR morphologies. UCHII regions exhibit the same Galactic scale-height,  $\sim 0.6^\circ$ , in CORNISH and RMS. Lumsden et al. [2013] estimated that the overall fraction of compact H II regions missing within the RMS survey area due to the

colour selection constraints is 10% (with around 50% of the largest compact H II regions missing).

Using the RMS survey to scale up the CORNISH UCHII sample, the total estimate is  $\sim 750$  UCHIIs in the Galaxy. This was obtained by scaling up the sample size (239 sources) by a geometric correction factor of  $\sim 3.1$  – the ratio between the detected number of RMS UCHII regions in the total RMS and CORNISH area – 500 and 160, respectively (see Lumsden et al. 2013; Urquhart et al. 2008). The underlying assumption is that UCHIIs were missed in RMS in a uniform manner with longitude. An important caveat is that the map of Galactic massive star formation provided by RMS relies on source selection from the *MSX* mid-IR point source catalogue (PSC) [Egan et al., 2003, 1999; Price et al., 2001]. A limitation to the reliability of the estimated scaling factor is thus imposed by the varying sensitivity of the *MSX* PSC towards different portions of the Galactic plane. The reliability of the source distribution map is generally better in the outer than inner Galaxy due to the lower source confusion outside the solar circle, so the detected source distribution in the inner Galaxy could be a lower limit [Lumsden et al., 2002; Price et al., 2001].

Practically the same scaling factor is obtained when taking the total RMS sample of 900 H II regions and the 297 RMS H II regions in the CORNISH area. Since the RMS UCHII counts in the total and in the CORNISH area were obtained in the same manner, their ratio should not be greatly affected by the systematic limitations of the IR-selection. Note that UCHIIs near the Galactic centre are missed in the total estimate, to avoid assumptions for the UCHII number density in this region not covered by RMS.

The sections below highlight limitations of the other UCHII search methods employed in Galactic plane surveys.

### 2.9.1 Sub-mm – ATLASGAL

Urquhart et al. [2013] identified a sample of molecular clumps with compact and ultra-compact H II regions in the region  $10^\circ < l < 60^\circ$  and  $|b| < 1^\circ$ . The authors matched the ATLASGAL sub-mm clumps to the CORNISH catalogue and recovered the majority of CORNISH H II regions. Similarly to the CORNISH UCHII sample identification (§2.2), Urquhart et al. [2013] utilised available IR data to aid the classification. They visually inspected GLIMPSE images (using the 4.5, 5.8, and 8.0  $\mu\text{m}$  IRAC bands) centred on the peak of the sub-mm emission to separate H II regions from contaminant sources. However, the depth of ATLASGAL falls short of detecting all UCHII regions within the common ATLASGAL-CORNISH area – about 30 UCHII regions were missed as a result.

Urquhart et al. [2013] used the ATLASGAL-CORNISH associations to compute the surface density of UCHII regions as a function of Galactocentric distance. They estimated that the Galactic UCHII population comprises  $\sim 400$  sources around B0 and earlier type stars, out of which only  $\sim 45$  around O6 or earlier type stars are detectable. The deeper SCUBA-2 survey should provide a higher detection certainty with the same search method (see e.g. Mackenzie et al. 2011).

### 2.9.2 Mid-IR – RMS

The whole CORNISH region is covered in RMS; despite this, about half of the CORNISH UCHIIs have RMS counterparts. There are  $\sim 40$  further associations with the more diffuse CORNISH H II sample (48 H II regions). Many of the UCHIIs ‘missing’ from RMS are, in fact, detected within big complexes but not listed as individual objects. Urquhart et al. [2013] discussed the larger total number of RMS versus ATLASGAL H II regions – the RMS H II sample contains extended regions identified from their mid-IR morphology, with radio

continuum emission lower than the CORNISH surface brightness sensitivity. The RMS sample thus includes fewer individually listed UCHII regions, together with a number of more extended H II regions.

### 2.9.3 Previous radio surveys of the Galactic plane

Giveon et al. [2008] found 494 MSX matches to the White et al. [2005] catalogue within the area shared with CORNISH ( $\sim 23\%$ ). Giveon et al. [2005] believe their sample is dominated by UCHII regions. As discussed in §2.3.1, through visual inspection only 162 CORNISH UCHII regions are found in common with the lower-resolution 6 cm data. A catalogue table cross-match found even fewer sources in common – 111, with 20 cross-matches to 37 CORNISH diffuse H II regions within the shared area. This corresponds to a factor of 3-4 fewer UCHIIs than implied by Giveon et al. [2005, 2008] – the vast majority of their sample are not genuine ultra-compact H II regions but rather represent more extended H II region phases.

## 2.10 Conclusions

The CORNISH UCHII sample is the largest complete and unbiased high-resolution collection of ultra-compact H II regions to date. Within the mapped region ( $10^\circ < l < 65^\circ, |b| < 1^\circ$ ), 239 UCHIIs have been confirmed from 240 candidates visually identified at 5 GHz radio-continuum emission. In this chapter, the observational properties, spectral indices, physical characteristics and spectral energy distributions of this early stage of massive star formation were explored. In summary:

1. The selection procedure for the CORNISH UCHIIs is robust and the nature of the sample as a whole was reliably identified.

2. The majority ( $\sim 82\%$ ) of UCHIIs have spectral indices that are consistent with the expected theoretical limits for thermal free-free emission. The results are also consistent with the theoretical model developed by Bojičić et al. [2011] for uniform ionised nebulae. The majority of sources scatter around the optically thin limit and sources approaching a spectral index of 1 are likely situated in a much less uniform environment than the rest of the sample. The instances of non-thermal spectral indices could be naturally resulting from the difference in VLA configuration between the higher- and lower-frequency datasets, or are the result of combining 6 cm and 20 cm fluxes of variable thermal sources from two epochs. Further in-depth investigation of additional data and comparison to theoretical models are required, beyond the scope of this thesis.
3. G011.0328+00.0274, G011.9786−00.0973, G014.5988+00.0198, G023.4553−00.2010, G030.7579+00.2042 and G037.7347−00.1128 were, to the best of our knowledge, detected for the first time at 6 cm. They are likely short-timescale variables, together with at least three more sources (G016.3913−00.1383, G018.1460−00.2839, G025.7157+00.0487). At least 5% of UCHIIs appear to have exhibited a significant flux increase (by  $\sim 50\%$  or more) between two observational epochs separated by  $\sim 15$  years.
4. Distances were computed for 21 UCHIIs which had no literature distance (or their KDA had not been previously resolved) prior to this work. The derived physical properties of the UCHII sample agree well with theoretical expectations. This, in turn, allowed the computations of their physical properties alongside the rest of the sample. The peaks in the heliocentric and galactocentric distance distributions are in agreement with the previously reported by Urquhart et al. [2013] and hence with the current models of the structure of the Milky Way.

5. Results of extended source photometry of UCHII regions in the mid- and near-IR were presented. The GLIMPSE and UKIDSS colours of the sample follow the expected trends set by results obtained from earlier, smaller samples. The mid-IR results are expected to be particularly reliable, as they combine the precise knowledge of position, radio size and shape provided by the CORNISH survey with the good correspondence (in the vast majority of cases) to the mid-IR counterparts. The results of the extended near-IR photometry (particularly the J and H bands) should be used with much more care, due to the difficulty in accurate subtraction of the stellar contamination in the busy, diffuse environments of star forming regions seen at these wavelengths.
6. Extinctions towards the UCHII regions were computed using the intrinsic H- and K-band to radio flux ratio from Willner et al. [1972], as well as from the  $J - H$  and  $H - K$  nebular colours. It is recommended that the computed extinctions of each source from all four methods are treated as a limiting range for each source, rather than taken individually.
7. The average spectral energy distribution of the UCHII sample (from gathering available multi-wavelength data and combining them with the new near- and mid-IR results) is in excellent agreement with the expected shape, with a peak between 70 and 160  $\mu\text{m}$ . Bolometric luminosities were computed by fitting the individual SEDs. In a plot of radio luminosity against bolometric luminosity, the CORNISH UCHII sample is clearly a separate population to confirmed MYSO jets. About a third of the UCHIIs exhibit a Lyman excess.
8. High resolution blind radio surveys are the best way to definitively find the UCHII population of the Galaxy. Radio selection provides a more reliable statistic than infrared and mm selection. A factor of 3-4 fewer

---

genuine ultra-compact H II regions than in previous lower resolution radio areal surveys were found. This result, in conjunction with up-to-date models (see Davies et al. 2011), goes towards alleviating the lifetime problem posed by Wood and Churchwell [1989b].



# Chapter 3

## Higher-resolution follow-up of point-like CORNISH UCHII regions

### 3.1 Introduction

In this chapter, high spatial resolution follow-up JVLA observations of UCHII regions unresolved or insufficiently resolved in the CORNISH VLA survey are presented. The main objective is to determine the morphologies of these smaller, and possibly younger, UCHII regions, as they reveal the distribution of matter in the immediate vicinity of the newborn massive stars. This, in turn, allows the morphological classification of the most complete to-date UCHII region sample in its (near-) entirety, and thus in its full range of ages and spectral classes.

The reduction, the imaging process and the quality analysis of the high resolution data are described in this chapter. Special attention is given to busy fields, with focus on the imaging techniques applied in the case of the W49A star-forming region. Noteworthy cases, such as re-observed resolved

CORNISH sources that have revealed further complexity of structure through the higher-resolution data, are discussed.

Flux density estimates, source angular extents, and derived properties such as physical sizes are presented. Taking advantage of the 10 GHz flux measurements and the available/measured CORNISH UCHII radio fluxes at lower frequencies (see the previous chapter), spectral indices were obtained from least-squares fitting and are discussed in the context of the CORNISH UCHII sample findings.

A full morphological classification of the CORNISH UCHII sample, including the JVLA follow-up, is at the core of Chapter 4. Instances where the ionising star is potentially seen with the higher sensitivity are also discussed in the next chapter.

## **3.2 The JVLA A-configuration targeted survey of CORNISH UCHIIs**

### **3.2.1 Target selection**

Visual inspection of the original sample of UCHII regions found in CORNISH showed that the morphology of all sources smaller than  $2.7''$  cannot be reliably determined [Hoare et al., 2012]. This comprises 107 sources. A total of 22 of these unresolved CORNISH UCHIIs (with  $\delta < 15^\circ$ ) were not included in the follow-up, as they were already observed in the VLA extended north arm hybrid BnA configuration (see Hoare et al. 2012). Since this provides resolutions better than the smaller configuration of the hybrid (B), these sources would likely not have been resolved at the new resolution. Excluding all cases where the morphology was clearly established through previous high-resolution radio continuum observations, as well as seven particularly compact sources which

Table 3.1 Summary of observational parameters. The synthesised beam depends on the declination and hour angle. The rms noise was measured in *CASA* from emission-free regions near field centres (the average for all target fields).

Parameter	Value
Band	X (8-12 GHz)
Primary beam	$\sim 4.2'$
Synthesised beamwidth	$\sim 0.2''-0.3''$
Theoretical rms	0.01 mJy beam $^{-1}$
Measured rms	0.01 mJy beam $^{-1}$
Largest angular scale	5.3''
Image pixel size	0.05''-0.08''

required even higher resolution (Q-band) observations, the target sample size was reduced to 69 sources.

### 3.2.2 JVLA observational set-up

The follow-up targeted survey was observed with the Jansky Very Large Array (JVLA) in continuum mapping mode, and in A configuration – thus achieving resolution 7.5 times higher than CORNISH. Employing the X band (8-12 GHz) ensured additional resolution, and sensitivity significantly higher than the CORNISH survey (for which the C band was used).

Follow-up observations of unresolved CORNISH sources were undertaken on 6/04/2014 and 14/04/2014, in six-hour observing blocks (observer: Prof Melvin G. Hoare, proposal ID: VLA/14A-085)<sup>1</sup>. For this purpose, the A-configuration of the JVLA was used, with 27 functional antennas at the time. The minimum antenna baseline for this configuration is 0.68 km, and the maximum – 36.4 km<sup>2</sup>. The X-band continuum observations covered targeted CORNISH UCHIIs with  $16^\circ < l < 65^\circ$ . A total bandwidth of  $2 \times 2$  GHz was used to observe these frequencies. Each 2 GHz portion is allotted into 16

<sup>1</sup>The CORNISH survey observations were conducted in the 2006 and 2007/2008 VLA observing seasons - see Table 1 in Purcell et al. [2013].

<sup>2</sup><https://science.nrao.edu/facilities/vla/docs/manuals/oss2016A/performance/resolution>

Table 3.2 Comparison of tabulated (fifth and sixth columns) and newly measured (final column) JVLA calibrator fluxes.

Calibrator	Type	$\alpha$ (J2000)	$\delta$ (J2000)	$F_{3.7\text{cm}}$ (Jy)	$F_{2\text{cm}}$ (Jy)	Measured $F_{3\text{cm}}$ (Jy)
1832–1035	Phase	18 <sup>h</sup> 32 <sup>m</sup> 20.836 <sup>s</sup>	−10°35′11.200″	1.28	1.25	1.04 ± 0.01
1856+0610	Phase	18 <sup>h</sup> 56 <sup>m</sup> 31.839 <sup>s</sup>	+06°10′16.754″	0.3	–	0.182 ± 0.001
1922+1530	Phase	19 <sup>h</sup> 22 <sup>m</sup> 34.699 <sup>s</sup>	+15°30′10.032″	1.0	0.7	1.04 ± 0.01
1925+2106	Phase	19 <sup>h</sup> 25 <sup>m</sup> 59.605 <sup>s</sup>	+21°06′26.162″	1.0	1.8	0.767 ± 0.001

spectral windows, 128 MHz each, to reduce bandwidth smearing. The smallest achieved beam size was  $0.2'' \times 0.14''$ , with a typical beam size of  $\sim 0.3'' \times 0.2''$ . The largest reliable angular scale (i.e., that can be imaged reasonably well in full synthesis observations) for this setup is  $\sim 5.3''$ . The largest observed individual source has a deconvolved major axis of  $\sim 5.3''$ , and all science targets are smaller than  $2.7''$  in CORNISH, as discussed above.

### 3.3 Data reduction

#### 3.3.1 Quality check – calibrator fluxes

The target UCHIIs were grouped by position into small blocks; a short observation of a nearby phase calibrator (usually 1-2 minutes, depending on its flux density) was conducted before and after observing each block. The phase calibrators 1832–105, 1856+061, and 1925+211, as well as 1922+1530, were used in the CORNISH follow-up to correct for fluctuations in the amplitude and phase due to atmospheric and instrumental effects. As can be seen in Fig. 3 in Hoare et al. [2012], these sources provide coverage of the entire CORNISH area, as all survey blocks are located within  $\sim 10^\circ$  of a calibrator. The quasar 1331+305 (also known as 3C 286<sup>3</sup>), one of the four primary VLA calibrators, was used for the absolute calibration of the flux density. The primary flux calibrator was targeted at the beginning of each of the two observing sessions,

<sup>3</sup>In the Third Cambridge Catalogue of Radio Sources.

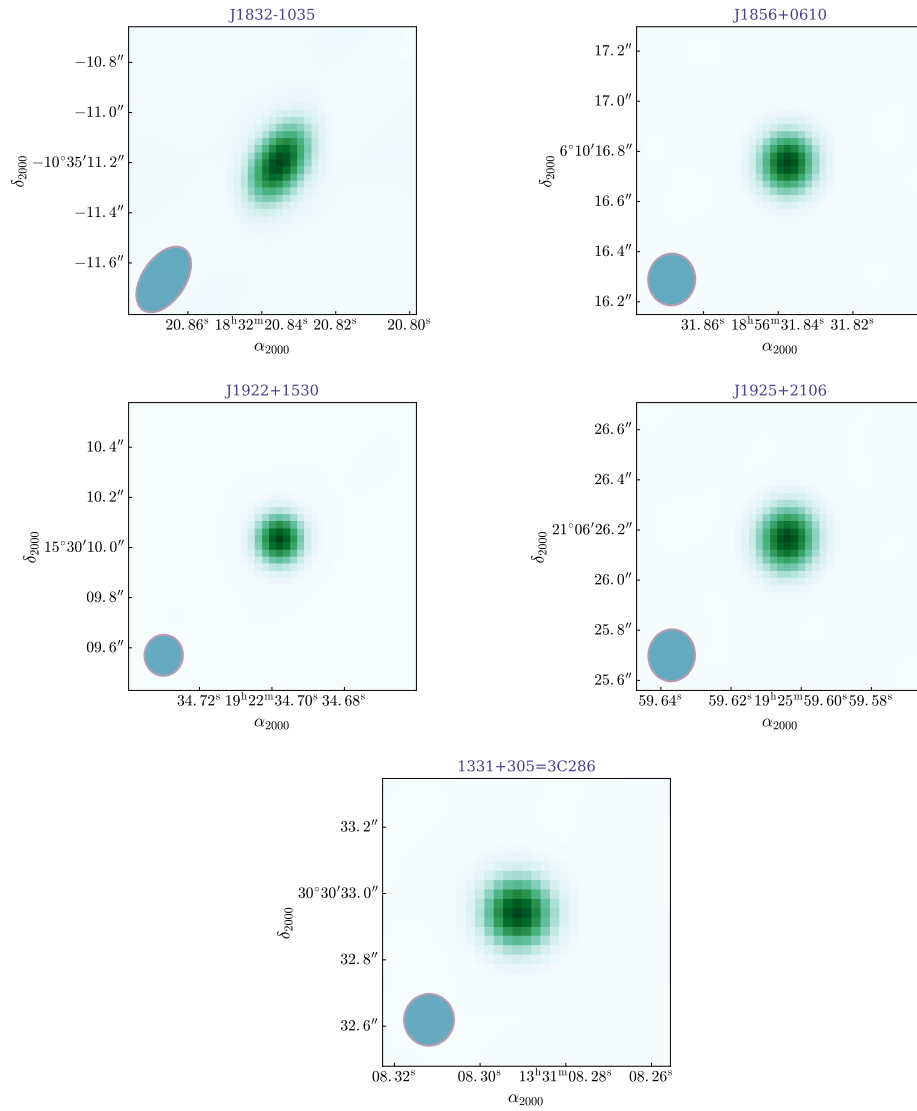


Fig. 3.1 Phase calibrators (1832–105, 1856+061, 1922+153, 1925+211) and flux calibrator (1331+305) used in the JVL A follow-up observations. The clean beam is illustrated in the bottom left corner of each panel.

with a scan length of 10 minutes each time. Images of all calibrators are shown in Fig. 3.1.

For the target UCHII regions (and the phase calibrators), the total scan time amounted to about 10 minutes (8 minutes on-source, with additional time for overheads). This exposure time was needed to obtain a noise level of  $11 \mu\text{Jy beam}^{-1}$ . The lower limit to the target radio surface brightness was calculated by considering the  $7\sigma$  CORNISH sensitivity of  $2 \text{ mJy beam}^{-1}$  for a  $1.5''$  beam – this translates to  $\sim 33 \mu\text{Jy beam}^{-1}$  for a  $0.2''$  beam at 5 GHz. All targets are expected to be brighter at 10 GHz than at 5 GHz, as the turnover frequency is expected to be around 5-15 GHz.

Table 3.2 presents a comparison between the newly measured and the catalogued fluxes of the calibrators<sup>4</sup>. The results are comparable, noting that the flux density values included in the VLA calibrator manual are more than 10 years out-of-date and that calibrators are typically intrinsically variable (and thus differences with current values by more than a factor of 2 may be expected).

### 3.3.2 Pipeline processing and flagging

The data (comprising two blocks corresponding to the two observing sessions) were reduced with the NRAO Common Astronomy Software Applications package (CASA, see Rau and Cornwell [2011]), by utilising the standard JVLA calibration pipeline and methodology for continuum emission<sup>5,6</sup>. Known radio frequency interference (RFI), e.g. from commercial broadcasting, and other issues (e.g., shadowed data, edge channels of sub-bands, system problems) were

<sup>4</sup>See <https://science.nrao.edu/facilities/vla/observing/callist>.

<sup>5</sup>See <https://casa.nrao.edu/> and <https://science.nrao.edu/facilities/vla/data-processing/pipeline>.

<sup>6</sup>A small portion of the dataset (11 UCHII regions) had previously been reduced and morphologically classified as a part of an MPhys project [Miley, 2017], but all available data were re-reduced.

automatically flagged during the pipeline processing. Additional editing was performed to mark and exclude any data still plagued by problems, such as remaining significant phase and amplitude excursions (for example from RFI from sporadic naturally-occurring or human-made sources, which is also highly polarised). The X band has a decreased sensitivity at the higher end of its frequency range, and the effects were seen in the data inspection. The final five frequency channels (total bandwidth of 640 MHz) were the most affected, and up to 84% of the data in the first two of these were flagged, and virtually all data (>94%) in the final three channels were excised. About 10% of all data were flagged per antenna (from all antenna cross-correlations), about 9% on average per channel, and about 5.5% per polarisation. The pipeline was re-run to apply the new flags to the data. This was done to ensure good imaging sensitivity, as any remaining issues can severely reduce it or even cause calibration to fail. Each of the two 6-hour dataset blocks was split into individual target fields prior to the second round of flagging, to expedite the visual quality inspection.

All viable spectral windows (out of the 32 unique ones) were combined; the frequency of the resulting fields is thus  $\sim 10$  GHz. The computed theoretical rms noise is  $11 \mu\text{Jy beam}^{-1}$  at medium elevation ( $25^\circ$ - $50^\circ$ )<sup>7</sup>.

The typical measured  $1\sigma$  rms noise (close to the field centres) was in excellent agreement with predictions – typically ranging from  $\sim 8$ - $12 \mu\text{Jy beam}^{-1}$  between fields. The new data are thus 40 times more sensitive than CORNISH (a  $7\sigma$  sensitivity limit of  $\sim 0.07$  mJy vs 2.8 mJy), and thus should be sensitive enough to detect all targeted CORNISH UCHII, as well as weaker sources such as MYSO jets, and in some cases possibly the stellar wind contribution from the OB star ionising the H II region (candidate ionising OB stars seen at near-

---

<sup>7</sup>The theoretical rms was computed with the NRAO JVLA Exposure Calculator v18A for semester 18A. The tool accounts for the RFI levels characteristic for the 8-12 GHz frequency range, which can be up to 15%.

IR and X-ray wavelengths are presented in Chapters 4 and 5, respectively). Towards the edges of fields, the rms noise levels reach  $26 \mu\text{Jy beam}^{-1}$ , or a  $7\sigma$  sensitivity limit of  $\sim 0.18 \text{ mJy}$  – this is considered the sensitivity limit for non-targets found within the observed fields. Such sources were also analysed and are subsequently discussed (the ‘neighbour group’ from here on).

### 3.3.3 Imaging

#### Overall method

The frequency-averaged, split, and calibrated target fields were imaged with *CASA* and converted to FITS format. Deconvolution was performed using the standard task *clean* (see §1.3 in the Introduction), to remove the artefacts from the dirty beam. Each image was cleaned down to a conservative threshold of  $0.15 \text{ mJy}$  or, in several cases,  $0.1 \text{ mJy}$  – a  $7\sigma$  cutoff level was found to be optimal through visual inspection with the *CASA viewer* (to avoid potential *clean* ‘bias’). The exact value was determined depending on the individual noise level of each field – by measuring the rms noise levels in the central portion of the field, as well as near the field edge. Interactive cleaning was performed whenever necessary, to remove artefacts resulting from bright sources in the primary beam – this entailed ‘boxing’ bright neighbours prior to focusing on the field target. The issue occurred in fields where the target UCHII was relatively weak. The weaker flux is ‘cleaned’ at a later stage, thus incurring larger flux errors unless the bright neighbour is handled appropriately. This effect was not prominent in most of the fields containing a multitude of sources, as the data averaged over all (available after the flagging stage) spectral windows were used, ensuring a good signal-to-noise ratio.

Imaging was sensitivity-limited, with the exception of busier fields where bright, evolved H II regions are also present. In the latter instance, which

is the case for  $\sim 10\%$  of the maps, results are limited by the dynamic range. Imaging was thus first approached in a more automated manner, the resulting clean maps were examined visually and the best successfully deconvolved maps were selected. An individual approach was used in all cases with one or more especially bright neighbours in the field, as well as in otherwise challenging cases.

### **Choice of clean parameters**

The `clean` task parameters were set to standard values. The MS-MFS (multiscale-multifrequency) deconvolution algorithm was used, as it is appropriate for wide-band synthesis-imaging. It is capable of reconstructing the spatial (and the spectral) structure of compact and extended emission at the resolution permitted by the highest sampled frequency and at the continuum sensitivity limit (as described by Rau and Cornwell 2011).

Briggs weighting was applied to the visibilities, with a Briggs robustness parameter of 0.5. This was chosen as a compromise between natural (high-sensitivity) and uniform (high-resolution) weighting, while slightly favouring sensitivity [Briggs, 1995].

The fast ‘clark’ algorithm was used instead of the classic ‘hogbom’ algorithm to calculate the synthesized beam used for the minor cycles in the image plane. The brightest points are cleaned jointly, to be subtracted during the subsequent major cycle, and the residuals are calculated more accurately than with the classic method. Cell sizes of  $0.05''$  or  $0.08''$  (close to a third of the beam size) gave the best results for the whole dataset. The smaller cell size results in sources of smaller extent appearing smoother, whereas the larger size was found to be more appropriate for more extended targets. A run with a  $0.03''$  cell size was also performed on the data. This gave a better sampling of more compact sources but resulted in longer imaging times and ‘grainy’ images of

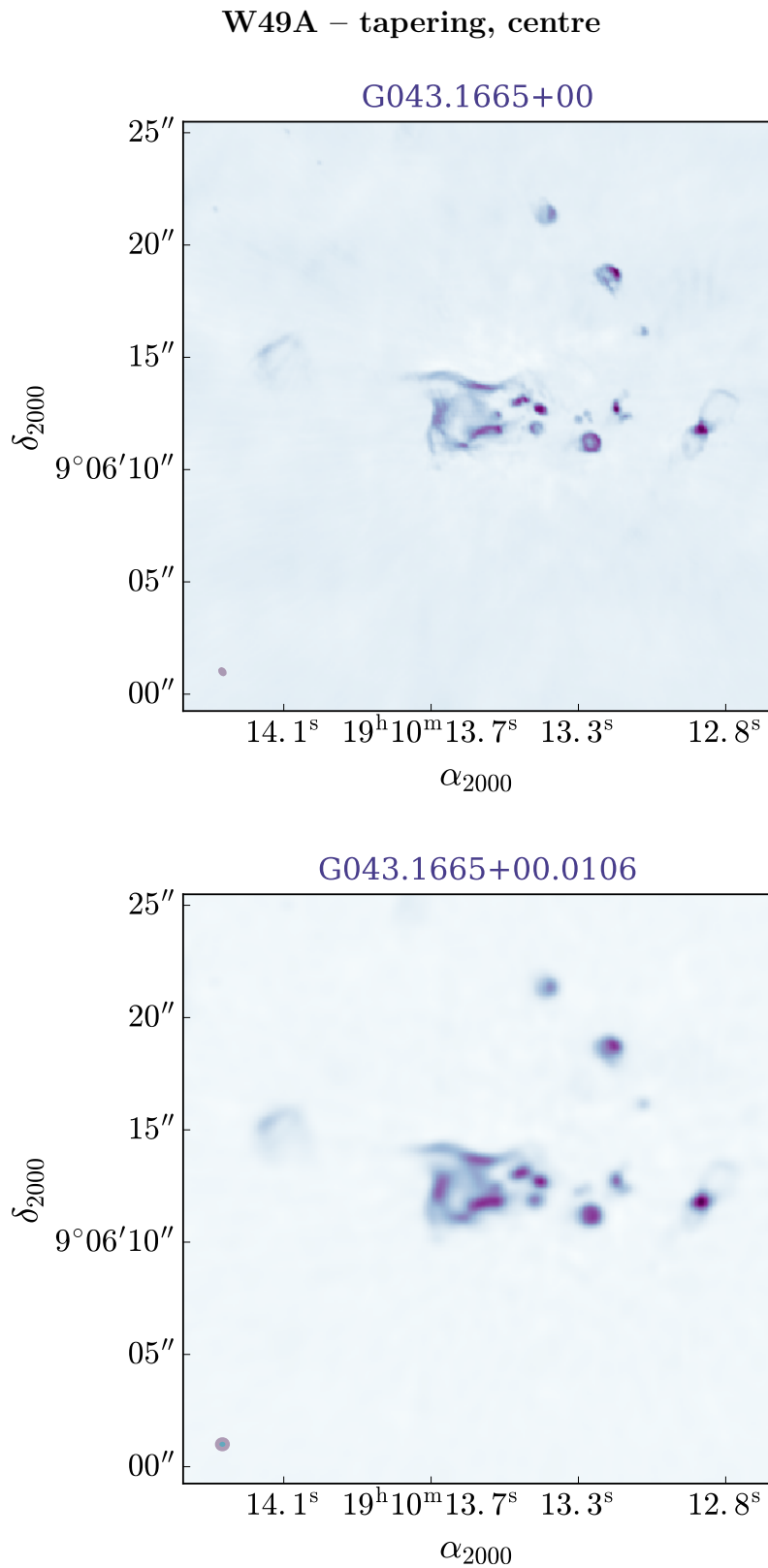


Fig. 3.2 Comparison between standard cleaning (top panel) and multi-scale clean (at 0, 5, 10, 20, and 50 pixels, with a 2.5-pixel beam) with 0.5'' tapering of the outer baselines in the uv-plane, and small scale bias parameter set to 0.9 (bottom panel), for the central portion of the W49A complex. The standard method does a good job close to the field centre and preserves the high resolution.

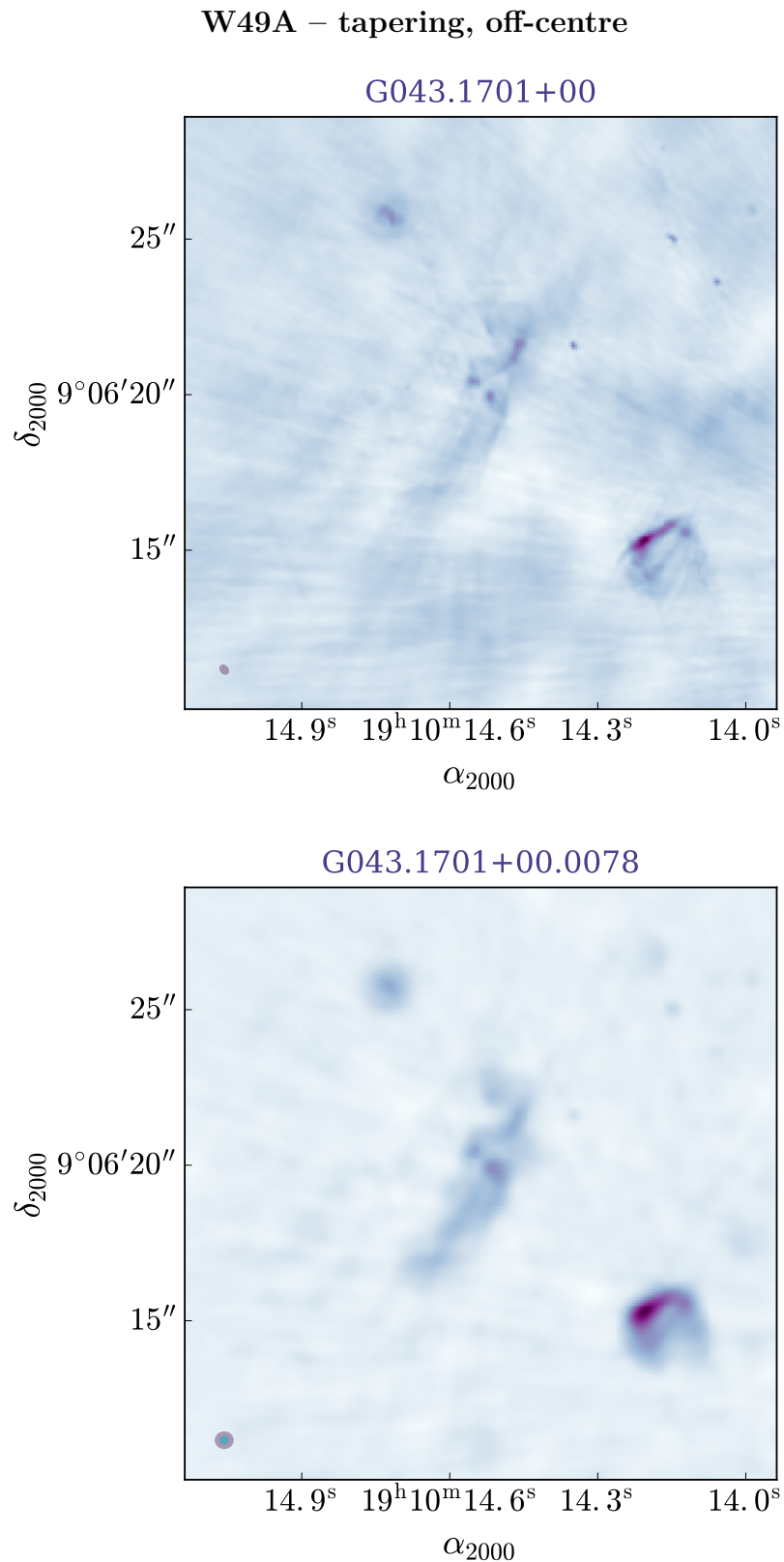


Fig. 3.3 Comparison between standard cleaning (top panel) and multi-scale clean (at 0, 5, 10, 20, and 50 pixels, with a 2.5-pixel beam) with 0.5'' tapering of the outer baselines in the uv-plane, and small scale bias parameter set to 0.9 (bottom panel), for an off-centre portion of the W49A complex. The latter method allows to image weaker and more extended sources better in the vicinity of bright, compact sources.

more extended ones (as the gaps in coverage appear too pronounced). The variation in cell sizes and cleaning thresholds was kept small to also preserve homogeneity as much as possible, while also aiming to produce individual maps of high quality.

Most image sizes were chosen to be  $1024 \times 1024$  pixels or  $1280 \times 1280$  pixels, except when imaging W49A. In this case, a size of  $2560 \times 2560$  pixels was used and a multi-scale clean with tapering was applied. It should be noted that map sizes larger than  $1280 \times 1280$  pixels were avoided as this slowed down imaging significantly. The relevant CORNISH survey 5 GHz images (those containing the follow-up targets) were inspected to help decide on the smallest required map size for each target and its neighbours. Multiscale imaging and uv tapering were also utilised sparingly and in individual cases – only when needed rather than in the initial automated runs – as they also slowed down the overall imaging progress dramatically. Tapering the weight of visibilities in the uv plane was used to shape the synthesized beam. It lowers the sidelobes and improves the signal-to-noise ratio but comes at the cost of decreased resolution and should be used sparingly, with moderate strength, to increase the brightness sensitivity of more extended sources. This is illustrated with Fig. 3.2 and Fig. 3.3, showing the centre of the W49A complex, and sources to the east of it, respectively. The standard method without tapering works well close for the bright sources and preserves the high resolution (Fig. 3.2), whereas tapering is useful for the weaker, more extended sources in the vicinity (Fig. 3.3).

### **Note on busy fields with different-brightness neighbours**

A common issue was posed by confusing sources outside the target area, for example in the case of G018.4433–00.0056. This is one example of a source with a bright neighbour at the edge of the imaged field (in this case, the four times brighter G018.4614–00.0038). Setting an area around the confusing

source to deconvolve with the main image lead to better results. In this and similar instances, much improved maps were achieved by setting ‘outlier’ fields in `clean` by specifying the outliers’ phase centres and mask box sizes. In the case of G020.0797–00.1337, with the  $>40$  times brighter G020.0809–00.1362 only  $9''$  away, the map was improved but still left with bright streaks. This was also the case for G045.0694+00.1323,  $6.3''$  away from the 14 times brighter G045.0712+00.1321.

### Other imaging hurdles

Some targets have no bright sources in their vicinity, but are very bright themselves and cause significant sidelobes in the image. The most extreme example for this effect is G061.7207+00.8630, which required a greater number of cleaning cycles for successful deconvolution (and cleaning down to a slightly decreased threshold of 0.1 mJy).

## 3.4 Target detection statistics

The dataset covers 68 target fields of interest.

All but two targets were successfully detected and imaged, the exceptions being G034.2571+00.1466 and G043.7960-00.1286 (the reasons for this are discussed in §3.5.1). The higher-resolution observations revealed that, for the target group, six CORNISH sources are, in fact, spatially close pairs.

The source G065.2462+00.3505, a target of the JVLA follow-up, was reclassified as a radio star in this project (see §2.8). It is unresolved in the IR. Its corresponding target field was not imaged<sup>8</sup>.

---

<sup>8</sup>As there are no other sources within the field, the nearest CORNISH  $7\sigma$  source is a radio galaxy,  $\sim 8.4'$  away from the field centre.

Table 3.3 Observed properties (position, integrated and peak flux, major and minor source axes) of the candidate MYSO-jet components found next to the UCHII G027.1859–00.0816 (field clean beam size of  $0.33'' \times 0.17''$ ).

Comp.	$\alpha$ (J2000)	$\delta$ (J2000)	$S_{\text{int}}$ (mJy)	$S_{\text{peak}}$ (mJy/beam)	$\theta_{\text{M}}$ ( $''$ )	$\theta_{\text{m}}$ ( $''$ )
(A)	$18^{\text{h}}41^{\text{m}}13.32^{\text{s}}$	$-05^{\circ}08'59.80''$	$0.45 \pm 0.04$	$0.18 \pm 0.01$	$0.46 \pm 0.04$	$0.30 \pm 0.02$
(B)	$18^{\text{h}}41^{\text{m}}13.23^{\text{s}}$	$-05^{\circ}09'00.54''$	$0.35 \pm 0.04$	$0.18 \pm 0.01$	$0.32 \pm 0.02$	$0.22 \pm 0.01$
(C)	$18^{\text{h}}41^{\text{m}}13.20^{\text{s}}$	$-05^{\circ}09'01.06''$	$0.79 \pm 0.13$	$0.26 \pm 0.03$	$0.45 \pm 0.08$	$0.17 \pm 0.01$
(D)	$18^{\text{h}}41^{\text{m}}13.15^{\text{s}}$	$-05^{\circ}09'01.39''$	$0.61 \pm 0.05$	$0.51 \pm 0.02$	$0.31 \pm 0.02$	$0.22 \pm 0.01$

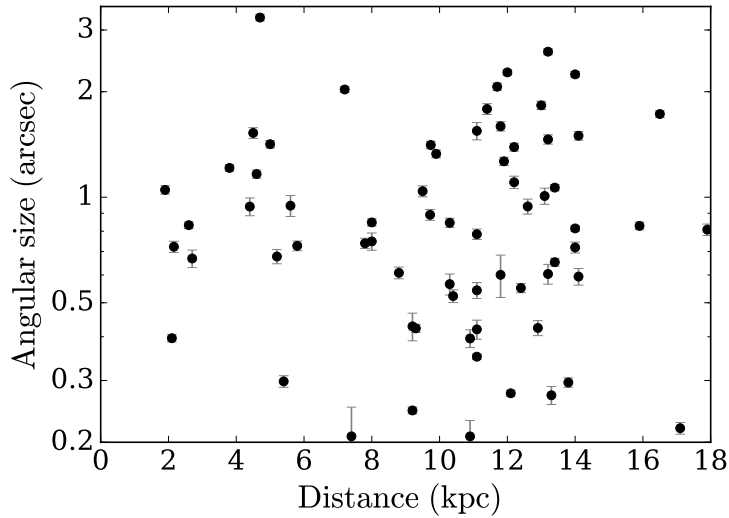


Fig. 3.4 Measured JVLAs 10 GHz angular diameters for the target UCHII regions against distances.

MYSO candidates that were not picked up by CORNISH due to the lower sensitivity and observation frequency are also seen within the target fields. A string of four aligned MYSO-jet-like unresolved knots are seen ahead of the cometary G027.1859–00.0816 (see Fig. 3.5), but are not seen in CORNISH. The main observables of the MYSO candidates are summarised in Table 3.3.

### 3.5 Target maps

All target maps are presented in this section, zoomed in at the relevant CORNISH source (Fig. 3.5). The panels are centred on the JVLAs pointing centres. Contours are overplotted to aid the morphological classification (explored in

the next chapter). The levels start at  $7\sigma$ , in individually computed numbers of steps depending on the dynamic range in each observed field, up to the peak flux of each source (or the brightest source, if more than one occupy the same image).

The flux densities and angular sizes of the targets are summarised in Table D.1 in Appendix D. The distribution of angular diameters with distances is shown in Fig. 3.4. The plot shows no correlation, as would be expected for a subset containing sources that are genuinely young, rather than sources appearing compact due to their distance.

The vast majority of target UCHIIs were sufficiently resolved to be morphologically classified (see the next chapter). One target UCHII is still unresolved at the higher resolution – this is G027.9352+00.2056, at a distance of 12.1 kpc [Urquhart et al., 2012] (giving an upper limit to its physical diameter of 0.016 pc). Target UCHIIs that are just resolved (and thus their subsequent morphological classification is ambiguous) are G026.0083+00.1369, G026.1094–00.0937, G030.0096–00.2734, and G038.6529+00.0875.

As mentioned in §3.4, six of the CORNISH targets appear at the higher resolution to be merged pairs of sources. Three CORNISH UCHIIs are comprised of one extended and one unresolved source (G018.6654+00.0294, G030.5887–00.0428, and G044.3103+00.0410). Two targets were resolved into two extended components (G033.8100–00.1864 and G043.7954–00.1274). One target, G020.9636–00.0744, was revealed at the higher resolution to consist of a bright and a dim extended component. The unresolved components could be younger or less luminous sources, particularly in the cases where the flux of the unresolved component is quite low (relative to the resolved companion), and are discussed below.

G018.6654+00.0294 (see Fig. 3.5) belongs to the massive protocluster G18.67+0.03, explored by Cyganowski et al. [2012]<sup>9</sup>. Figure 1d in Cyganowski et al. [2012] shows the closest association, G18.67+0.03 – CM1, at a separation of 0.27'' from our JVLA field pointing centre, and coincident with the compact source indicated here as G018.6654+00.0294b (see Table D.1 in Appendix D). The resolution of the 24.64 GHz continuum contours is insufficient to reveal the compact component which can be seen in the 10 GHz map (see Fig. 3.12). The source G18.67+0.03 – CM1 is associated only with Class I CH<sub>3</sub>OH masers (no hot core line emission), which supports the authors' conclusion that Class I masers may be excited not exclusively by young (hot core) MYSOs, but also by older 'UCHII MYSO' stages within the same protocluster, in contrast with other studies (see the references in Cyganowski et al. [2012]). If G018.6654+00.0294b is in fact a representative of a younger evolutionary phase, this may not be the case.

G030.5887–00.0428, also with a compact component ahead of a cometary, is associated with an interstellar hydroxyl (OH) maser – another signpost for recent massive star formation [Argon et al., 2000]. The maser is found 1.12'' away from the CORNISH centre coordinates and is coincident with the compact component G030.5887–00.0428a.

The two-component G044.3103+00.0410 is very red in the colour GLIMPSE image and has a water maser ( $\sim 22$  GHz) association. Water masers occur in both high- and low-mass star-forming regions and are thought to be associated with molecular outflows (Urquhart et al. 2011 and the references therein).

---

<sup>9</sup>See also Cyganowski et al. 2009, 2011 for a VLA radio continuum survey toward a sample of GLIMPSE Extended Green Objects (EGOs) with maser associations (in particular, 6.7 GHz Class II CH<sub>3</sub>OH masers, which are thought to be associated exclusively with MYSOs).

---

The MYSO-jet-like component C (see Table 3.3 and Fig.3.5) ahead of the cometary G027.1859–00.0816 is exactly coincident with a water maser (18385–0512 in Beuther et al. 2002).

The properties and morphologies of the resolved targets are explored in more detail in the next chapter.

Fig. 3.5 Target maps. The clean beam is shown in the bottom-left corners. The contour levels start at  $7\sigma$ , up to the measured peak flux (darkest purple).

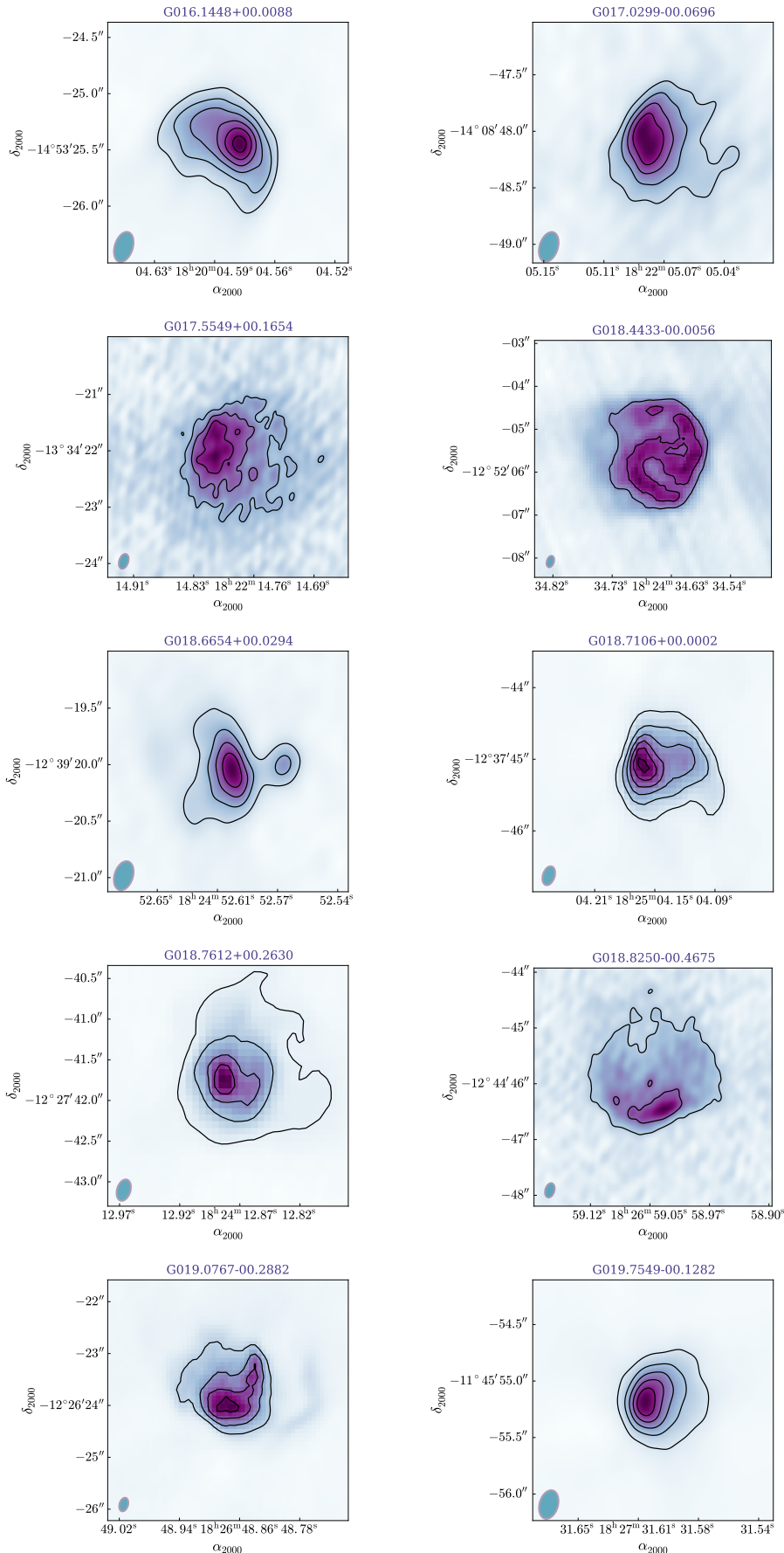


Fig. 3.6 Target maps, continued.

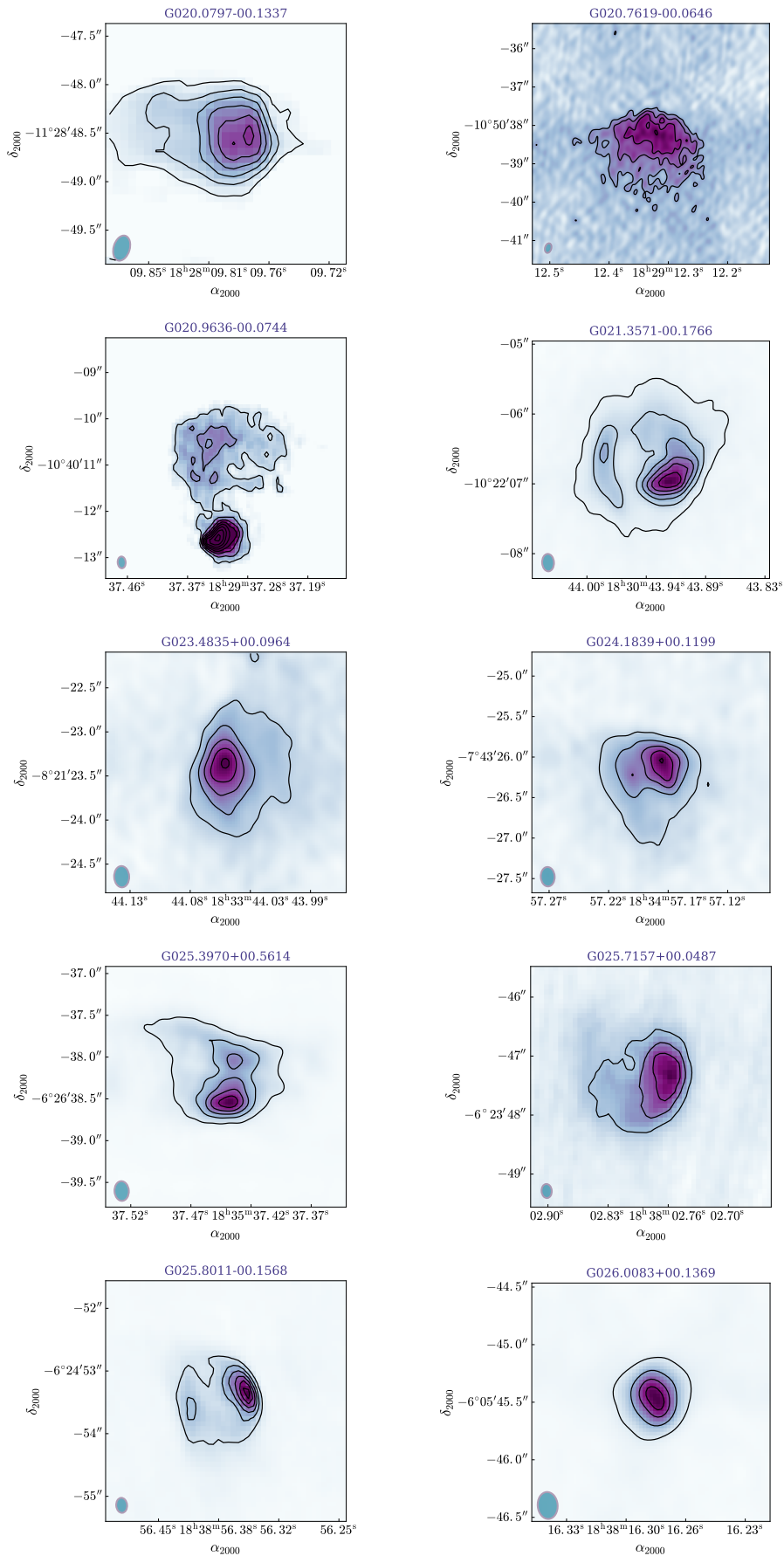


Fig. 3.7 Target maps, continued.

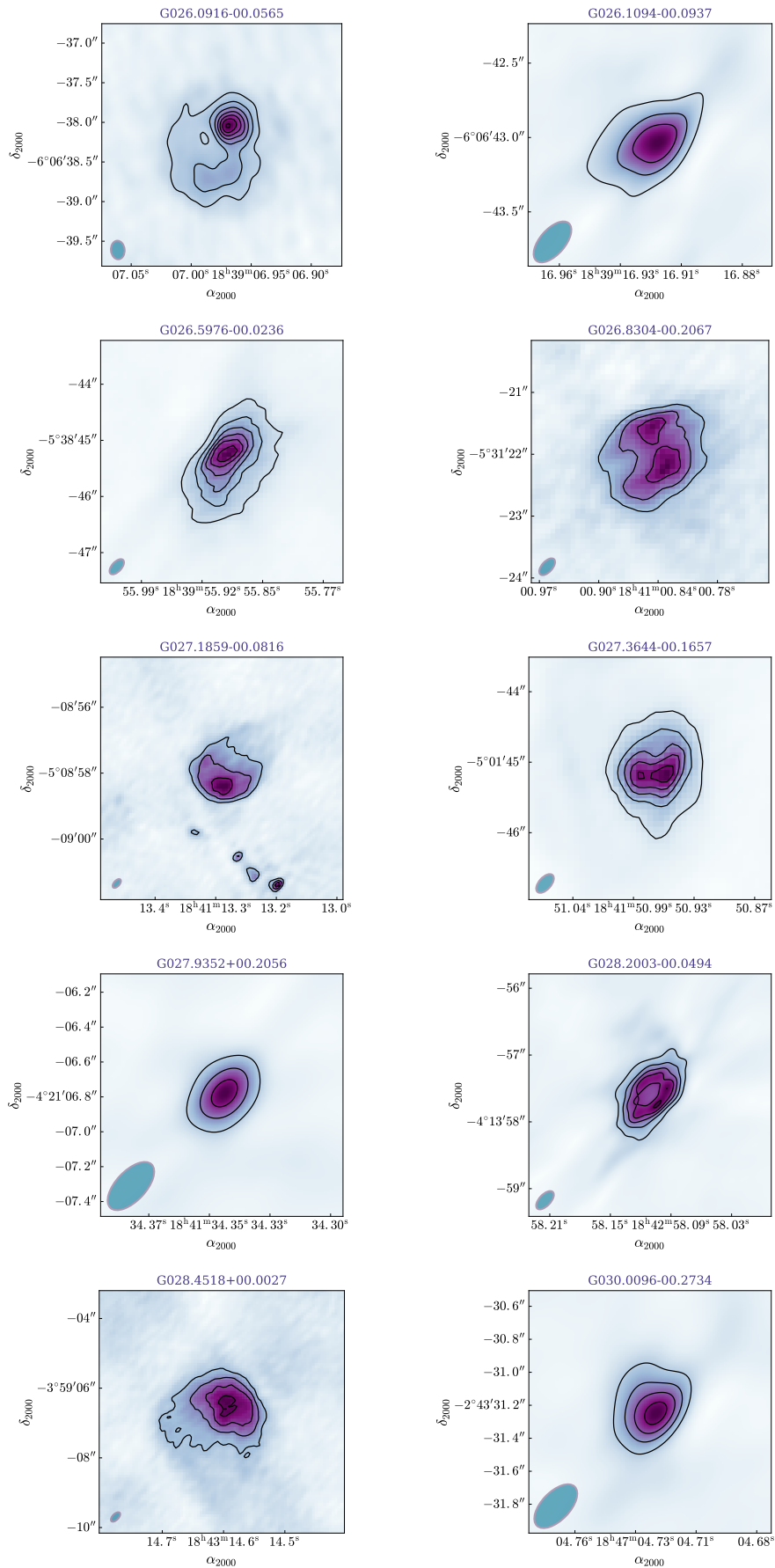


Fig. 3.8 Target maps, continued.

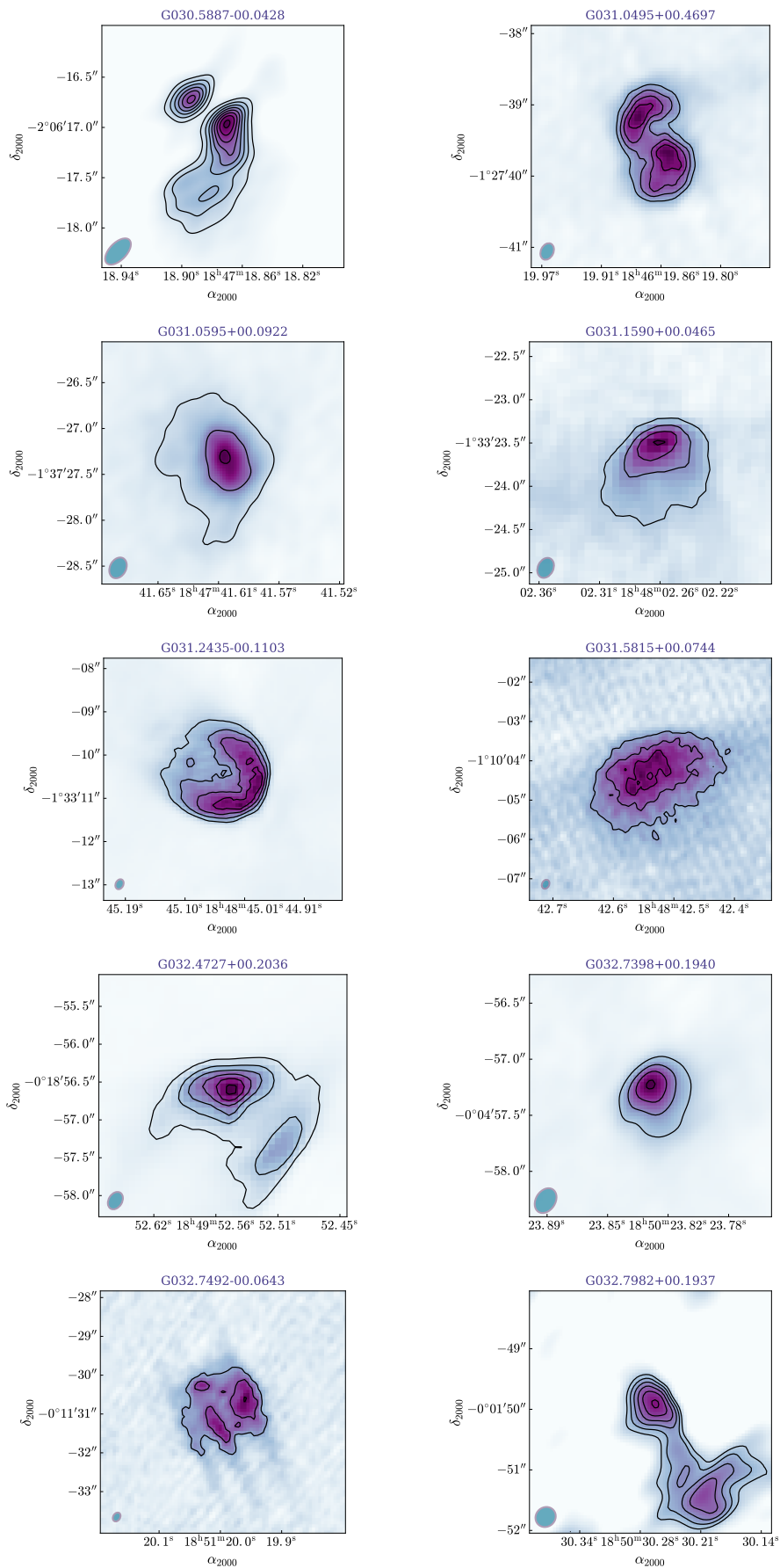


Fig. 3.9 Target maps, continued.

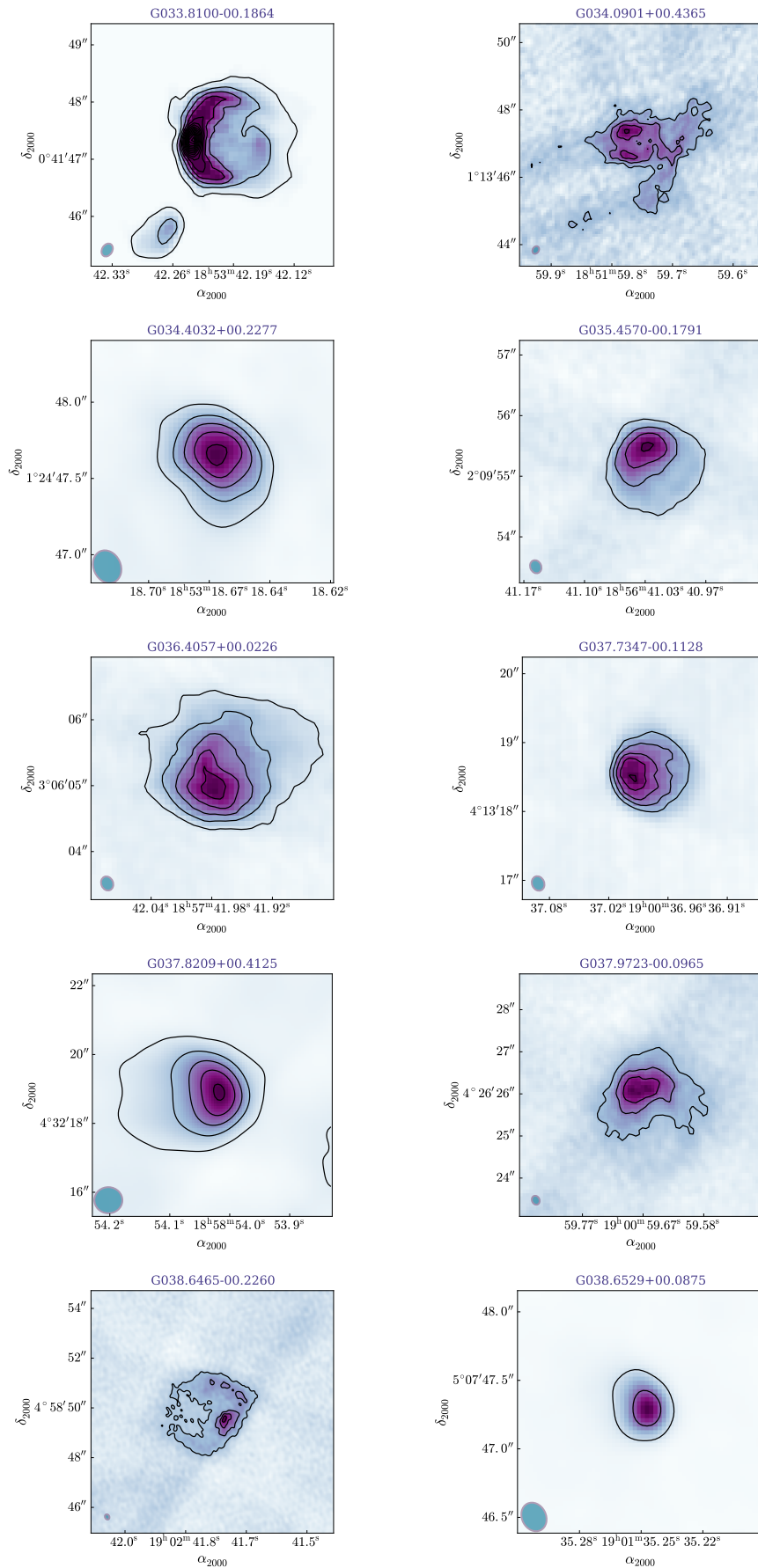


Fig. 3.10 Target maps, continued.

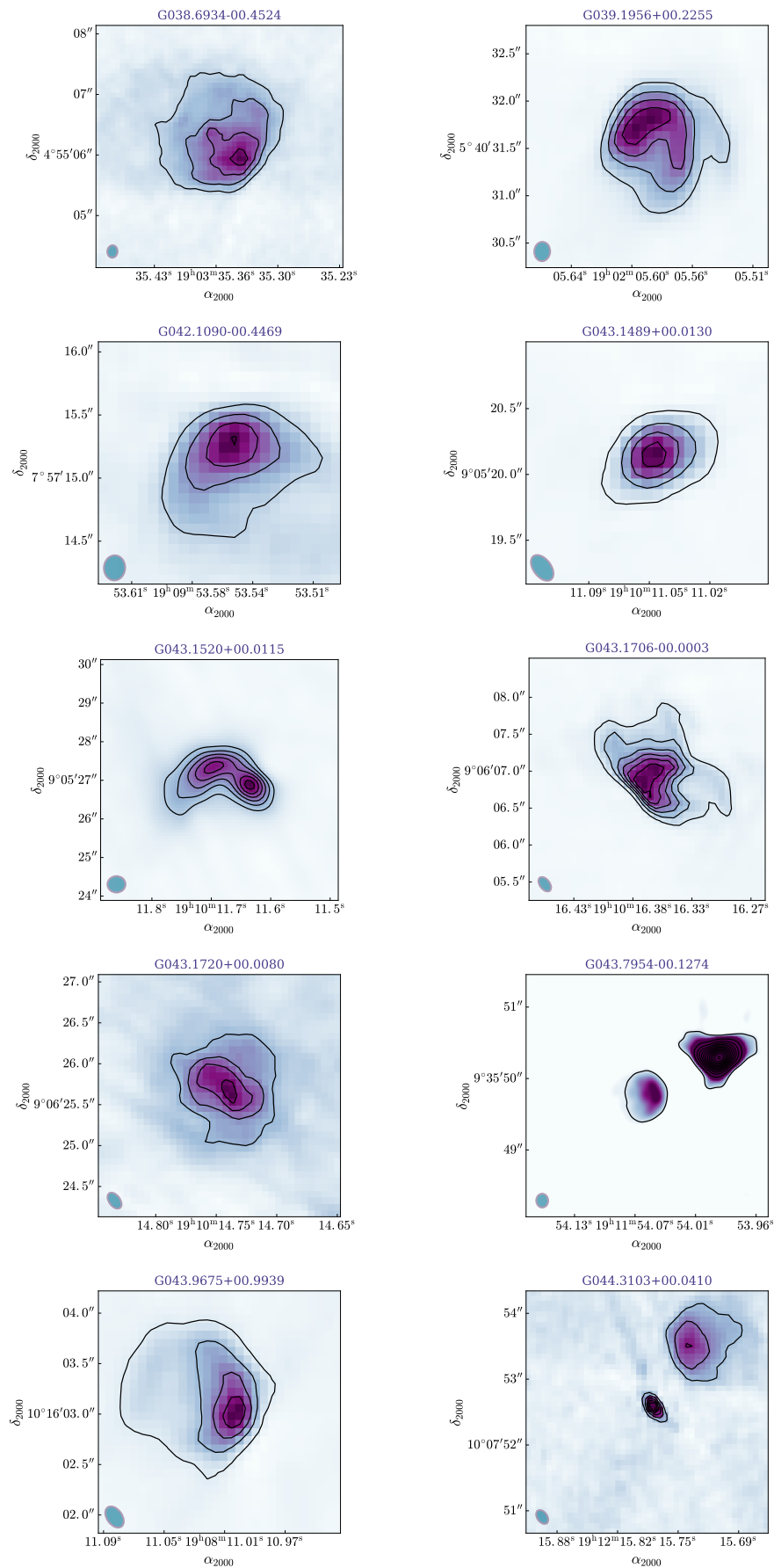
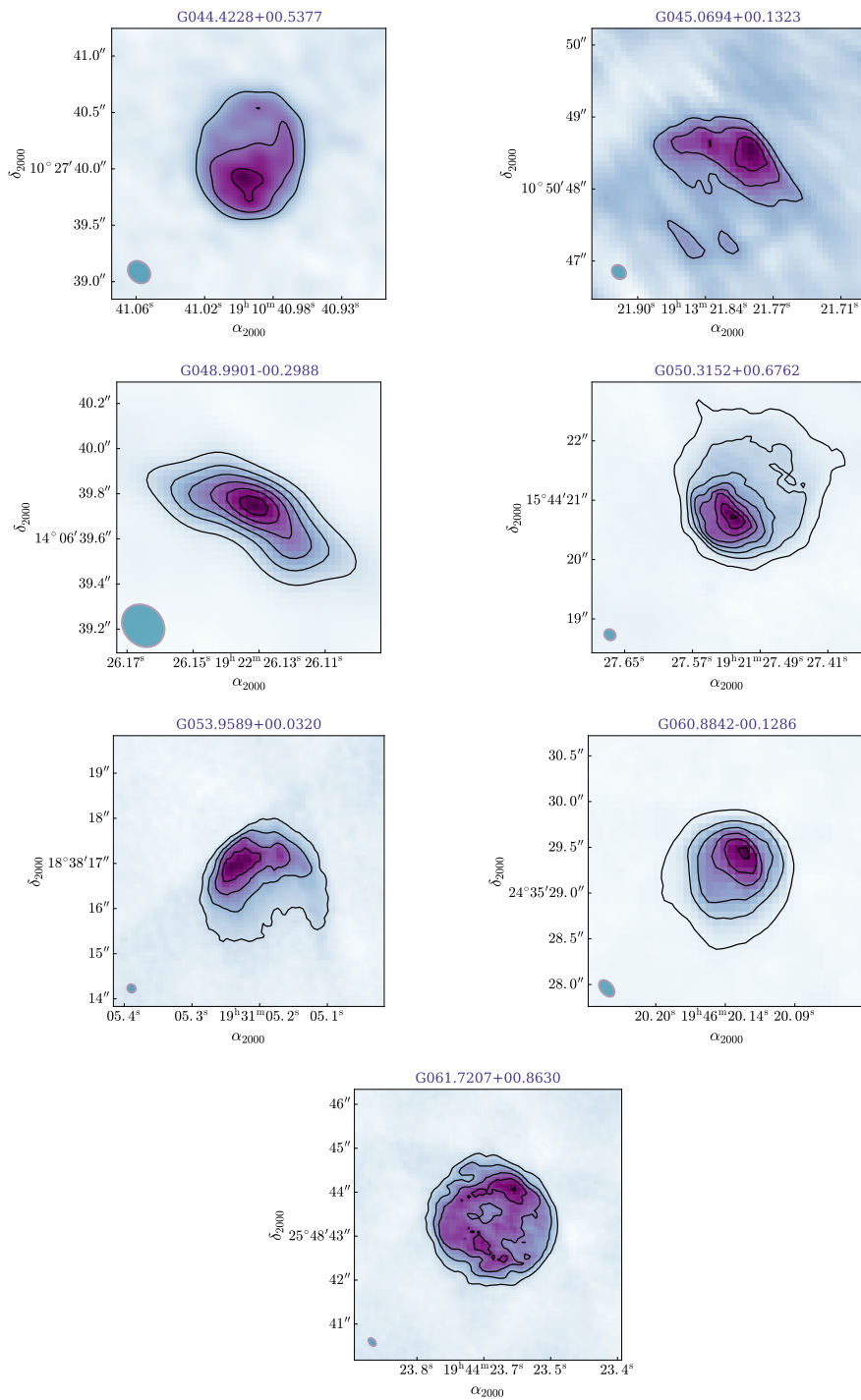


Fig. 3.11 Target maps, continued.



### 3.5.1 Two target non-detections?

Two of the targets of the follow-up JVLA observations are discernible neither in the dirty nor the clean maps, despite the careful flagging, reduction and imaging of the latter. Both target maps are clearly dynamic-range- (rather than sensitivity-) limited.

One of these is G034.2571+00.1466. It has a CORNISH flux density and size of 47.80 mJy and 2.43'', respectively, translating to a surface brightness of 0.33 mJy per 0.2'' beam. It is found in the same field as the 1.8 Jy (at 5 GHz) cometary G034.2572+00.1535, even brighter at 10 GHz:  $2.44 \pm 0.03$  Jy. The rms noise in the field pointing centre is about five times higher than for sensitivity-limited maps ( $\sim 90$   $\mu$ Jy per beam), but the target should still have been detected at nearly  $7\sigma$ , assuming its 10-to-5 GHz flux ratio is  $\sim 1$  (the sample average for non-merged sources is 1.12). Assuming the lowest for the (non-merged source) sample 10-to-5 GHz flux ratio of  $\sim 0.3$ , the source would not be convincingly detected, at just below  $2\sigma$ .

The other non-detection is G043.7960–00.1286 – with an integrated flux of 9.78 mJy and angular size of 2.38'' in CORNISH. The source surface brightness is thus only  $\sim 0.07$  mJy per 0.2'' beam. It is located next to a bright two-component CORNISH UCHII G043.7954–00.1274. The integrated flux of the latter is  $\sim 25$  mJy at 5 GHz (for the merged source) and  $\sim 55$  mJy at 10 GHz (for the brighter component). The field rms noise toward the pointing centre is four times higher than for sensitivity-limited maps ( $\sim 40$   $\mu$ Jy per beam), so the target source would be detected at only  $2\sigma$ , assuming a 10-to-5 GHz flux ratio close to 1<sup>10</sup>.

---

<sup>10</sup>Self-calibration and truncating the  $uv$  coverage could be employed to boost sensitivity in the cases of non-detections.

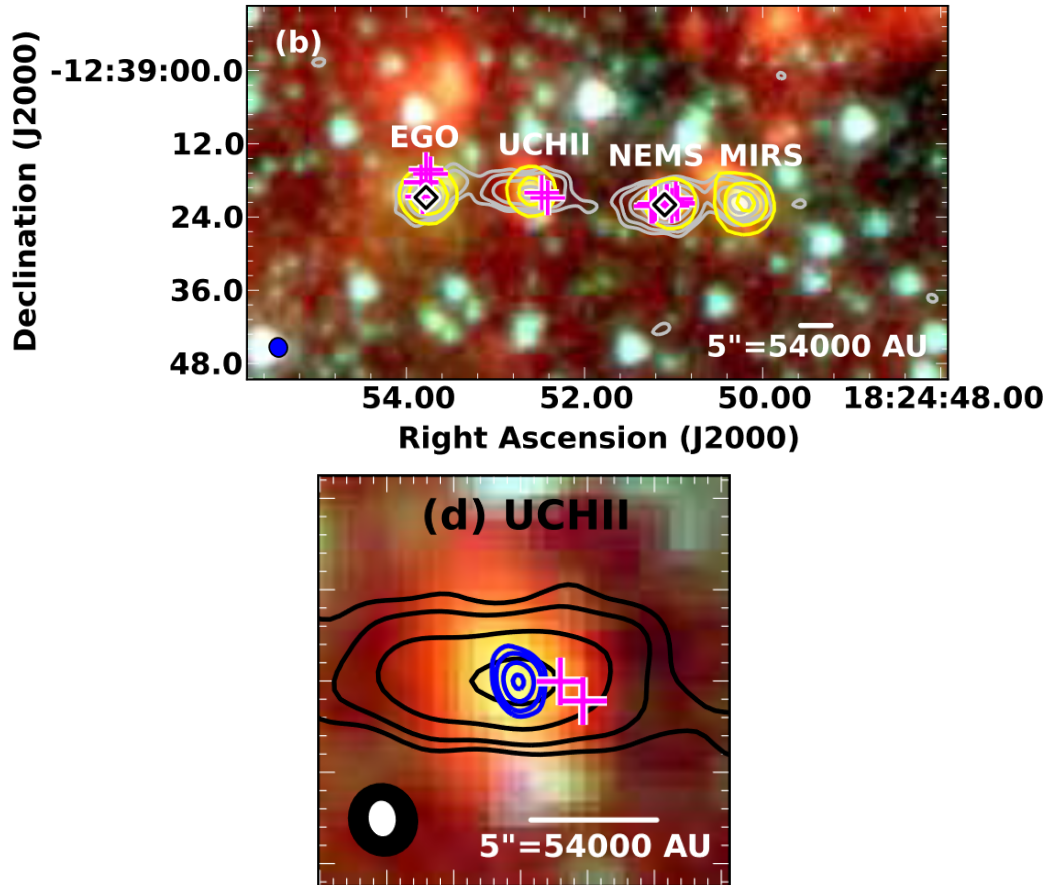


Fig. 3.12 Panels (b) and (d) from Fig. 1 in Cyganowski et al. [2012], showing the three-colour Spitzer image (8, 4.5, and 3.6  $\mu\text{m}$ ) of G18.67+0.03 (G018.6654+00.0294 in CORNISH) with marked positions of  $\text{CH}_3\text{OH}$  masers from Cyganowski et al. [2009]. Class I masers associated with Class II masers are marked with  $\diamond$ , and Class I masers with no Class II associations – with  $+$ . In the top panel, Submillimeter Array (SMA) 1.3 mm continuum emission contours are shown in gray, and MIPS 24  $\mu\text{m}$  emission is shown in yellow. The blue contours in the bottom panel show the UCHII VLA 1.2 cm (24.64 GHz) continuum contours; there, the SMA 1.3 mm continuum emission is marked in black.

## 3.6 Neighbour maps

A total of 15 sources comprise the neighbour group – those CORNISH UCHIIs that were not observation targets but are found within the imaged fields. The neighbour maps are presented in Fig. 3.13, centred on the CORNISH source coordinates of each counterpart. The contours were plotted in the same manner as for the target sources. The photometric results for all neighbours of interest are presented in D.2 in Appendix D.

The neighbour CORNISH UCHIIs found in the target fields have a greater variation in (CORNISH) angular size than the targets, and at the higher resolution some reveal complex morphology and a multitude of components. This includes newly resolved pairs and multiples that are the counterparts to CORNISH UCHII regions, as well as clumpy extended CORNISH UCHIIs. A search was performed for high-resolution maps of the neighbour sources, and, when available, those were inspected to help separate (by assigning a component label and measuring the component fluxes and sizes, as shown in Table D.2) the individual components comprising each merged CORNISH source. A notable example is G032.7966+00.1909, appearing in CORNISH as an extended UCHII of irregular morphology, appears broken up into four individual components (3 of which with cometary morphology). Another source, G036.4062+00.0221, neighbour to G036.4057+00.0226, appears as two individual compact sources.

Notably, the bright region G043.1665+00.0106 is a well-explored source in the ‘ring’ of UCHII regions in W49A. This is source G in Fig. 2 in De Pree et al. [1997b], where it can be seen in the multi-frequency, multi-configuration maps as a collection of sub-clumps, despite the slightly larger beam size (0.8"). Another merged CORNISH source in the W49A map is G043.1657+00.0116, corresponding to the cometary-shaped components B and D in the same figure in De Pree et al. [1997b]. Component E is also seen as two unresolved knots.

Another example of underlying complex structure is G032.7966+00.1909. This CORNISH source appears to have irregular structure and extent of  $10''$ , but the 10 GHz maps reveal four bright main components, each with distinct morphology, and is likely a cluster of young sources in CORNISH rather than a broken-up, over-resolved single source in the A-configuration maps.

G020.0809–00.1362 presents an intriguing ‘russian-doll’-like structure – a bright knot ahead of two consecutive, increasing in size shells. The same curious pattern continues in the 5 GHz maps and the mid-IR images, as the source is ahead of a larger bubble (corresponding to the  $\sim 20''$  CORNISH H II region G020.0789–00.1383).

Fig. 3.13 Neighbour maps. Multiple resolved components of a single CORNISH UCHII are shown together.

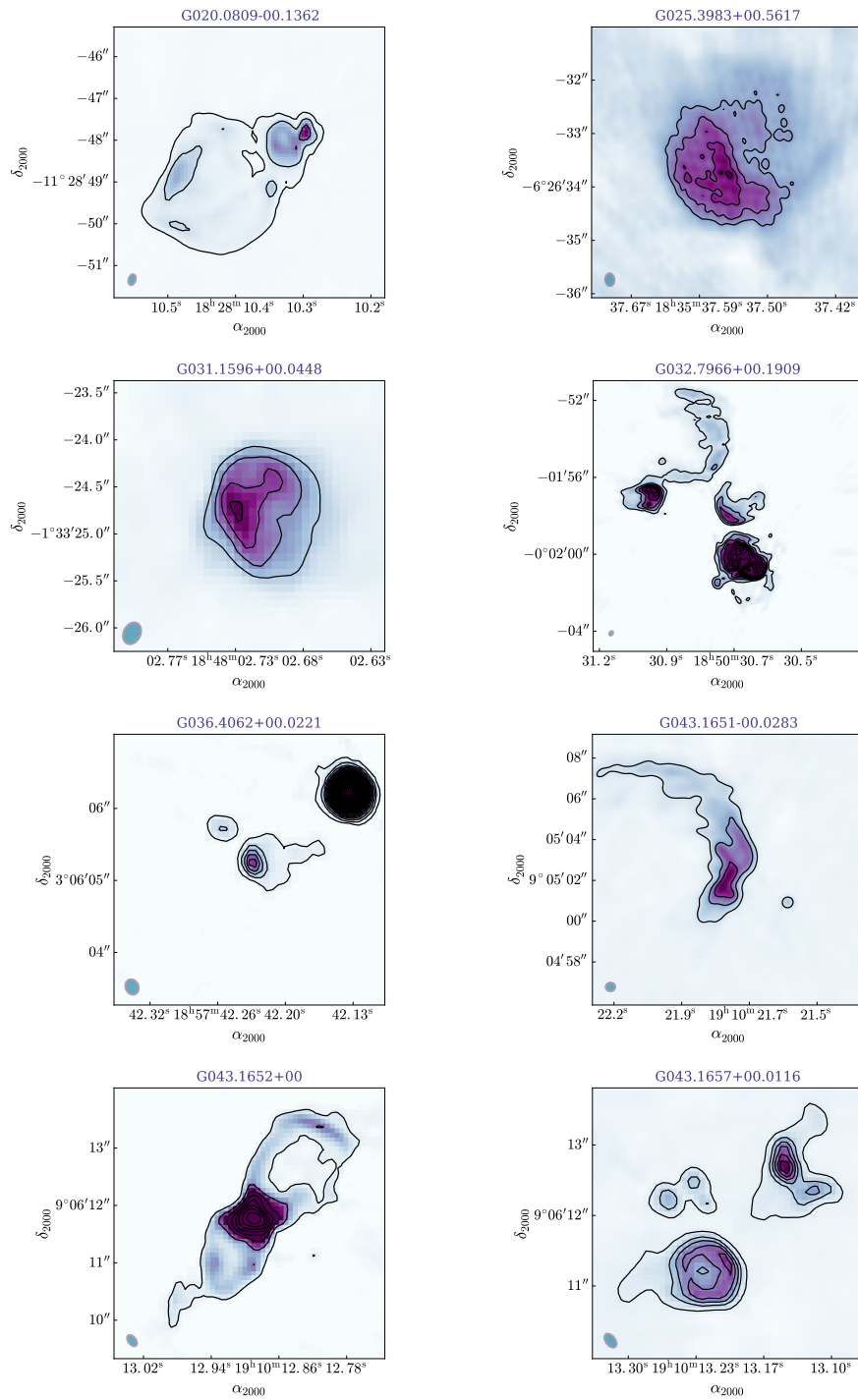
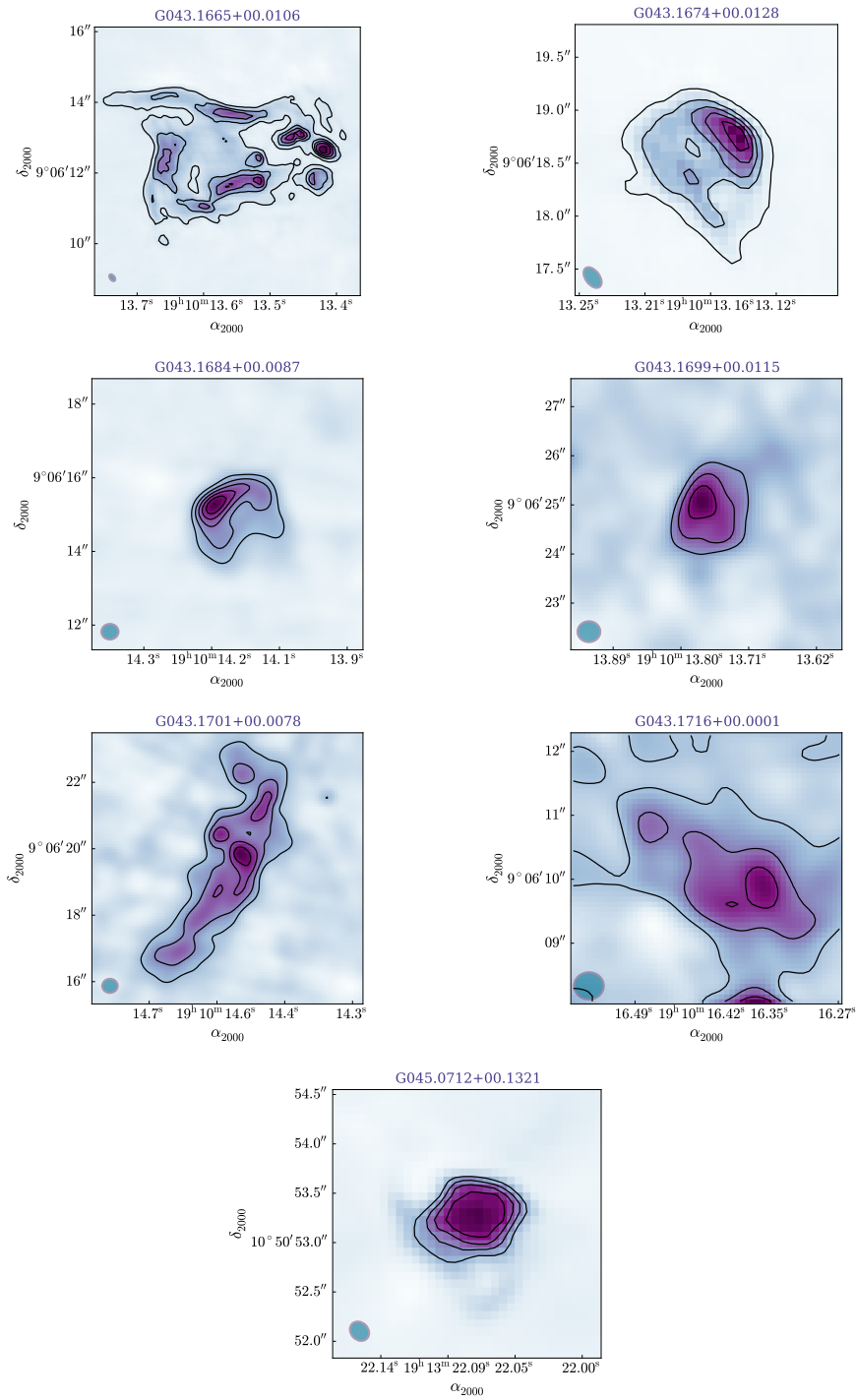


Fig. 3.14 Neighbour maps, continued.



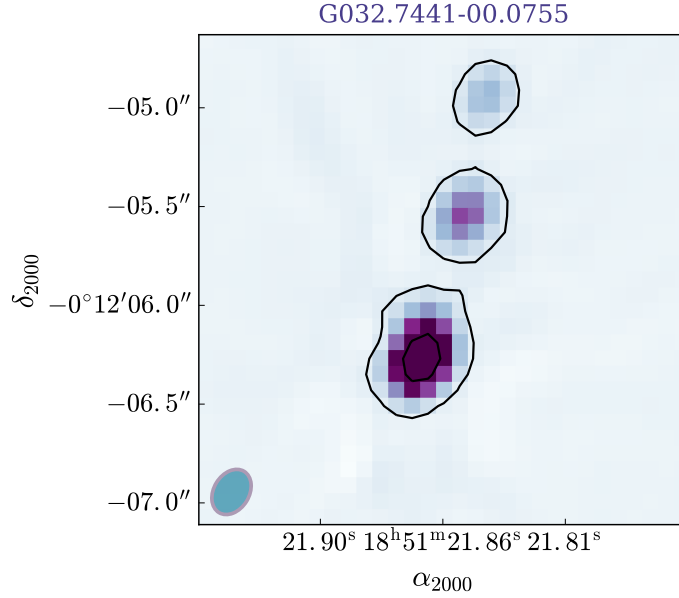


Fig. 3.15 G032.7441–00.0755 was classified as a candidate IR-dark H II region in the CORNISH survey. The higher-resolution JVLA data shows a neat row of three sources, likely young UCHII regions, their spatial order reminiscent of MYSO-jet knots.

Table 3.4 Observed properties (position, integrated and peak flux, major and minor source axes) of the components corresponding to the candidate IR-dark H II region G032.7441–00.0755 (field clean beam size of  $0.24'' \times 0.18''$ ).

Comp.	$\alpha$ (J2000)	$\delta$ (J2000)	$S_{\text{int}}$ (mJy)	$S_{\text{peak}}$ (mJy/beam)	$\theta_M$ ( $''$ )	$\theta_m$ ( $''$ )
(A)	$18^{\text{h}}51^{\text{m}}21.86^{\text{s}}$	$-00^{\circ}12'06.26''$	$10.67 \pm 0.22$	$8.15 \pm 0.10$	$0.28 \pm 0.01$	$0.20 \pm 0.01$
(B)	$18^{\text{h}}51^{\text{m}}21.85^{\text{s}}$	$-00^{\circ}12'05.54''$	$2.58 \pm 0.10$	$2.20 \pm 0.05$	$0.25 \pm 0.01$	$0.20 \pm 0.01$
(C)	$18^{\text{h}}51^{\text{m}}21.84^{\text{s}}$	$-00^{\circ}12'04.95''$	$1.18 \pm 0.04$	$1.08 \pm 0.02$	$0.25 \pm 0.01$	$0.19 \pm 0.01$

Other sources found within the JVLA fields (as neighbours to targets) are G026.0907–00.0575, G032.7441–00.0755, G065.2462+00.3505, and the bright G034.2572+00.1535 (the well-studied cometary G34.26+0.15) with its neighbouring components (unresolved here) G034.2581+00.1533 and G034.2573+00.1523. Due to its extent, the new flux results of G026.0907–00.0575 were unreliable, and this source was not revisited. The other source, G032.7441–00.0755, is not part of the original UCHII sample; it was classified in the CORNISH survey as a dark H II region (previously unresolved). This source now appears

as three aligned bright knots, the brightest of which is likely a young UCHII region, based on its radio flux density, too high for it to be a MYSO. As the original classification suggests, there is no near- or mid-IR counterpart to this source. It is not seen in the 20 cm MAGPIS image – MYSO spectra peak at higher frequencies than UCHIIs, and are optically thick at 1.4 GHz, unlike the majority of our CORNISH sample UCHII. The source has strong counterparts in Hi-GAL and at 24  $\mu\text{m}$  in MIPS GAL. The spatial configuration is reminiscent of MYSO-jet knots.

### 3.7 Flux densities and source sizes

The new photometric results for the targets are presented in Table D.1 in Appendix D. The sources were identified first through their CORNISH coordinates and angular extents. With the higher-resolution data, more precise positions of the source centres, particularly for CORNISH sources comprising multiple components, were obtained. The properties, such as the integrated and peak fluxes, the source major- and minor-axis length and position angle, were derived with the *CASA* task `imfit` (deconvolved from the beam). The presented source angular diameter is the geometric average of the measured deconvolved major and minor axes of each source. The clean beam major and minor axes are also included in the table. The good signal-to-noise ratio ensures good accuracy of the parameter uncertainties overall, but the uncertainty estimates for components with some spatial overlap could be more unreliable due to the limitations of the fitting routine<sup>11</sup>.

Individual components of CORNISH UCHIIs are treated as separate sources in the table in the cases where the morphology of at least one of the components

<sup>11</sup>See [https://casa.nrao.edu/casadocs-devel/stable/global-task-list/task\\_imfit/about](https://casa.nrao.edu/casadocs-devel/stable/global-task-list/task_imfit/about) for a detailed discussion of the fitting limitations.

is distinct, and, more importantly, the components are not found within a common outermost ( $7\sigma$ ) contour, which is assumed to be the source boundary.

## 3.8 Observed and derived properties

### 3.8.1 10 GHz sample properties

Figure 3.16 shows the expected for Gaussian fits clear trend for the ratio of integrated to peak 10 GHz flux of the target UCHII regions, increasing with angular size.

Figure 3.17 provides a summary of the observational properties, brightness temperatures, optical depths and physical sizes of the UCHIIs at 10 GHz (computed as in §2.6). The median 10 GHz flux density of the single-component targets is slightly lower than at 5 GHz for the same sub-sample ( $\sim 16.3$  mJy vs.  $\sim 18.7$  mJy) (Fig. 3.17a), and the median brightness temperature is the same ( $\log_{10}(T_B) \approx 2.5$  K, Fig. 3.17b). The optical depths at 10 GHz are presented in Fig. 3.17e. For  $\sim 76\%$  of the targets, the difference between the measured and the theoretical unattenuated flux is below 10%. The deconvolved angular size histogram (Fig. 3.17c) peaks at  $\sim 0.9''$ . From visual inspection, sources cannot be morphologically classified if their convolved major axis is  $\lesssim 1.5$  times the clean beam size (i.e.,  $< 0.4\text{--}0.5''$  in most cases, except where tapering was applied and this limit becomes  $\sim 0.6\text{--}0.7''$ ). The largest target, G038.6465–00.2260, is  $\sim 3.3''$  in diameter at 10 GHz (slightly larger than its corresponding size of  $2.5''$  at 5 GHz).

The distributions of physical sizes of the UCHIIs are shown in Fig. 3.17d. They were obtained from the distances in Table B.1 and the measured angular diameters (as presented in Table D.1 in Appendix D). The median physical diameter of the targets, which are the smallest CORNISH UCHIIs, is  $\sim 0.03$  pc,

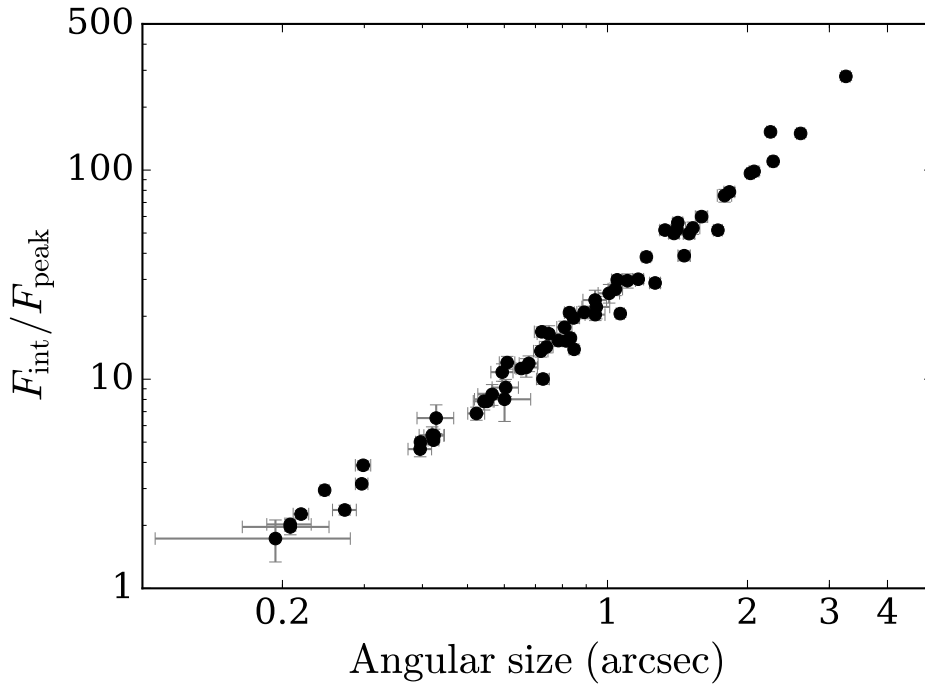


Fig. 3.16 Ratio of measured integrated to peak flux of the target UCHII regions, against deconvolved angular size (computed as the geometric average of the deconvolved major and minor source axes).

and ranges from  $\sim 0.004$  pc to  $\sim 0.17$  pc (with an upper limit of 0.003 pc for the unresolved component of G044.3103+00.0410 being the smallest value). All target sources have an available distance estimate (assuming the same distance for each source in multi-component CORNISH UCHIIIs).

The results computed for the neighbour subset are also plotted in the histograms. These have a larger span, reaching up to larger values than the target subset, as expected for a subset encompassing a random, broader range of sizes and ages. The largest observed neighbour, G043.1665+00.0106 – a clumpy source in the Welch ring in the W49A complex [De Pree et al., 1997a], discussed in §3.6, is  $\sim 3.8''$  in diameter. The median physical diameter ranges from  $\sim 0.004$  pc to  $\sim 0.20$  pc for the neighbours.

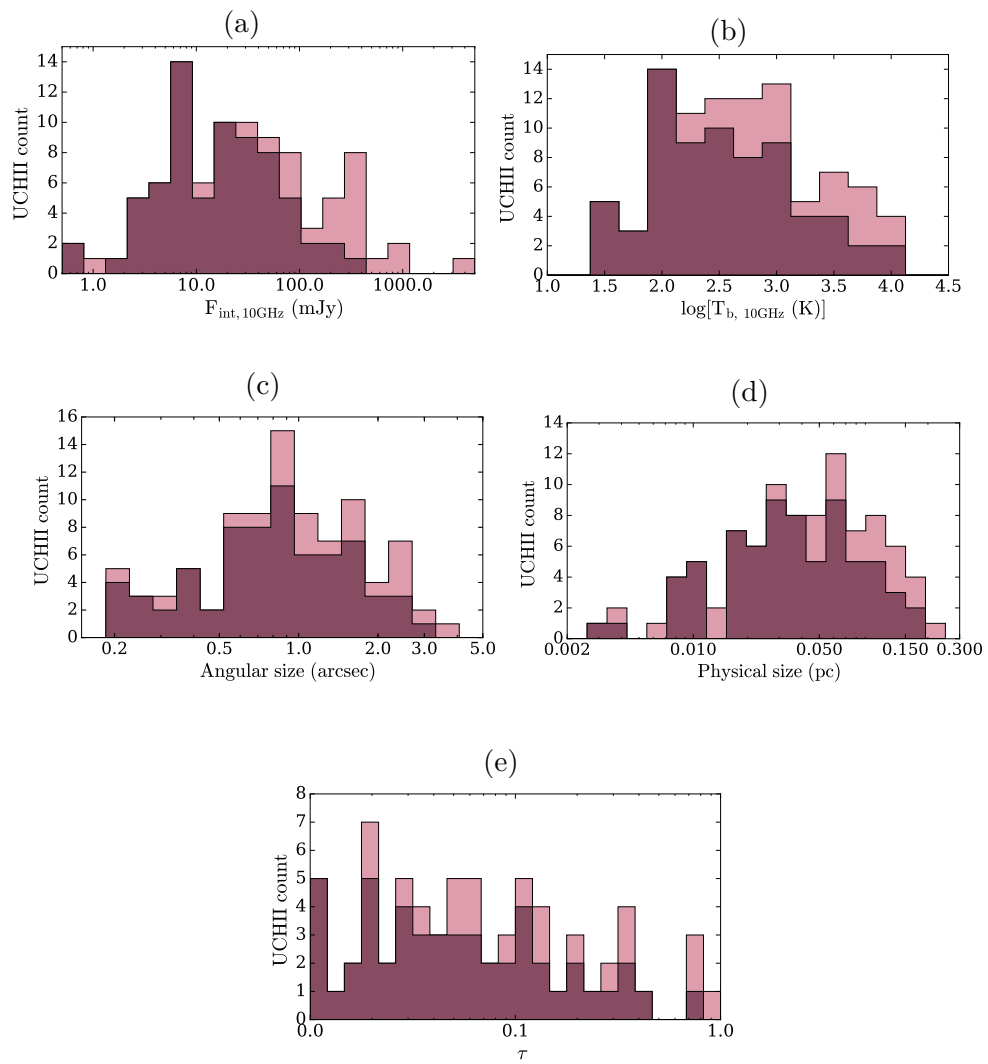


Fig. 3.17 Histograms of the observational properties, brightness temperatures, optical depths, and physical sizes of the target (in wine red) and neighbour (in pink) UCHIIs at 10 GHz.

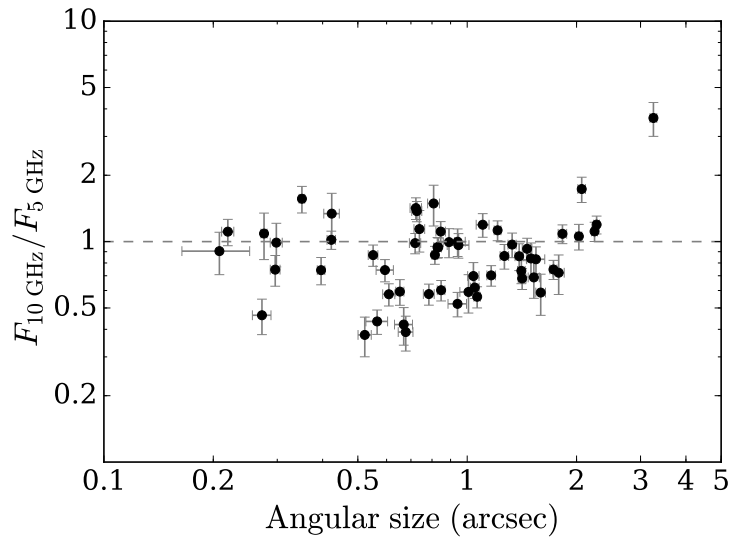


Fig. 3.18 Measured JVLA 10 GHz integrated flux over CORNISH 5 GHz integrated flux of the target UCHII regions, against angular size at 10 GHz (excluding resolved pairs).

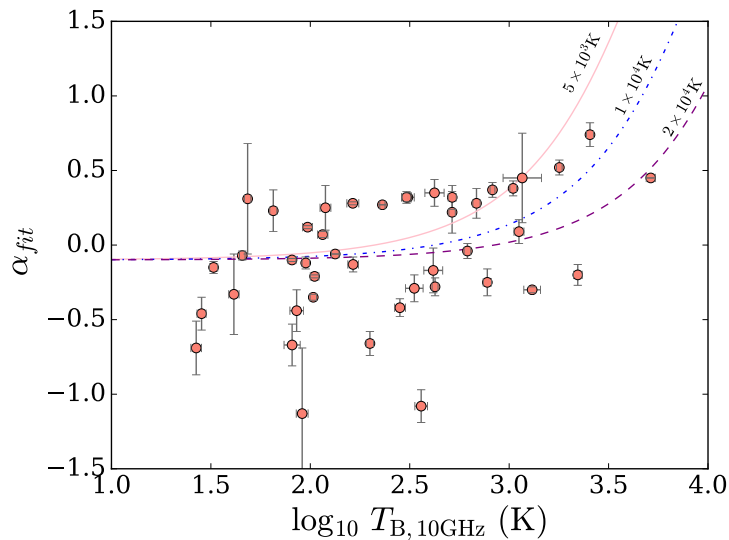


Fig. 3.19 Spectral indices estimated from least-squares fits to the available 10 GHz, 5 GHz and 1.4 GHz integrated flux of the target UCHII regions (excluding MAGPIS 6 cm), against brightness temperature at 10 GHz (excluding sources merged at 1.4 GHz and/or 5 GHz).

### 3.8.2 10GHz–1.4GHz spectral indices

Figure 3.19 shows spectral indices computed using least squares fitting of the available for the JVLA targets 10 GHz, 5 GHz, and 1.4 GHz fluxes (Tables D.1 and A.1 in the Appendix), against brightness temperature at 10 GHz. The plotted theoretical models were adapted from Siódmiak and Tyłenda [2001] and Bojičić et al. [2011], similarly to §2.3.2, in this case showing the model predictions for the 1.4 GHz – 10 GHz range at the three different electron temperatures. The individual linear fits are shown in Figure 3.20. Flux upper limits for all non-detections of 20 cm counterparts in the MAGPIS images are included. Note that the MAGPIS 6 cm fluxes are shown for comparison only, and were not taken into account in the fits. CORNISH UCHIIs that comprise distinct pairs or multiples of sources at the higher resolution were not fitted.

As discussed in §2.3.2, individual spectral indices are reliable only in cases where the source is unresolved at all fitted frequencies. This is clearly not the case here, as the fitted UCHIIs are compact at 1.4 and 5 GHz but extended at 10 GHz. The different VLA configurations used at each frequency further limit the reliability of the results. Therefore, the estimated 10 GHz–1.4 GHz spectral indices should be considered as lower limits. A method to improve the  $uv$  coverage and include zero-spacing flux is to combine interferometric data with single-dish data (see e.g. Tian and Leahy 2005). However, this is beyond the scope of this thesis and the available archival data. The computed from the linear fits 10 GHz–1.4 GHz spectral indices were not used for detailed spectral analysis of individual sources, but to compare the properties of the sample of most compact CORNISH UCHIIs to those of the general sample (see §2.3.2).

A well-sampled radio SED could indicate whether the turnover frequency of the source is within the available spectral range. Flat or falling spectral indices and optically thin emission are characteristic for UCHIIs (§2.3.2). The youngest

UCHIIs and HCHIIIs, however, have higher turnover frequencies and rising spectra between 1.4 and 5 GHz, which suggests a mix of optically thin and thick emission due to a much less uniform environment [Kurtz, 2005; Yang et al., 2018]. The majority of the targets studied here are expected to be particularly young UCHIIIs (§3.5) and thus to have a turnover frequency between 5 and 15 GHz. Given the very limited number of data points, the plots only hint at the shape of the radio SED in the available range. Only about 41% of the radio SEDs appear to be well described by a single straight line. In this subset, about 23% appear to have rising spectra. Thus, at least 23% of the targets may have a turnover frequency above 10 GHz and could thus be particularly young.

As expected, the majority of sources scatter around the optically thin limit in Figure 3.19 at low  $T_b$ . A larger relative fraction of negative indices is found below the  $-0.1$  limit, when compared to the 5 GHz–1.4 GHz spectral indices (Fig. 2.6) – 32% in the former and 18% in the latter, taking errors into account. This is because in nearly 45% of the cases (including errors), the 10 GHz flux is lower than the 5 GHz flux. The effect is not systematically increasing with angular size, as is shown in Figure 3.18, so filtering of extended emission (due to the difference in sensitivity and also since the 5 GHz values in the 10 GHz–5 GHz plot belong predominantly to unresolved sources) may not be the primary cause in all cases. In fact, sources smaller than (a deconvolved angular diameter of)  $\sim 0.7''$  have the smallest 10-to-5 GHz flux ratios (around 0.5). These are G017.0299–00.0696, G023.4835+00.0964, and G031.1590+00.0465. At the other extreme, the target with the largest flux ratio of  $\sim 4.3$ , G038.6465–00.2260, also has one of the largest angular extents – about  $3.3''$ . In this case, the angular extent is also larger than the one measured in CORNISH ( $2.51''$ ). However, the 5 GHz flux measured in the MAGPIS image is comparable to the 10 GHz result (Fig. 3.19).

The three steepest positive spectral indices ( $\gtrsim 0.5$ ) are found at the largest brightness temperatures and belong to G018.7106+00.0002, G019.7549–00.1282, and G028.2003–00.0494. These thus appear in the optically thick region of the model shown in Fig. 3.19 (see §2.3.2 for details), between 1.4 GHz and 10 GHz. The 10 GHz images of G018.7106+00.0002 and G028.2003–00.0494 show hints of two-component structure, which could become more apparent at even higher resolution. G019.7549–00.1282 is a compact cometary-shaped source at 10 GHz.

The list of UCHIIs with fitted steep negative slopes ( $\lesssim -0.4$ ) from good fits includes G017.0299–00.0696, G020.7619–00.0646, G023.4835+00.0964, G026.1094–00.0937, G028.4518+00.0027, G031.0595+00.0922, as well as G031.1590+00.0465, G034.0901+00.4365, G042.1090–00.4469, and G043.1520+00.0115. In these cases, the respective 1.4 GHz–5 GHz slopes are clearly also steep and negative. As these sources are compact at both 1.4 GHz and at 5 GHz due to the lower resolution at these frequencies, they are more likely to be truly non-thermal, rather than entirely the effect of filtering of flux with change in  $uv$  coverage. All of these sources have distinctly cometary morphologies. G043.1520+00.0115 and the relatively extended G034.0901+00.4365 could be parts of, or superimposed on a much larger bubble, as hinted by their 10 GHz morphologies.

The UCHIIs in the 10 GHz sub-sample are likely younger than the rest of the CORNISH UCHII sample (§3.5). It is clear from a comparison between the radio maps that improving the resolution reveals at each step further morphological complexity, and often multiplicity of source components. The computed negative spectral indices could be evidence of an underlying non-thermal component, such as from e.g. bow shocks from runaway massive stars (see del Valle and Pohl 2018; Pereira et al. 2016), or stellar wind interactions in massive binaries [De Becker, 2007]. More complete radio SEDs could be

studied in the future to look for an underlying physical mechanism causing the non-thermal appearing spectral indices.

Time variability of the continuum flux density (see §2.4) is another possible explanation, as the radio data are from different observational epochs. About 5% of the CORNISH UCHIIs could be time-variable, based on the 5 GHz flux densities from two epochs  $\sim 15$  years apart (see §2.4). Assuming a similar fraction of the UCHIIs would exhibit apparent time variability at 10 GHz, 3-4 variable sources would be expected in the smaller, JVLA subset. The JVLA follow-up was conducted  $\sim 7$  years after CORNISH. However, none of the follow-up targets are among the 5 GHz variable candidates. Multi-epoch data at each individual (1.4, 5 and 10 GHz) frequency are needed to look for variability.

Fig. 3.20 Radio spectral energy distributions and fitted spectral indices of UCHIs with available 1.4 GHz, 5 GHz (where the CORNISH fluxes are marked in black and the MAGPIS 6 cm results – in red) and 10 GHz flux densities. The least-squares fitted line is plotted. Only 10 GHz targets which appear as single sources at all three frequencies are included.

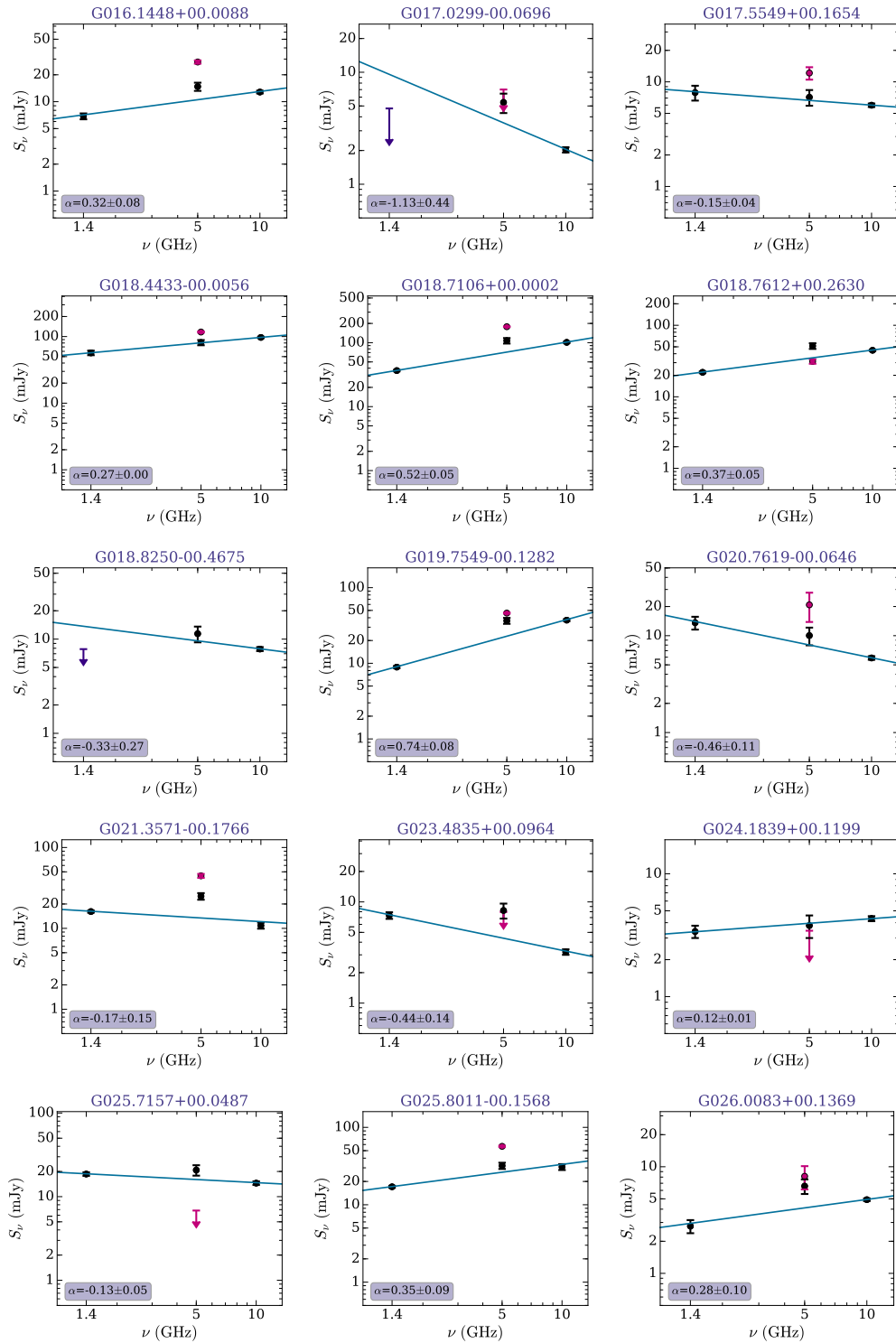


Fig. 3.21 Radio spectral energy distributions, continued.

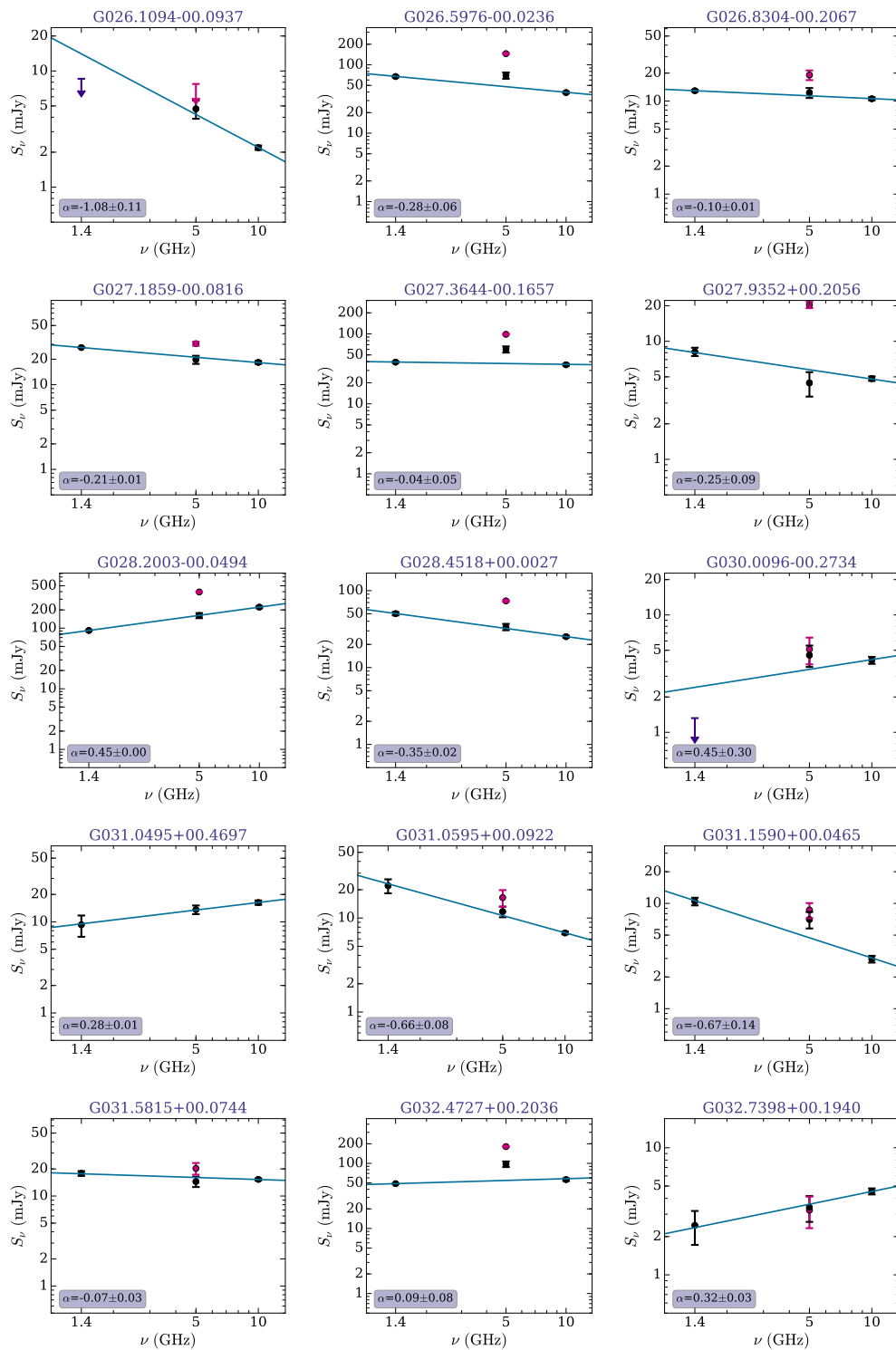
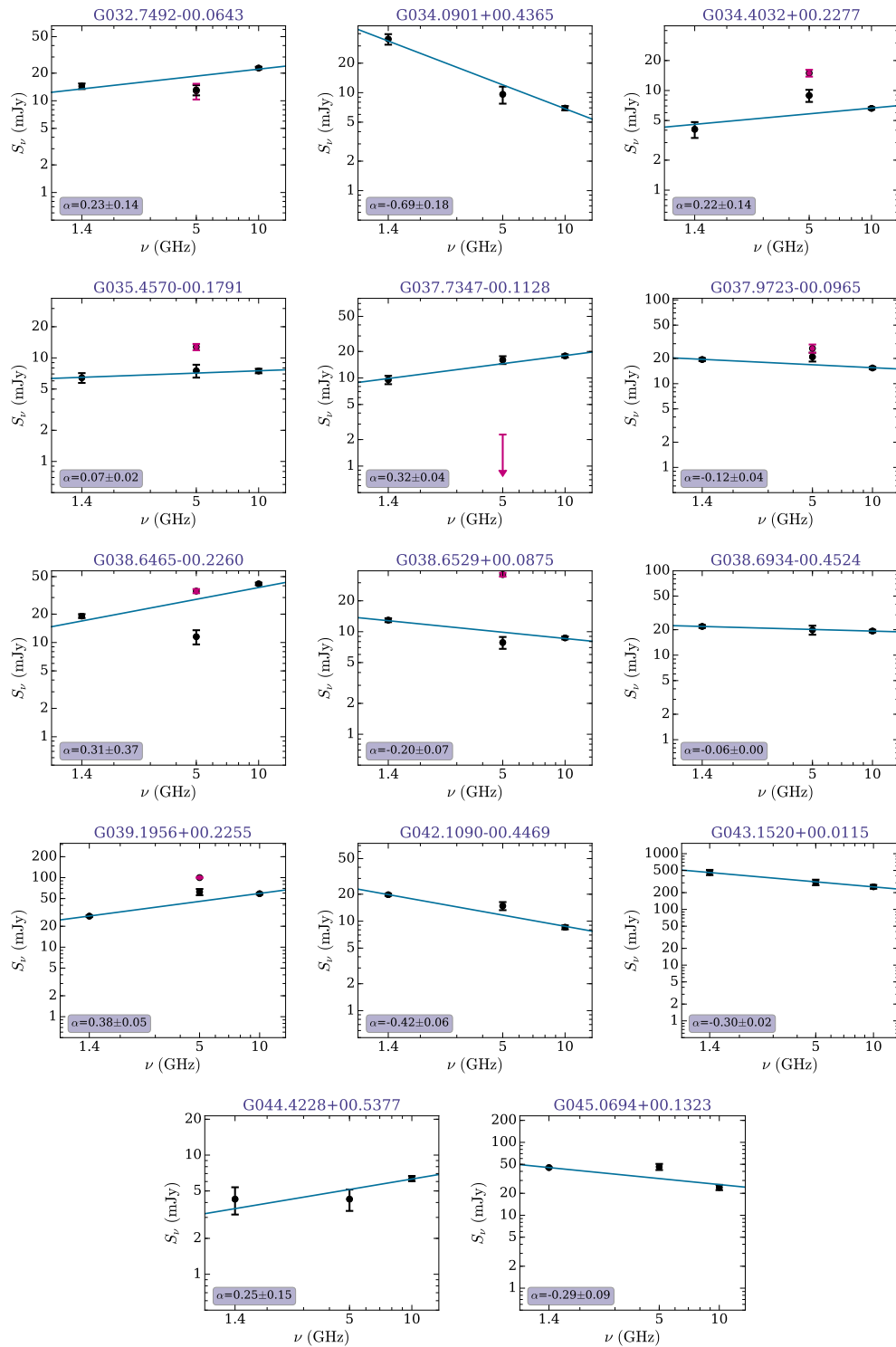


Fig. 3.22 Radio spectral energy distributions, continued.



### 3.9 Conclusions

High-resolution 10-GHz continuum observations were presented, following up on CORNISH UCHII regions smaller than the limit at which sufficient morphological information is available from the 5 GHz maps (2.7").

The observed fields were successfully reduced and deconvolved, resulting in good quality images. All but two of the target UCHII regions were detected, the likely explanation being the lower (dynamic-range limited due to bright neighbours) sensitivity in their respective maps compared to their expected surface brightness.

A multitude of other CORNISH UCHIIs, and candidate MYSOs/MYSO jet components, were also detected as neighbours to the targets within the observed fields. All individual CORNISH UCHIIs or UCHII components with distinct morphologies are smaller than the maximum reliable observed spatial scale in A configuration, resulting in reliable fluxes, despite the slightly decreasing sensitivity with distance from the field pointing centres.

At the  $\sim 0.2''$  resolution, about 9% of the target UCHIIs were shown to be comprised of at least two components which are likely distinct sources – either UCHII pairs or an UCHII with an unresolved companion. Some of the CORNISH UCHIIs with extents exceeding 2.7" could also be hiding multiplicity at the 1.5" resolution, as was the case for the four UCHIIs merged within G032.7966+00.1909 at 5 GHz. The presence of compact components ahead of cometary UCHIIs fits well with the sequential structure formation hypothesis of Kim and Koo [2001, 2002, 2003], as discussed in the next chapter.

Photometric measurements of the 10 GHz flux densities of all target and neighbour sources of interest were presented. The spectral indices corresponding to the target subset were estimated from least squares fits to all available (from this chapter and the work described in the previous chapter) radio fluxes at

three frequencies. About 32% of the fitted spectral indices of the target UCHII regions were found below the lower limit for thermal free-free emission ( $-0.1$ ) and could be investigated in the future for a possible non-thermal contribution to the radio continuum emission.

The angular sizes were used to compute the physical extents of all target and neighbour sources of interest (using the distances listed in Table B). The follow-up targets sizes are very compact, as expected, ranging from  $\sim 0.004$  pc to  $\sim 0.17$  pc in size and with a typical physical diameter of  $\sim 0.03$  pc.

The observed and derived properties of the high-resolution sub-sample show that the UCHII regions comprising it are likely the youngest CORNISH UCHII regions. The presented maps therefore provide morphological information on the immediate environments of the newborn massive stars powering these radio continuum sources. To take advantage of this, the morphologies are classified and explored in more detail in the next chapter.



# Chapter 4

## UCHII region morphology

### 4.1 Introduction

When a massive star reaches the necessary Lyman continuum flux threshold to illuminate the surrounding density distribution of interstellar matter, it reveals not only a snapshot of the geometry present soon after the formation of the massive star and its general environment, but also supplies observers with clues on the outflow and infall history and the stellar wind strength [Hoare et al., 2007]. Ultra-compact H II regions are typically found in associations with other H II regions (e.g. Kurtz et al. 1994, Kim and Koo 2001, Chapter 2/Kalcheva et al. 2018) and manifest a limited distribution of morphologies (De Pree et al. 2005; Wood and Churchwell 1989a,b). Their regular appearance strongly suggests that a set of ordered physical processes take place during massive star formation. Thus, observational evidence of the earliest stages of massive star formation gives crucial insight into the initial conditions of this process and provides necessary guidance and constraints for theoretical models. In this chapter, the available rich resource of high-quality, high-resolution coordinated and unbiased radio and infrared data is utilised to attempt a new type of morphological classification – a more complete, multi-wavelength one. The

statistical results of this new classification are compared to those when using the standard radio-only scheme, as well as to those obtained through using only the IR data (GLIMPSE). The dependence of morphological class proportions on resolution is also investigated. The observed morphologies are also discussed in the context of their physical properties and immediate environment. The properties of the morphological subsets are also discussed in light of current theoretical models, with focus on the predominant cometary class and the location of the ionising star.

## 4.2 Radio and mid-IR morphological classification of UCHIIs

The original morphological classification by Wood and Churchwell [1989b] and the modified classification by De Pree et al. [2005] are discussed in §1.2.2. The more up-to-date De Pree et al. [2005] classification (as illustrated in Fig. 1.7) formed the basis of the radio, IR, and multi-wavelength classifications presented in this chapter. The CORNISH UCHIIs fall into five morphological classes: cometary, shell-like/shell (used interchangeably here), spherical, bipolar, and irregular.

UCHIIs were classified as cometary if their ionisation front is parabolic, with a well-defined leading edge and a tail, and the surface brightness decreases gradually from the head to the tail along the axis of symmetry of the parabola [Wood and Churchwell, 1989b]. The tail is often significantly brighter/more extended at mid-IR than radio wavelengths, due to the limit on the dynamic range in the case of radio interferometric observations.

Shell-like UCHIIs appear as complete or partially complete/broken ‘rings’ of emission, forming a more than 50% complete circular arc. In higher-sensitivity

radio images, cavities evacuated by the stellar wind can cause shell-like/limb-brightened appearance.

UCHIIs were assigned the spherical class in cases where the radio and mid-IR shape can be best represented by a two-dimensional Gaussian brightness distribution. Insufficiently resolved UCHIIIs or cometaries seen along their symmetry axes can appear spherical.

Bipolar UCHIIIs are elongated and have an axial ratio of at least 2 : 1. The bipolar structure is often quite symmetric and more pronounced in the mid-IR, sometimes with an IR-dark lane seen perpendicularly across the centre of the long axis.

The irregular class includes miscellaneous shaped UCHIIIs with multiple peaks within a common envelope of lower surface brightness, which is detected at least at  $5\sigma$ . At higher resolution, such irregulars can be resolved into pairs or multiples. Broken-up, noisy-appearing UCHIIIs which are likely the result of over-resolution of extended sources in interferometric observations are here not considered to be ‘true’ irregulars. Such instances were identified by comparing their mid-IR and radio appearance.

The radio, IR, and multi-wavelength classifications have the following methodology in common:

- Dynamic-range dependent contours were overplotted on the images (see Thompson et al. 2006); the images were scaled with asinh scaling wherever needed to boost contrast for the visual inspection;
- One class was chosen as the most likely for each UCHII, based on the examined radio/mid-IR image, and the total count for each class was quoted as percentage of the *resolved* sample used for each method;

- The visual classification was done twice per resolution and per classification method, with a time jump of at least a few months, and conflicts were re-inspected and reclassified if deemed necessary.

### 4.2.1 Radio classification

Example images used in the radio-only morphological classification are shown in Figure 4.1. The radio-based classification was carried out separately for both available high-resolution radio datasets – at  $1.5''$  (the CORNISH data, see Chapter 2) and  $0.3''$  (the JVLA data, see Chapter 3). Note that the latter group predominantly comprises UCHII regions unresolved in CORNISH, together with several UCHII regions (some of which resolved at  $1.5''$ ) that are field neighbours to the unresolved at  $1.5''$  targets. Thus the CORNISH-only and JVLA-only radio classifications are a good way to compare the morphology distributions of more extended and of more compact/younger UCHII regions. To achieve this, the insufficiently resolved sources in each dataset were excluded from the comparison. This comprises 45% (107) of the UCHII regions observed at  $1.5''$  resolution. As for the JVLA-observed UCHII regions, only one target was not resolved. Out of all detected in the JVLA follow-up survey UCHII regions (including neighbour UCHII regions, §3.6), seven are point-like at the higher resolution. Those were all excluded from the results (shown in Fig. 4.4). Over-resolved UCHII regions were also excluded.

### 4.2.2 Infrared classification

The extended emission from PAHs is seen in the environment of UCHII regions in the GLIMPSE mid-IR images. The PAHs outside the swept-up bubbles of H II regions form shells, which are clearly seen through their strong PAH features at the IRAC band wavelengths. The inner radius of the PAH shell is

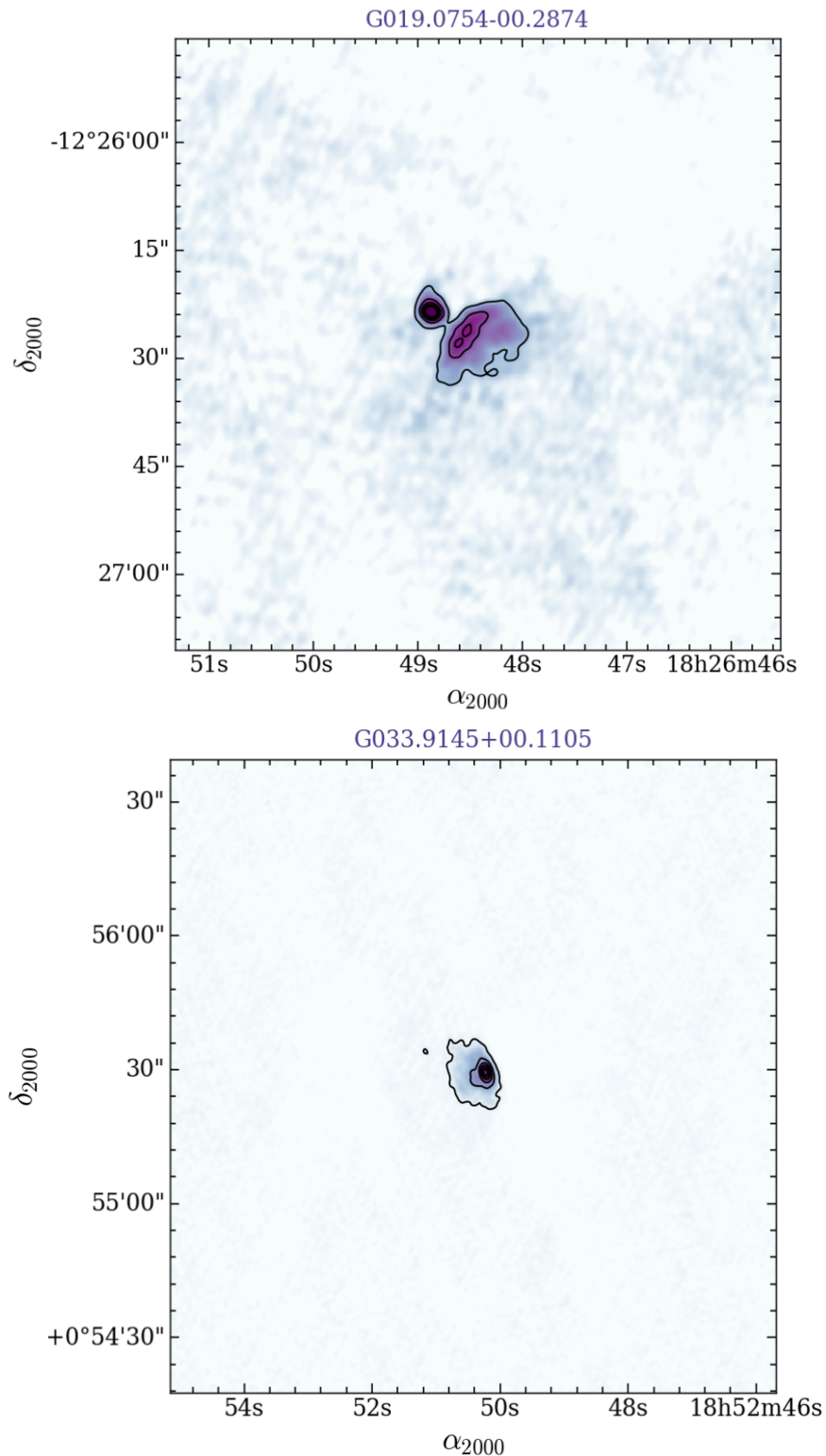


Fig. 4.1 Example CORNISH images used in the radio-only morphological classification. Dynamic-range dependent contours are overlotted to aid the classification, starting at  $5\sigma$ . The source names in the plot titles corresponds to the source central to each image. The mid-IR counterparts are shown in Fig. 4.2.

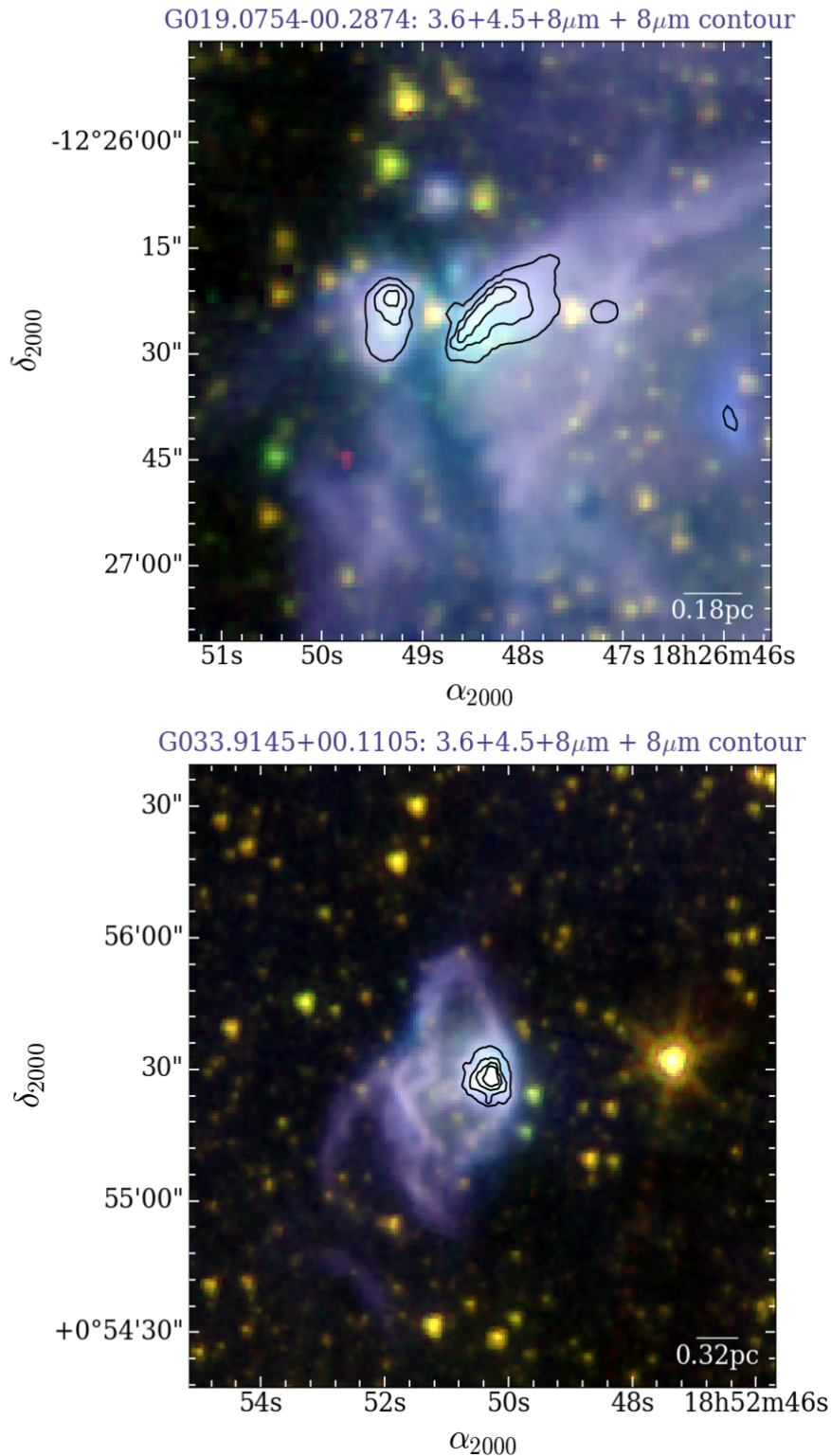


Fig. 4.2 Example false-colour images used in the mid-IR-only morphological classification (3.6+4.5+8 $\mu$ m, RGB in this order). Dynamic-range dependent contour levels from the best available (i.e. not saturated at the source location) PAH-band (8, 5.8, or 3.6 $\mu$ m, in order of preference) image were overplotted, starting at  $5\sigma$  ( $\sigma$  was computed from a region in the images free from diffuse emission). The images are centred at the CORNISH counterpart coordinates and titled accordingly. The 6 cm counterparts are shown in Fig. 4.1.

equal to the PAH destruction radius from the ionising star and closely matches the observed radio morphology, unless affected by extinction (see §1.2.4 for a more detailed discussion). The mid-IR emission is much more sensitive to diffuse, extended, low-level structures, such as in the tail of cometary UCHII regions (as seen when comparing Figs. 4.1 and 4.2).

For the purposes of the mid-IR morphological classification, the GLIMPSE images in all bands except the 4.5  $\mu\text{m}$  band (where there is a gap in PAH emission) were visually examined. This was done in order to select the most suitable image per source for the classification, in the cases where the source was saturated in the 8.0  $\mu\text{m}$  image. Whenever the 8.0  $\mu\text{m}$  image was of sufficient quality, it was preferred over the other bands, as it offers a view that is closest to the radio image. The final selection of images consists of 205 images in the 8.0 band, 32 images in the 5.8  $\mu\text{m}$  band, and 2 images in the 3.6  $\mu\text{m}$  band. The selected PAH-band images were used to plot dynamic-range dependent contours on 3-colour GLIMPSE images, as shown in Fig. 4.2 (3.6+4.5+8  $\mu\text{m}$ , note that 3.6 is plotted as red and 8  $\mu\text{m}$  – blue). These multi-band images highlight the PAH- and stellar emission from and around the mid-IR UCHII counterparts. The 4.5  $\mu\text{m}$  band shows signposts associated with younger phases, such as line emission from  $\text{H}_2$  and CO shocked by protostellar outflows (which appears as extended green objects (EGOs) in the colour *Spitzer* images, see Cyganowski et al. 2008).

An infrared-dark lane is seen across the mid-IR UCHII counterpart in 7% (16) of the GLIMPSE images, and in some of these cases it was not possible to reliably determine the mid-IR morphology.

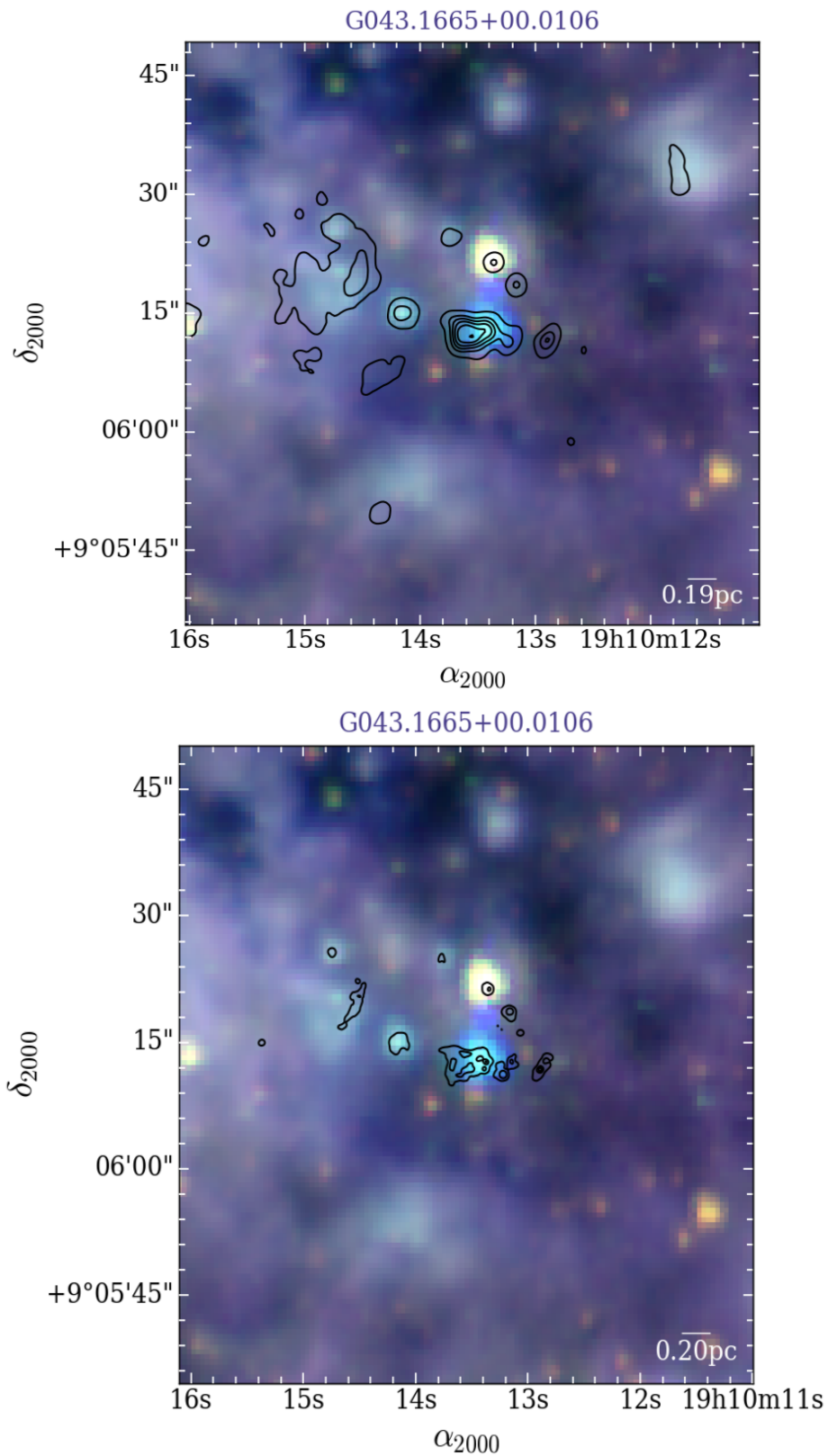


Fig. 4.3 Example images of W49A (centered at the bright, multiply-peaked G043.1665+00.0106) used in the joint morphological classification. Dynamic-range dependent contour levels starting at  $5\sigma$  in the top panel (CORNISH) and at  $7\sigma$  in the bottom panel (JVLA) are plotted onto the 3-colour GLIMPSE image (3.6+4.5+8  $\mu\text{m}$ , RGB in this order).

### 4.2.3 Joint radio-IR classification

#### Aims of the joint morphological classification

Combining the available radio and IR images to utilise the advantages of both is at the core of the new, joint morphological classification. As discussed in §2.2 and §1.2.4, the use of mid-IR data is not only necessary for the reliable UCHII identification, but is also highly advantageous as it is not dynamic-range-limited, unlike snapshot Galactic plane surveys such as CORNISH. Examining the mid-IR counterparts to the UCHIIs in conjunction with the radio data can compensate for the loss of morphological information at extended scales and thus mimic the reliability achieved by morphological classification of deep, multi-configuration radio observations. With this method, the UCHII region location and radio extent can be precisely pinpointed, and its mid-IR ‘context’ is seen concurrently (Fig. 4.3).

Noting the morphology alone, with any of the described above methods, means obtaining information on the UCHII region as an isolated entity. To understand the morphologies and obtain a complete picture of the interactions of massive stars with their parent molecular clouds, their location with respect to larger structures, ability to trigger further star formation, and role in cloud dynamics and maser pumping should be explored [Kurtz et al., 1994]. With this goal in mind, additional information on the relation of each CORNISH UCHII region to its environment, such as possible relation to younger and/or to more evolved sources, was noted during the visual inspection alongside picking a morphological class. These additional ‘categories’ were added after a careful initial visual inspection and reflect the most commonly seen patterns in the immediate surroundings of each source, to quantify the recurrent observational properties of the CORNISH UCHIIs within their molecular clouds (described in Table 4.1). This is not aimed as a complete description; the good number

statistics of resolved UCHII regions provided by the CORNISH sample and the JVLA follow-up were utilised to spot patterns that are likely common for most Galactic UCHII regions and their immediate surroundings.

This thus provides a statistic on the number of UCHII regions found within or at the edge of a bubble or shell, as a head of a larger cometary region, ahead of a more evolved H II region (i.e. in search of candidate triggered UCHII regions), and/or within a close association of UCHII regions. Other features of interest that were included are coincidence between the mid-IR and the radio tail direction for cometary regions, MYSOs, EGOs and masers located within the ‘sphere of influence’ of the UCHII, as well as the presence of an infrared-dark lane ahead or across the UCHII. In this case, determining the sphere of influence meant simply computing the angular radii corresponding to the typical size of molecular clumps in which UCHII regions are found – 0.5-1 pc in diameter [Hoare et al., 2007]. This translates to a maximum cross-match radius of  $\lesssim 1'$  for the CORNISH UCHII regions, to avoid complex considerations such as the interplay between gravity, stellar winds, shocks, magnetic fields in their possible role and relative importance in star formation triggering.

Each UCHII region can thus belong to several of these categories and patterns can be noted. An example of such a recurring pattern that was quantified in this way is the number of radio cometary regions which have a mid-IR counterpart of comparable size, with the same morphology and tail direction, situated at the head of a larger mid-IR cometary or shell. Set-analysis visualization software (commonly used in e.g. macroeconomics and genetics) was utilized in search of such patterns, through locating the intersections between the visually identified sets [Lex et al., 2014]. To efficiently pinpoint and rectify any possible issues with this extended joint classification which may arise due to its complexity, the same software was also used to inspect all subgroups and make sure no sources were missed.

Table 4.1 Description of the additional categories the UCHIIs were assigned to alongside a morphological class. Examples to illustrate each category are included in the third column.

Category	Description	Fig.
<b>Based on visual inspection:</b>		
Part of bubble	The mid-IR counterpart to the UCHII is located within or at the edge of a larger mid-IR PAH bubble or shell.	4.11f
Head of larger cometary	The mid-IR counterpart of the UCHII is at the head of a larger mid-IR cometary region (likely as part of the same source).	4.15g
Middle of larger bipolar	The mid-IR counterpart of the UCHII is at the centre of a larger mid-IR bipolar region (likely as part of the same source).	4.11i
Larger H II ahead	The UCHII is located ahead of a more evolved H II region, as seen in the CORNISH and/or MAGPIS maps (H II within $\sim 30''$ radius).	4.11h
In radio double	The UCHII is in a close pair of CORNISH UCHIIs, where the neighbour is situated no more than about one angular diameter away. This category contains the UCHIIs flagged in the CORNISH catalogue as having a $7\sigma$ overlapping neighbour.	4.15f
In radio multiple	The UCHII is within a UCHII association, with area of radio group $\lesssim 1$ sq. arcmin.	4.3
Dark lane ahead	There is a mid-IR dark lane ahead of the mid-IR counterpart to the UCHII.	4.15b
Dark lane across	There is a mid-IR dark lane across the mid-IR counterpart to the UCHII.	4.11j
<b>For cometary sources:</b>		
Same tail direction	The direction of the radio tail coincides with the mid-IR counterpart.	4.15i
<b>Cross-matches to catalogues:</b>		
EGO(s) ahead	There are EGOs within 0.5 pc radius of the UCHII location. (matched from the Cyganowski et al. [2008] catalogue)	4.11d
MYSO(s) ahead	There are RMS MYSOs within 0.5 pc radius of the UCHII location.	4.10a
Maser(s) ahead	There are known methanol masers within 0.5 pc radius of the UCHII location (match to the Pandian et al. [2007] methanol maser GPS).	4.11e
Has K nebula	The UCHII has a K nebula counterpart (Chapter 2).	4.15j

### Multi-wavelength methodology

The combined method consisted of visual classification based on the available radio images and the 3-colour GLIMPSE images (produced as discussed in the previous two sections). The radio contours were plotted onto the corresponding mid-IR images. Plots showing different sky areas with respect to the UCHII regions were produced to examine different scales – typically  $3\times$ ,  $6\times$  and  $12\times$  the angular diameter of each UCHII. All CORNISH 6 cm images, together with maps of all targets from the JVLA follow-up, were used to overlay radio contours (in separate images corresponding to the different resolutions). The JVLA-observed neighbours were also included – being particularly useful for very compact resolved CORNISH UCHIIs (i.e. sizes only slightly in excess of  $2.7''$  – the upper limit for the selected JVLA targets), where it was otherwise still difficult to determine the morphology. Images of the more extended UCHIIs in the JVLA neighbour group supply further detail of the compact parts of resolved CORNISH UCHIIs even in cases where the extended emission was filtered out (Fig. 4.3).

The multi-wavelength resource of the CORNISH survey database was referred to in order to determine the morphology of ambiguous cases – for example for irregulars and UCHIIs with conflicting IR and radio morphological classes (as assigned through the aforementioned methods). The MAGPIS 6 and 20 cm images were examined to look for evolved H II regions coinciding in position, size and shape with extended PAH bubbles seen in the GLIMPSE images found ahead/around the CORNISH UCHIIs, to count the UCHIIs that could have been the product of sequential star formation. Relation to larger-scale structures, signposts of younger phases, and UCHII multiplicity, were categorised by assigning the relevant categories (if any) from Table 4.1 to each UCHII. The presence of near-IR nebula associations was quantified in

Table 4.2 UCHII counts in each morphological class (presented as fractions of the total in each method), with Poisson errors indicating the lower bounds of the associated uncertainty.

Classification	cometary (%)	bipolar (%)	shell-like (%)	irregular (%)	spherical (%)
CORNISH	$59 \pm 7$	$13 \pm 3$	$4 \pm 2$	$20 \pm 1$	$4 \pm 2$
JVLA	$74 \pm 10$	$1 \pm 1$	$1 \pm 1$	$19 \pm 1$	$5 \pm 3$
CORNISH+JVLA	$64 \pm 6$	$10 \pm 2$	$3 \pm 1$	$19 \pm 1$	$5 \pm 2$
GLIMPSE	$65 \pm 7$	$9 \pm 3$	$6 \pm 2$	$12 \pm 1$	$8 \pm 2$
Final	$71 \pm 6$	$8 \pm 2$	$5 \pm 1$	$14 \pm 1$	$2 \pm 1$

Chapter 2 and those associations were inspected again in search of candidate ionising stars.

### 4.3 Morphology statistics

The main findings are presented as described here. First, the statistic of the morphological classes is discussed, following up on the older classifications. Next, some of the main physical properties of the different morphological UCHII subsets, such as physical sizes, electron densities, and luminosities (as computed in §2.6, §3.8.1, and §2.8), are compared in search of any dependences, and thus possible physical differences, between the sources belonging to different morphological groups (§4.4). A gallery and discussion for each morphological type is presented in §4.5 and Figs. 4.10–4.15. The findings obtained through the additional categories of the joint radio-IR classification, as described in the previous section and summarised in Table 4.1, are explored through subset statistics in §4.6.

Figure 4.4 summarises the results of the radio-only, the mid-IR, and the joint visual classifications. The De Pree et al. [2005] classification groups are a good description of the CORNISH UCHII sample, at both available resolutions (1.5'' and 0.3''), and examples of all classes were found. Thus it successfully

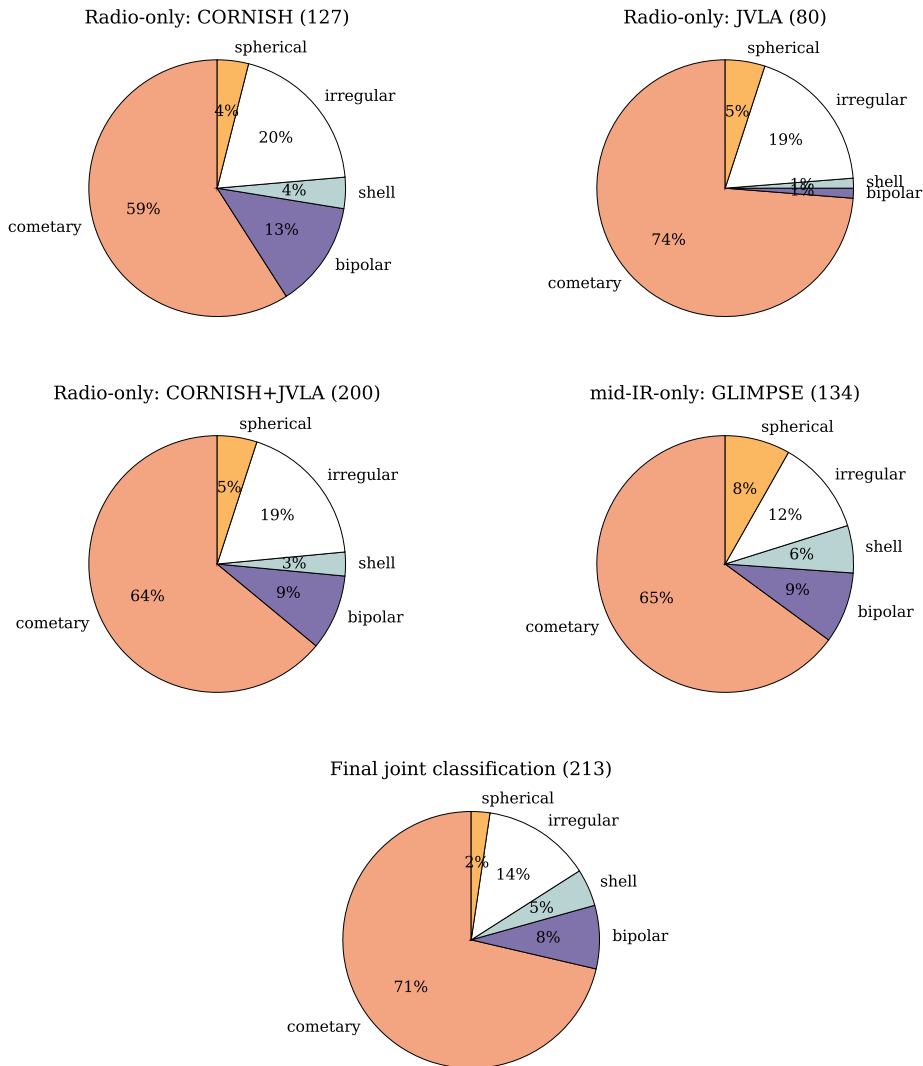


Fig. 4.4 Results from different morphological classification methods – radio-only (at 1.5'' vs. 0.3''), mid-IR, and combined multi-wavelength + multi-resolution. In all cases, sources without sufficient morphological information were excluded (this can be unresolved, barely-resolved, or over-resolved sources which appear irregular but lack multiply-peaked structure). The total UCHII count in each case is given in brackets. The JVLA and the combined radio classifications includes all (morphologically classified) JVLA multiples as separate sources. GLIMPSE saturated counterparts were also excluded – the mid-IR morphology was then determined from the non-saturated PAH-band images, if any. For the mid-IR classification, UCHIIs which have a mid-IR-dark lane across were not classified.

served as a foundation for the joint morphological classification introduced in this chapter.

Cometary UCHII regions are the most widespread morphological type, as found through all classification methods and at both resolutions. They comprise  $\gtrsim 60\%$  of all UCHIIs (71% in the final, joint classification). Irregulars rank second in ubiquity, at  $\sim 14\%$  of the total in the final classification. In all classifications except for the JVLA-only one, this is followed by the bipolar class ( $\sim 8\%$ ). Members of the spherical and shell classes are the rarest overall, and have a similar frequency of occurrence to one another ( $\sim 2\text{-}5\%$ ). The counting errors on the fractions of UCHIIs belonging to each morphological category are presented in Table 4.2. Poisson errors likely underestimate the uncertainty associated with the visual classification and should be treated as lower bounds on the error.

### 4.3.1 Dependence on resolution and wavelength

Excluding sources without sufficient morphological information (unresolved, barely-resolved, or over-resolved sources which appear irregular but lack multiply-peaked structure), 213 UCHIIs were assigned a class (different than ‘point’) in the joint classification. This corresponds to 208 CORNISH UCHIIs, out of which 4 have two or more morphologically classified components in the JVLA images. In the CORNISH-only classification, 127 UCHIIs were assigned a morphological type. In the JVLA-only classification, this number is 80 (including neighbour sources). Two hundred UCHIIs were classified in the joint radio classification (as 8 of the JVLA neighbour sources were resolved also in CORNISH). When using only the GLIMPSE images, 134 UCHIIs were classified. The number of morphologically classified mid-IR counterparts exceeds the corresponding CORNISH count, as the mid-IR images show greater extent to their CORNISH

counterpart, which provides sufficient morphological information to several radio-unresolved sources in these cases, despite the slightly lower resolution in GLIMPSE. This is due to the filtering of extended emission in the radio images, combined with the fact that the PAH emission arises at the outermost ‘boundary’ of the H II region.

As evident from Fig. 4.4, the statistical difference is the largest between the lower and higher resolution radio classifications – 15% more cometaries were found in the JVLA set in comparison to CORNISH. The fraction of irregular and spherical sources is in excellent agreement with the CORNISH-only classification. However, there are only one bipolar and two shell-like UCHIIs in the higher-resolution set. The number statistic is smaller in the JVLA sample than in the CORNISH-only sample (80 vs. 127 resolved UCHIIs), but is not likely to be the main reason for the statistical differences. This is evident from Fig. 4.6, which shows the distribution of morphological classes with physical size and electron density. All the smallest resolved CORNISH UCHIIs – with computed physical sizes  $\lesssim 0.04$  pc and the highest electron densities in the sample ( $\log(n_e) > 3.75 \text{ cm}^{-3}$ ) – were classified as cometary. The JVLA set includes the smallest CORNISH UCHIIs, with median physical diameter of 0.09 pc; this value is 0.18 pc for the resolved CORNISH set. The UCHIIs in the JVLA set are also denser and brighter, with median  $\log(n_e) \approx 3.85 \pm 0.04 \text{ cm}^{-3}$  and  $\log(L_{\text{bol}}) \approx 4.65 \pm 0.10 L_{\odot}$ , in comparison to  $\log(n_e) \approx 3.68 \pm 0.03 \text{ cm}^{-3}$  and  $\log(L_{\text{bol}}) \approx 4.45 \pm 0.10 L_{\odot}$  for the resolved CORNISH set. This points towards a fundamental difference between the two UCHII sets – the higher densities and smaller sizes at comparable luminosities indicate that the JVLA UCHIIs are likely younger and therefore have had less time to expand (possibly into less ordered/asymmetric shapes). Due to the degeneracy between density and luminosity, an alternative explanation is that a density gradient in a high-density portion of the molecular cloud can result in the formation of

small, trapped cometaries (and the morphologies at the same luminosity but lower density could be more varied).

The results from the ‘three-colour’ mid-IR and the multi-wavelength classification are similar; however it should be noted that those are the results after excluding GLIMPSE images which were saturated at the source location. Due to the  $2''$  resolution, more sources were insufficiently resolved than in CORNISH, and were also excluded. The sample size in the multi-wavelength classification is the largest in comparison, providing better number statistics. It was only possible to classify sources in particularly busy regions by outlining the radio extent together with the mid-IR contours, which could have introduced a bias. A fully independent mid-IR classification of UCHIIs is clearly not possible without guidance from the radio data.

The agreement between the radio-only and mid-IR-only classifications for individual sources was estimated, as it could indicate the reliability of the joint classification for each morphological group. When the CORNISH+JVLA and the mid-IR classification results are compared, the classification is in agreement for 65% of cometaries, 44% of shell-like UCHIIs, 33% of spherical UCHIIs, 33% of bipolars, and 27% of irregulars. The agreement is slightly better overall when taking into account only the radio and mid-IR images of comparable resolution, i.e. when comparing the CORNISH-only to the mid-IR results. In this case, 66% of cometaries, 57% of shell-like UCHIIs, 33% of spherical UCHIIs, 35% of bipolars, and 26% of irregulars were assigned the same type in both classifications. A higher fraction of sources what were assigned the same class in both classifications would suggest a higher degree of reliability of the final, joint classification for this class. However, it should be noted that the relative fractions are clearly also affected by the vastly different number statistics between the cometary class and the other morphological types. The joint classification is the most reliable overall – rather than preferring one

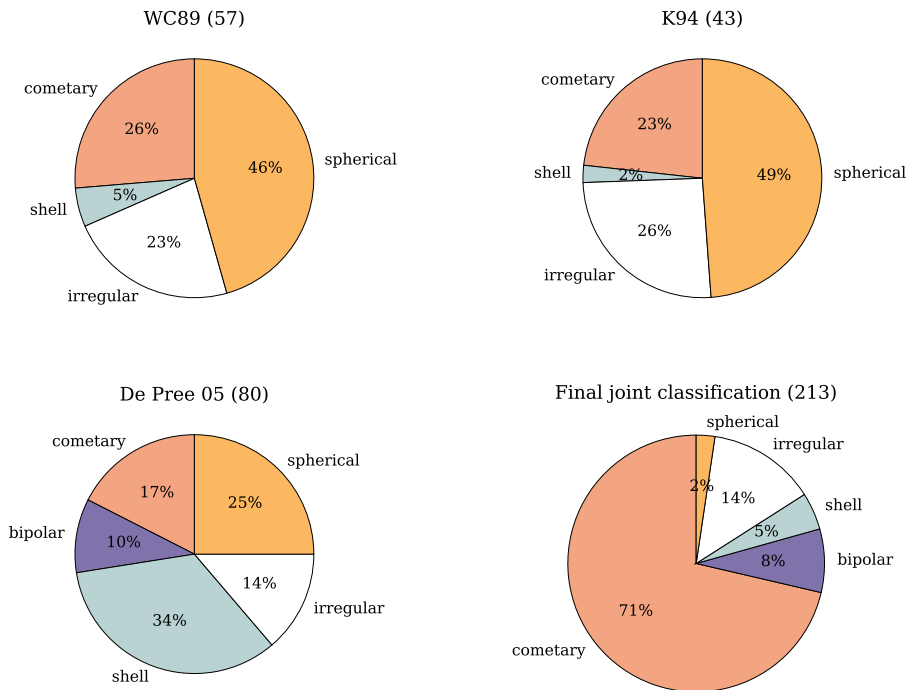


Fig. 4.5 Comparison of morphology distributions. All unresolved and core-halo UCHIIs were excluded from the statistic. The new total UCHII counts are shown in brackets. The bipolar class was introduced by De Pree et al. [2005]. The resolution of the De Pree sample is  $2''-0.04''$ ,  $\sim 1''$  for the Kurtz sample,  $0.4''$  for the Wood and Churchwell sample, and  $1.5''/0.3''$  for the CORNISH/JVLA images.

method over the other, the classification was performed anew, taking advantage of the best available data for each UCHII.

### 4.3.2 Comparison to previous classifications

The obtained morphology fractions are markedly different to the findings of previous classifications, as seen in Fig. 4.5. The bipolar class was introduced by De Pree et al. [2005]. This hinders an exact comparison to the Wood and Churchwell [1989b] (WC89) and Kurtz et al. [1994] (K94) results, but the main trends, such as e.g. the relative statistic of cometary to spherical sources, remain clear. It is unclear whether bipolar sources were previously most often classified as irregular, core-halo, other, or not seen at all, without re-inspecting

the WC89 and K94 maps. To aid the comparison somewhat, the unresolved and core-halo counts were excluded from the quoted results of the previous classifications – the former is not a true morphological class as it supplies no morphological information, whereas the latter is considered obsolete [De Pree et al., 2005; Hoare et al., 2007]<sup>1</sup>. Only the final, joint classification statistic is considered in this comparison.

The counts of the irregular sources are the most consistent between all classifications. As discussed by the authors, the numerous shell-like sources observed by De Pree et al. [2005] are likely the by-product of the much deeper observations of two crowded pointings (towards the SFRs Sgr B2 and W49A), when compared to snapshot surveys. Observing cometaries at a greater sensitivity and resolution would make them appear more shell/ring-like. An example of the latter can be seen in Fig. 4.12c, as well as in some of the JVLA maps presented in Chapter 3. In addition to this, as discussed by De Pree et al. [2005], the highly clustered, high source density star-forming environments of their sample of UCHIIs residing in Sgr B2 and W49A could significantly differ to the predominantly isolated SFRs studied by WC89 and K94. De Pree et al. [2005] suggest that highly ordered morphologies – such as cometaries and shells – are typical for smoother molecular environments. In contrast, environments with greater fluctuations in ambient pressure due to density, temperature, or turbulence, lead to more pronounced asymmetries during the expansion phase, and produce more irregular morphologies.

The CORNISH UCHII sample is a better representation of the Galactic UCHII population than the earlier samples, due to its unbiased, homogeneous nature, and improved number statistics; thus the main morphology trends are expected to be true for the Galactic UCHII population overall. To minimise

---

<sup>1</sup>A summary of the results of these classifications, as reported originally, can be found in Table 1 in De Pree et al. [2005].

Table 4.3 Slopes and correlation coefficients from least-squares fits of the electron densities as a function of physical diameter for each morphological type.

Type	Slope	r
spherical	$-0.85 \pm 0.82$	-0.48
shell-like	$-1.05 \pm 0.03$	-0.91
bipolar	$-0.62 \pm 0.09$	-0.46
irregular	$-0.51 \pm 0.03$	-0.52
cometary	$-0.51 \pm 0.003$	-0.62

possible misclassifications due to human error/the subjective nature of visual classifications, the inspection can be performed by more than one person in the future. Still, the effect is unlikely to be the main contributor to the major statistical discrepancies with the previous works, as class descriptions were closely followed in the visual classifications (and those were performed twice).

## 4.4 Physical properties and morphologies

The main findings and overall statistic resulting from applying all described classification methods are in good agreement. The morphological classes of the CORNISH UCHIIs are presented in Table B.1 in Appendix B. The results from the joint radio+IR classification are the most reliable, with their improved with respect to the other methods number statistics, achieved by including the higher resolution images and the addition of all IR-classified UCHIIs (in cases where these could not be reliably classified from their available radio maps alone). Only the joint classification results are referred to in all subsequent sections of this chapter.

### 4.4.1 Sizes and electron densities

As discussed by Kurtz et al. [1994], the bow-shock model predicts ram-pressure confinement of the ionised gas for the star moving through the molecular

cloud. In this picture, the size and density of the UCHII are not bound by a size-density-age relationship, but by the balance of ram pressure against stellar wind. Garay et al. [1993] found evidence supporting the former by analysing the densities and sizes of their H II regions (without distinction between morphological types). Kurtz et al. [1994] investigated the WC89 morphological groups together with their classified follow-up UCHII sample in a similar fashion; De Pree et al. [1997a] classified and analysed in this way UCHIIIs belonging to the W49A complex.

Using the final, joint morphological classification, the electron densities of each morphological type of UCHIIIs (computed in Chapter 2 from the radio continuum at 6 cm) were plotted in Fig. 4.6 as a function of physical diameter. Spherical, shell-like, bipolar, and irregular UCHIIIs are plotted with different symbols in the top panel, as shown in the legend. Cometaries are plotted separately in the bottom panel of the figure, to avoid overcrowding. For all morphological classes, there is a clear negative correlation between the electron density and physical size, consistent with expanding UCHIIIs. The distributions of cometaries and irregulars both have the same slope of  $\sim -0.51$  (respective uncertainties of  $\pm 0.003$  and  $0.03$ , and correlation coefficients of  $-0.62$  and  $-0.52$ ); the other three types suffer from small number statistics, but their slopes are steeper in comparison: bipolar:  $-0.62 \pm 0.09$ , shell-like:  $-1.05 \pm 0.03$ , and spherical:  $-0.85 \pm 0.82$  (with correlation coefficients of  $-0.46$ ,  $-0.91$ , and  $-0.48$ , respectively). These are summarised in Table 4.3. De Pree et al. [1997a] examined their cometary and unresolved+spherical sources in this manner, and found that the two groups lie on the same negative density-size correlation (close to  $-1$ , see their Fig. 8). Kurtz et al. [1994] estimated a slope of  $-0.65 \pm 0.09$  for their unresolved+spherical group, with a correlation coefficient of  $-0.72$ . For cometary+core-halo UCHIIIs, they find no correlation (coefficient of  $-0.24$ ). Using peak densities vs. sizes, they find a correlation

coefficient of  $-0.52$ . The fit is greatly affected by the core-halo sources, which have a much greater range of rms electron densities (see their Fig. 151). The trend exhibited by the CORNISH UCHIIs suggests that the same main mechanisms serve to confine the observed different morphological types.

#### 4.4.2 Luminosities and spectral types

Figure 4.7 shows the Lyman continuum flux distribution with distance (§2.6) for the different morphological classes, using the findings of the final, joint classification. Again, all types except for cometary are plotted in the top panel. Bipolars have the second largest  $N_i$  distribution (after cometary, shown in the bottom panel), spanning more than three orders of magnitude. The largest irregulars have the highest computed Lyman continuum fluxes. Representatives of the spherical, shell, and irregular types (in this order) are found at the furthest heliocentric distances for the sample. Their median distances are  $13.7 \pm 1.2$  kpc,  $11.8 \pm 1.9$  kpc, and  $11.1 \pm 1$  kpc, respectively. The cometary and bipolar groups are found at median distances of  $9.4 \pm 0.4$  kpc and  $5.5 \pm 1$  kpc, respectively. CORNISH UCHIIs with bipolar morphology are small (median diameter of  $\sim 0.14 \pm 0.05$  pc) and relatively nearby, and such sources could thus be relatively young. The median size of shell-like UCHIIs is the largest for the sample –  $\sim 0.31 \pm 0.1$  pc. Spherical UCHIIs have a median diameter of  $\sim 0.26 \pm 0.05$  pc. For irregular and cometary sources, this value is  $\sim 0.21 \pm 0.04$  pc and  $\sim 0.11 \pm 0.01$  pc, respectively. It is unclear from the distribution of distances and sizes whether irregulars are more likely to be merged clusters of sources, or rare, luminous sources seen at greater distances (or a mix of the two).

The distribution of shell-like and spherical UCHIIs is consistent with the hypothesis that these morphological types are special cases of cometary orien-

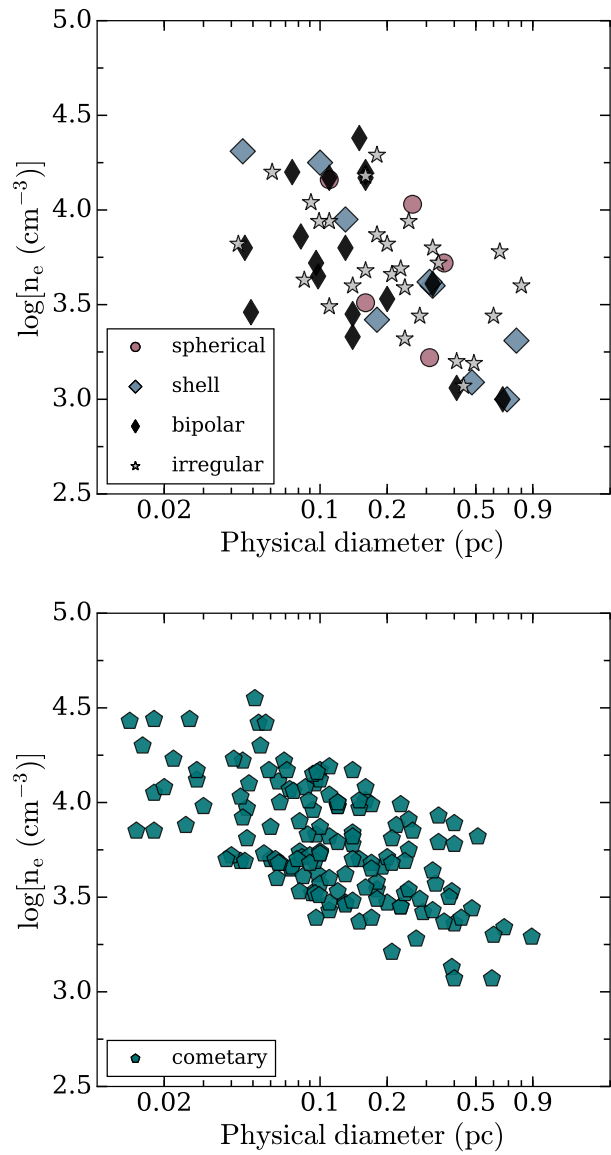


Fig. 4.6 Electron density vs physical diameter for the different morphological classes (based on the joint classification).

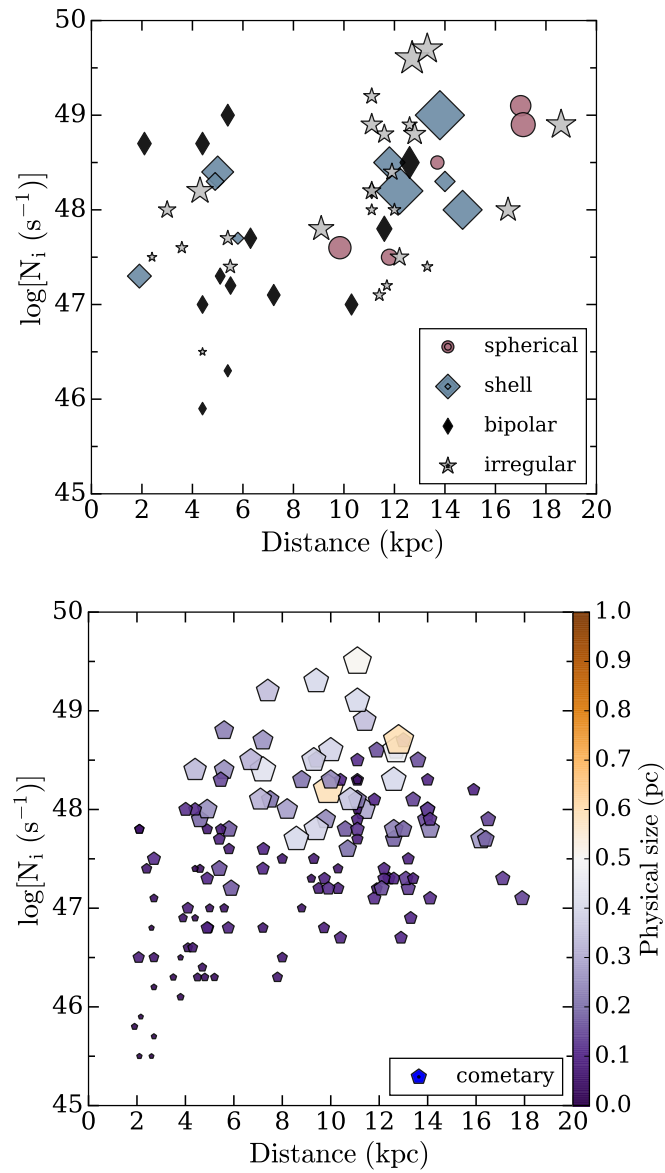


Fig. 4.7 Lyman continuum flux vs distance for the different morphological classes (based on the joint classification). The marker sizes show the relative physical sizes of the UCHII regions.

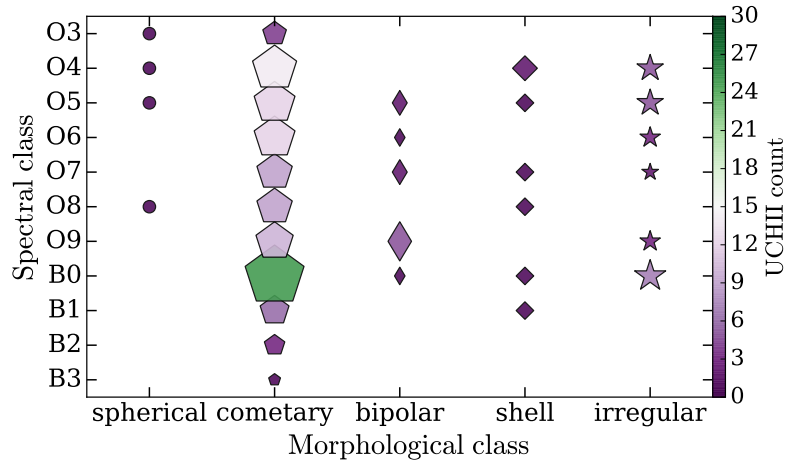


Fig. 4.8 Distribution of spectral types (based on the IR-SED-fitted  $L_{\text{bol}}$ ) and morphological classes (based on the joint classification). The marker sizes represent the UCHII counts corresponding to each spectral type.

tation (l.o.s. along the axis of symmetry), or are at least produced by the same physical mechanism to one another. In this scenario, equally luminous cometary UCHIIs seen along their axis of symmetry would appear shell-like when nearer, and spherical when further away (and/or smaller), as summarised in Fig. 4.9. As seen in Fig. 4.7, shell-like UCHIIs with equal Lyman continuum fluxes (and comparable physical sizes and electron densities) to spherical UCHIIs are indeed found at nearer distances.

The probability density function of a uniform distribution of UCHII inclinations w.r.t. the observer can be represented as  $g(\cos i) = 1$ , where  $i$  is the isotropic inclination angle, defined between  $0^\circ$  and  $90^\circ$  (the range for projected angles along the l.o.s). This is because for isotropic inclination angles,  $\cos i$  is uniformly distributed<sup>2</sup>. The average inclination of the CORNISH UCHII sample would then be  $\cos i = 0.5$  (as the  $\cos i$  range is from 0 to 1), i.e.  $i = 60^\circ$ . The group of shell-like and spherical UCHIIs comprises 7% of the total sample (Fig. 4.4), translating to  $g = 0.07$ , from which  $i \approx 86^\circ$ . It can be investigated with theoretical models whether UCHIIs appear spherical or shell-like for  $i \gtrsim$

<sup>2</sup>See <http://keatonb.github.io/archivers/uniforminclination>.

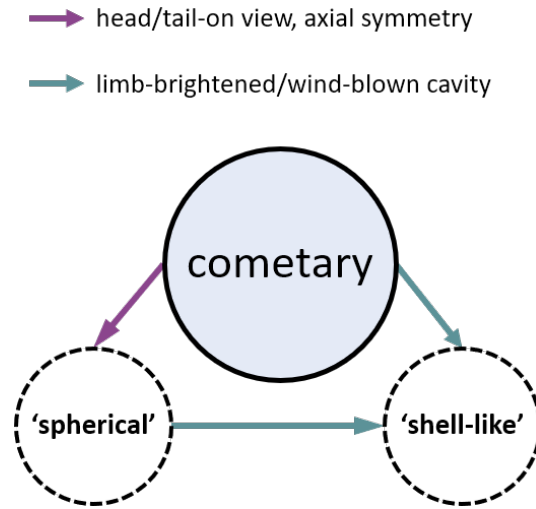


Fig. 4.9 Possible origins of the observed spherical and shell-like morphologies, assuming that the physical mechanism shaping cometary UCHIIs is also responsible for those classes, and the appearance is due to a few common types of observational and/or physical orientation effects.

$86^\circ$ , and start appearing cometary for  $i \lesssim 86^\circ$ . In such a case, the statistics of the the observed shell-like and spherical UCHIIs would be consistent with random orientation of cometary UCHIIs.

The spectral types and their statistics according to the morphological subsets are summarised in Figure 4.8. The spectral types of the stars ionising each UCHII region were identified using the computed in §2.8 bolometric luminosities estimated through fitting the SEDs (spanning from near-IR to sub-mm wavelengths and not taking into account the radio fluxes). Table 1 from Mottram et al. [2011] lists the spectral type corresponding to a given luminosity. When using the computed bolometric luminosities rather than the Lyman continuum flux estimates (the latter being lower limits, see §2.6), the spherical and cometary UCHIIs are ionised by the brightest (type O3) stars in the sample. As the associated SED fits are good, the difference could be attributed to the different methods used. The largest portions of the cometary and irregular samples were matched to the B0 spectral type, as is to be expected as these stars are capable of producing sufficiently luminous H II regions to be seen from

large distances, and are more numerous than O-type stars. Unsurprisingly, fewer H II regions are seen when approaching the lower limit for H II region formation — spectral type B3 (see §1.2).

This ‘reading off’ the spectral types from the table (through performing a cross-match to select the closest tabulated luminosity and its corresponding spectral class) is underpinned by the assumption of a single ionising source per region. This should be a good enough approximation, as the effects of close external ionising sources – compact or extended – are expected to be minimal given the good IR resolution of the UKIDSS, GLIMPSE, and Hi-GAL data, which make up the brightest portion of the reconstructed UCHII region SEDs (see Cesaroni et al. 2015 and Chapter 2 for more details on the *Herschel* data). The effect of massive binaries/multiples on the observed bolometric luminosity and thus spectral type depends on how common such systems are. The well-studied Trapezium cluster, at a distance of  $\sim 440$  pc, is located in the centre of the nearest massive star formation region – the Orion nebula [McCaughrean and Stauffer, 1994; Schulz et al., 2001]. Companions to OB stars in the Orion Nebula Cluster have been observationally confirmed – for their sample of two O and three B-type stars observed with long-baseline interferometry, Grellmann et al. [2013] found an average of 2.5 known companions per primary. Estimates for the binary fraction among massive stars vary and are typically lower limits (see the discussion by Kobulnicky and Fryer 2007 and the references therein). Garcia and Mermilliod 2001 reported the multiplicity statistics for O stars in a variety of cluster environments. They concluded that the binary fraction ranges between 14% – 80% (lower for denser clusters). This is in agreement with more recent estimates, such as e.g. Chini et al. [2012], who found that over 80% of stars more massive than  $16 M_{\odot}$  form close binary systems. Observational evidence suggests that Wolf-Rayet binaries likely do not comprise the majority of the WR population [Garmany et al., 1982]. Kobulnicky and Fryer [2007]

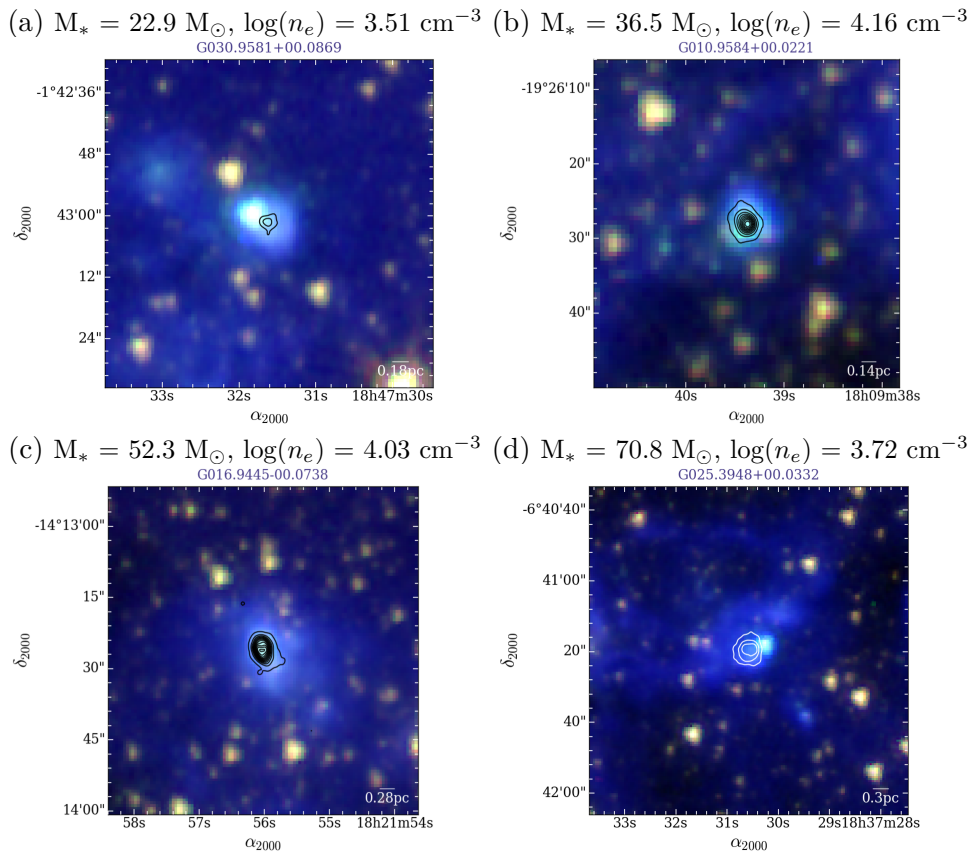


Fig. 4.10 UCHIIs classified as spherical in the joint classification, ordered by mass of the ionising star. The computed electron density is also shown.

predict that massive stars preferentially have massive companions. Garmany et al. [1980] found that the mass ratio distribution is either flat or peaked toward massive companions.

## 4.5 Gallery of morphological types

### 4.5.1 Spherical UCHIIs

Only 2% of the resolved UCHIIs were classified as spherical. The few observed sphericals have (somewhat) extended morphologies and Gaussian profiles in their radio and mid-IR images, but only approximate a well-defined circular shape, particularly in their radio contours (Fig. 4.10). G030.9581+00.0869

(Fig. 4.10a) has a close RMS MYSO neighbour. It is a point source ahead of the mid-IR nebula, and is not seen in the JHK images (see discussion in §4.6.3).

The observed spherical morphology of these UCHIIs could be the result of conditions close to the idealised Strömgren sphere scenario (see §1.2.2), or of observing bright, distant cometaries along their axis of symmetry (§4.4.2), or observing UCHIIs that form in the same manner as cometaries but with their expansion confined by an attribute of their environment and/or the properties of the ionising star – e.g. a higher-density environment and/or a lower-mass/later OB star.

### 4.5.2 Bipolar UCHIIs

Following the De Pree et al. [2005] definition, bipolars are elongated sources with an axial ratio of at least 2 : 1. In the joint classification, UCHIIs were classified as bipolar if this was clearly met in at least one of the wavelengths – radio or mid-IR. About 8% of the sample belongs to this group.

De Pree et al. [2005], who introduced this morphological type, suggested that its characteristic shape is linked with the bipolar outflow phase of early stellar evolution. They based this on the shape and velocity gradient observed along the long axis, interpreted as ionized gas flowing away from the young massive star at highly supersonic velocities [De Pree et al., 2004].

Examination of the structure and immediate environment of the UCHIIs classified as bipolar in the extended joint classification reveals that about 47% form the central part of a larger, mid-IR bipolar region (Fig. 4.11). Half of these bipolar UCHIIs are bifurcated by a dark lane almost perpendicular to their centre – these are G030.7579+00.2042 (Fig. 4.11a), G024.4921–00.0386 (Fig. 4.11b), G011.9368–00.6158 (Fig. 4.11i), and G012.8050–00.2007 (Fig. 4.11j).

This structure is reminiscent of the well-known, more evolved representative of the bipolar type – S 106 (see e.g. Smith et al. 2001). Such bipolars could thus alternatively result when an H II region forms within a dense molecular cloud filament or sheet, and in its expansion it breaks out on the sides and into the surrounding lower-density gas. Deharveng et al. [2015] studied six large bipolar H II regions in detail and identified their parental filaments (or edge-on sheets). The observed butterfly-like morphologies are also reminiscent of a much smaller-scale version of simulated primordial massive stars formed in shielded filaments (e.g. Fig. 2 in Abel et al. [2007]).

A small ( $\sim 0.075$  pc), highly symmetric example of the bipolar type from the CORNISH UCHII sample re-observed at the higher JVLA resolution is G043.1652+00.0129 (Fig. 4.11l and §3.6), located amidst the busy MSFR W49A. High resolution images of this source can also be seen in Fig. 1.7 as the archetypal bipolar UCHII of the De Pree et al. [2005] classification – this is W49A/A from De Pree et al. [1997a]. Most of the bipolar UCHIIs in the sample ( $\sim 71\%$ ) are situated at the edges of large mid-IR bubbles.

Zhu et al. [2008] conducted a velocity study of G011.9368–00.6158 (Fig. 4.11i), and their [Ne II]  $12.8 \mu\text{m}$  map (right panel of their Fig. 7) matches the bipolar mid-IR morphology well. They fitted single Gaussian profiles to emission peaks in the SE ‘half’ of the UCHII, with centre velocities close to the velocity of the molecular cloud ( $v_{\text{LSR}} \sim 39 \text{ km s}^{-1}$ ). On the NW side, they report broad lines, with most of the emission between  $v_{\text{LSR}} \sim 30\text{--}60 \text{ km s}^{-1}$ .

### 4.5.3 Shell-like UCHIIs

The CORNISH UCHIIs classified as shell-like comprise 5% of the sample and are presented in Fig. 4.12. In many cases, the shape is that of an incomplete ‘diamond-ring’ (i.e. a brighter peak close to the centre of a more

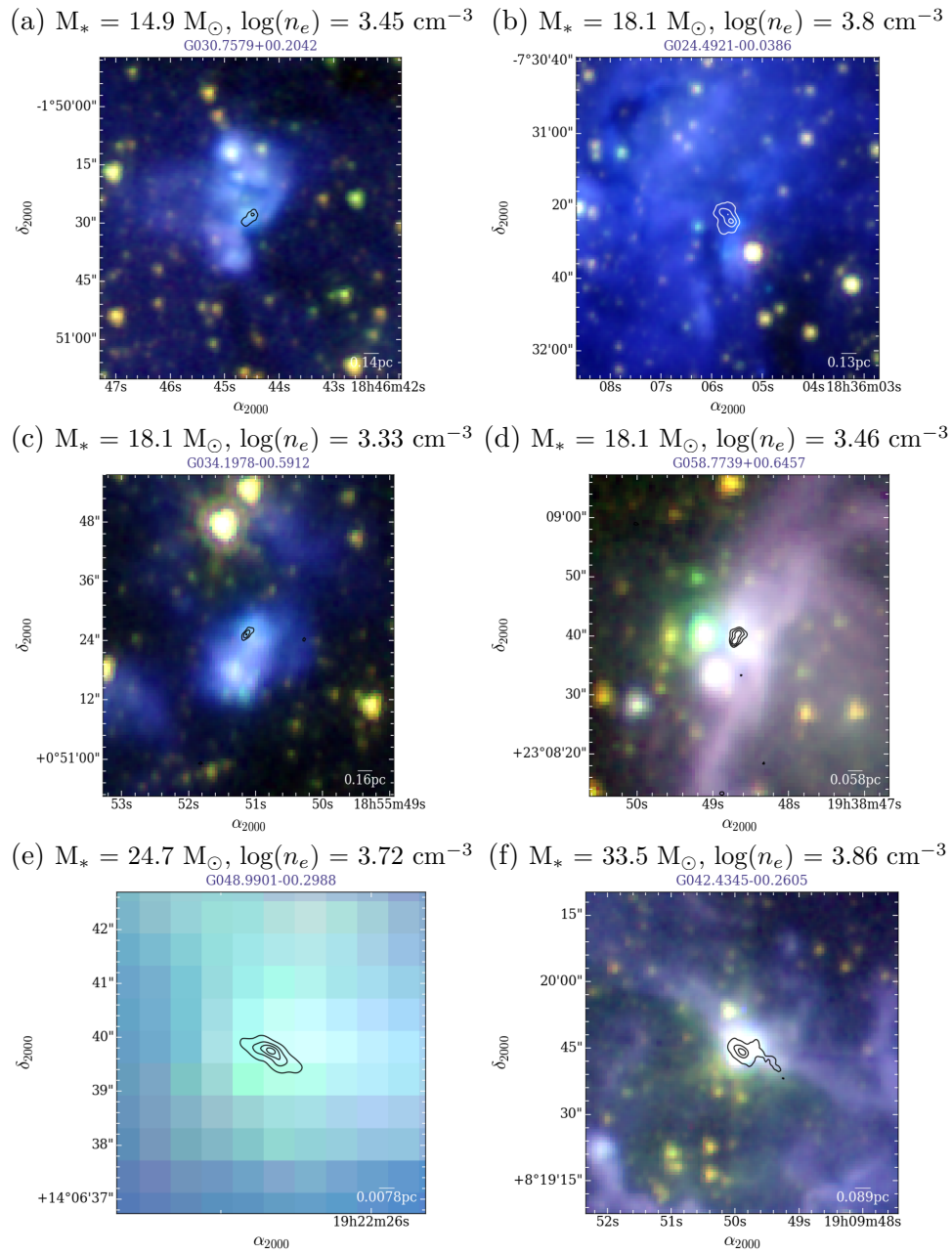


Fig. 4.11 UCHIIs classified as bipolar in the joint classification, ordered by mass of the ionising star. The computed electron density is also shown.

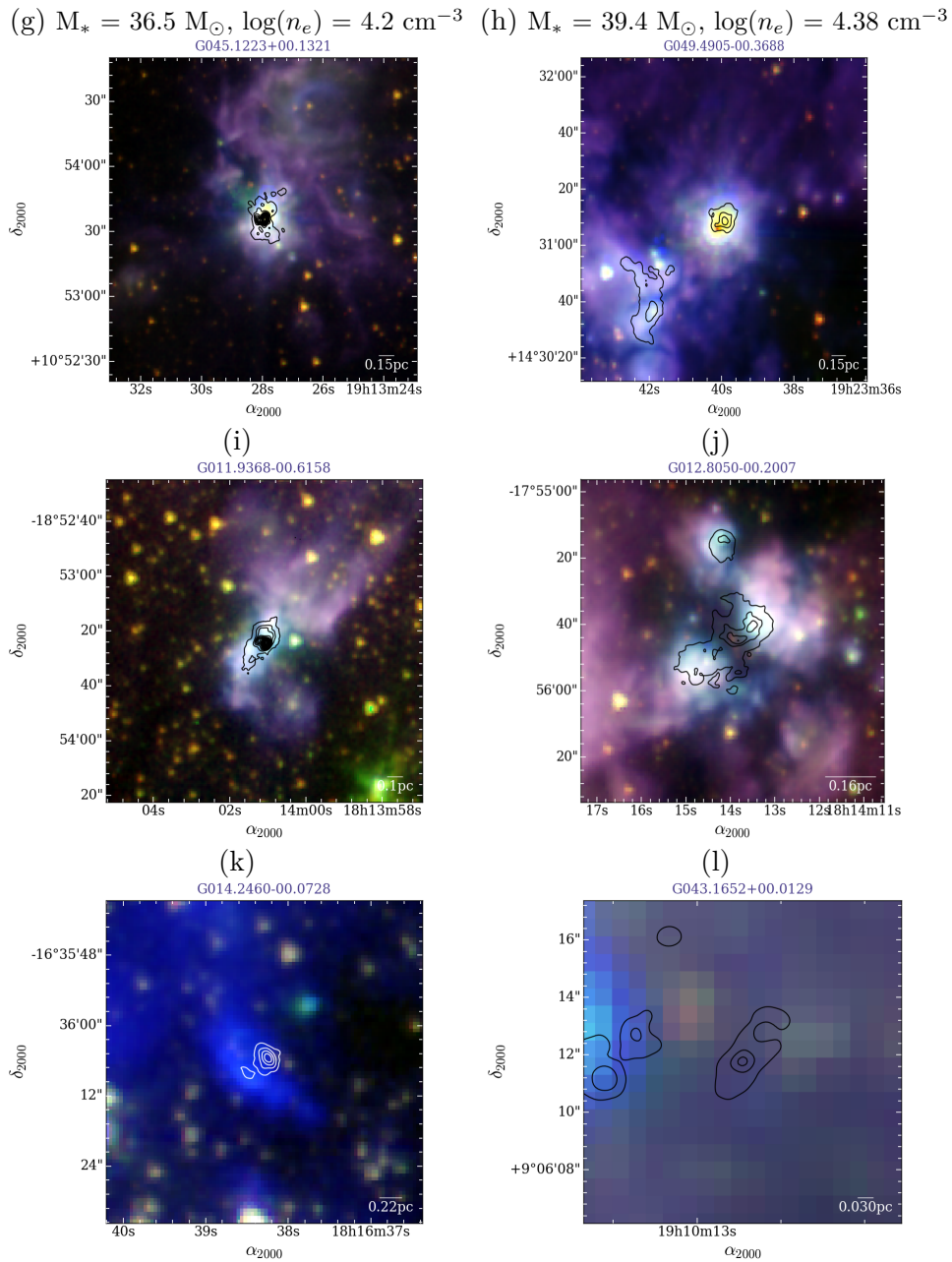


Fig. 4.11 UCHIIs classified as bipolar in the joint classification – continued.

than 50% complete circular arc). Examples are G041.7419+00.0973 (Fig. 4.12c), G021.8751+00.0075 (Fig. 4.12d), and G023.9564+00.1493 (Fig. 4.12f). Such sources could also be highly limb-brightened cometaries. The ionising star is possibly seen in the case of G021.8751+00.0075 (Fig. 4.12d) and G023.9564+00.1493 (Fig. 4.12f).

The JVLA targets G028.2003–00.0494 and G061.7207+00.8630 (Fig. 4.12g and Fig. 4.12h, §3.5) appear as complete, thick shells. G028.2003–00.0494 has an oval shape, and an outer diameter of 0.02 pc. G061.7207+00.8630 is circular and has an outer diameter  $\approx 0.15$  pc. Sewiło et al. [2008] studied G028.2003–00.0494 (G28.20–0.04N in their work) with the VLA at 0.15'' resolution (line+continuum emission at 0.7 cm), and found it to be an expanding shell-like hyper-compact H II region with inner and outer diameter of  $\sim 0.011$  pc and 0.024 pc, respectively. Thick shells<sup>3</sup> cannot readily be explained by the ionisation of a shell/bubble swept-up by the stellar wind (González-Avilés et al. 2005, Lizano 2008). Sewiło et al. [2008] suggest that the detected expansion along the minor axis of G028.2003–00.0494 could be due to a rotating torus around a 28  $M_{\odot}$  object, and the line-broadening along the major axis could be the result of an outflow perpendicular to the line of sight.

#### 4.5.4 Irregular UCHIIs

UCHIIs classified as irregular exhibit the most miscellaneous collection of shapes, with the majority having a multiply-peaked structure (Fig. 4.13). These comprise 14% of the CORNISH UCHII sample – the second largest group after the cometary type.

There is a minority of radio over-resolved/noisy UCHIIs in the CORNISH sample (5%). Over-resolved or noisy irregulars have an overall shape suggestive

---

<sup>3</sup>Where the ratio of the difference between the external and the internal radii to the external radius is close to 0.5. For a thin shell, this ratio  $\ll 1$  [Lizano, 2008].

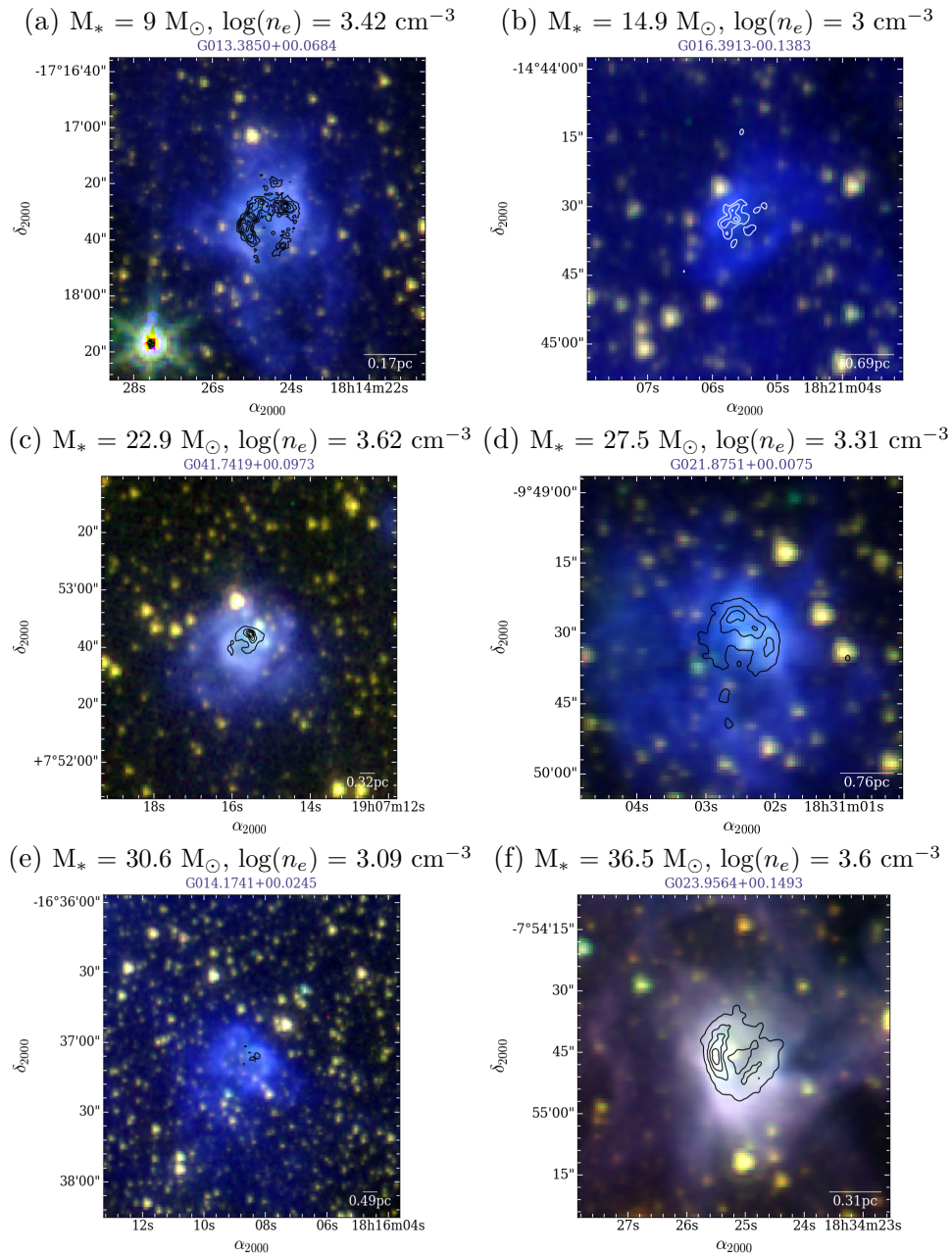


Fig. 4.12 UCHIIs classified as shell-like in the joint classification, ordered by mass of the ionising star. The computed electron density is also shown.

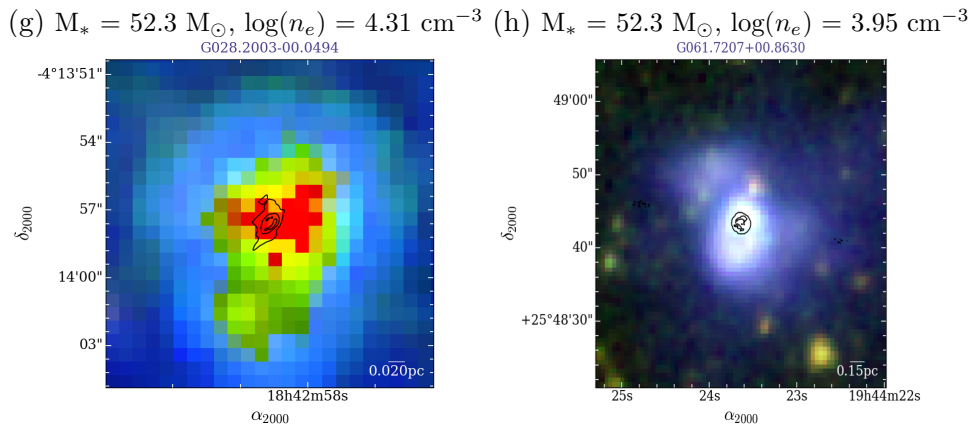


Fig. 4.12 UCHIIs classified as shell-like in the joint classification – continued.

of a single source, but grainy and broken up due to noise/over-resolution in their CORNISH images (where another class could not be assigned during the multi-wavelength inspection). The reason for treating these as a separate group is that they likely comprise more evolved/larger lone UCHIIs, and their observed shape is likely a result of instrumentation/imaging effects rather than due to their nature. Two such UCHIIs could not be assigned a class in the joint classification. These UCHIIs are G018.1460–00.2839 and G031.3959–00.2570. In the case of G018.1460–00.2839, the mid-IR counterpart is partially hidden behind a dust lane and multi-configuration, high-resolution radio observations are required to reliably determine the morphology (Fig. 4.14). G031.3959–00.2570 appears somewhat cometary in MAGPIS, and as either an irregular or a bipolar situated near the edge of a larger H II region (seen in MAGPIS and its associated large PAH bubble in GLIMPSE). These sources were excluded from the results summary in Fig. 4.4.

True multiply-peaked sources – i.e., the images are of good quality, and a common diffuse ‘envelope’ (detected at  $5\sigma$  or more) is seen around two or more emission peaks – are here considered to be ‘genuine’ irregulars. These could contain a close, insufficiently resolved UCHII pair or association, or are the result of irregularities in the environment where they form, which leads to the

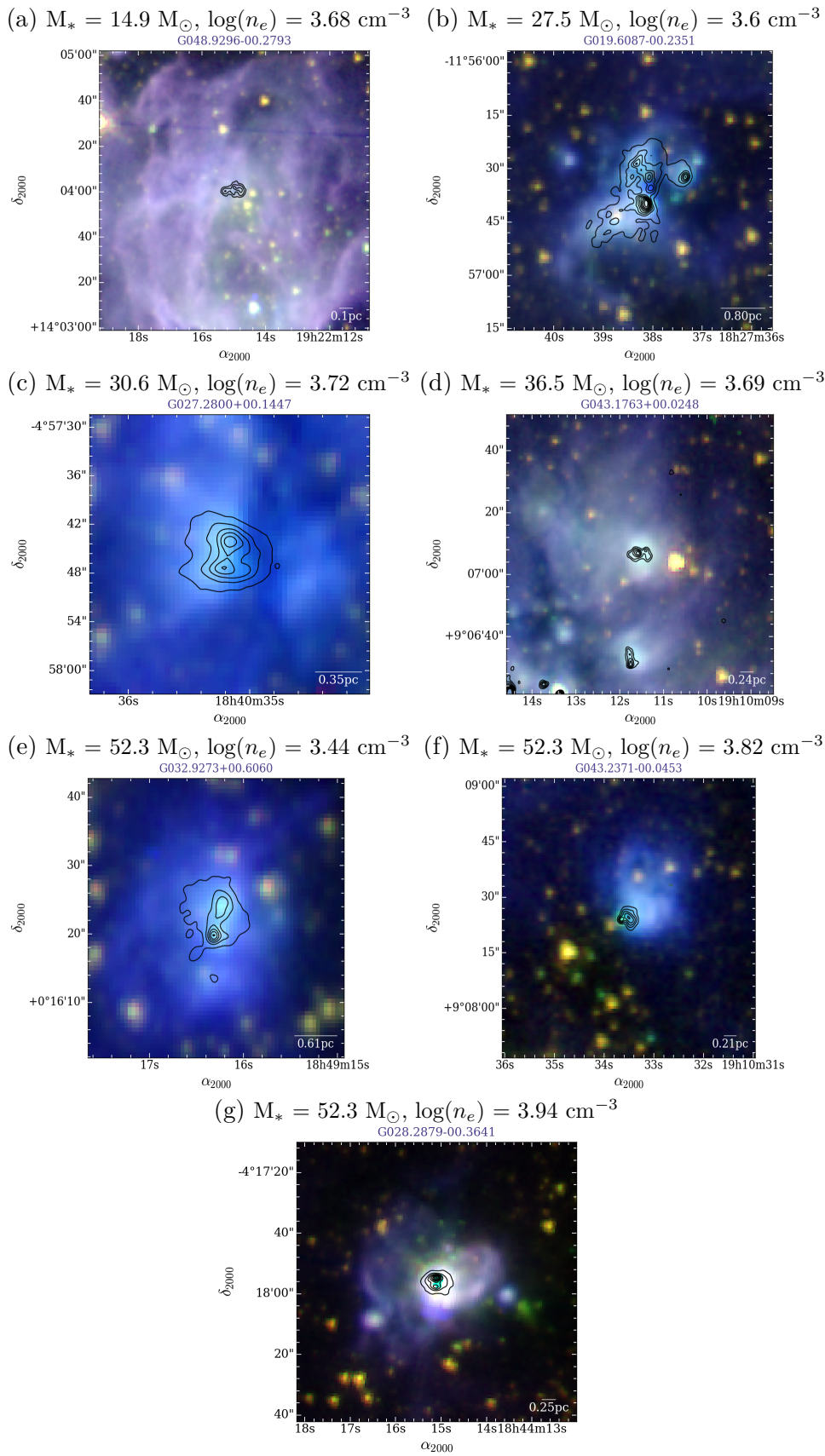


Fig. 4.13 Example UCHIIs classified as irregular in the joint classification, ordered by mass of the ionising star. The computed electron density is also shown.

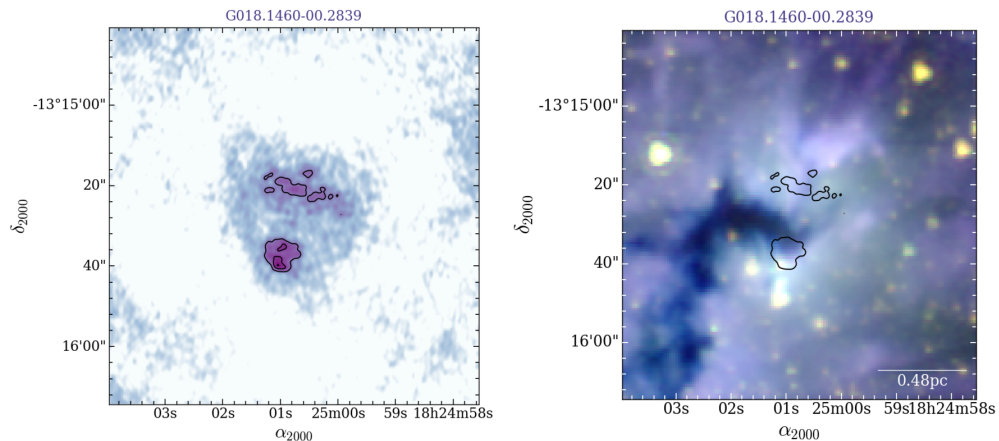


Fig. 4.14 CORNISH and  $3.6+4.5+8.0\mu\text{m}$  GLIMPSE images of the irregular UCHII G018.1460–00.2839. The radio  $5\sigma$  outlines are shown in the GLIMPSE panel. G018.1460–00.2839 is likely a lone UCHII, suffering from noise and over-resolution in the CORNISH image, as well as heavy extinction across its middle caused by a dark lane (seen in the mid-IR). Overresolved irregularly-shaped UCHIIs were excluded from the analysis as their classification requires targeted multi-configuration observations.

highly asymmetric shapes. Such irregulars most often appear as a grouping of point-like sources, or in rare cases some peaks exhibit distinct shapes within the common envelope. Examples for this are G031.0495+00.4697 (possible pair of cometary) and G043.1665+00.0106 (possible association, the south-western peak has a cometary shape), as seen in the JVLA maps (Figs. 3.5 and 3.13).

Such a visual distinction is somewhat subjective and was used to attempt to crudely quantify the number of over-resolved/noisy UCHIIs and the number of multiply-peaked sources with substructure (at the best available resolutions for each UCHII and considering the available multi-wavelength data). Dendrogram analysis<sup>4</sup> is a type of structure-tree analysis which can be applied in future work on a source-to-source basis for multiply-peaked UCHIIs in order to extract information on the observed continuum peaks, such as their brightness and extent. In this way, a better distinction can be made between these two groups.

<sup>4</sup>See e.g. <https://dendrograms.readthedocs.io/en/stable/>.

### 4.5.5 Cometary UCHIIs with ionising star candidates

The vast majority (71%) of the CORNISH UCHIIs were classified as cometary in the joint classification. Parallels to their individual observed shapes can be found in the simulated UCHII grids (of varying mass, density, age, and distance from the parent cloud<sup>5</sup>) by Steggle et al. [2017]. A common feature in some cases is the presence of a bar at the end of the tail (see e.g. G021.3571–00.176, G033.8100–00.1864, G044.4228+00.5377, in Fig. 3.5, and G043.1674+00.0128, in Fig. 3.13). However, the majority of observed cometary shapes have longer, more open tails than the simulated ones.

The Arthur and Hoare [2006] and Steggle et al. [2017] models impose an off-centre location of the star in the density gradient. This location of the massive star ionising the H II region is a feature of these models that is not a verified observational property of the UCHII population as a whole due to the low numbers of confirmed ionising stars. Such a location in the models is appropriate for stars formed at the edge of a molecular cloud core, where expansions in an offset power-law density distribution would occur, rather than in an uniform, spherically symmetric power-law density distribution [Arthur, 2007]. Based on the visual inspection of the larger-scale surroundings, as discussed in §4.6, such a scenario is quite appropriate for the CORNISH UCHIIs.

Candidate ionising stars were identified by visual inspection for the portion of the classified cometary sources with a visible JHK nebula (§2.7.2). The mid- and near-IR images of these UCHIIs are displayed, with overlaid radio contours, in Fig. 4.15. The candidate ionising stars are located just behind the central portions of the arcs of the cometary head. The candidates were selected if they appear as very red point sources in the JHK images and have no bright mid-IR counterpart, to avoid the inclusion of foreground stars, MYSOs, or

<sup>5</sup>All of these parameters were found to affect the simulated morphologies.

Table 4.4 Measurements of  $D_0$  and  $D_{\pi/2}$  – the distances from the star to the edge of the cometary H II region along a direction with polar angle 0 (i.e. between the star and the centre of the cometary head) or  $\pi/2$  (i.e. between the star and the side of the cometary region). The UCHIIs are ordered according to mass of the ionising star (value corresponding to  $L_{\text{bol}}$  matched from Mottram et al. 2011). These are compared to the corresponding values in the UCHII grid in Table 3 in Steggles et al. [2017] for the closest masses after 50 kyr evolution and for initial number densities at the stellar position (‘model’ in the table). Note that the model UCHIIs are all viewed projection angle of  $45^\circ$ , unlike the observed UCHIIs, which have random inclinations.

$M_\star$ ( $M_\odot$ )	$n_e$ ( $10^4 \text{ cm}^{-3}$ )	Name	$D_{\pi/2}$ (pc)	$D_0$ (pc)
14.9	11	G043.8894–00.7840	0.08	0.06
15	12.8	model	0.08	0.07
<18.1*	4.5	G010.6297–00.3380	0.31	0.1
20	3.2	model	0.24	0.19
19.4	9.3	G039.8824–00.3460	0.1	0.09
20	12.8	model	0.15	0.13
30.6	4.6	G019.0754–00.2874	0.17	0.13
30	3.2	model	0.34	0.23
	6.8	G023.7110+00.1705	0.13	0.1
	6.4	model	0.26	0.21
	9.8	G025.3981–00.1411	0.25	0.14
	12.8	model	0.21	0.18
39.4	6.6	G043.1651–00.0283	0.27	0.24
40	6.4	model	0.34	0.24
52.3	2.6	G030.5353+00.0204	0.27	0.24
40	3.2	model	0.44	0.26
	8.5	G029.9559–00.0168 <sup>‡</sup>	0.32	0.21
	6.4	model	0.34	0.24
70.8	4.9	G037.8683–00.6008	0.3	0.18
70	6.4	model	0.48	0.26

\* The bolometric luminosity was adopted from Mottram et al. [2011] – note that it is for the clump as a whole and thus the mass is an upper limit.

‡ Watson et al. [1997] determined a lower limit to the stellar mass of G029.9559–00.0168 of about  $60 M_\odot$ . This is slightly higher than the mass of  $52.3 M_\odot$  matched to the fitted in this work bolometric luminosity of the UCHII.

unrelated sources. This expectation to see the ionising star in this particular off-centre location is based on the location of the star ionising the prototypical cometary UCHII region G29.96 (G029.9559–00.0168 in CORNISH, Fig. 4.15e), as identified by Martín-Hernández et al. [2003]. The authors observed the ionising star directly in the near-IR. Confirming the candidates to be the true ionising stars of these cometary UCHIIs (beyond the scope of this work) would bring further confidence in the results of the theoretical simulations with off-centre stars.

In the bow-shock model [Van Buren et al., 1990] the size of the H II region is the ‘stand-off’ distance between the star and the shock. At this distance, the ram pressure of the stellar wind equals the pressure of the surrounding material. In the context of the champagne-flow model, the stand-off distance is a parameter used to characterise the nebula, and depends on many factors, such as the H II region density and expansion over the stellar lifetime.

The measured stand-off distances ( $D_\theta$ ) for the candidate ionising stars (Fig. 4.15) are presented in Table 4.4.  $D_\theta$  was measured from the star to the edge of the cometary H II region along a direction with polar angle  $\theta$  (i.e. from the star towards the centre of the cometary head) or  $\pi/2$  (i.e. from the star towards the side of the cometary region). The measured  $D_0$  and  $D_{\pi/2}$  are shown in Table 4.4, alongside a comparison to the distances reported by Steggle et al. [2017] for simulated UCHIIs with comparable densities and masses of the ionising stars.

It should be noted that any comparison between the observed and model parameters and morphologies is crude. All model values from Steggle et al. [2017] were obtained for 50 kyr evolution, whereas the sizes of real UCHIIs will change at different ages as the region expands with time. All model UCHIIs are viewed at a projection angle of  $45^\circ$ , unlike the observed UCHIIs, which have random inclinations (and the average inclination for the sample is  $60^\circ$

assuming a flat distribution, see §4.4.2). The quoted model densities are the initial number densities at the stellar position, whereas the computed in §2.6 densities are the current average electron densities of the CORNISH UCHII regions.

It is clear from Fig. 4.15 that the measured  $D_0$  and  $D_{\pi/2}$  for the observed cometaries with ionising star candidates are approximations – the sources naturally exhibit different degrees of asymmetry from the model cometary shapes. The cometaries shown in Figures 4.15b, 4.15h, and 4.15j – G019.0754–00.2874, G039.8824–00.3460, and G043.8894–00.7840 – are the most symmetric from the group and thus allow a closer comparison. The comparison is better for the  $D_{\pi/2}$  parameter than for  $D_0$  – this is expected as the projected distance to the cometary edge is not as affected by the inclination as the projected distance to the head.

Despite the limitations of this comparison, the observational results compare reasonably well with the theoretical estimates. This could be indicating that the UCHII sizes change less with time than they do with the other parameters, and that comparing initial model number densities to the current UCHII electron density is not a poor assumption.

### **Spectral types of the candidate ionising stars**

The spectral types of the candidate ionising stars presented in Fig. 4.15 were estimated from three methods, as shown in Table 4.5. To check whether the spectral classification of these stars is consistent with massive stars, the apparent K-band magnitudes from the UKIDSS point source catalogue were used [Lucas et al., 2008]. The apparent magnitudes (extinction-corrected using the computed for the nebulae  $A_K$  values, see §2.7.2) were converted to absolute K-band magnitudes (with the distances in Appendix B). Table 1 from Mottram et al. [2011] was used to read off the spectral types from the absolute magnitudes.

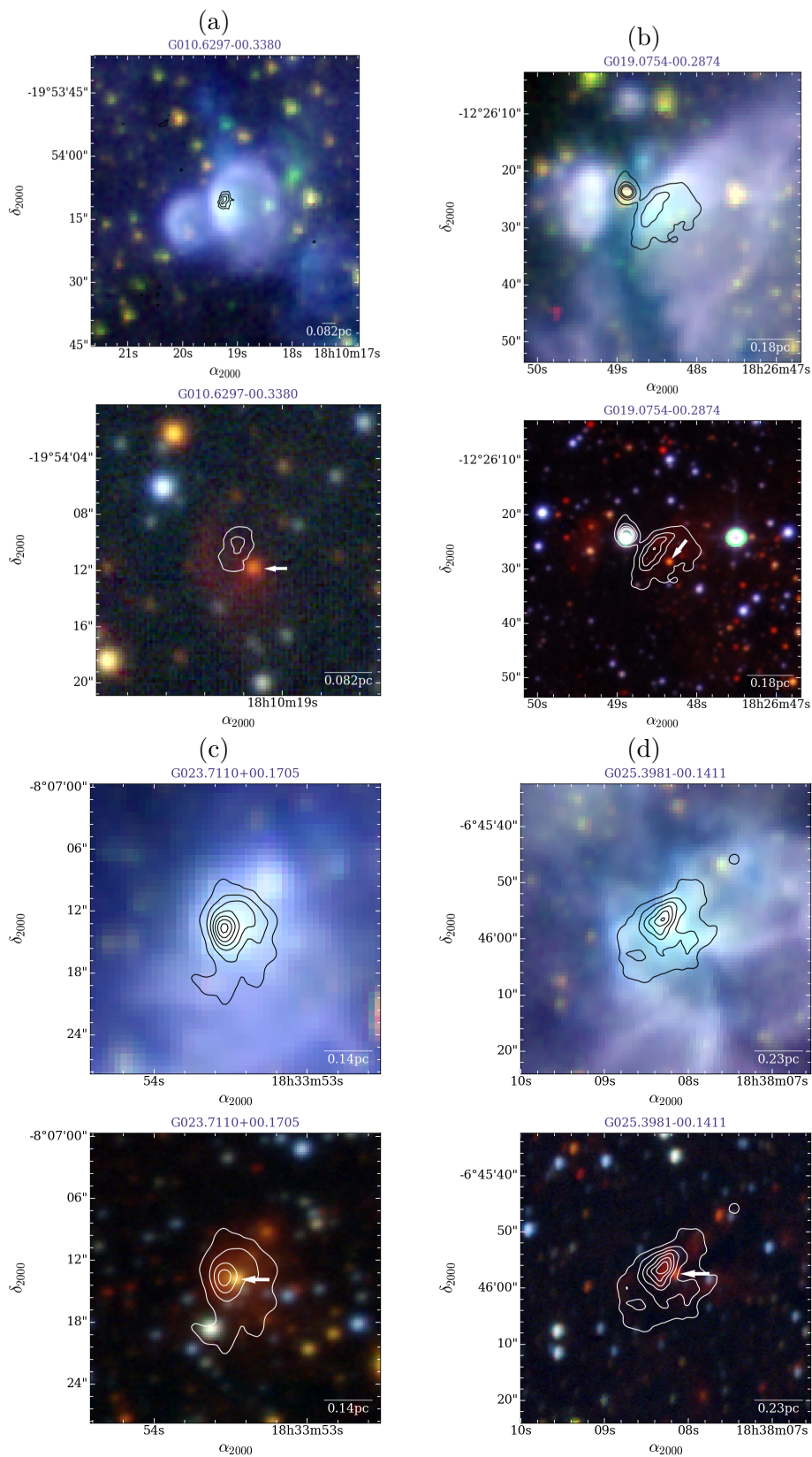


Fig. 4.15 UCHIIs classified as cometary in the joint classification. The JHK counterpart is shown below each panel, with an arrow indicating the candidate ionising star.

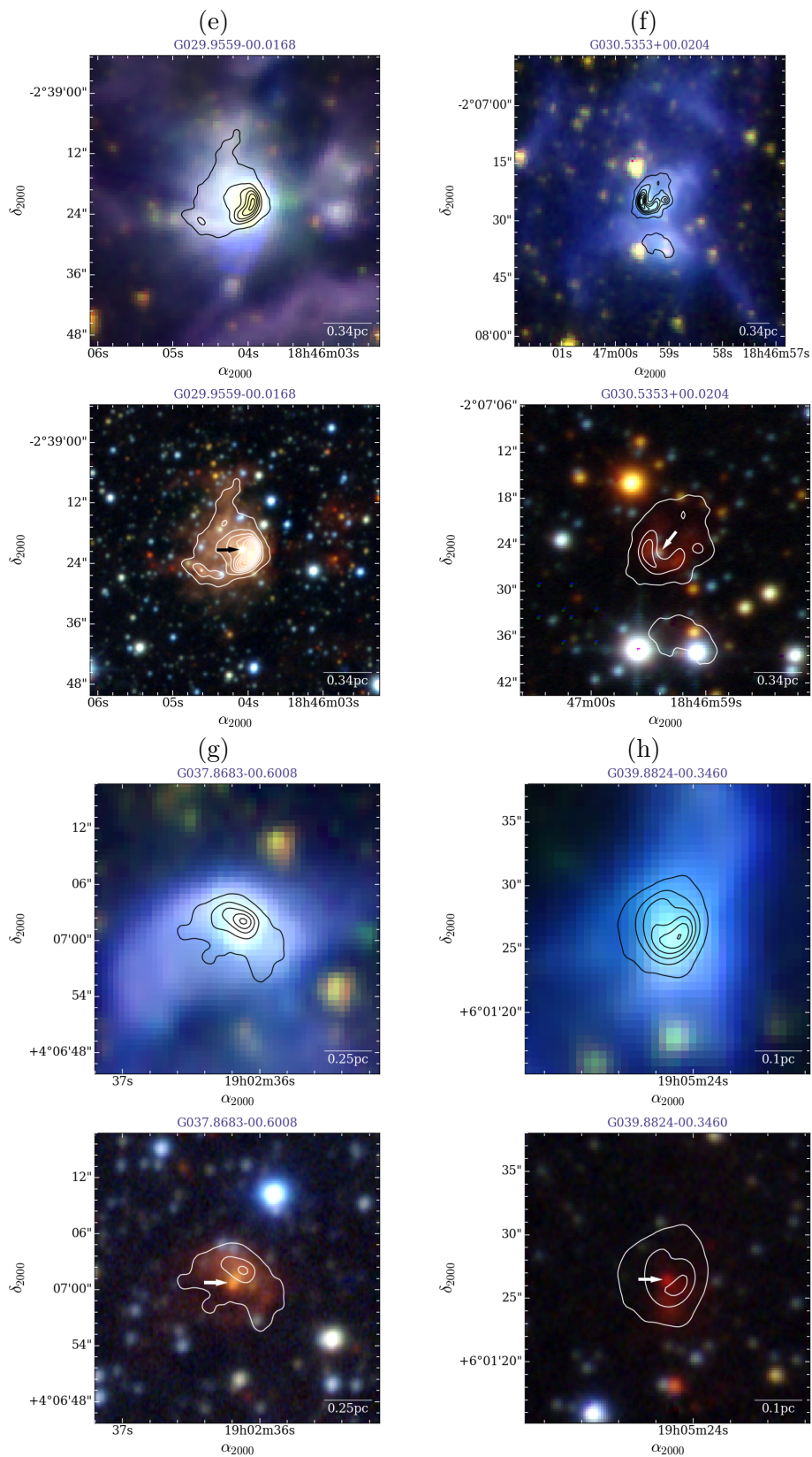


Fig. 4.15 UCHIIs classified as cometary in the joint classification. The JHK counterpart is shown below each panel, with an arrow indicating the candidate ionising star – continued.

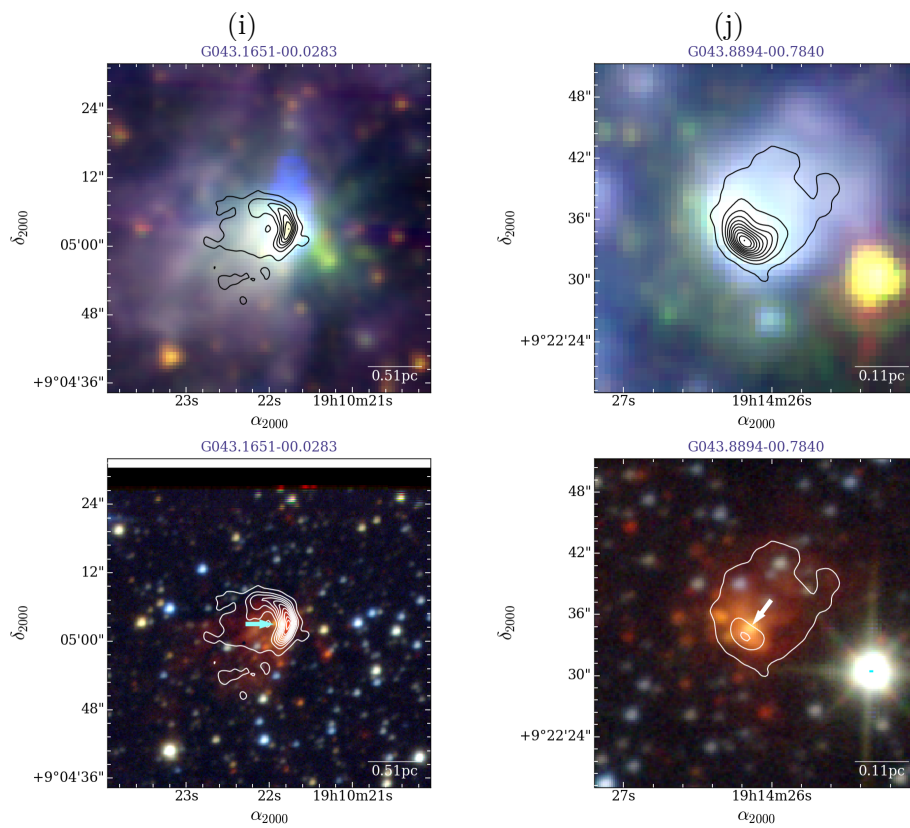


Fig. 4.15 UCHIIs classified as cometary in the joint classification. The JHK counterpart is shown below each panel, with an arrow indicating the candidate ionising star – continued.

This was done by first converting the Mottram et al. [2011] absolute visual magnitudes  $M_V$  to  $M_K$  using the intrinsic  $V - K$  colour for MS stars from Table 3 in Koornneef [1983]. All candidate ionising stars are consistent with OB stars.

The spectral types obtained from the computed UCHII parameters (§2.6) are also included in Table 4.5. These are the spectral classes obtained from  $L_{\text{bol}}$  and  $N_i$ . The fitted bolometric luminosities of the UCHII were matched to spectral types using Mottram et al. [2011], as discussed in §4.4.2. In the case of the  $N_i$  estimates, the spectral type was read off from Vacca et al. [1996].

The differences in the spectral classifications are likely due to the uncertainties and limitations associated with using the different methods. As discussed in §2.6, the computed Lyman continuum fluxes (and hence the matched spectral types) should be treated as lower limits. The models used in the SED fitting to estimate  $L_{\text{bol}}$  do not take into account additional sources of dust heating in the H II region, such as Lyman- $\alpha$  (§2.8). The stellar atmosphere models adopted by Vacca et al. [1996] for their Lyman continuum flux estimates suffer from the limitations associated with most non-LTE models, which predict higher effective temperatures than empirical estimates (see the discussion by e.g. Penny et al. 1997). The uncertainties associated with different methods to obtain the extinction are discussed in §2.7.2. The main difficulty when measuring the nebular extinctions was the accurate subtraction of the stellar contamination in the busy, diffuse environments. Other factors could affect the K band magnitude. There could be hot dust contribution to the K band in some cases, or contribution from unresolved clusters of stars. In both of these cases, an earlier spectral type would be assigned.

Table 4.5 Estimated spectral types of candidate ionising stars from three methods. These are shown in the last three columns. The distances and computed nebular K-band extinctions are also included (the first two columns).

CORNISH	$d_h$ (kpc)	$A_K$ (mag)	$m_K$ (mag)	$M_{K,0}$ (mag)	Sp. type* $M_{K,0}$	Sp. type $^\ddagger$ $L_{bol}$	Sp. type $^\diamond$ $\log N_i$
G010.6297–00.3380	4.95	$1.9 \pm 0.46$	13.91	–1.5	B1	–	B3
G019.0754–00.2874	4.6	$1.54 \pm 0.10$	12.61	–2.2	B0	O6.5	B0.5
G023.7110+00.1705	6.5	$2.12 \pm 0.13$	12	–4.2	O4	O6.5	B0.5
G025.3981–00.1411	5.6	$5.29 \pm 0.54$	19	–0.1	B3	O6.5	O8
G029.9559–00.0168	7.4	$2.33 \pm 0.07$	10.31	–6.4	O2	O4	O6.5
G030.5353+00.0204	11.4	$2.17 \pm 0.08$	13.18	–4.3	O4	O4	O8.5
G037.8683–00.6008	10	$2.7 \pm 0.25$	12.76	–4.9	O3	O3	O9.5
G039.8824–00.3460	9.1	$4.39 \pm 0.61$	14.70	–4.5	O4	O9	O9.5
G043.1651–00.0283	11.1	$4.51 \pm 0.13$	14.33	–5.4	O2	O5	O5
G043.8894–00.7840	4.4	$2.83 \pm 0.12$	12.09	–4	O5	B0	B0

\* Obtained from  $M_{K,0}$  using the intrinsic  $V - K$  colour for MS stars from Table 3 in Koornneef [1983] and Table 1 in Mottram et al. [2011].

$^\ddagger$  The fitted bolometric luminosity was matched to spectral types using Mottram et al. [2011].

$^\diamond$  Match to the spectral type corresponding to MS stars using Vacca et al. [1996].

## 4.6 Findings of the extended joint classification

The results of the extended classification, as described in Table 4.1, are presented in this section.

### 4.6.1 Cometary morphologies at all studied scales

With the extended joint classification, common observed patterns in the immediate environment (within a square arcminute) of the CORNISH UCHIIs were quantified. The most common, cometary morphology, is recurrent at all studied scales, from the best available subarcsecond resolution JVLA images to the extended structures in the mid-IR. The smallest classified UCHIIs are cometary (Fig. 4.7). Many representatives of the cometary type are found at the head of a larger, mid-IR cometary source. Figure 4.16 shows the portion of the cometary CORNISH UCHIIs situated at the head of larger mid-IR cometary nebulae (42 UCHIIs, or  $\sim 28\%$  of all cometary), as well as those radio cometary which were found to have a mid-IR counterpart of the same morphology, tail direction, and comparable size (49 UCHIIs, or  $\sim 33\%$ ). A total of 22 cometary ( $\sim 15\%$ ) belong to both subsets – the radio and mid-IR counterparts compare well with each other and are at the head of a larger mid-IR cometary nebula (i.e., they all likely belong to the same source). For 20 cometary, the tail direction of the mid-IR counterpart is unknown in the mid-IR (e.g. in the case of a compact mid-IR counterpart to the resolved radio source), or the direction of the radio and mid-IR counterparts is not the same (i.e., they likely do not belong to the same source).

There are numerous instances of cometary regions found spatially close to each other, which are likely to be related/coevolving (due to the low statistical

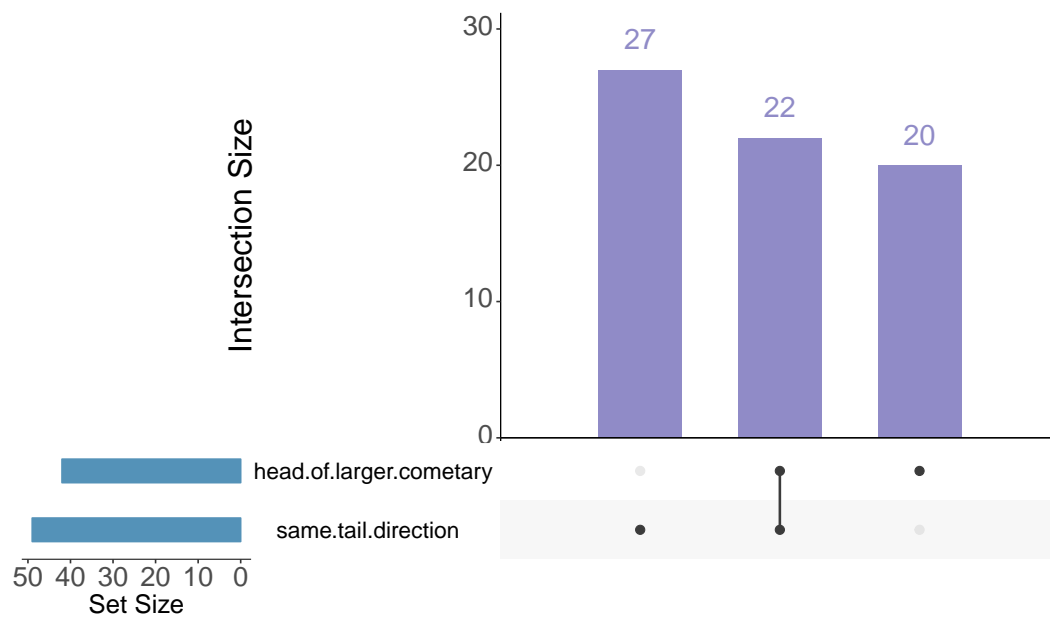


Fig. 4.16 Intersections of commonly observed categories associated with the cometary CORNISH UCHIIs. The leftmost subplot presents the total subset sizes. In this simple case, the histogram is equivalent to a Venn diagram showing the subset in common between the two groups – 22 UCHIIs in common between the two groups containing 49 and 42 UCHIIs, respectively. The UCHII count belonging to each intersection between categories is shown above each corresponding bar. This visualization was produced with the UpSetR package by Lex et al. [2014].

chance for such a coincidental alignment) and therefore could have affected each other's morphology. About 14% of cometaries are in a 'radio double' (as described in Table 4.1). Examples of this are G019.0754–00.2874 (Fig. 4.15b) and G030.5353+00.0204 (Fig. 4.15f). A further 4% could be close, just-resolved pairs (e.g. G025.8011–00.1568, G026.8304–00.2067, G031.0495+00.4697, G032.4727+00.2036, G043.1520+00.0115, see Fig. 3.5). As discussed by Cyganowski et al. [2003], studying double cometary systems is important, as these provide a good opportunity to investigate the relative motion of the H II regions, their internal velocity structures, as well as their motion w.r.t. the surrounding material. While a velocity study is beyond the scope of this thesis, the statistic of double and multiple systems, for cometary and other regions, is a possible foundation of future exploration. The significant fraction of such sources indicates that theoretical models incorporating the formation of UCHII pairs and multiples are needed.

### 4.6.2 Environment and multiplicity

The statistics of the CORNISH UCHII regions and their extended surroundings, as classified from the joint radio-IR images, is consistent with the hierarchical structure hypothesis [Kim and Koo, 2001, 2002, 2003]. A summary of the results is shown in Table 4.6. A dark lane is situated ahead of the UCHII region for 14% of the sample. The presence of dense gas ahead of the UCHII is consistent with a density gradient and champagne flow picture (see e.g. Wendker et al. 1983). About 45% of all classified CORNISH UCHIIs are part of a larger mid-IR bubble/shell, or bipolar source, and at least 23% are found immediately ahead of a larger radio-detected H II region (based on visually examining CORNISH, MAGPIS 6 cm and 20 cm images and thus generally not considering extended scales exceeding 1').

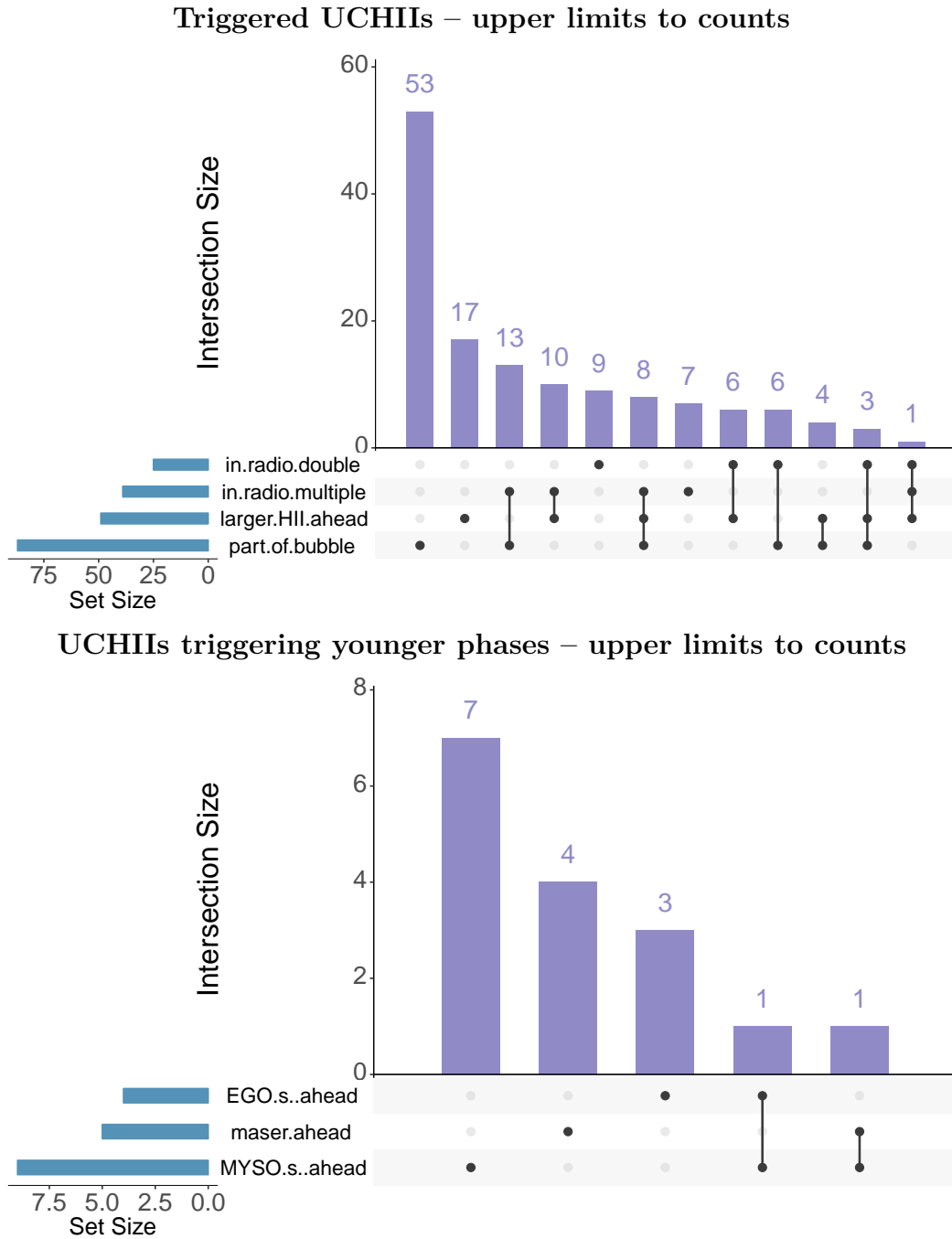


Fig. 4.17 Intersections of some of the categories presented in Table 4.6 to look for triggered/trigging CORNISH UCHIIs (top/bottom panel, respectively). The leftmost subplot presents the total subset sizes. The histograms shows the frequency of the different types of intersections between the sets. The order is by decreasing frequency of intersections between sets. UCHIIs belonging to only one of the included categories are also shown. This visualization was produced with the UpSetR package by Lex et al. [2014].

Table 4.6 Fractions of classified CORNISH UCHII regions belonging to the additional categories assigned alongside a morphological class, as defined in Table 4.1. Note that these categories overlap.

Category	Count	Fraction (%)
Part of bubble	87	41
Head of larger cometary	50	23
Middle of larger bipolar	8	4
Larger H II region ahead	49	23
In radio double	25	12
In radio multiple	39	18
Dark lane ahead	29	14
Dark lane across	16	7
<b>For cometary sources:</b>		
Same tail direction	49	33
<b>Cross-matched:</b>		
EGO(s) ahead	4	2
MYSO(s) ahead	9	4
Maser(s) ahead	5	2

Multiplicity of the UCHII regions is an important characteristic of the sample (and thus likely of the general UCHII population) as a whole, as 30% of the CORNISH UCHII regions are part of a double or multiple UCHII association. The UCHII morphologies in the CORNISH/JVLA maps in 16% of the sample suggests internal multiplicity (i.e. possible pairs/multiples within a common  $5/7\sigma$  envelope).

The vast majority of the CORNISH UCHII regions – 74% – belong to at least one of the categories in Table 4.6 associated with possible sequential massive star formation. Statistics on the intersections between the categories of sources from the extended joint classification provides information to select candidate triggered UCHII regions, as shown in Fig. 4.17. The top panel of Fig. 4.17 shows a break-down of the counts of the UCHII regions that could have been triggered by another source, such as a larger H II region. Using the histogram, it was computed that close UCHII pairs or UCHII associations are found ahead/at the edge of a larger H II region/bubble in  $\sim 15\%$  of the classified sample. For

7% of the classified UCHIIs, the larger H II region is seen in the radio (in the CORNISH/MAGPIS maps) while its encompassing PAH bubble is seen in the mid-IR image. It should be noted that the visual selection discriminates against any possible cases where the triggered UCHII and triggering source are aligned along the line of sight. Cases where the UCHII could be triggering younger MSF phases are discussed in the next section.

### 4.6.3 Signposts of younger MSF stages

Younger signposts of massive star formation such as MYSOs, EGOs, and masers are likely evidence for feedback and triggering (§4.2.3). Matches to the RMS MYSO catalogue [Lumsden et al., 2013] and the Cyganowski et al. [2008] EGO catalogue reveal that 9 UCHIIs have MYSO matches, and 9 more have EGO matches. Only sources not coinciding with the UCHII extents but within 0.5 pc of their outer (radio) edges were considered, to avoid any misclassified UCHIIs. Five UCHIIs (three cometary and two bipolars) have methanol masers within their radii of influence in the covered by the Arecibo GPS area:  $32.5^\circ < l < 53.7^\circ$ ,  $|b| < 0.41^\circ$  (see §4.1 and Pandian et al. 2007)<sup>6</sup>.

A break-down of the intersections between the matched sets of EGOs, MYSOs and methanol masers is shown in the bottom panel of Fig. 4.17. G034.4032+00.2277 (a cometary UCHII) has both a MYSO and an EGO within its radius of influence, and G048.9901–00.2988 (a bipolar UCHII) has a MYSO and methanol maser.

The extended classification only provides an upper limit to the number of triggered sources (be it UCHIIs triggered by larger H II regions or younger sources triggered by nearby UCHIIs). The methodology summarised in Table 4.1 can be further developed in future projects depending on aims. For example,

<sup>6</sup>For reference, CORNISH covers  $10^\circ < l < 65^\circ$ ,  $|b| < 1^\circ$ , and the scale height of UCHIIs is  $|b| < 0.6^\circ$ .

the CORNISH dataset is large and measuring precise respective H II region orientation in groups of sources (important when looking for candidate triggered H II regions) is not practical, but it can be readily done for individual studies of candidates of interest that were selected through the intersecting sets.

## 4.7 Conclusions

In this chapter, a new classification methodology was introduced to incorporate the latest available coordinated multi-wavelength and high-resolution data, building upon the standard radio classification scheme introduced by Wood and Churchwell [1989b] and modified by De Pree et al. [2005].

The morphology distribution of 213 UCHII regions in the CORNISH survey was obtained. Cometary UCHII regions were found to be the predominant morphological type, comprising 71% of the resolved sample. A larger relative fraction of cometary UCHII regions was found in the higher resolution set in comparison to the lower resolution set – 74% at 0.3" compared to 64% at 1.5". In conjunction with the physical properties associated with the morphological groups, this indicates that the observed fraction of cometary UCHII regions likely depends on age. The fraction of cometary UCHII regions found in the CORNISH survey is much larger than in the previous, radio-only, classifications, where more spherical or shell-like than cometary UCHII regions were found. The CORNISH sample has the advantage of being a large, unbiased sample of confirmed UCHII regions, whose properties are expected to be representative of the Galactic UCHII population as a whole.

The electron density-physical size relationship exhibited by the CORNISH UCHII regions suggests that the same main mechanisms are responsible for the confinement of the observed different morphological types. This is in agreement

with De Pree et al. [1997a], and when obsolete categories are not considered, also with the findings of Kurtz et al. [1994].

The distributions of Lyman continuum fluxes with distance for spherical and shell-like UCHIIs, as well as their numbers, fit a scenario where these classes are cometaries observed along their symmetry axes, and at different luminosities and/or distances.

Ten candidates for stars ionising cometary UCHII regions were identified, and their stand-off distances were measured. The results were found to be in good agreement with the respective values for the theoretical counterparts, selected from a distribution of densities and masses of the ionising star simulated by Steggle et al. [2017].

The new classification scheme could be applied to future large-scale UCHII region studies, which will take advantage of the available high-resolution, multi-wavelength data. The joint classification methodology minimises the need for time-consuming multi-configuration radio observations to determine the morphology. The extended joint classification was developed in attempt to identify the common patterns in the immediate surroundings of the CORNISH UCHII regions, and to quantify candidate triggered sources. The results of the extended classification supply a rich resource for future studies testing the initial conditions of the massive star formation process and for tests of hydrodynamical models of massive star formation. It will be particularly useful for comparison to models of multiple systems and the role of feedback and triggering in massive star formation.

# Chapter 5

## X-ray view of UCHIIs

### 5.1 Introduction

Probing the OB stars ionising H II regions is a challenging task. Adaptive optics imaging is required to convincingly distinguish the ionising star and the nebula in the near-IR (see e.g. Alvarez et al. 2004). As discussed in §1.2.5, X-rays can overcome the large column densities around newly-formed massive stars and supply information on the innermost region and even the ionising star itself, through detecting the direct effects of its stellar wind. Such effects could be traced by point-like X-ray emission, which is typically seen in more evolved H II regions, and is likely caused by shocks within a radiatively-driven stellar wind. Interactions with the surrounding nebula are another possible origin in the case of younger phases. Diffuse emission is typically seen on larger scales, associated with clusters of massive stars exciting a large complex. The diffuse X-ray emission likely results from the interaction between the stellar winds and the H II region – hard X-rays can reach the neutral material just outside the nebula and partially ionise a layer of it [Hoare et al., 2007].

High-resolution and high positional accuracy X-ray data can help pinpoint the extent and origin of the X-ray emission within massive star-forming regions.

Spectral analysis can reveal the dominant mechanism of X-ray production coincident with H II regions.

Fitting standard models to X-ray spectral data gives an independent estimate for the hydrogen column density  $N_{\text{H}}$ , which can be compared to the typical measured values from IR and other studies for low- and high-mass SFRs. For example, in Bihr et al. [2015], the measured H I column densities for GMCs exceed by an order of magnitude the ones found for low-mass regions. As well as this, a value for  $k_{\text{B}}T$  can be fitted to determine whether the source is spectrally hard ( $k_{\text{B}}T > 2\text{keV}$ ) or soft ( $k_{\text{B}}T < 2\text{keV}$ ). In the case of UCHIIs, the X-ray spectra are expected to be thermal and therefore should be fitted well by models similar to the prototypical UCHII G29.96 – an absorbed collisionally- or photo-ionised thermal plasma [Charles and Seward, 1995]. If a power law is required for a good fit, this could be evidence of an underlying non-thermal source (such as an X-ray binary) within the region from which the spectrum was extracted.

In this chapter, the location, extent, and X-ray to bolometric luminosity ratios of counterparts to CORNISH UCHII regions are investigated, through high-resolution, high-positional accuracy data from the latest *Chandra* catalogue and database. Results from spectral modelling of three X-ray associations with sufficient counts in their *XMM-Newton* spectra are also presented and discussed.

## 5.2 The new *Chandra* Source Catalog 2.0

With their sub-arcsecond on-axis point spread function [Evans et al., 2010; Weiskopf et al., 2000], comparable with the sizes of the most compact CORNISH UCHII regions, the latest *Chandra* X-ray data<sup>1</sup> are suitable to look for X-ray associations to the CORNISH UCHII regions. *Chandra* provides resolution of

---

<sup>1</sup><http://cxc.harvard.edu/csc2/>

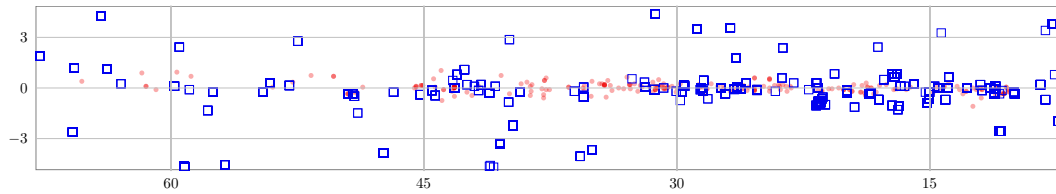


Fig. 5.1 Galactic latitude vs galactic longitude plot in degrees of the CORNISH UCHIIs (red dots) and the *Chandra* sky coverage of the GLIMPSE region. Blue squares mark the FOV around each *Chandra* pointing centre.

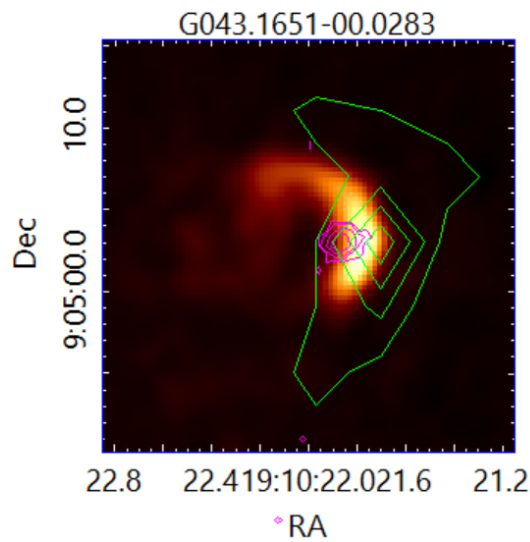


Fig. 5.2 Comparison between the *Chandra* (pink contour) and *XMM-Newton* (green contour) X-ray detection corresponding to G043.1651–00.0283. The resolution of *XMM* is  $\sim 6''$ ; it is  $\sim 0.5''$  for *Chandra*, and  $1.5''$  for the shown CORNISH image.

$\lesssim 0.5''$  (PSF at FWHM) and a half-power diameter (HPD)  $\lesssim 1''$ , as measured during ground calibration [Weisskopf et al., 2000]. The on-board instruments of the *Chandra* X-ray observatory are the Advanced CCD Imaging Spectrometer (ACIS, Bautz et al. 1998) and the High Resolution Camera (HRC, Murray et al. 2000). The effective pixel sizes of the ACIS and HRC detectors on the sky are  $\sim 0.5''$  and  $\sim 0.13''$ , respectively. Out of the two instruments, ACIS provides better spectral energy resolution, whereas HRC provides higher spatial resolution of  $\sim 0.4''$ . The average positional error of the *Chandra* data is  $0.2''$  on-axis, increasing to  $\sim 3.5''$  at an off-axis angle of  $\sim 14'$  for weak ( $\sim 20$  counts) sources [Evans et al., 2010]. The positional uncertainty is generally  $<1''$  (95% uncertainty circle) and is energy-independent for significant sources, even at an off-axis distance of  $10'$  [Civano et al., 2016].

The good positional accuracy of *Chandra* allows a cross-match with the CORNISH UCHII sample using the radio source angular size (and corresponding error) as the matching radius. A search was performed around the *Chandra* pointing centres, to check the Galactic plane coverage, as shown in Fig. 5.1. The pointing centres and tile sizes are to scale on the sky plot, and the CORNISH UCHII regions are plotted as red dots with exaggerated size for clarity. Many CORNISH UCHIIs are in the FOV.

At the beginning of this project, no CORNISH counterparts were found from cross-matching to the previous *Chandra* Source Catalog (CSC) 1.1. Visual inspection of several X-ray fields covering CORNISH UCHII regions showed that often data products were extracted from the X-ray images only for the target source of any given observation. This was the case for the cometary region G043.1651–00.0283, which has a coincident source in the *Chandra* images and also has a lower-resolution *XMM-Newton* counterpart (Fig. 5.2). There could be more instances of X-ray emission from UCHII regions that were missing

from the source catalogue at the time due to not having been extracted rather than not having been detected.

In 2018, the new *Chandra* Source Catalog 2.0 is undergoing a rolling release (with the latest data added on 13/11/2018)<sup>2</sup>. This catalogue contains sources extracted from ACIS and HRC<sup>3</sup>. The latest release builds up on the previous one by including more (previously unextracted and/or fainter) sources from the existing *Chandra* data<sup>4</sup>. This is achieved by stacking fields, extracting sources and spectra, conducting quality checks for all bands – the ACIS broad (0.5-7 keV), hard (2-7 keV), medium (1.2-2 keV), soft (0.5-1.2 keV) and ultrasoft (0.2-0.5 keV) energy bands, and fitting spectra with standard absorbed thermal, blackbody, and power-law models. This is done for all spectra with enough counts by adopting standard fitting parameters such as Galactic H I column densities and  $k_B T$  values, depending on the type of model. Only results from the best fits are included in the released catalogue table. The ranges 0.1-0.5 keV and 7-10 keV are excluded in the fits, as those parts of the *Chandra* spectra have much higher degrees of uncertainty due to the technical specifications of ACIS (the point spread function is of poor quality.).

Spectral hardness ratios between the hard, medium, and soft bands are included in the catalogue as a proxy for detailed spectral fitting. They serve as an approximate measure of the spectral shape, to allow categorising weak sources ( $< 150$  net background-subtracted counts in the energy range 0.5-7.0 keV). The hardness ratio of any two bands with fluxes  $A$  and  $B$  are computed as  $(A - B)/(S + M + H)$ , where  $S + M + H$  is sum of the exposure-corrected fluxes detected in the soft, medium, and hard energy bands.

---

<sup>2</sup>See [http://cxc.harvard.edu/csc2/processing\\_status.html](http://cxc.harvard.edu/csc2/processing_status.html).

<sup>3</sup>The HRC results contain the full *Chandra* energy range (0.1-10 keV), but none of the UCHII counterparts presented in this chapter have been observed with this instrument.

<sup>4</sup>The data are from 2014, gathered over an 8-year observing period.

Table 5.1 Chandra ACIS X-ray counterparts to CORNISH UCHIIs – summary of properties. The cross-match separation is included. The source region aperture off-axis angle  $\theta$  is the mean value from all stacked observations. The X-ray luminosity was computed from the CSC2.0 catalogued broad-band flux (0.5-7 keV), and  $L_X$  denotes the absorbed luminosity. The fitted bolometric luminosities from §2.8 were used to compute  $L_X/L_{\text{bol}}$ . The bolometric luminosity of WR 121a was adopted from Table 2 in Anderson et al. [2011]. The spectral hardness ratios (hard-soft, hard-medium, and medium-soft) from the CSC2.0 catalogue are also included. The extinction  $A_V(H - K)$  towards the UCHIIs was computed in §2.7.2 and converted to hydrogen column densities  $N_H$  using the average ratio of  $2.08 \times 10^{21} \text{ cm}^{-2} \text{ mag}^{-1}$  for the Galaxy [Zhu et al., 2017]. Note that  $L_{X,0}$  and  $\log(L_{X,0}/L_{\text{bol}})$  are absorption-corrected using  $N_H$ .

CORNISH	<i>Chandra</i> 2CXO	Sep. (")	$\theta$ (')	S/N	$L_X$ ( $10^{31}$ erg s $^{-1}$ )	$\log(L_X/L_b)$	HS	HM	MS	$N_H$ ( $10^{22}$ cm $^{-2}$ )	$L_{X,0}$ ( $10^{32}$ erg s $^{-1}$ )	$\log(L_{X,0}/L_b)$
G011.1104–00.3985	J181131.9–193042 $\ddagger$ $\star$	1.04	4.13	5.6	9.4	–7.3	1	1	1	>6.74	<6.9	<–6.4
G012.8050–00.2007	J181413.9–175538 $\square$	6.54	11.35	7.8	8.7		0.9	1	–1	5.72	7.6	
G018.1460–00.2839	J182501.1–131544 $\square$	18.37	7.73	5.6	21.9	–5.3	1	0.8	1	1.99	37.3	–4.1
G025.3809–00.1815	J183815.2–064801 $\square$	3.85	10.47	12.8	22.1		0.9	0.6	0.6	1.76	39.3	
G028.6523+00.0273	J184331.4–034745 $\square$	0.53	6.7	5.6	15	–6.4	1	1	–1			
G029.9559–00.0168	J184604.0–023921 $\star$	1.56	0.51	11	74.4	–6.3	1	0.8	1	3.57	95.5	–5.1
	J184604.7–023922	8.62	0.58	4.5	19.1	–6.8	1	1	–1	3.57	24.5	–5.7
G030.7661–00.0348	J184736.6–015633 $\diamond$	2.62	0.23	9.5	1180	–5.7	1	1	1	7.26	780	–4.9
G034.4032+00.2277	J185318.6+012446 $\star$	1.09	0.36	2.4	0.2	–7	1	1	1	>5.51	<0.2	<–6.1
	J185318.6+012449	1.66	0.39	3.4	0.4	–6.8	1	1	–1	>5.51	<0.4	<–5.8
G043.1460+00.0139	J191010.6+090512 $\star$	1.32	1.73	5	2.8							
G043.1651–00.0283	J191021.8+090502 $\star$	2.08	1.07	45.3	562	–5.3	1	1	0.6	6.18	451	–4.4
G043.1665+00.0106	J191013.4+090612 $\star$	0.86	1.6	3.3	11.2	–7.2	1	1	–1			
G043.1706–00.0003	J191016.3+090606 $\star$	0.61	1.19	2.7	4.4	–7.8	1	1	–1			
G043.2371–00.0453	J191033.7+090822	3.29	8.46	5.2	15	–6.9	1	1	–1			
G049.4905–00.3688	J192339.9+143108 $\ddagger$ $\star$	0.89	0.23	6.1	6.1	–7.2	0.9	0.8	0.5	4.42	6.7	–6.1
	J192340.1+143107	3.9	0.28	6.8	37.4	–6.4				4.42	41.2	–5.3
	J192340.1+143105 $\ddagger$	4.5	0.3	11.9	8	–7				4.42	8.8	–6.0

$\star$  Candidate ionising star counterpart.

$\square$  Extended X-ray counterpart.

$\ddagger$  Flagged as variable in CSC2.0.

$\diamond$  Counterpart to WR 121a.

## 5.3 18 X-ray associations to 14 CORNISH UCHII regions

### 5.3.1 Summary of X-ray properties

After a coverage catalogue match (which included all available CSC2.0 sources, and not just reduced stacked fields), 14 UCHII were matched to 21 X-ray images, 18 of which are reduced and their photometric and spectral results are included in the latest catalogue rolling release. The 18 counterparts and their properties, such as cross-match separation from the CORNISH source centre, X-ray luminosity (computed from the catalogued aperture-corrected energy flux measured in the ACIS 0.5-7.0 keV band), highest flux significance (S/N), X-ray to bolometric luminosity ratios (§2.8), and catalogued hardness ratios, are summarised in Table 5.1. The X-ray luminosity of O-type stars scales with their bolometric luminosity by a factor of  $\sim 10^{-7}$  [Sciortino et al., 1990].

One of the associations is within the cross-match error radius but is not coincident with the UCHII G030.7661–00.0348. This is a known X-ray counterpart to the binary Wolf-Rayet (WR) star WR 121a – the brightest member of the W43 star cluster [Anderson et al., 2011; Veen et al., 1998]. As WR 121a is a WR binary star emitting hard X-ray emission (single WR stars usually emit soft X-rays, see §1.2.5), it is a good example of a potential contaminant to such a cross-match, particularly in cases where the X-ray point source is found close to the edge of its counterpart UCHII region. It is thus kept for comparison to the other X-ray associations in the plots and tables presented in this chapter. The UCHII G030.7661–00.0348 itself is a candidate radio variable in this work and more detailed description of its complex environment, including the WR star, can be found in §2.4.

All X-ray matches to the 14 UCHII regions have a highest flux significance (S/N) across all stacked observations and energy bands above 3, except for G034.4032+00.2277, with S/N of 2.4. Two-thirds have significance  $>6\sigma$ . The X-ray counterpart to G043.1651–00.0283 is the brightest X-ray UCHII counterpart, coincident with the candidate ionising star seen in Fig. 4.15i. This source has an absorbed  $L_X \approx 5.62 \times 10^{33} \text{ erg s}^{-1}$ , and S/N  $\sim 45.3$ .

The spectra of all X-ray sources with spectral information are hard, with almost all of the detected flux between 2 and 7 keV – the hardness ratios between the hard and the soft band are  $\sim 0.9$  or 1, and the hard and medium band between 0.6 and 1. This is consistent with X-ray emission from deeply embedded sources, where only hard X-rays can overcome the large column densities [Anderson et al., 2011]. A difference between the X-ray spectral shapes is seen in the medium-soft hardness ratios, as these are negative in half of the cases, although this is likely due to the photon counting uncertainties, given the low photon counts in those bands and the decreasing ACIS PSF quality towards lower spectral energies. All but two of the *Chandra* sources have spectra with fewer than 150 counts and therefore only their hardness ratios were reported in the CSC2.0 catalogue, and no results from the automated spectral fitting routines were included. The spectra of the counterparts to G025.3809–00.1815 and G043.1651–00.0283 were successfully modelled with the standard absorbed power-law and absorbed thermal model (with the automated fitting routines), with no statistically significant difference in their minimised  $\chi^2$  values between the two models. The G025.3809–00.1815 counterpart has a photon index  $\Gamma \sim 2.2$ , hydrogen column density  $N_H \sim 2 \times 10^{22} \text{ cm}^{-2}$  and a plasma temperature  $k_B T \sim 5.1 \text{ keV}$ . In the case of G043.1651–00.0283, these values are  $\Gamma \sim 2$ ,  $N_H \sim 7 \times 10^{22} \text{ cm}^{-2}$ , and  $k_B T \sim 8.5 \text{ keV}$ .

These fitted column densities are in good agreement with the corresponding  $N_H$  values presented in Table 5.1. The column densities were computed from

$A_V(H - K)$  towards the UCHIIs (§2.7.2) using the average ratio of  $N_H/A_V \sim 2.08 \times 10^{21} \text{ cm}^{-2} \text{ mag}^{-1}$  for the Galaxy [Zhu et al., 2017]. Detailed spectral modelling of the low-count spectra is beyond the scope of this chapter<sup>5</sup>. Unabsorbed luminosities for these sources were roughly estimated, using the IR-derived column density values, as described in §5.3.3, in order to compare the X-ray to bolometric luminosity ratios of the X-ray associations and to the ratios of more evolved sources reported in literature.

Three X-ray counterparts to two UCHIIs have a variability flag, indicating that the source displays flux variability within one or more observations, or between observations, in one or more energy bands. These are the counterpart to G011.1104–00.3985, as well as the central and the outermost counterparts to G049.4905–00.3688. Note that their flux results in the catalogue table, and thus their X-ray luminosities (Table 5.1) have been computed without taking into account their temporal variability. A possible reason for short-term variability is a close binary system. The near-IR image of G049.4905–00.3688 (a  $\sim 4$  Jy UCHII in CORNISH, also known as W51-D1, see e.g. Wood and Churchwell 1989b) shows three bright stars coinciding with the X-ray sources (Fig. 5.3).

### 5.3.2 Location and extent of the X-ray associations

The CSC contains point and extended ( $< 30''$ ) sources. The point-like and the extended X-ray counterparts are overplotted in the mid-IR/radio UCHII images in Figures 5.3 and 5.4, respectively, and their extents and location w.r.t. the UCHII region are marked in Table 5.1. The dependence of the PSF with the off-axis angle  $\theta$  of the observation is taken into account in the catalogue data processing and observations of the same source at different off-axis angles

---

<sup>5</sup>More caution, e.g. use of Cash statistics, is necessary when unbinned spectral data are modelled in cases of low-count spectra to achieve reliable results.

are matched [Evans et al., 2010]. Four of the 14 UCHIIs have extended X-ray counterparts, and other four have marginally resolved counterparts<sup>6</sup>. The major axes<sup>7</sup> of these X-ray sources range between  $0.3'' < \theta < 12.9''$ .

Two groups of point-like X-ray counterparts are marked in Table 5.1. Associations coinciding with the expected location of the ionising star, as discussed in §4.5.5, are marked as candidate ionising star counterparts. Their emission could be X-rays penetrating the winds of the stars ionising the UCHII regions. As discussed by e.g. Hoare et al. [2007], Oskinova et al. [2010], such X-ray emission can be used to analyse the stellar wind properties, such as wind clumping parameters – a prerequisite for obtaining empirically correct mass-loss rates for massive stars. The likely ionising star is seen in the near-IR image in the case of G029.9559–00.0168 (see Watson et al. 1997 and §4.5.5), G043.1651–00.0283 (§4.5.5), and possibly G049.4905–00.3688. This is exactly coincident with the X-ray sources (Fig. 5.3). In the cases where the extinction has completely obscured the nebula in the near-IR, the point-like X-ray emission coincident with the UCHII centre reveals the likely location of the ionising star. Such candidates are G011.1104–00.3985 and G043.1460+00.0139, and the JVLA-resolved bipolar G043.1706–00.0003 and cometary G034.4032+00.2277 (note that for the sources observed at small  $\theta$ , the *Chandra* PSF is comparable in size with the JVLA beam).

X-ray point-like sources were found at the edges of two UCHIIs. The off-centre associations to G029.9559–00.0168 and G043.2371–00.0453 have fluxes in the 2-10 keV band  $\sim 3 \times 10^{-14}$  erg s<sup>-1</sup> cm<sup>-2</sup> and  $\sim 10^{-14}$  erg s<sup>-1</sup> cm<sup>-2</sup>, respectively. No stellar counterpart is seen in the near-IR image. Extragalactic sources dominate the hard-X-ray background (2-10 keV) below a flux threshold

<sup>6</sup>The table extent flag signifies that the sources is extended, or that the deconvolved source extent is inconsistent with a point source at the 90% confidence level in one or more observations and energy bands.

<sup>7</sup>This corresponds to the  $1\sigma$  radius along the major axis of the ellipse of the deconvolved source extent in the broad ACIS band [Evans et al., 2010].

of  $10^{-13}$  erg s $^{-1}$  cm $^{-2}$ , and a predominantly Galactic source population dominates it above this value [Hands et al., 2004]. Mushotzky et al. [2000] conducted a *Chandra* survey of the SSA13 field with sensitivity comparable to that of the CSC2.0 catalogue. They accounted for 75% of the hard X-ray background sources, finding that in most cases, the X-ray emission is associated with either the nuclei of otherwise normal bright galaxies or with optically faint sources (such as high-redshift quasars or active galactic nuclei hidden behind dust). Hands et al. [2004] combined measurements from the *XMM-Newton* Galactic Plane Survey (XGPS-I, 3 square degrees near  $l = 20^\circ$  in the 2-10 keV band) and *Chandra* and found that the source density down to a limiting flux around  $\sim 2 \times 10^{-14}$  erg s $^{-1}$  cm $^{-2}$  is between 100 and 200 sources per square degree. As noted in §5.2, the cross-match radius is the radio source angular size, which in this case does not exceed 25'' (and is  $\lesssim 10''$  on average). In a conservative estimate, fewer than 0.009 chance alignments per match are expected. Thus, the off-centre counterparts to G029.9559–00.0168 and G043.2371–00.0453 are unlikely to be unrelated sources in the background. Both X-ray counterparts to G029.9559–00.0168 were observed on-axis. The relatively large off-axis angle in the case of the counterpart to G043.2371–00.0453 ( $\sim 8.5'$ ) could be resulting in an increased positional error; given that S/N  $\approx 5.2$ , the positional uncertainty is still unlikely to exceed 1'' (§5.2). The off-centre counterparts could also be due to wind interactions of deeply embedded younger phases such as MYSOs<sup>8</sup> (see e.g. Parkin et al. 2009, Nebot Gómez-Morán et al. 2015). As discussed in the previous chapter, the close co-existence of consecutive evolutionary phases is a likely indicator of feedback and triggering (§4.2.3 and §4.6.3).

The hard X-ray emission associated with the irregular UCHII G043.1665+00.0106 (source G in the Welch ring in W49A, De Pree et al. 1997a) was detected for the first time by Tsujimoto et al. [2006] with *Chandra*. They

<sup>8</sup>Additional high-resolution observations/analysis would be required to confirm this.

reported extended X-ray emission from the region ( $5''$ ), with its centre coincident with the catalogued point source shown in Fig. 5.3. Tsujimoto et al. [2006] fitted the spectrum by an absorbed thermal model, with best-fit values for  $N_{\text{H}} \sim 5 \times 10^{23} \text{ cm}^{-2}$ , plasma temperature  $k_{\text{B}}T \sim 7 \text{ keV}$ , and  $L_{\text{X}}$  (3.0-8.0 keV) of  $\sim 3 \times 10^{33} \text{ erg s}^{-1}$ .

As shown in Fig. 5.4, the extended UCHII counterparts are associated with G012.8050–00.2007, G018.1460–00.2839, G025.3809–00.1815 (and its neighbour G025.3824–00.1812), and G028.6523+00.0273 (Figure 5.4)<sup>9</sup>. In the case of G018.1460–00.2839, the extended emission is from a region just outside the edge of the UCHII and could be linked to the stars seen at its centre rather than the UCHII. In the remaining cases, the extended X-ray emission coincides with the location and radio extent of the UCHII. The UCHII counterparts have varied morphologies – G025.3809-00.1815 is in a close cometary pair with G025.3824–00.1812; G012.8050-00.2007 is bipolar and also has a nearby cometary neighbour towards the NE. The extended X-ray counterpart to G028.6523+00.0273 appears to have two bright peaks, the northern of which coincides with the UCHII centre, and the southern is coincident with a point-like  $4.5\mu\text{m}$  source.

### 5.3.3 X-ray to bolometric luminosity ratios

The absorbed ( $I(E)$ ) and unabsorbed ( $I_0(E)$ ) X-ray spectra are related as

$$I(E) = e^{-\sigma_{\text{ISM}}(E)N_{\text{H}}} I_0(E) , \quad (5.1)$$

where  $\sigma_{\text{ISM}}(E)$  is the energy-dependent photoionization cross section of the ISM (which gives rise to X-ray absorption in the ISM), at energy  $E$ . This relationship

<sup>9</sup>The counterparts to G029.9559–00.0168, G030.7661–00.0348, G043.1651–00.0283, and G049.4905–00.3688 are flagged as extended in the catalogue table but are only marginally resolved and show no structure in their X-ray images.

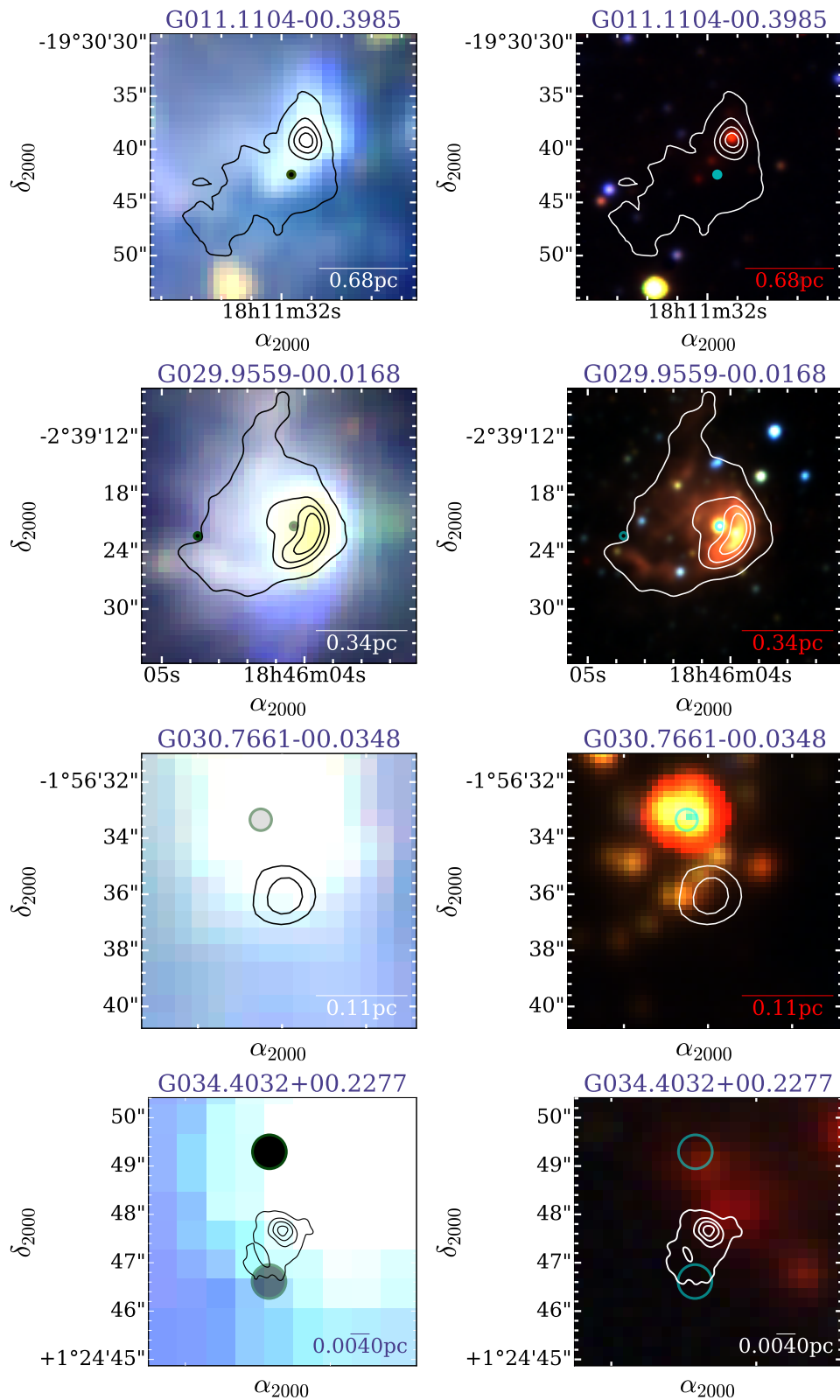


Fig. 5.3 GLIMPSE (*left panels*) and UKIDSS JHK (*right panels*) images of the CORNISH UCHII regions, with overlaid CORNISH or JVA contours, and matched point-like Chandra associations marked with circles (in different colours for clarity). Note that the X-ray source in the G030.7661–00.0348 images is a counterpart to the binary WR star WR 121a – the brightest member of the W43 star cluster [Anderson et al., 2011; Veen et al., 1998] – and not the UCHII.

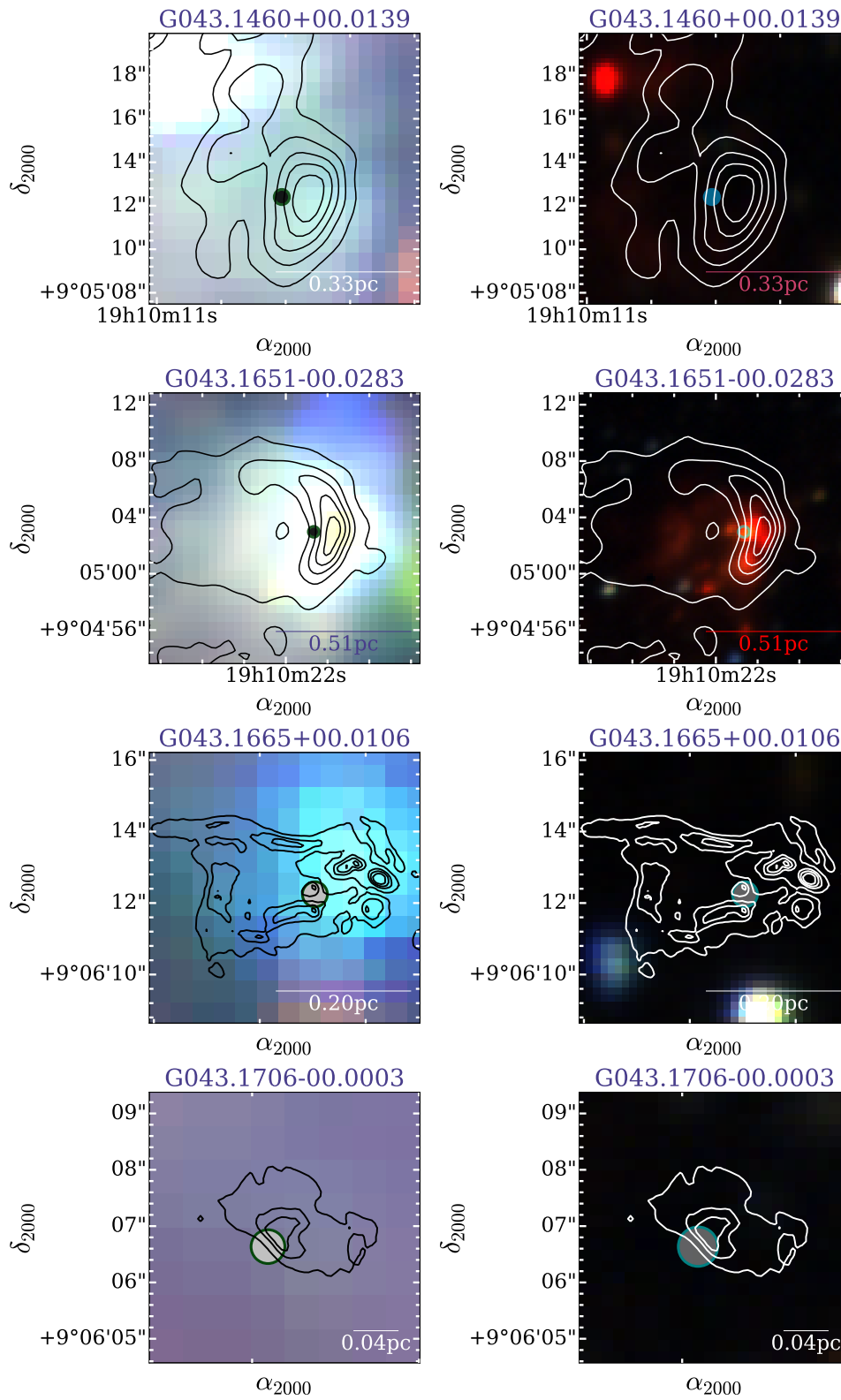


Fig. 5.3 CORNISH UCHII regions with point-like Chandra counterparts – continued.

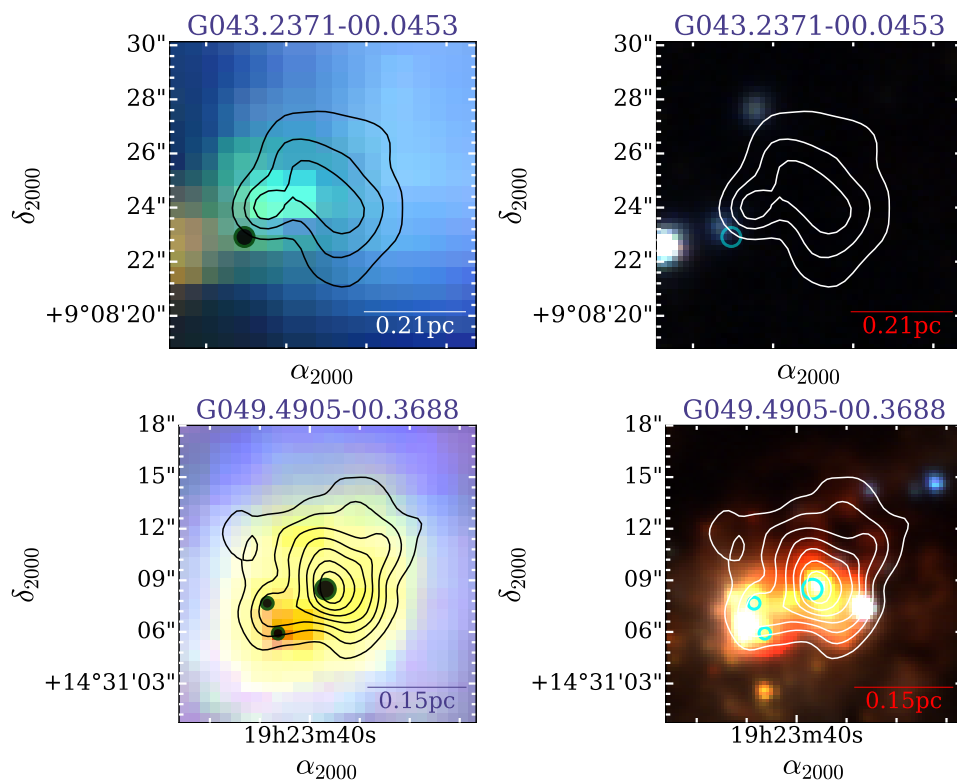


Fig. 5.3 CORNISH UCHII regions with point-like Chandra counterparts – continued.

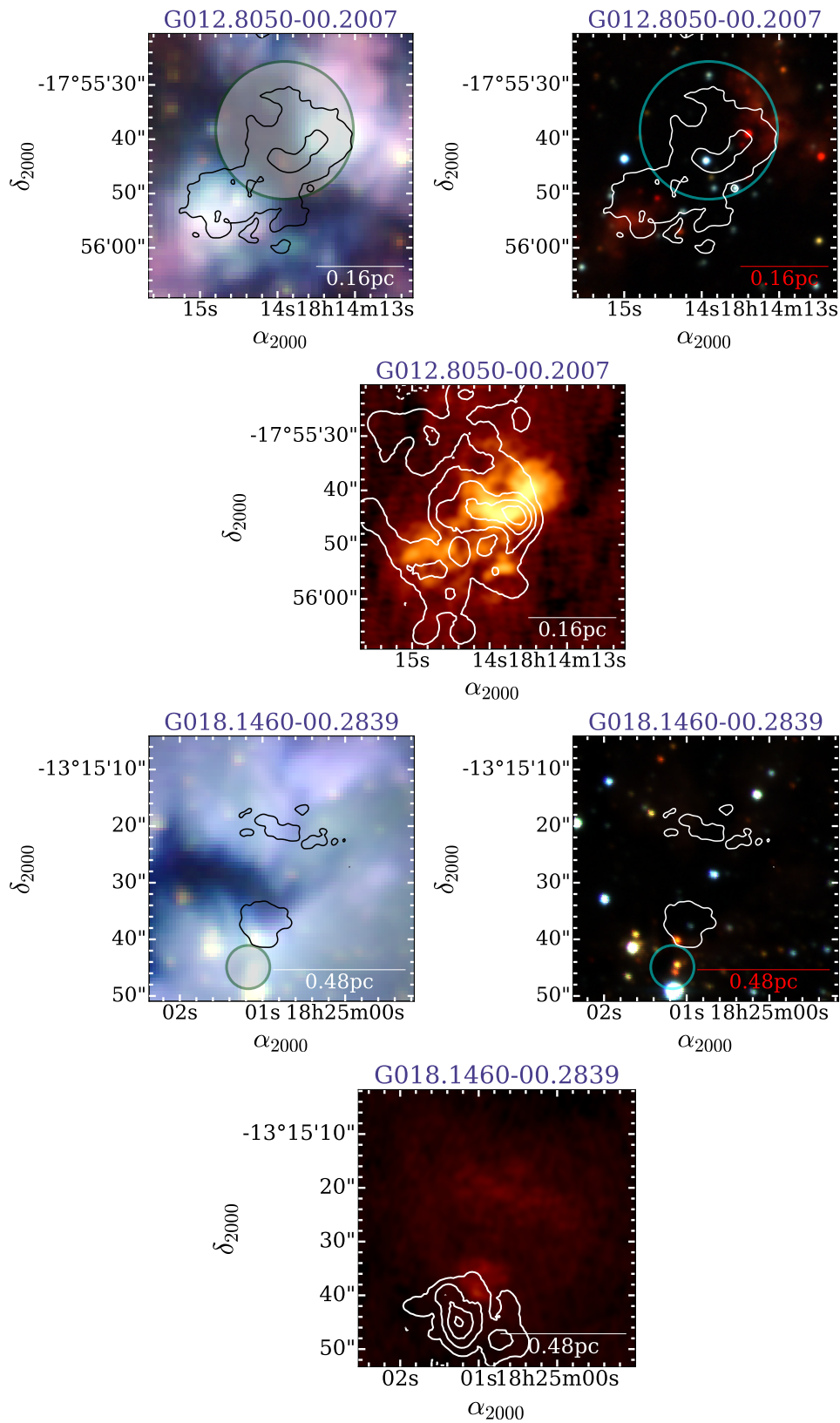


Fig. 5.4 *Left/right panels:* GLIMPSE and UKIDSS JHK images of the CORNISH UCHII regions, with overlaid CORNISH contours. The extended *Chandra* counterparts are marked with circles with radii corresponding to the CSC2.0 catalogued source extent. *Central panels:* CORNISH images of the UCHII regions, with overlaid *Chandra* contours (Gaussian-smoothed).

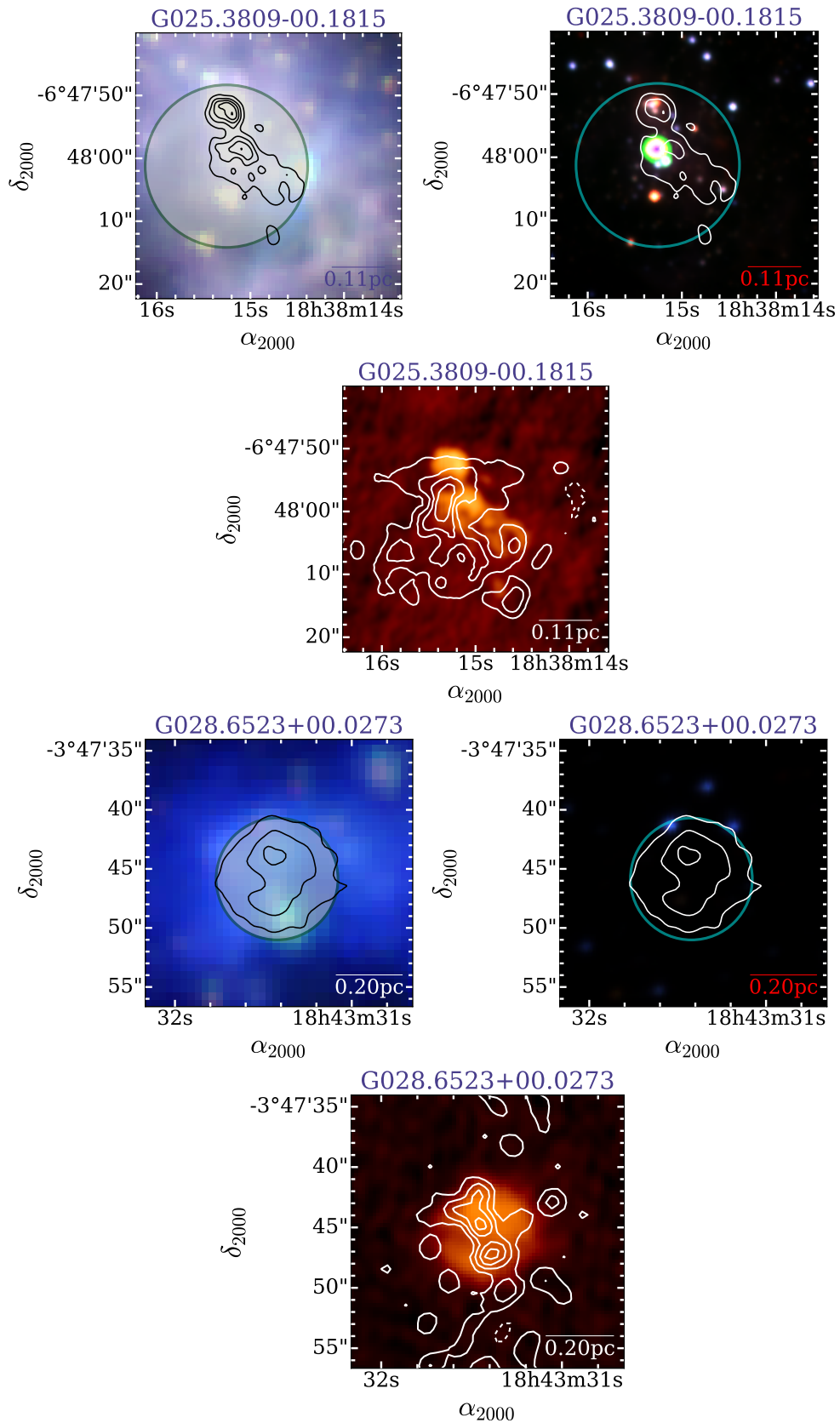


Fig. 5.4 CORNISH UCHII regions with extended *Chandra* associations – continued.

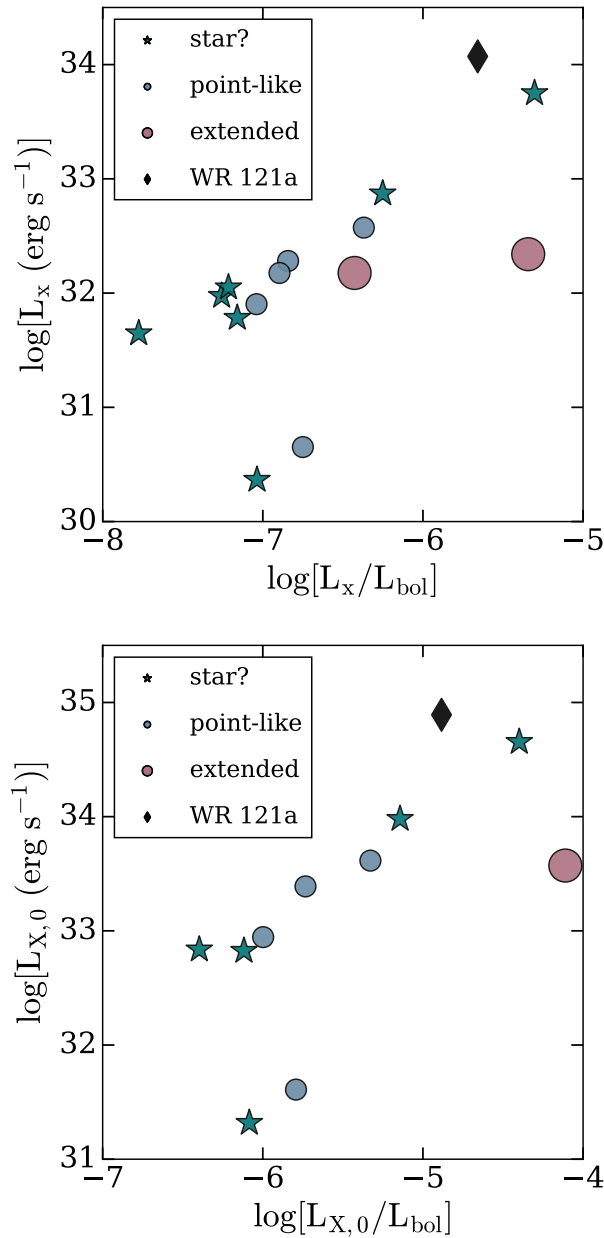


Fig. 5.5 X-ray luminosity against X-ray to bolometric luminosity ratios of UCHII region X-ray associations. The bolometric luminosity of WR 121a was adopted from Table 2 in Anderson et al. [2011]. Note that all values in the top panel are lower limits as the absorbed X-ray luminosities are plotted. The bottom panel shows the absorption-corrected luminosities for the sources with computed in §2.7.2  $A_V$ .

is used in the standard spectral fitting routines for *XMM-Newton* and *Chandra* data to compute the unabsorbed X-ray flux [Wilms et al., 2000].

The cross-section  $\sigma_{\text{ISM}}$  was computed for the middle of the spectral energy range of interest, using Eqn. (19) from Yan et al. [1998] (valid for energies above  $\sim 100$  eV). Equation 5.1 was rearranged and integrated over the 0.5-7 keV interval to obtain a rough estimate of the intrinsic X-ray luminosity of each UCHII region with an  $A_V(H - K)$  (and thus  $N_{\text{H}}$ ) value (see §2.7.2). This is not meant as a substitute for detailed spectral fitting and was done to allow a comparison of the X-ray to bolometric luminosity ratios between the point and extended UCHII associations and field OB/WR stars from literature. The  $L_X/L_{\text{bol}}$  ratios are shown in Fig. 5.5. The limitations of optical extinction estimates from near-IR colours are discussed in §2.7.2. As a check, the corrected  $\log[L_{X,0}/L_{\text{bol}}]$  of WR 121a is  $-4.88$ , and Anderson et al. [2011] estimate a range of possible values  $\sim -5.4 - -5$  (adopting their bolometric luminosity value for WR 121a). Fitting an absorbed thermal model to the available high-count *XMM-Newton* spectrum of WR 121a results in  $\log[L_{X,0}/L_{\text{bol}}] \sim -4.95$  (§5.4). The crude ratio calculation thus appears to be an overestimate of the intrinsic X-ray fluxes, but not unreasonably so.

As seen in both panels of Fig. 5.5, the three groups of detected X-ray sources (those associated with the ionising star, point-like emission near the edge of the H II region, or extended associations) show a possible dependence of the  $L_X/L_{\text{bol}}$  ratios on type – most of the candidate ionising-star counterparts have the lowest X-ray luminosities and  $\log[L_{X,0}/L_{\text{bol}}]$  ratios  $\sim -6$ ; off-centre point-like counterparts are brighter, with  $-6 < \log[L_{X,0}/L_{\text{bol}}] < -5$ ; the extended counterpart to G018.1460–00.2839 has an overluminous  $\log[L_{X,0}/L_{\text{bol}}] \sim -4$ .

For comparison, the O-stars in Cyg OB2 have  $\log[L_{X,0}/L_{\text{bol}}] \sim -7.2$ ; single Wolf-Rayet stars have typical ratios of  $\sim -9 - -8$  [Rauw et al., 2015]. The typical ratio for most single O-stars and WN (WR stars with dominant spectral

lines of ionised nitrogen) and O star massive binaries is  $\approx -7$ , but many overluminous, (likely single) O and WN stars have been detected, with ratios around  $-6.5$  [Anderson et al., 2011]. Larger values could be associated with colliding wind binary systems, such as the case of WR 121a.

The crude range of ratios obtained for the CORNISH UCHII associations could be suggestive of an evolutionary sequence, where O stars in the late stages of their lives have ratios  $\sim -8$ , field O stars – around  $-7$ , and newborn O stars, for which the stellar wind interacts with the H II region – around  $-6.5 - -5$ . However, no clear dependence between the X-ray and bolometric luminosities of WR stars or X-ray-detected B-type stars has been established as of yet [Rauw et al., 2015]. Longer *Chandra* observations to obtain statistically significant spectra are needed to determine the X-ray production mechanism of each X-ray UCHII counterpart (i.e. whether the X-ray luminosity production is dominated by a thermal or non-thermal process) and to obtain intrinsic X-ray luminosities from the best model fits.

## 5.4 *XMM-Newton* counterparts – spectral fits

In this section, model fits to *XMM-Newton* X-ray spectra positionally associated with G025.3809–00.1815, G043.1651–00.0283, and G030.7661–00.0348/WR 121a are presented and discussed. These X-ray spectra are of sufficient exposure and contain enough counts to allow binning of the spectra and statistically meaningful fits. Future longer-exposure *Chandra* spectra can be modelled and analysed in a similar manner as presented here, to investigate the X-ray production mechanism for the three groups of detected X-ray sources in more detail and to obtain more reliable  $L_X/L_{\text{bol}}$  ratios.

Prior to the addition of new data products to the CSC database, available *XMM-Newton* catalogues were searched for X-ray sources coinciding with the

CORNISH radio source positions. The 3XMM-DR5<sup>10</sup> was successfully matched to the CORNISH sample, leading to 9 matched rows within 5'' coordinate separation, corresponding to 8 sources. Within this match, four sources: G030.7661–00.0348, G043.1651–00.0283, G025.3809–00.1815 and G025.3824–00.1812, had spectra and time series available from the *XMM-Newton* archive<sup>11</sup>. The 3XMM source J183815.1–064758 was matched to G025.3809–00.1815 (and its close neighbour G025.3824–00.1812). J184736.6–015633 was matched to G030.7661–00.0348 and J191021.8+090503 to G043.1651–00.0283 (Fig. 5.6). Note that the *XMM-Newton* spectra are extracted from a 5'' or 6'' region. This region is instrument-dependent, the *XMM-Newton* instruments being pn, MOS1 and MOS2. Therefore, a single XMM spectrum can in principle contain a whole cluster. As seen in the higher-resolution *Chandra* associations, the X-ray counterpart to G025.3809–00.1815 and G025.3824–00.1812 is extended; the source matched to G030.7661–00.0348 is counterpart to WR 121a, and the X-ray counterpart to G043.1651–00.0283 appears to be associated with its candidate ionising star.

The obtained *XMM-Newton* pn and MOS spectra for each of the three sources contained sufficient counts for meaningful fits. For each source, all available spectra were fitted simultaneously. The spectrum and analysis of the WR 121a counterpart is included for comparison to the other results.

The X-ray spectra (with energy range 0.3–10 keV) were fitted with standard absorbed models. As expected, absorbed power law/collisionally ionised plasma models gave the best fits. However, no statistically significant difference was found between these two types of models. Thus, the best-fit parameters in each fit were examined. The results from fitting standard absorbed thermal

<sup>10</sup>Note that this is the version available as of the beginning of this project. The latest available version is 3XMM-DR8, including observations up to November 2017, at [http://xmmssc.irap.omp.eu/Catalogue/3XMM-DR8/3XMM\\_DR8.html](http://xmmssc.irap.omp.eu/Catalogue/3XMM-DR8/3XMM_DR8.html).

<sup>11</sup><http://xmm-catalog.irap.omp.eu> and <http://nxsa.esac.esa.int/nxsa-web/#search>

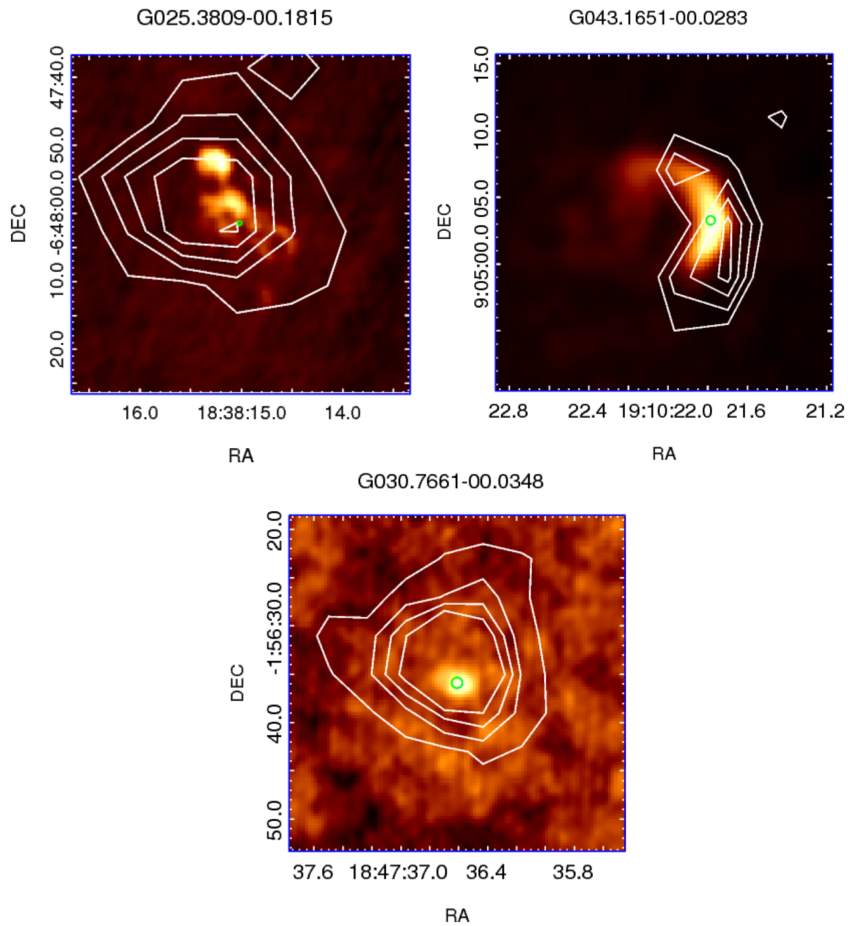


Fig. 5.6 CORNISH UCHII regions with overlaid 3XMM-DR5 sources. The pointing accuracy is  $\sim 1.5''$ . The X-ray source in the first image is J183815.1-064758, matched to G025.3824-00.1812 and G025.3809-00.1815, and has an angular extent of about  $13.9''$ . The other two X-ray sources are J191021.8+090503 (matched to G043.1651-00.0283), and J184736.6-015633 (coinciding with WR 121a near G030.7661-00.0348). The X-ray contours are 99.5% limits, with a linear scale, and the 3XMM X-ray emission centre coordinates are marked by green circles.

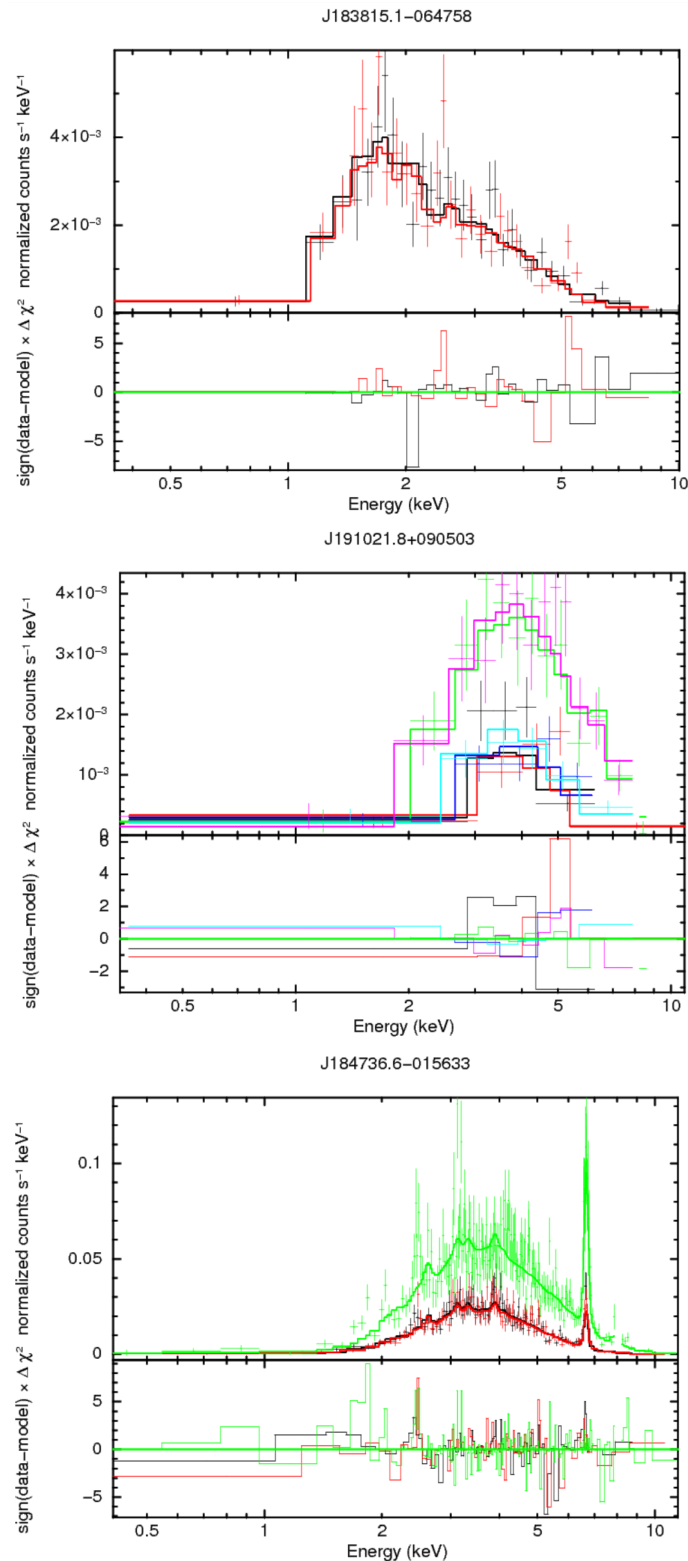


Fig. 5.7 The *XMM-Newton* spectra of the three associations fitted by an absorbed thermal model (with spectral lines). The data from available observations with all EPIC cameras (pn, MOS1, and MOS2) are shown in different colours. The offset between the spectra is due to the differences in the flux calibration of the pn and MOS data. This was taken into account by adding a normalization constant to the fit (initially set to 1 for MOS1 and free for the other models).

<b>J183815.1–064758</b>		<b>Fitted models</b>	
G025.3809–00.1815			
Parameter	Thermal	Non-thermal	
$N_{\text{H}}$ [cm <sup>-2</sup> ]	$2.30^{+0.40}_{-0.36} \times 10^{22}$	$2.49^{+0.24}_{-0.21} \times 10^{22}$	
$k_{\text{B}}T$ [keV]	$4.73^{+2.26}_{-1.22}$	–	
Photon index ( $\Gamma$ )	–	$2.00^{+0.13}_{-0.13}$	
$L_{\text{X,abs}}$ [erg s <sup>-1</sup> ]	$2.96^{+0.09}_{-0.09} \times 10^{32}$	$3.04^{+0.13}_{-0.14} \times 10^{32}$	
$L_{\text{X}}$ [erg s <sup>-1</sup> ]	$5.51^{+0.16}_{-0.16} \times 10^{32}$	$7.03^{+0.29}_{-0.28} \times 10^{32}$	
$\log(L_{\text{X}}/L_{\text{bol}})$	$> -6.2$		
<b>J191021.8+090503</b>		<b>Fitted models</b>	
G043.1651–00.0283			
Parameter	Thermal	Non-thermal	
$N_{\text{H}}$ [cm <sup>-2</sup> ]	$1.20^{+0.14}_{-0.12} \times 10^{23}$	$1.20^{+0.14}_{-0.12} \times 10^{23}$	
$k_{\text{B}}T$ [keV]	$5.86^{+3.31}_{-1.55}$	–	
Photon index ( $\Gamma$ )	–	$1.84^{+0.22}_{-0.22}$	
$L_{\text{X,abs}}$ [erg s <sup>-1</sup> ]	$9.08^{+0.29}_{-0.31} \times 10^{33}$	$9.46^{+0.31}_{-0.32} \times 10^{33}$	
$L_{\text{X}}$ [erg s <sup>-1</sup> ]	$2.56^{+0.08}_{-0.08} \times 10^{34}$	$2.99^{+0.09}_{-0.10} \times 10^{34}$	
$\log(L_{\text{X}}/L_{\text{bol}})$	$-4.6$		
<b>J184736.6–015633</b>		<b>Fitted models</b>	
WR 121a			
Parameter	Thermal	Thermal with non-thermal	
$N_{\text{H}}$ [cm <sup>-2</sup> ]	$1.34^{+0.04}_{-0.04} \times 10^{23}$	$1.52^{+0.03}_{-0.03} \times 10^{23}$	
$k_{\text{B}}T$ [keV]	$2.98^{+0.12}_{-0.11}$	$2.74^{+0.08}_{-0.08}$	
Photon index ( $\Gamma$ )	–	$9.5^{+0.46}_{-0.33}$	
$L_{\text{X,abs}}$ [erg s <sup>-1</sup> ]	$1.42^{+0.02}_{-0.02} \times 10^{34}$	$1.41^{+0.01}_{-0.01} \times 10^{34}$	
$L_{\text{X}}$ [erg s <sup>-1</sup> ]	$6.68^{+0.10}_{-0.10} \times 10^{34}$	$7.63^{+0.07}_{-0.07} \times 10^{34}$	
$\log(L_{\text{X}}/L_{\text{bol}})$	$-4.9$		

Table 5.2 Parameters obtained from the X-ray spectral fits. The luminosity errors are not taking into account the distance errors. Both the absorbed and unabsorbed X-ray luminosities were estimated. Note that the bolometric luminosity used for G025.3809–00.1815 was adopted from Urquhart et al. [2013]. It was estimated for its entire associated clump, and the corresponding luminosity ratio is thus a lower limit.

and non-thermal models are presented in Table 5.2. The  $k_{\text{B}}T$  values show that the three investigated X-ray sources are spectrally hard, with  $k_{\text{B}}T > 2$  keV, which corresponds to a region with  $T > 10^7$  K. The calculated absorbed and unabsorbed X-ray luminosities compare very well to literature values for MSFRs with detected hard diffuse X-ray emission (see e.g. Table 5 in Oskinova et al. 2010). The fitted spectra are shown in Fig. 5.7. Note the difference between the spectral shapes of the UCHII counterparts (top and middle panel) and the WR star counterpart (bottom panel) – stronger line emission is seen in the latter, as expected for the spectra for O stars in their advanced nuclear burning stages which are losing mass at high rates (see e.g. Tsujimoto et al. 2006).

Both J191021.8+090503 (G043.1651–00.0283) and J183815.1–064758 (G025.3809–00.1815) were fit equally well by the absorbed thermal and absorbed power-law models, in agreement with the automated-fitting results reported in CSC2.0 (§5.3.1).

G043.1651–00.0283 corresponds to the well-known UCHII region W49A South. The compact source is situated ahead of a cometary structure powered by another star [De Pree et al., 1997a]. The *XMM-Newton* contours (situated ahead of the radio counterpart) seem to follow the cometary shape of the radio source. However, this curious shape is likely caused by distortion of the PSF due to the location of the X-ray source close to the edge of the field. The source is just-resolved by *XMM-Newton* and point sources located towards the edges in the same field have similarly distorted shapes. The obtained unabsorbed luminosity and  $L_{\text{X},0}/L_{\text{bol}}$  compare reasonably well, given the limitations, with the estimates in §5.3.3 –  $\log[L_{\text{X},0}/L_{\text{bol}}] \sim -4.4$  from the CSC-based estimate, and  $-4.6$  using the fitted unabsorbed flux.

G025.3809–00.1815 is also a well-known UCHII region. It is situated in the W42 giant H II region, which harbours a massive stellar cluster containing

many YSOs, as well as an O5.5 star (W42 1)  $3.23''$  away from the CORNISH source coordinates, but likely located in the foreground (see Blum et al. 2000; Thompson et al. 2006). The bolometric luminosity of G025.3809–00.1815 was not obtained previously in this work. Adopting  $L_{\text{bol}}$  of the associated clump from Urquhart et al. [2013] gives a lower limit to the luminosity ratio of  $-6.2$ .

The possibility for these X-ray sources to have an underlying non-thermal source could not be rejected. This is due to still having insufficient counts to statistically favour the thermal model over the non-thermal one and due to the large extraction area of the spectra ( $> 6''$ ). However, the spectral shape in both cases suggests the presence of emission lines, as would be expected for SFRs, and in such case the thermal model is clearly the more physical one.

J184736.6–015633 (G030.7661–00.0348 in the W43 cluster) shows point X-ray emission ( $< 6''$ ) and was found to be close to the binary Wolf-Rayet star (WR 121a,  $2.74''$  away), a known source of hard X-ray emission [Anderson et al., 2011; Luque-Escamilla et al., 2011]. This is the true origin of the X-ray emission detected by *XMM-Newton*, as seen in the higher-resolution *Chandra* image (Fig. 5.3). J184736.6–015633 was fit successfully by an absorbed thermal fit. The shape of the WR spectrum differs from the other two X-ray counterparts. The spectra for this source contain more counts in comparison to the other sources, and it was clearly not possible for an absorbed non-thermal model (i.e. without spectral lines due to thermal emission) to provide a statistically good fit. Adding a non-thermal emission component in the second fit did not provide any new information, apart from a very unphysical value for the photon index  $\Gamma$  (see Table 5.2). In conclusion, J184736.6–015633 presents itself as purely thermal. A noticeable feature is the fluorescent  $K\alpha$  line at 6.4 keV, suggesting the presence of cold matter (§1.2.5).

## 5.5 Conclusions

A total of 17 X-ray counterparts to 13 CORNISH UCHII regions (and one to WR 121a) were found from a cross-match with the latest CSC2.0 release. The catalogued hardness ratios of the low-count *Chandra* spectra indicate that all these associations are spectrally hard, as expected for X-ray emission associated with deeply embedded UCHII regions. The X-ray luminosities are also within the range expected for massive star-forming regions.

Eight of the X-ray counterparts could be associated with the ionising stars, based on the point-like appearance and location within the UCHII radio extent. Point-like associations at the UCHII outer edges were also found, and could be due to young, deeply embedded neighbours, or X-rays escaping the H II nebula to partially ionise some of the neutral material in its vicinity. Four UCHII regions have extended X-ray counterparts, and their future detailed exploration can reveal more about the interactions between the UCHII regions and their immediate environment.

The mechanism responsible for the X-ray production can be determined by spectral modelling of future longer-exposure *Chandra* X-ray observations of the presented X-ray counterparts. Early estimates of the X-ray to bolometric luminosity ratios of these sources could suggest an evolutionary sequence seen through the X-ray emission, from young to evolved O stars, which remains to be verified. In-depth spectral modelling of the hard X-ray emission from UCHII regions could also help guide models for the stellar winds and thus the mass-loss rates from newborn massive stars.

Considering the area in common between the current *Chandra* release and CORNISH, as many as 10%-15% of the CORNISH UCHII regions have associated hard X-ray emission. With future longer-exposure follow-up observations

and spectral modelling to confirm X-ray UCHII counterparts, a census of the Galactic UCHII regions with X-ray emission will be obtained.

# Chapter 6

## Conclusions and outlook

The pivotal role of OB stars in shaping their surroundings, from their immediate neighbourhoods to their parent galaxies, merits building a complete, multi-wavelength picture to better understand the initial conditions of their formation. With present observational capabilities, studying UCHII regions is the most reliable way to find the global characteristics of the formation sites of nascent massive stars. It is possible to achieve much better number statistics of confirmed UCHII regions than of sources belonging to younger MSF stages.

Exploring the properties of the ultra-compact H II region population of the Milky Way has been the focus of this thesis. This most visible phase in the formation of massive stars was investigated on a large-scale, statistical basis, through the rich supply of high-quality, high-resolution, multi-wavelength information available from Galactic plane surveys. These surveys probe the emission from dust and molecules present at the massive star formation sites, and the gas ionised by the young OB stars. A multi-wavelength exploration of the observed and physical properties of the largest confirmed, complete, resolved, and unbiased UCHII sample was presented. A new, multi-wavelength morphological classification scheme was proposed, and the possible influence on and links to the surroundings of the sources were quantified on a large scale

for the first time. In the following sections, the main findings of this thesis and their context are summarised (§6.1), and their implications for and links to future endeavours in the field are discussed (§6.2).

## 6.1 Conclusions

The largest complete and unbiased UCHII region sample to date was previously detected and visually identified at 5 GHz continuum emission in the context of the CORNISH survey. The nature of 239 out of 240 UCHII region candidates was confirmed in this work, through their spectral indices, observational and physical characteristics, and spectral energy distributions.

High resolution blind radio surveys are the most reliable way to obtain the size of the Galactic UCHII population, as was illustrated through comparing UCHII search methods. By scaling up the size of the CORNISH sample of genuine UCHII regions to the area of the RMS survey, the total UCHII census was estimated –  $\sim 750$  UCHIIs in the Galaxy. This is a factor of 3-4 fewer than found in previous large area radio surveys. The CORNISH sample size was scaled by a geometric correction factor of  $\sim 3.1$  – the ratio between the detected number of RMS UCHII regions in the total RMS and CORNISH area. These are 500 and 160, respectively (see Lumsden et al. 2013; Urquhart et al. 2008).

In the majority of cases, the estimated spectral indices are consistent with optically-thin thermal free-free emission. The cases where the spectral index is non-thermal could be due to differences between the VLA configurations, or an underlying physical mechanism resulting in a non-thermal contribution to the flux. About 5% of the UCHIIs were identified as candidate short-timescale variables, as their 5 GHz flux densities could have increased by 50% or more, based on observations  $\sim 15$  years apart. The changes in the detected flux

density could be caused by the difference in the instrumental set-up, or a short-timescale physical process. Non-thermal spectral indices and candidate variable UCHII regions should be investigated through additional data and comparison to models to identify their origin. The heliocentric and galactocentric distance distributions of the UCHII regions (including distances measured in this work) show the peaks expected in the latest Galactic structure models. All computed physical properties, such as physical diameters, Lyman continuum fluxes, electron densities, and emission measures, are in good agreement with theoretical expectations.

From the near-IR to the X-ray regime, a census of counterparts to the UCHII regions was built throughout this work. Extended source photometry results of the near- and mid-IR counterparts to the CORNISH UCHII regions were presented and combined with available data up to the sub-mm regime to reconstruct the UCHII sample SEDs. The average spectral energy distribution of the sample is in excellent agreement with the expected for UCHII regions shape. Based on their radio and SED-fitted bolometric luminosities, the CORNISH UCHII regions are clearly a separate population from confirmed MYSO jets. Visual extinction estimates from four methods were presented, based on near-IR nebular colours. The calculated IR properties were found to be in good agreement with expected trends set by results obtained from earlier, smaller samples.

The density structure of the ionised gas in 213 UCHII regions was explored through the rich morphological information provided by the mid-IR and radio data, by using these in unison for a new type of multi-wavelength morphological classification. Both the available 5 GHz, 1.5'' resolution data, and 0.3'' resolution data from follow-up 10 GHz observations, the latter reduced in this work, were utilised for this joint morphological classification. A significantly larger fraction of cometary UCHII regions – 71% – was found in comparison to previous, smaller-scale, radio-based morphological classifications. The electron density-

physical size relationship of the CORNISH UCHIIs suggests that the same main mechanisms are responsible for the confinement of the observed different morphological types.

Multiplicity of UCHII regions is an important feature of the CORNISH sample, and thus likely for Galactic UCHII regions in general. About 30% of the CORNISH UCHIIs are found in a double or multiple UCHII association, and, based on their morphologies, up to 16% of the UCHIIs could be pairs/multiples within a common  $5/7\sigma$  envelope. The extended joint classification methodology proposed in this work addressed the IR and radio sources found in the sphere of influence of UCHII regions, as well as their larger-scale surroundings. The patterns in the observed structures are consistent with hierarchical structure formation in 74% of the cases. Statistics of the candidate triggered UCHII and UCHII triggering younger MSF phases identified through this extended classification were presented. The joint classification methodology can be applied to future large-scale UCHII region studies.

Ionising star candidates were identified from the available high-resolution data in near-IR and X-ray emission – in  $\sim 4\%$  and  $\sim 8\%$  of the UCHII regions with data available at these wavelengths, respectively. As many as 10%-15% of the UCHII regions have hard X-ray associations. Based on very early estimates, the X-ray luminosities of UCHII regions could scale with bolometric luminosity by a factor of  $\sim 10^{-6.5} - 10^{-5}$  (whereas for field O-stars, the empirical scaling relation factor is  $\sim 10^{-7}$ ).

Building upon the results of this work could help answer outstanding questions about the formation of massive stars, through theoretical models and follow-up observations of the confirmed UCHII sample.

Survey	$\nu$ (GHz)	$\theta$ ( $''$ )	RMS (mJy)	Coverage	Obs.
CORNISH	5 GHz	1.5 $''$	0.4 mJy	$10^\circ \leq l \leq 65^\circ$ ; $ b  < 1^\circ$	VLA-B/BnA 400 hrs
South	4.5–6.5 GHz; 8–10 GHz	3 $''$	0.2 mJy	$295^\circ \leq l \leq 350^\circ$ ; $ b  < 1^\circ$	ATCA 450 hrs

Table 6.1 Comparing the CORNISH and CORNISH-South surveys.

## 6.2 Outlook

### CORNISH-South

The second half of the CORNISH survey was conducted with ATCA<sup>1</sup> (Table 6.1). The CORNISH-South survey reduction and the source identification are under way [Irabor, prep]. The census of Galactic UCHII regions can be revisited with the addition of southern CORNISH UCHII regions.

### UCHII population synthesis

Steggles [2016] simulated the CORNISH survey for stars in a range of local densities to investigate how well the Steggles et al. [2017] models describe H II region evolution. A Galactic density distribution, a stellar accretion model, and a model for the evolution of cometary H II regions were assumed. The models reproduce the number of UCHIIs in the CORNISH survey, as well as the distributions of angular and physical sizes and flux densities, but produce a broader latitude distribution (Figs. 2.3 and 2.9c). Generally, better fits were obtained for distributions of stars in higher local densities, consistent with the CORNISH UCHIIs being embedded in dense environments (with initial number densities at the location of the star between  $6.4 \times 10^4 \text{ cm}^{-3} - 1.3 \times 10^5 \text{ cm}^{-3}$ ). This is consistent with the CORNISH electron density distribution estimated in this work (Fig. 2.9h), which does not exceed  $10^5 \text{ cm}^{-3}$ . The overall good

<sup>1</sup><http://www.narrabri.atnf.csiro.au/>

agreement between the CORNISH UCHII properties and the early population synthesis results, together with the lower census of Galactic UCHII regions computed in this work in comparison to previous estimates, could suggest that champagne flows are sufficient to confine the UCHII phase. Expanding on this work could thus provide a solution to the lifetime problem posed by Wood and Churchwell [1989b]. Such a scenario would also have important implications for the large observed fraction of cometary UCHII regions. UCHII regions widely forming off-centre in their natal clouds would be consistent with triggering/hierarchical structure formation being the main driver of massive star formation. In such a case, this process would need to be taken into account in future theoretical MSF models.

### **UCHII velocity studies**

In Chapter 4, the morphological distribution of the CORNISH UCHII sample was quantified. Continuum imaging alone is not enough to model and fully interpret the small number of observed UCHII morphological types. The appearance of an UCHII is due to an amalgamation of factors, such as its age, motion relative to the surrounding material, the density structure of this material, the dynamics of the ionised and the molecular gas. The primary shaping mechanism is therefore difficult to isolate [Churchwell, 2002]. The physical process that shapes UCHII regions must also explain their lifetimes. Churchwell [1999] discussed the hypotheses existing to explain UCHII lifetimes or morphologies, such as champagne flow, pressure confinement (when the ambient pressure exceeds that of the UCHII) and stellar-wind-supported bow shock, arguing that they could all be true at different stages of the UCHII development and its location with respect to its parent molecular cloud. As these hypotheses predict different ionised gas kinematics, a way to test them

is to conduct high resolution velocity distribution observations of the gas [Churchwell, 2002].

Follow-up high-resolution observations of the kinematics of both the ionized and molecular gas associated with the CORNISH UCHII region sample can thus reveal more about the formation mechanism and the effect of these sources on their molecular environment. Kinematics studies can be used to check what portion of the candidate triggered/trigging sources, as identified in Chapter 4, are indeed related and thus in congruence with the predictions of hierarchical structure formation. This includes UCHIIs and neighbouring more evolved H II regions, as well as UCHIIs possibly triggering younger MSF phases.

The capabilities of the JVLA, its successor, the Next Generation VLA (ngVLA)<sup>2</sup>, and the SKA (for the southern sky), are up to such a task. The ngVLA will resolve the kinematics of the most compact H II regions through probing their radio recombination line (RRL) emission [Galván-Madrid et al., 2018]. RRL parameters also provide information about turbulent motions [Balser et al., 2018]. With its large instantaneous bandwidth (of the order of the central frequency), the ngVLA can detect UCHII/HCHII short-timescale variability, and candidate variable sources (§2.4) can be followed-up.

MSFR observations with the ngVLA will be complemented at lower frequencies with the SKA (see Manoj et al. 2016; Thompson et al. 2015). Wide area spectroscopic surveys of thousands of radio recombination lines are possible with the SKA. Exploring UCHII kinematics in this way alongside their density distributions will clarify the relative role of stellar winds and radiation pressure in the evolution of H II regions, crucial in population synthesis models [Thompson et al., 2015].

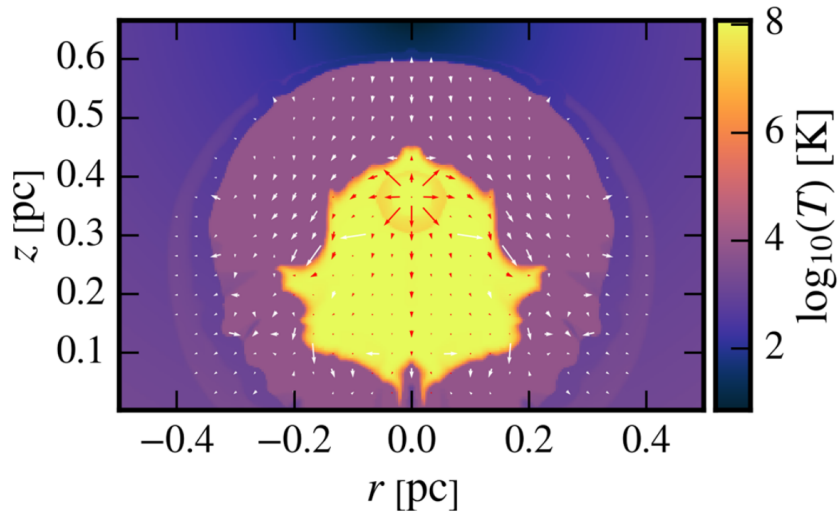


Fig. 6.1 Temperature map of a simulated UCHII region around a  $30 M_{\odot}$  star at an age of 50 kyr by Steggle et al. [2017]. The red arrows mark velocities between  $30$  and  $2700 \text{ km s}^{-1}$ .

### Modelling X-ray emission from UCHII regions

Massive stars can lose a substantial part of their initial mass through their strong winds, and understanding the processes involved is closely linked with understanding the formation and evolution of the star itself. Quantitative measures of the mass-loss rates are needed in stellar evolution models. A complication to this is that the winds driven by hot stars generate highly structured or clumped flows rather than smooth ones (see e.g. the review by Langer 2012 and the references therein). Strong OB winds have a noticeable effect on the UCHII region phase, by sweeping up a cavity in the ionised gas (e.g. Hoare et al. 2007; Wood and Churchwell 1989b). Arthur and Hoare [2006] found that in the case of shallow density gradients the stellar wind can become more important in shaping the UCHII morphology than the champagne flow.

As noted in §5.1, X-rays associated with UCHII regions are likely a direct effect of shocks within the clumpy stellar wind and/or its interactions with the surrounding material. Magnetically channelled gas within the stellar wind is

<sup>2</sup><http://ngvla.nrao.edu/>

another possibility for massive stars with a sufficiently strong magnetic field [Rauw et al., 2015]. Wind–wind collisions in massive star binaries result in X-ray emission that is typically harder than from single massive stars [Pittard and Dawson, 2018].

The observed empirical scaling relation  $\log[L_X/L_{\text{bol}}] \sim -7$  for O-type stars has been recovered in theoretical models (see Owocki et al. 2013; Rauw et al. 2015). Owocki et al. 2013 predicted changes in this relation towards the most and the least luminous O stars. The possible existence of a similar scaling relation for newborn and for more evolved O stars (or for B stars), or a similar relation between their wind luminosity and the X-ray luminosity, have not yet been observationally confirmed [Rauw et al., 2015].

The X-ray associations of the CORNISH UCHII regions (Chapter 5) can be followed-up with longer-exposure *Chandra* observations to identify the dominant X-ray production mechanism in the case of these UCHII regions through spectral modelling, and to estimate their intrinsic  $L_X$ . A detailed check for short-term variability (which could help identify young massive star binaries) can also be performed. These results can be compared to predictions from theoretical models. Shocked winds have been successfully simulated in the hydrodynamical models of cometary H II regions by Steggle et al. [2017], paving the way towards models to study the X-ray emission from the youngest massive stars (Fig. 6.1).



# References

- Abel, T., Wise, J. H., and Bryan, G. L. (2007). The H II region of a primordial star. *The Astrophysical Journal Letters*, 659(2):L87.
- Acord, J., Churchwell, E., and Wood, D. (1998). The expansion rate of and distance to G5.89–0.39. *The Astrophysical Journal Letters*, 495(2):L107.
- Afflerbach, A., Churchwell, E., Acord, J., Hofner, P., Kurtz, S., and Depree, C. (1996). Galactic temperature and metallicity gradients from ultracompact H II regions. *The Astrophysical Journal Supplement Series*, 106:423.
- Alvarez, C., Feldt, M., Henning, T., Puga, E., Brandner, W., and Stecklum, B. (2004). Near-infrared subarcsecond observations of ultracompact H II regions. *The Astrophysical Journal Supplement Series*, 155(1):123.
- Anderson, C. N., Hofner, P., Shepherd, D., and Creech-Eakman, M. (2011). X-ray emission from young stars in the massive star-forming region iras 20126+ 4104. *The Astronomical Journal*, 142(5):158.
- Anderson, L. and Bania, T. (2008). Resolution of the distance ambiguity for galactic H II regions. *The Astrophysical Journal*, 690(1):706.
- Anderson, L., Bania, T., Jackson, J., Clemens, D., Heyer, M., Simon, R., Shah, R., and Rathborne, J. (2009). The molecular properties of galactic H II regions. *The Astrophysical Journal Supplement Series*, 181(1):255.
- Anglada, G. (1995). Centimeter continuum emission from outflow sources. *Revista Mexicana de Astronomia y Astrofisica Conference Series*, 1:67.
- Argon, A., Reid, M., and Menten, K. M. (2000). Interstellar Hydroxyl Masers in the Galaxy. I. The VLA Survey. *The Astrophysical Journal Supplement Series*, 129:159.
- Arthur, S. J. (2007). Off-center H II regions in power-law density distributions. *The Astrophysical Journal*, 670(1):471.
- Arthur, S. J. and Hoare, M. (2006). Hydrodynamics of cometary compact H II regions. *The Astrophysical Journal Supplement Series*, 165(1):283.
- Balser, D. S., Anderson, L., Bania, T., Dickey, J. M., Roshi, D. A., Wenger, T. V., and Wilson, T. (2018). Science with an ngVLA: Radio recombination lines from H II regions. *arXiv preprint arXiv:1810.06664*.

- Banerjee, R. and Pudritz, R. E. (2007). Massive star formation via high accretion rates and early disk-driven outflows. *The Astrophysical Journal*, 660(1):479.
- Bautz, M. W., Pivovarov, M. J., Baganoff, F., Isobe, T., Jones, S. E., Kissel, S. E., LaMarr, B., Manning, H. L., Prigozhin, G. Y., Ricker, G. R., et al. (1998). X-ray CCD calibration for the AXAF CCD imaging spectrometer. *X-Ray Optics, Instruments, and Missions*, 3444:210–225.
- Becker, R., White, R., Helfand, D., Gregg, M., and Perley, R. (1994). The FIRST VLA Survey: the First Year. *Bulletin of the American Astronomical Society*, 26:915.
- Benjamin, R. A., Churchwell, E., Babler, B. L., Bania, T., Clemens, D. P., Cohen, M., Dickey, J. M., Indebetouw, R., Jackson, J. M., Kobulnicky, H. A., et al. (2003). Glimpse. i. an sirtf legacy project to map the inner galaxy. *Publications of the Astronomical Society of the Pacific*, 115(810):953.
- Benson, J. and Johnston, K. (1984). Arc second resolution maps of the compact sources in Sagittarius B2 and G34.3+0.2. *The Astrophysical Journal*, 277:181–188.
- Beuther, H., Schilke, P., Menten, K., Motte, F., Sridharan, T., and Wyrowski, F. (2002). High-mass protostellar candidates. II. Density structure from dust continuum and CS emission. *The Astrophysical Journal*, 566:945.
- Bihl, S., Beuther, H., Ott, J., Johnston, K., Brunthaler, A., Anderson, L., Bigiel, F., Carlhoff, P., Churchwell, E., Glover, S., et al. (2015). THOR: The H I, OH, Recombination line survey of the Milky Way-The pilot study: H I observations of the giant molecular cloud W43. *Astronomy & Astrophysics*, 580:A112.
- Blum, R., Conti, P., and Damini, A. (2000). The stellar content of obscured galactic giant H II regions. II. W42. *The Astronomical Journal*, 119(4):1860.
- Bohm-Vitense, E. (1981). The effective temperature scale. *Annual Review of Astronomy & Astrophysics*, 19(1):295–318.
- Bojičić, I. S., Parker, Q. A., Filipović, M., and Frew, D. J. (2011). Radio-continuum detections of Galactic Planetary Nebulae – I. MASH PNe detected in large-scale radio surveys. *Monthly Notices of the Royal Astronomical Society*, 412(1):223–245.
- Bonnell, I., Bate, M., Clarke, C., and Pringle, J. (2001). Competitive accretion in embedded stellar clusters. *Monthly Notices of the Royal Astronomical Society*, 323(4):785–794.
- Bonnell, I. A. and Bate, M. R. (2005). Binary systems and stellar mergers in massive star formation. *Monthly Notices of the Royal Astronomical Society*, 362(3):915–920.
- Bonnell, I. A., Bate, M. R., and Zinnecker, H. (1998). On the formation of massive stars. *Monthly Notices of the Royal Astronomical Society*, 298(1):93–102.

- Bontemps, S., Motte, F., Csengeri, T., and Schneider, N. (2010). Fragmentation and mass segregation in the massive dense cores of Cygnus X. *Astronomy & Astrophysics*, 524:A18.
- Brand, J. and Blitz, L. (1993). The velocity field of the outer Galaxy. *Astronomy & Astrophysics*, 275:67.
- Briggs, D. (1995). in American Astronomical Society Meeting Abstracts. *BAAS*, 27:1444.
- Brussaard, P. and Van de Hulst, H. (1962). Approximation formulas for nonrelativistic bremsstrahlung and average Gaunt factors for a Maxwellian electron gas. *Reviews of Modern Physics*, 34(3):507.
- Cantó, J., Raga, A., and Rodríguez, L. (2000). The hot, diffuse gas in a dense cluster of massive stars. *The Astrophysical Journal*, 536(2):896.
- Cardelli, J. A., Clayton, G. C., and Mathis, J. S. (1989). The relationship between infrared, optical, and ultraviolet extinction. *The Astrophysical Journal*, 345:245–256.
- Carey, S., Noriega-Crespo, A., Mizuno, D., Shenoy, S., Paladini, R., Kraemer, K., Price, S., Flagey, N., Ryan, E., Ingalls, J., et al. (2009). Mipsgal: A survey of the inner galactic plane at 24 and 70  $\mu\text{m}$ . *Publications of the Astronomical Society of the Pacific*, 121(875):76.
- Castor, J., McCray, R., and Weaver, R. (1975). Interstellar bubbles. *The Astrophysical Journal*, 200:L107–L110.
- Cesaroni, R., Pestalozzi, M., Beltrán, M. T., Hoare, M. G., Molinari, S., Olmi, L., Smith, M. D., Stringfellow, G. S., Testi, L., and Thompson, M. A. (2015). Infrared emission of young H II regions: a *Herschel*/Hi-GAL study. *Astronomy & Astrophysics*, 579:A71.
- Cesaroni, R., Sánchez-Monge, Á., Beltrán, M., Molinari, S., Olmi, L., and Treviño-Morales, S. (2016). Origin of the Lyman excess in early-type stars. *Astronomy & Astrophysics*, 588:L5.
- Charbonnel, C., Montmerle, T., and Klessen, R. (2011). Star formation in molecular clouds. *European Astronomical Society Publications Series*, 51:133–167.
- Charles, P. A. and Seward, F. D. (1995). *Exploring the X-ray Universe*. CUP Archive.
- Chini, R., Hoffmeister, V., Nasserri, A., Stahl, O., and Zinnecker, H. (2012). A spectroscopic survey on the multiplicity of high-mass stars. *Monthly Notices of the Royal Astronomical Society*, 424(3):1925–1929.
- Churchwell, E. (1990). Ultracompact H II regions: the impact of newly formed massive stars on their environment. *The Astronomy & Astrophysics Review*, 2(2):79–123.

- Churchwell, E. (1999). Massive star formation. *The Origin of Stars and Planetary Systems*, pages 515–552.
- Churchwell, E. (2002). Ultra-compact H II regions and massive star formation. *Annual Review of Astronomy & Astrophysics*, 40(1):27–62.
- Churchwell, E., Babler, B. L., Meade, M. R., Whitney, B. A., Benjamin, R., Indebetouw, R., Cyganowski, C., Robitaille, T. P., Povich, M., Watson, C., et al. (2009). The Spitzer/GLIMPSE surveys: a new view of the Milky Way. *Publications of the Astronomical Society of the Pacific*, 121(877):213.
- Civano, F., Marchesi, S., Comastri, A., Urry, M., Elvis, M., Cappelluti, N., Puccetti, S., Brusa, M., Zamorani, G., Hasinger, G., et al. (2016). The *Chandra* COSMOS Legacy survey: overview and point source catalog. *The Astrophysical Journal*, 819(1):62.
- Cyganowski, C., Brogan, C., Hunter, T., and Churchwell, E. (2009). A class I and class II CH<sub>3</sub>OH maser survey of EGOs from the GLIMPSE survey. *The Astrophysical Journal*, 702:1615.
- Cyganowski, C., Brogan, C., Hunter, T., and Churchwell, E. (2011). Deep Very Large Array radio continuum surveys of GLIMPSE extended green objects (EGOs). *The Astrophysical Journal*, 743:56.
- Cyganowski, C., Brogan, C., Hunter, T., Zhang, Q., Friesen, R., Indebetouw, R., and Chandler, C. (2012). The Protocluster G18. 67+ 0.03: A Test Case for Class I CH<sub>3</sub>OH Masers as Evolutionary Indicators for Massive Star Formation. *The Astrophysical Journal Letters*, 760:L20.
- Cyganowski, C., Reid, M. J., Fish, V., and Ho, P. (2003). Dual cometary H II regions in DR 21: Bow shocks or champagne flows? *The Astrophysical Journal*, 596(1):344.
- Cyganowski, C., Whitney, B., Holden, E., Braden, E., Brogan, C., Churchwell, E., Indebetouw, R., Watson, D., Babler, B., Benjamin, R., et al. (2008). A catalog of extended green objects in the GLIMPSE survey: a new sample of massive young stellar object outflow candidates. *The Astronomical Journal*, 136(6):2391.
- Davies, B., Hoare, M. G., Lumsden, S. L., Hosokawa, T., Oudmaijer, R. D., Urquhart, J. S., Mottram, J. C., and Stead, J. (2011). The Red MSX Source survey: critical tests of accretion models for the formation of massive stars. *Monthly Notices of the Royal Astronomical Society*, 416(2):972–990.
- De Becker, M. (2007). Non-thermal emission processes in massive binaries. *The Astronomy and Astrophysics Review*, 14(3-4):171–216.
- de La Fuente, E., Porras, A., Grave, J., Kumar, M., Trinidad, M., Kurtz, S., Kemp, S., Franco, J., and Quevedo, G. (2009). Spitzer-IRAC imagery and photometry of ultracompact H II regions with extended emission. *Revista Mexicana de Astronomia y Astrofisica Conference Series*, 37:13–20.
- De Pree, C., Goss, W., and Gaume, R. (1998). Ionized gas in sgr b2 main on scales of 0.065 arcsecond (600 au). *The Astrophysical Journal*, 500:847.

- De Pree, C., Mehringer, D. M., and Goss, W. (1997a). Multifrequency, high-resolution radio recombination line observations of the massive star-forming region W49A. *The Astrophysical Journal*, 482(1):307.
- De Pree, C., Mehringer, D. M., and Goss, W. (1997b). Multifrequency, high-resolution radio recombination line observations of the massive star-forming region W49A. *The Astrophysical Journal*, 482:307.
- De Pree, C. G., Wilner, D., Deblasio, J., Mercer, A., and Davis, L. (2005). The morphologies of ultracompact H II regions in W49A and Sagittarius B2: The prevalence of shells and a modified classification scheme. *The Astrophysical Journal Letters*, 624(2):L101.
- De Pree, C. G., Wilner, D., Mercer, A., Davis, L., Goss, W., and Kurtz, S. (2004). Broad recombination line objects in W49 North on 600 au scales. *The Astrophysical Journal*, 600(1):286.
- Deharveng, L., Zavagno, A., Samal, M., Anderson, L., LeLeu, G., Brevot, D., Duarte-Cabral, A., Molinari, S., Pestalozzi, M., Foster, J., et al. (2015). Bipolar H II regions – Morphology and star formation in their vicinity – I. G319.88+00.79 and G010.32-00.15. *Astronomy & Astrophysics*, 582:A1.
- del Valle, M. V. and Pohl, M. (2018). Nonthermal emission from stellar bow shocks. *The Astrophysical Journal*, 864(1):19.
- Di Francesco, J., Johnstone, D., Kirk, H., MacKenzie, T., and Ledwosinska, E. (2008). The SCUBA Legacy Catalogues: Submillimeter-Continuum Objects Detected by SCUBA. *The Astrophysical Journal Supplement Series*, 175(1):277.
- Dobbs, C., Krumholz, M., Ballesteros-Paredes, J., et al. (2014). Protostars and Planets VI, ed. H. Tucson, AZ: Univ. Arizona Press.
- Draine, B. T. and Li, A. (2007). Infrared emission from interstellar dust. IV. The silicate-graphite-PAH model in the post-Spitzer era. *The Astrophysical Journal*, 657(2):810.
- Dyson, J., Williams, R., and Redman, M. (1995). Clumpy ultracompact H II regions – I. Fully supersonic wind-blown models. *Monthly Notices of the Royal Astronomical Society*, 277(2):700–704.
- Egan, M., Price, S., and Kraemer, K. (2003). in AAS Meeting Abstracts. *BAAS*, 35:1301.
- Egan, M., Price, S., Moshir, M., Cohen, M., and Tedesco, E. (1999). The Midcourse Space Experiment Point Source Catalog Version 1.2 Explanatory Guide.
- Ellingsen, S. P., Shabala, S., and Kurtz, S. (2005). Extended emission associated with young H II regions. *Monthly Notices of the Royal Astronomical Society*, 357(3):1003–1012.

- Evans, I. N., Primini, F. A., Glotfelty, K. J., Anderson, C. S., Bonaventura, N. R., Chen, J. C., Davis, J. E., Doe, S. M., Evans, J. D., Fabbiano, G., et al. (2010). The *Chandra* source catalog. *The Astrophysical Journal Supplement Series*, 189(1):37.
- Feigelson, E., Townsley, L., Güdel, M., and Stassun, K. (2007). X-ray properties of young stars and stellar clusters. *Protostars and Planets V*, pages 313–328.
- Feigelson, E. D., Gaffney III, J. A., Garmire, G., Hillenbrand, L. A., and Townsley, L. (2003). X-rays in the Orion Nebula cluster: constraints on the origins of magnetic activity in pre-main-sequence stars. *The Astrophysical Journal*, 584(2):911.
- Feigelson, E. D. and Montmerle, T. (1999). High-energy processes in young stellar objects. *Annual Review of Astronomy & Astrophysics*, 37(1):363–408.
- Feldt, M., Stecklum, B., Henning, T., Hayward, T., Lehmann, T., and Klein, R. (1998). The ultracompact H II region G45.45+ 0.06. A pearl necklace in the sky. *Astronomy & Astrophysics*, 339:759–772.
- Flaccomio, E., Damiani, F., Micela, G., Sciortino, S., Harnden Jr, F., Murray, S., and Wolk, S. (2003). *Chandra* X-ray observation of the Orion Nebula cluster. II. Relationship between x-ray activity indicators and stellar parameters. *The Astrophysical Journal*, 582(1):398.
- Franco-Hernández, R. and Rodríguez, L. F. (2004). Time variation in the radio flux density from the bipolar ultracompact H II region NGC 7538 IRS 1. *The Astrophysical Journal Letters*, 604(2):L105.
- Fryer, C. L. and Heger, A. (2005). Binary merger progenitors for gamma-ray bursts and hypernovae. *The Astrophysical Journal*, 623(1):302.
- Galván-Madrid, R., Beltrán, M., Ginsburg, A., Carrasco-González, C., Liu, H. B., Rodríguez, L. F., and Kurtz, S. (2018). Resolving the structure and kinematics of the youngest H II regions and radio jets from young stellar objects. *arXiv preprint arXiv:1806.10225*.
- Galván-Madrid, R., Peters, T., Keto, E. R., Mac Low, M.-M., Banerjee, R., and Klessen, R. S. (2011). Time variability in simulated ultracompact and hypercompact H II regions. *Monthly Notices of the Royal Astronomical Society*, 416(2):1033–1044.
- Galván-Madrid, R., Rodríguez, L. F., Ho, P. T., and Keto, E. (2008). Time variation in G24.78+0.08 A1: Evidence for an accreting hypercompact H II region? *The Astrophysical Journal Letters*, 674(1):L33.
- Garay, G., Reid, M., and Moran, J. (1985). Compact H II regions-Hydrogen recombination and OH maser lines. *The Astrophysical Journal*, 289:681–697.
- Garay, G., Rodríguez, L. F., Moran, J. M., and Churchwell, E. (1993). VLA observations of strong IRAS point sources associated with compact H II Regions. *The Astrophysical Journal*, 418:368.

- Garcia, B. and Mermilliod, J. (2001). High-mass binaries in the very young open cluster NGC 6231 – Implication for cluster and star formation. *Astronomy & Astrophysics*, 368(1):122–136.
- Garmany, C., Conti, P., and Chiosi, C. (1982). The initial mass function for massive stars. *The Astrophysical Journal*, 263:777–790.
- Garmany, C., Conti, P., and Massey, P. (1980). Spectroscopic studies of O type stars. IX – Binary frequency. *The Astrophysical Journal*, 242:1063–1076.
- Garwood, R., Perley, R., Dickey, J., and Murray, M. (1988). A VLA snapshot continuum survey of the first quadrant of the Galactic plane at 1.5 GHz. *The Astronomical Journal*, 96:1655–1670.
- Gaume, R., Claussen, M., De Pree, C., Goss, W., and Mehringer, D. (1995). The Sagittarius B2 star-forming region. I. Sensitive 1.3 centimeter continuum observations. *The Astrophysical Journal*, 449:663.
- Getman, K. V., Flaccomio, E., Broos, P. S., Grosso, N., Tsujimoto, M., Townsley, L., Garmire, G., Kastner, J., Li, J., Harnden Jr, F., et al. (2005). *Chandra* Orion Ultradeep Project: observations and source lists. *The Astrophysical Journal Supplement Series*, 160(2):319.
- Gibb, E., Whittet, D., Boogert, A., and Tielens, A. (2004). Interstellar ice: the infrared space observatory legacy. *The Astrophysical Journal Supplement Series*, 151(1):35.
- Giveon, U., Becker, R., Helfand, D., and White, R. (2005). A New Catalog of Radio Compact H II Regions in the Milky Way. II. The 1.4 GHz Data. *The Astronomical Journal*, 130(1):156.
- Giveon, U., Becker, R., and White, R. (2008). The radio content of GLIMPSE. *The Astronomical Journal*, 135(5):1697.
- Goldader, J. D. and Wynn-Williams, C. (1994). Near-infrared observations of W51. *The Astrophysical Journal*, 433:164–178.
- Gómez, L., Rodríguez, L. F., Loinard, L., Lizano, S., Allen, C., Poveda, A., and Menten, K. M. (2008). Monitoring the large proper motions of radio sources in the Orion BN/KL region. *The Astrophysical Journal*, 685(1):333.
- González-Avilés, M., Lizano, S., and Raga, A. C. (2005). Evolution of H II regions inside hot molecular cores. *The Astrophysical Journal*, 621(1):359.
- Green, J., Caswell, J., Fuller, G., Avison, A., Breen, S., Brooks, K., Burton, M., Chrysostomou, A., Cox, J., Diamond, P., et al. (2008). The 6-GHz multibeam maser survey – I. Techniques. *Monthly Notices of the Royal Astronomical Society*, 392(2):783–794.
- Grellmann, R., Preibisch, T., Ratzka, T., Kraus, S., Helminiak, K., and Zinnecker, H. (2013). The multiplicity of massive stars in the Orion Nebula Cluster as seen with long-baseline interferometry. *Astronomy & Astrophysics*, 550:A82.

- Grosso, N., André, P., Bontemps, S., Montmerle, T., and Feigelson, E. (2000). X-rays and regions of star formation: a combined ROSAT-HRI/near-to-mid IR study of the rho Oph dark cloud. *Astronomy & Astrophysics*, 359(astroph/0005391):113.
- Hands, A. D., Warwick, R., Watson, M. G., and Helfand, D. (2004). X-ray source populations in the Galactic plane. *Monthly Notices of the Royal Astronomical Society*, 351(1):31–56.
- Hanson, M., Luhman, K., and Rieke, G. (2002). A near-infrared survey of radio-selected ultracompact H II regions. *The Astrophysical Journal Supplement Series*, 138(1):35.
- Helfand, D. J., Becker, R. H., White, R. L., Fallon, A., and Tuttle, S. (2006). MAGPIS: a multi-array Galactic plane imaging survey. *The Astronomical Journal*, 131(5):2525.
- Hewett, P. C., Warren, S. J., Leggett, S. K., and Hodgkin, S. T. (2006). The UKIRT Infrared Deep Sky Survey ZY JHK photometric system: passbands and synthetic colours. *Monthly Notices of the Royal Astronomical Society*, 367(2):454–468.
- Hoare, M., Kurtz, S., Lizano, S., Keto, E., and Hofner, P. (2007). Ultra-compact H II regions and the early lives of massive stars. *Protostars and Planets*, 5:181.
- Hoare, M., Purcell, C., Churchwell, E., Diamond, P., Cotton, W., Chandler, C., Smethurst, S., Kurtz, S., Mundy, L., Dougherty, S., et al. (2012). The coordinated radio and infrared survey for high-mass star formation (the cornish survey). i. survey design. *Publications of the Astronomical Society of the Pacific*, 124(919):939.
- Hoare, M. G., Roche, P. F., and Glencross, W. M. (1991). Submillimetre emission and the dust content of compact H II regions. *Monthly Notices of the Royal Astronomical Society*, 251(4):584–599.
- Högbom, J. (1974). Aperture synthesis with a non-regular distribution of interferometer baselines. *Astronomy & Astrophysics Supplement Series*, 15:417.
- Hollenbach, D., Johnstone, D., Lizano, S., and Shu, F. (1994). Photoevaporation of disks around massive stars and application to ultracompact H II regions. *The Astrophysical Journal*, 428:654–669.
- Hu, B., Menten, K. M., Wu, Y., Bartkiewicz, A., Rygl, K., Reid, M. J., Urquhart, J. S., and Zheng, X. (2016). On the relationship of UCHII regions and class II methanol masers. I. Source catalogs. *The Astrophysical Journal*, 833(1):18.
- Hummer, D. and Storey, P. (1987). Recombination-line intensities for hydrogenic ions – I. Case B calculations for H I and He II. *Monthly Notices of the Royal Astronomical Society*, 224(3):801–820.

- Immer, K., Cyganowski, C., Reid, M., and Menten, K. (2014). The cometary H II regions of DR 21: Bow shocks or champagne flows or both? *Astronomy & Astrophysics*, 563:A39.
- Indebetouw, R., Mathis, J., Babler, B., Meade, M., Watson, C., Whitney, B., Wolff, M., Wolfire, M., Cohen, M., Bania, T., et al. (2005). The wavelength dependence of interstellar extinction from 1.25 to 8.0  $\mu\text{m}$  using GLIMPSE data. *The Astrophysical Journal*, 619(2):931.
- Irabor, T. (in prep.).
- Israel, F. (1977). Aperture synthesis observations of Galactic H II regions. VII – a ‘quick look’ survey of Galactic H II regions. *Astronomy & Astrophysics*, 61:377.
- Israel, F. (1978). H II regions and CO clouds – The blister model. *Astronomy & Astrophysics*, 70:769–775.
- Israel, F., Habing, H., and De Jong, T. (1973). Aperture synthesis observations of H II regions. I. A group of H II regions around  $l = 111$ . *Astronomy & Astrophysics*, 27:143–160.
- Jackson, J., Rathborne, J., Shah, R., Simon, R., Bania, T., Clemens, D., Chambers, E., Johnson, A., Dormody, M., Lavoie, R., et al. (2005). The boston university–five college radio astronomy observatory galactic ring survey. *Bulletin of the American Astronomical Society*, 37:1304.
- Kahn, F. et al. (1954). The acceleration of interstellar clouds. *Bulletin of the Astronomical Institutes of the Netherlands*, 12:187.
- Kalcheva, I., Hoare, M., Urquhart, J., Kurtz, S., Lumsden, S., Purcell, C., and Zijlstra, A. (2018). The Coordinated Radio and Infrared Survey for High-Mass Star Formation III. A catalogue of northern ultra-compact H II regions. *Astronomy & Astrophysics*, 615:A103.
- Keto, E. (2007). The formation of massive stars: Accretion, disks, and the development of hypercompact H II regions. *The Astrophysical Journal*, 666(2):976.
- Keto, E., Welch, W., Reid, M., and Ho, P. (1995). Line broadening in the W3 (OH) champagne flow. *The Astrophysical Journal*, 444:765–769.
- Kim, K.-T. and Koo, B.-C. (2001). Radio continuum and recombination line study of ultracompact H II regions with extended envelopes. *The Astrophysical Journal*, 549:979.
- Kim, K.-T. and Koo, B.-C. (2002). Interaction between ionized and molecular gas in the active star-forming region W31. *The Astrophysical Journal*, 575:327.
- Kim, K.-T. and Koo, B.-C. (2003). Molecular Counterparts of Ultracompact H II Regions with Extended Envelopes. *The Astrophysical Journal*, 596:362.
- Klassen, M., Peters, T., and Pudritz, R. E. (2012a). H II region variability and pre-main-sequence evolution. *The Astrophysical Journal*, 758(2):137.

- Klassen, M., Pudritz, R. E., and Peters, T. (2012b). Simulating protostellar evolution and radiative feedback in the cluster environment. *Monthly Notices of the Royal Astronomical Society*, 421(4):2861–2871.
- Kobulnicky, H. A. and Fryer, C. L. (2007). A new look at the binary characteristics of massive stars. *The Astrophysical Journal*, 670(1):747.
- Kolpak, M. A., Jackson, J. M., Bania, T., Clemens, D., and Dickey, J. M. (2003). Resolving the kinematic distance ambiguity toward Galactic H II regions. *The Astrophysical Journal*, 582(2):756.
- Koornneef, J. (1983). Near-infrared photometry. II—intrinsic colours and the absolute calibration from one to five micron. *Astronomy and Astrophysics*, 128:84–93.
- Krumholz, M. R. and McKee, C. F. (2005). A general theory of turbulence-regulated star formation, from spirals to ultraluminous infrared galaxies. *The astrophysical journal*, 630(1):250.
- Kuiper, R., Klahr, H., Beuther, H., and Henning, T. (2010). The role of accretion disks in the formation of massive stars. *Proceedings of the International Astronomical Union*, 6(S270):215–218.
- Kurtz, S. (2005). Hypercompact H II regions. *Proceedings of the International Astronomical Union*, 1(S227):111–119.
- Kurtz, S., Cesaroni, R., Churchwell, E., Hofner, P., Walmsley, C., Mannings, V., Boss, A., and Russell, S. (2000). Hot molecular cores and the earliest phases of high-mass star formation. *Protostars and Planets IV*, page 299.
- Kurtz, S., Cesaroni, R., Felli, M., Churchwell, E., and Walmsley, M. (2005). Massive star birth: a crossroads of astrophysics. *IAUS*, 227:111.
- Kurtz, S., Churchwell, E., and Wood, D. (1994). Ultracompact H II regions. 2: New high-resolution radio images. *The Astrophysical Journal Supplement Series*, 91:659–712.
- Kurtz, S. E., Watson, A. M., Hofner, P., and Otte, B. (1999). Ultracompact H II regions with extended radio-continuum emission. *The Astrophysical Journal*, 514(1):232.
- Lada, C. J. and Shu, F. H. (1990). The formation of sunlike stars. *Science*, 248(4955):564–572.
- Langer, N. (2012). Presupernova evolution of massive single and binary stars. *Annual Review of Astronomy and Astrophysics*, 50.
- Langston, G., Minter, A., D’Addario, L., Eberhardt, K., Koski, K., and Zuber, J. (2000). The first Galactic plane survey at 8.35 and 14.35 GHz. *The Astronomical Journal*, 119(6):2801.
- Larios, G. R. and Phillips, J. (2005). An analysis of 2MASS near-infrared photometry for Galactic planetary nebulae. *Monthly Notices of the Royal Astronomical Society*, 357(2):732–752.

- Larson, R. B. (1969). Numerical calculations of the dynamics of a collapsing proto-star. *Monthly Notices of the Royal Astronomical Society*, 145(3):271–295.
- Larson, R. B. (1985). Cloud fragmentation and stellar masses. *Monthly Notices of the Royal Astronomical Society*, 214(3):379–398.
- Law, C. and Yusef-Zadeh, F. (2004). X-ray observations of stellar clusters near the Galactic center. *The Astrophysical Journal*, 611(2):858.
- Lemoine-Goumard, M., Renaud, M., Martin, P., Ferrara, E., and Grondin, M.-H. (2011). Fermi-LAT detection of gamma-ray emission in the vicinity of the star forming regions W43 and Westerlund 2. *Mem. Soc. Ast. It.*, 82:739.
- Lex, A., Gehlenborg, N., Strobel, H., Vuillemot, R., and Pfister, H. (2014). UpSet: Visualization of intersecting sets. *IEEE Transactions on Visualization and Computer Graphics (Info Vis '14)*, 20:1983–1992.
- Lizano, S. (2008). Hypercompact H II regions. In *Massive Star Formation: Observations Confront Theory*, volume 387, page 232.
- Lucas, P., Hoare, M. G., Longmore, A., Schröder, A., Davis, C. J., Adamson, A., Bandyopadhyay, R. M., De Grijs, R., Smith, M., Gosling, A., et al. (2008). The ukidss galactic plane survey. *Monthly Notices of the Royal Astronomical Society*, 391(1):136–163.
- Lumsden, S. and Hoare, M. (1996). An IR study of the velocity structure of the cometary compact H II region G29.96-0.02. *The Astrophysical Journal*, 464:272.
- Lumsden, S., Hoare, M., Oudmaijer, R., and Richards, D. (2002). The population of the Galactic plane as seen by MSX. *Monthly Notices of the Royal Astronomical Society*, 336(2):621–636.
- Lumsden, S., Hoare, M., Urquhart, J., Oudmaijer, R., Davies, B., Mottram, J., Cooper, H., and Moore, T. (2013). The Red MSX Source Survey: The Massive Young Stellar Population of Our Galaxy. *The Astrophysical Journal Supplement Series*, 208(1):11.
- Luque-Escamilla, P., Muñoz-Arjonilla, A. J., Sánchez-Sutil, J. R., Martí, J., Combi, J. A., and Sánchez-Ayaso, E. (2011). Infrared and radio study of the W43 cluster – Resolved binaries and non-thermal emission. *Astronomy & Astrophysics*, 532:A92.
- Mackenzie, T., Braglia, F. G., Gibb, A. G., Scott, D., Jenness, T., Serjeant, S., Thompson, M., Berry, D., Brunt, C. M., Chapin, E., et al. (2011). A pilot study for the SCUBA-2 ‘All-Sky’ Survey. *Monthly Notices of the Royal Astronomical Society*, 415(2):1950–1960.
- Manoj, P., Vig, S., Maheswar, G., Kamath, U., and Tej, A. (2016). Interstellar medium and star formation studies with the Square Kilometre Array. *Journal of Astrophysics and Astronomy*, 37:38.

- Martín-Hernández, N., Bik, A., Kaper, L., Tielens, A., and Hanson, M. (2003). A VLT spectroscopic study of the ultracompact H II region G29.96–0.02. *Astronomy & Astrophysics*, 405(1):175–188.
- Masci, F. (2009). Aperture photometry uncertainties assuming priors and correlated noise. *Version 2.0*.
- McCaughrean, M., Zinnecker, H., Andersen, M., Meeus, G., and Lodieu, N. (2002). Standing on the shoulder of a giant: ISAAC, Antu, and star formation. *The Messenger*, 109:28–36.
- McCaughrean, M. J. and Stauffer, J. R. (1994). High resolution near-infrared imaging of the Trapezium: A stellar census. *The Astronomical Journal*, 108:1382–1397.
- McKee, C. F. and Tan, J. C. (2002). Massive star formation in 100,000 years from turbulent and pressurized molecular clouds. *Nature*, 416(6876):59.
- Menten, K., Pillai, T., and Wyrowski, F. (2005). Initial conditions for massive star birth—Infrared dark clouds. *Proceedings of the International Astronomical Union*, 1(S227):23–34.
- Meynet, G. and Maeder, A. (2003). Stellar evolution with rotation – X. Wolf-Rayet star populations at solar metallicity. *Astronomy & Astrophysics*, 404(3):975–990.
- Mezger, P. and Henderson, A. (1967). Galactic H II regions. I. Observations of their continuum radiation at the frequency 5 GHz. *The Astrophysical Journal*, 147:471.
- Miley, J. M. (2017). Characterising the morphology of previously unresolved ultracompact H II regions. *MPhys project report*, University of Leeds.
- Miralles, M. P., Rodríguez, L. F., and Scalise, E. (1994). Radio continuum, ammonia, and water maser observations of bright, unassociated IRAS point sources. *The Astrophysical Journal Supplement Series*, 92:173–188.
- Molinari, S., Bally, J., Glover, S., Moore, T., Noreiga-Crespo, A., Plume, R., Testi, L., Vázquez-Semadeni, E., Zavagno, A., Bernard, J.-P., et al. (2014). The Milky Way as a star formation engine. *Protostars and Planets VI*, pages 125–148.
- Moore, T. J., Lumsden, S., Ridge, N., and Puxley, P. (2005). The near-infrared extinction law in regions of high  $A_V$ . *Monthly Notices of the Royal Astronomical Society*, 359(2):589–596.
- Motte, F., Bontemps, S., and Louvet, F. (2017). High-mass star and massive cluster formation in the Milky Way. *Annual Review of Astronomy & Astrophysics*, 56:1.
- Mottram, J. C., Hoare, M. G., Urquhart, J., Lumsden, S. L., Oudmaijer, R. D., Robitaille, T., Moore, T. J., Davies, B., and Stead, J. (2011). The Red MSX Source survey: the bolometric fluxes and luminosity distributions of young massive stars. *Astronomy & Astrophysics*, 525:A149.

- Murray, N. and Chang, P. (2012). Star formation in massive clusters via Bondi accretion. *The Astrophysical Journal*, 746(1):75.
- Murray, S. S., Austin, G. K., Chappell, J. H., Gomes, J. J., Kenter, A. T., Kraft, R. P., Meehan, G. R., Zombeck, M. V., Fraser, G. W., and Serio, S. (2000). In-flight performance of the *Chandra* high-resolution camera. *X-Ray Optics, Instruments, and Missions III*, 4012:68–81.
- Mushotzky, R., Cowie, L., Barger, A., and Arnaud, K. (2000). Resolving the extragalactic hard X-ray background. *Nature*, 404(6777):459.
- Nebot Gómez-Morán, A., Motch, C., Pineau, F.-X., Carrera, F. J., Pakull, M., and Riddick, F. (2015). Infrared identification of hard X-ray sources in the Galaxy. *Monthly Notices of the Royal Astronomical Society*, 452(1):884–901.
- Oskinova, L., Gruendl, R., Ignace, R., Chu, Y.-H., Hamann, W.-R., and Feldmeier, A. (2010). Hard X-ray emission in the star-forming region ON 2: discovery with *XMM – Newton*. *The Astrophysical Journal*, 712(2):763.
- Osorio, M., Fuente, A., Anglada, G., Báez-Rubio, A., Busquet, G., Goicoechea, J. R., Jiménez-Serra, I., Martín-Pintado, J., Mayen-Gijón, J. M., Palau, A., et al. (2015). The earliest stages of star formation: Massive protostars and the SKA. *The Spanish Square Kilometre Array White Book*, page 153.
- Owocki, S. P., Sundqvist, J. O., Cohen, D. H., and Gayley, K. G. (2013). Thin-shell mixing in radiative wind-shocks and the  $L_x$  vs  $L_{bol}$  scaling of O-star X-rays. *Monthly Notices of the Royal Astronomical Society*, 429(4):3379–3389.
- Panagia, N. and Walmsley, C. (1978). Radio source angular diameters. *Astronomy & Astrophysics*, 70:411.
- Pandian, J. D., Goldsmith, P. F., and Deshpande, A. A. (2007). The arecibo methanol maser Galactic plane survey. I. Data. *The Astrophysical Journal*, 656(1):255.
- Parkin, E., Pittard, J., Hoare, M., Wright, N., and Drake, J. (2009). The interactions of winds from massive young stellar objects: X-ray emission, dynamics and cavity evolution. *Monthly Notices of the Royal Astronomical Society*, 400(2):629–645.
- Peeters, E., Spoon, H., and Tielens, A. (2004). Polycyclic aromatic hydrocarbons as a tracer of star formation? *The Astrophysical Journal*, 613(2):986.
- Penny, L. R., Gies, D. R., and Bagnuolo Jr, W. G. (1997). Tomographic separation of composite spectra. IV. The physical properties of the massive close binary DH Cephei. *The Astrophysical Journal*, 483(1):439.
- Perault, M., Omont, A., Simon, G., Seguin, P., Ojha, D., Blommaert, J., Felli, M., Gilmore, G., Guglielmo, F., Habing, H., et al. (1996). First ISOCAM images of the Milky Way. *Astronomy & Astrophysics-Berlin*, 315(2):L165.
- Pereira, V., López-Santiago, J., Miceli, M., Bonito, R., and De Castro, E. (2016). Modeling nonthermal emission from stellar bow shocks. *Astronomy & Astrophysics*, 588:A36.

- Peters, T., Banerjee, R., Klessen, R. S., Mac Low, M.-M., Galván-Madrid, R., and Keto, E. R. (2010a). H II regions: witnesses to massive star formation. *The Astrophysical Journal*, 711(2):1017.
- Peters, T., Klessen, R. S., Mac Low, M.-M., and Banerjee, R. (2010b). Limiting accretion onto massive stars by fragmentation-induced starvation. *The Astrophysical Journal*, 725(1):134.
- Peters, T., Mac Low, M.-M., Banerjee, R., Klessen, R. S., and Dullemond, C. P. (2010c). Understanding spatial and spectral morphologies of ultracompact H II regions. *The Astrophysical Journal*, 719(1):831.
- Pittard, J. and Dawson, B. (2018). Colliding stellar winds structure and x-ray emission. *Monthly Notices of the Royal Astronomical Society*, 477(4):5640–5645.
- Pokhrel, R., Myers, P. C., Dunham, M. M., Stephens, I. W., Sadavoy, S. I., Zhang, Q., Bourke, T. L., Tobin, J. J., Lee, K. I., Gutermuth, R. A., et al. (2018). Hierarchical fragmentation in the Perseus molecular cloud: From the cloud scale to protostellar objects. *The Astrophysical Journal*, 853(1):5.
- Porter, J. M., Drew, J. E., and Lumsden, S. L. (1998). Broad band infrared spectroscopy of massive young stellar objects. *Astronomy & Astrophysics*, 332:999–1016.
- Price, S. D., Egan, M. P., Carey, S. J., Mizuno, D. R., and Kuchar, T. A. (2001). Midcourse Space Experiment survey of the Galactic plane. *The Astronomical Journal*, 121(5):2819.
- Purcell, C., Hoare, M., Cotton, W., Lumsden, S., Urquhart, J., Chandler, C., Churchwell, E., Diamond, P., Dougherty, S., Fender, R., et al. (2013). The coordinated radio and infrared survey for high-mass star formation. ii. source catalog. *The Astrophysical Journal Supplement Series*, 205(1):1.
- Purser, S., Lumsden, S., Hoare, M., Urquhart, J., Cunningham, N., Purcell, C., Brooks, K., Garay, G., Gúzman, A., and Voronkov, M. (2016). A search for ionized jets towards massive young stellar objects. *Monthly Notices of the Royal Astronomical Society*, 460(1):1039–1053.
- Purser, S. J. D. (2017). *PhD thesis*. University of Leeds.
- Quiroza, C., Rood, R. T., Bania, T., Balser, D. S., and Maciel, W. J. (2006). The electron temperature gradient in the Galactic disk. *The Astrophysical Journal*, 653(2):1226.
- Rau, U. and Cornwell, T. J. (2011). A multi-scale multi-frequency deconvolution algorithm for synthesis imaging in radio interferometry. *Astronomy & Astrophysics*, 532:A71.
- Rauw, G., Nazé, Y., Wright, N., Drake, J., Guarcello, M., Prinja, R., Peck, L., Colombo, J. A., Herrero, A., Kobulnicky, H., et al. (2015). X-ray emission from massive stars in Cyg OB2. *The Astrophysical Journal Supplement Series*, 221(1):1.

- Reid, M. and Ho, P. (1985). G34.3+0.2 – a ‘cometary’ H II region. *The Astrophysical Journal*, 288:L17–L19.
- Reid, M., Menten, K., Zheng, X., Brunthaler, A., Moscadelli, L., Xu, Y., Zhang, B., Sato, M., Honma, M., Hirota, T., et al. (2009). Trigonometric parallaxes of massive star-forming regions. vi. galactic structure, fundamental parameters, and noncircular motions. *The Astrophysical Journal*, 700(1):137.
- Robitaille, T. P., Whitney, B. A., Indebetouw, R., and Wood, K. (2007). Interpreting spectral energy distributions from young stellar objects. ii. fitting observed SEDs using a large grid of precomputed models. *The Astrophysical Journal Supplement Series*, 169(2):328.
- Rodríguez, L. F., Gómez, Y., and Tafuya, D. (2007). Changes in the radio appearance of MWC 349A. *The Astrophysical Journal*, 663(2):1083.
- Roelfsema, P., Cox, P., Tielens, A., Allamandola, L., Baluteau, J.-P., Barlow, M., Beintema, D., Boxhoorn, D., Cassinelli, J., Caux, E., et al. (1996). SWS observations of IR emission features towards compact H II regions. *Astronomy and Astrophysics*, 315:L289–L292.
- Rosolowsky, E., Dunham, M. K., Ginsburg, A., Bradley, E. T., Aguirre, J., Bally, J., Battersby, C., Cyganowski, C., Dowell, D., Drosback, M., et al. (2010). The Bolocam Galactic Plane Survey. II. Catalog of the image data. *The Astrophysical Journal Supplement Series*, 188(1):123.
- Roth, N., Stahler, S. W., and Keto, E. (2013). The dynamics of ultracompact H II regions. *Monthly Notices of the Royal Astronomical Society*, 438(2):1335–1354.
- Rubin, R. H. (1968). A discussion of the sizes and excitation of H II regions. *The Astrophysical Journal*, 154:391.
- Sánchez-Monge, Á., Beltrán, M., Cesaroni, R., Fontani, F., Brand, J., Molinari, S., Testi, L., and Burton, M. (2013). Different evolutionary stages in massive star formation – Centimeter continuum and H<sub>2</sub>O maser emission with ATCA. *Astronomy & Astrophysics*, 550:A21.
- Schuller, F., Menten, K., Contreras, Y., Wyrowski, F., Schilke, P., Bronfman, L., Henning, T., Walmsley, C., Beuther, H., Bontemps, S., et al. (2009). ATLASGAL–The APEX telescope large area survey of the galaxy at 870 $\mu$ m. *Astronomy & Astrophysics*, 504(2):415–427.
- Schulz, N. S., Canizares, C., Huenemoerder, D., Kastner, J. H., Taylor, S., and Bergstrom, E. (2001). *Chandra* observations of variable embedded X-Ray sources in Orion. I. Resolving the Orion Trapezium. *The Astrophysical Journal*, 549(1):441.
- Sciortino, S., Vaiana, G., Harnden Jr, F., Ramella, M., Morossi, C., Rosner, R., and Schmitt, J. (1990). Relationship between optical and X-ray properties of O-type stars surveyed with the *Einstein* observatory. *The Astrophysical Journal*, 361:621–643.

- Sewiło, M., Churchwell, E., Kurtz, S., Goss, W. M., and Hofner, P. (2008). Internal dynamics of the hypercompact H II region G28.20-0.04 N. *The Astrophysical Journal*, 681(1):350.
- Shu, F. H., Adams, F. C., and Lizano, S. (1987). Star formation in molecular clouds: observation and theory. *Annual review of Astronomy & Astrophysics*, 25(1):23–81.
- Siódmiak, N. and Tyłenda, R. (2001). An analysis of the observed radio emission from planetary nebulae. *Astronomy & Astrophysics*, 373(3):1032–1042.
- Skrutskie, M., Cutri, R., Stiening, R., Weinberg, M., Schneider, S., Carpenter, J., Beichman, C., Capps, R., Chester, T., Elias, J., et al. (2006). The two micron all sky survey (2MASS). *The Astronomical Journal*, 131(2):1163.
- Smith, N., Jones, T. J., Gehrz, R. D., Klebe, D., and Creech-Eakman, M. J. (2001). Thermal infrared imaging of the bipolar H II region S106. *The Astronomical Journal*, 121(2):984.
- Smith, R. J., Glover, S. C., and Klessen, R. S. (2014). On the nature of star-forming filaments – I. Filament morphologies. *Monthly Notices of the Royal Astronomical Society*, 445(3):2900–2917.
- Stahler, S. W. and Palla, F. (2008). *The formation of stars*, volume 1. John Wiley & Sons.
- Stead, J. and Hoare, M. (2009). The slope of the near-infrared extinction law. *Monthly Notices of the Royal Astronomical Society*, 400(2):731–742.
- Steggles, H. (2016). *PhD Thesis*. University of Leeds.
- Steggles, H., Hoare, M., and Pittard, J. (2017). Hydrodynamical models of cometary H II regions. *Monthly Notices of the Royal Astronomical Society*, 466(4):4573–4591.
- Stelzer, B., Flaccomio, E., Montmerle, T., Micela, G., Sciortino, S., Favata, F., Preibisch, T., and Feigelson, E. (2005). X-ray emission from early-type stars in the orion nebula cluster. *The Astrophysical Journal Supplement Series*, 160(2):557.
- Stil, J. M., Taylor, A., Dickey, J., Kavars, D., Martin, P., Rothwell, T., Boothroyd, A., Lockman, F. J., and McClure-Griffiths, N. (2006). The vla galactic plane survey. *The Astronomical Journal*, 132(3):1158.
- Strömngren, B. (1939). The physical state of interstellar hydrogen. *The Astrophysical Journal*, 89:526.
- Takagi, S.-i., Murakami, H., and Koyama, K. (2002). X-ray sources and star formation activity in the Sagittarius B2 cloud observed with *Chandra*. *The Astrophysical Journal*, 573(1):275.
- Tan, J. C., Beltrán, M. T., Caselli, P., Fontani, F., Fuente, A., Krumholz, M. R., McKee, C. F., and Stolte, A. (2014). Massive star formation. *Protostars and Planets VI*, pages 149–172.

- Tenorio-Tagle, G. (1979). The gas dynamics of H II regions. I – The champagne model. *Astronomy & Astrophysics*, 71:59–65.
- Thompson, M., Beuther, H., Dickinson, C., Mottram, J., Klaassen, P., Ginsburg, A., Longmore, S., Remijan, A., and Menten, K. (2015). The ionised, radical and molecular Milky Way: spectroscopic surveys with the SKA. *Advancing Astrophysics with the Square Kilometre Array (AASKA14)*.
- Thompson, M., Goedhart, S., Goedhart, S., Benaglia, P., Beuther, H., Blomme, R., Chrysostomou, A., Clark, J., Dickinson, C., Ellingsen, S., et al. (2016). MeerGAL: the MeerKAT Galactic Plane Survey. *Proceedings of MeerKAT Science: On the Pathway to the SKA*.
- Thompson, M., Hatchell, J., Walsh, A., MacDonald, G., and Millar, T. (2006). A SCUBA imaging survey of ultracompact H II regions – the environments of massive star formation. *Astronomy & Astrophysics*, 453(3):1003–1026.
- Thompson, R. (1984). Lyman and Balmer continuum ionization in zero-age main-sequence stars – Applications to the line excess phenomenon. *The Astrophysical Journal*, 283:165–168.
- Tian, W. and Leahy, D. (2005). Radio spectral index variations of the SNR HB3. *Astronomy & Astrophysics*, 436(1):187–193.
- Tigé, J., Motte, F., Russeil, D., Zavagno, A., Hennemann, M., Schneider, N., Hill, T., Luong, Q. N., Di Francesco, J., Bontemps, S., et al. (2017). The earliest phases of high-mass star formation, as seen in NGC 6334 by *Herschel*-HOBYS. *Astronomy & Astrophysics*, 602:A77.
- Tsujimoto, M., Hosokawa, T., Feigelson, E., Getman, K., and Broos, P. (2006). Hard x-rays from ultracompact H II regions in w49a. *The Astrophysical Journal*, 653(1):409.
- Urquhart, J., Hoare, M., Lumsden, S., Oudmaijer, R., and Moore, T. (2008). The RMS Survey: A Galaxy-wide Sample of Massive Young Stellar Objects. *Massive Star Formation: Observations Confront Theory*, 387:381.
- Urquhart, J., Hoare, M., Lumsden, S., Oudmaijer, R., Moore, T., Mottram, J., Cooper, H., Mottram, M., and Rogers, H. (2012). The RMS survey: resolving kinematic distance ambiguities towards a sample of compact H II regions using H I absorption. *Monthly Notices of the Royal Astronomical Society*, 420(2):1656–1672.
- Urquhart, J., Hoare, M. G., Purcell, C., Lumsden, S. L., Oudmaijer, R. D., Moore, T. J., Busfield, A., Mottram, J. C., and Davies, B. (2009). The RMS survey-6 cm continuum VLA observations towards candidate massive YSOs in the northern hemisphere. *Astronomy & Astrophysics*, 501(2):539–551.
- Urquhart, J., Moore, T. J., Hoare, M. G., Lumsden, S. L., Oudmaijer, R. D., Rathborne, J., Mottram, J. C., Davies, B., and Stead, J. J. (2010). The red msx source survey: distribution and properties of a sample of massive young stars. *Monthly Notices of the Royal Astronomical Society*, 410(2):1237–1250.

- Urquhart, J., Morgan, L., Figura, C., Moore, T., Lumsden, S., Hoare, M., Oudmaijer, R., Mottram, J., Davies, B., and Dunham, M. (2011). The Red MSX Source survey: ammonia and water maser analysis of massive star-forming regions. *Monthly Notices of the Royal Astronomical Society*, 418:1689–1706.
- Urquhart, J., Thompson, M., Moore, T., Purcell, C., Hoare, M., Schuller, F., Wyrowski, F., Csengeri, T., Menten, K., Lumsden, S., et al. (2013). ATLASGAL—properties of compact H II regions and their natal clumps. *Monthly Notices of the Royal Astronomical Society*, 435(1):400–428.
- Urquhart, J. S., Busfield, A., Hoare, M. G., Lumsden, S. L., Clarke, A., Moore, T. J., Mottram, J. C., and Oudmaijer, R. D. (2007). The RMS survey – radio observations of candidate massive YSOs in the southern hemisphere. *Astronomy & Astrophysics*, 461(1):11–23.
- Vacca, W. D., Garmany, C. D., and Shull, J. M. (1996). The Lyman-continuum fluxes and stellar parameters of O and early B-type stars. *Astrophys. J.*, 460:914.
- Van Buren, D., Mac Low, M.-M., Wood, D. O., and Churchwell, E. (1990). Cometary compact H II regions are stellar-wind bow shocks. *The Astrophysical Journal*, 353:570–578.
- Veen, P., Van Genderen, A., Van Der Hucht, K., Li, A., Sterken, C., Dominik, C., et al. (1998). WR 121 obscured by a dust cloud: the key to understanding occasional ‘eclipses’ of ‘dusty’ Wolf-Rayet WC stars? *Astronomy & Astrophysics*, 329:199.
- Veneziani, M., Elia, D., Noriega-Crespo, A., Paladini, R., Carey, S., Faimali, A., Molinari, S., Pestalozzi, M., Piacentini, F., Schisano, E., et al. (2013). An analysis of star formation with *Herschel* in the Hi-GAL survey-I. The science demonstration phase fields. *Astronomy & Astrophysics*, 549:A130.
- Walsh, A., Burton, M., Hyland, A., and Robinson, G. (1998). Studies of ultracompact H II regions—II. High-resolution radio continuum and methanol maser survey. *Monthly Notices of the Royal Astronomical Society*, 301:640–698.
- Walsh, A. J., Breen, S., Britton, T., Brooks, K., Burton, M. G., Cunningham, M., Green, J., Harvey-Smith, L., Hindson, L., Hoare, M. G., et al. (2011). The H<sub>2</sub>O Southern Galactic Plane Survey (HOPS) – I. Techniques and H<sub>2</sub>O maser data. *Monthly Notices of the Royal Astronomical Society*, 416(3):1764–1821.
- Watson, A. M., Coil, A. L., Shepherd, D. S., Hofner, P., and Churchwell, E. (1997). Direct observations of the ionizing star in the ultracompact H II region G29.96-0.02: A strong constraint on the stellar birth line for massive stars. *The Astrophysical Journal*, 487(2):818.
- Watson, C., Povich, M., Churchwell, E., Babler, B., Chunev, G., Hoare, M., Indebetouw, R., Meade, M., Robitaille, T., and Whitney, B. (2008). Infrared dust bubbles: Probing the detailed structure and young massive stellar populations of Galactic H II regions. *The Astrophysical Journal*, 681(2):1341.

- Weaver, R., McCray, R., Castor, J., Shapiro, P., and Moore, R. (1977). Interstellar bubbles. ii-structure and evolution. *The Astrophysical Journal*, 218:377–395.
- Weidmann, W. A., Gamen, R., van Hoof, P., Zijlstra, A., Minniti, D., and Volpe, M. G. (2013). Near-infrared photometry of galactic planetary nebulae with the VVV survey. *Astronomy & Astrophysics*, 552:A74.
- Weisskopf, M. C., Tananbaum, H. D., Van Speybroeck, L. P., and O’Dell, S. L. (2000). *Chandra* X-ray Observatory (CXO): overview. In *X-Ray Optics, Instruments, and Missions III*, volume 4012, pages 2–17. International Society for Optics and Photonics.
- Wendker, H., Schramm, K., and Dieckvoss, C. (1983). The Cygnus X region. XIII-The dark cloud between IC 1318b and C. *Astronomy and Astrophysics*, 121:69–76.
- White, R. L., Becker, R. H., and Helfand, D. J. (2005). New catalogs of compact radio sources in the Galactic plane. *The Astronomical Journal*, 130(2):586.
- Williams, J., Blitz, L., and McKee, C. (2000). Protostars and planets IV, ed.
- Willner, S., Becklin, E., and Visvanathan, N. (1972). Observations of planetary nebulae at 1.65 to 3.4 microns. *The Astrophysical Journal*, 175:699.
- Wilms, J., Allen, A., and McCray, R. (2000). On the absorption of X-rays in the interstellar medium. *The Astrophysical Journal*, 542(2):914.
- Wilson, T. L., Rohlfs, K., and Hüttemeister, S. (2009). *Tools of radio astronomy*, volume 5. Springer.
- Wood, D. O. and Churchwell, E. (1989a). Massive stars embedded in molecular clouds – their population and distribution in the Galaxy. *The Astrophysical Journal*, 340:265–272.
- Wood, D. O. and Churchwell, E. (1989b). The morphologies and physical properties of ultracompact H II regions. *The Astrophysical Journal Supplement Series*, 69:831–895.
- Yan, M., Sadeghpour, H., and Dalgarno, A. (1998). Photoionization cross sections of He and H<sub>2</sub>. *The Astrophysical Journal*, 496(2):1044.
- Yang, A., Thompson, M., Tian, W., Bihr, S., Beuther, H., and Hindson, L. (2018). A search for hypercompact H II regions in the Galactic plane. *Monthly Notices of the Royal Astronomical Society*, 482(2):2681–2696.
- Zhu, H., Tian, W., Li, A., and Zhang, M. (2017). The gas-to-extinction ratio and the gas distribution in the galaxy. *Monthly Notices of the Royal Astronomical Society*, 471(3):3494–3528.
- Zhu, Q.-F., Lacy, J. H., Jaffe, D. T., Richter, M. J., and Greathouse, T. K. (2008). [Ne II] observations of gas motions in compact and ultracompact H II regions. *The Astrophysical Journal Supplement Series*, 177(2):584.

- Zinnecker, H. (2004). The formation and evolution of massive young star clusters. *ASP Conf. Ser.*, 322:349–358.
- Zinnecker, H. (2006). Gamma ray bursts from proto-globular clusters? In *Stellar Evolution at Low Metallicity: Mass Loss, Explosions, Cosmology*, volume 353, page 339.
- Zinnecker, H. and Yorke, H. W. (2007). Toward understanding massive star formation. *Annu. Rev. Astron. Astrophys.*, 45:481–563.
- Zoonematkermani, S., Helfand, D., Becker, R., White, R., and Perley, R. (1990). A catalog of small-diameter radio sources in the Galactic plane. *The Astrophysical Journal Supplement Series*, 74:181–224.

# Appendix A

## Radio fluxes and spectral indices

Table A.1 Fluxes of the MAGPIS counterparts to CORNISH UCHIIs at 6 cm and 20 cm, as remeasured in this work (described in §2.3.1), and computed spectral indices (CORNISH 6 cm – MAGPIS 20 cm). Missing values are due to missing MAGPIS 6 cm images. In all cases of unreliable photometric results or non-detections, the  $3\sigma$  upper limits are included.

Name	$S_C$ (mJy)	$S_{M,6\text{cm}}$ (mJy)	$S_{M,20\text{cm}}$ (mJy)	$\alpha_{C6\text{cm}-M20\text{cm}}$
G010.3009–00.1477	$631.39 \pm 59.3$	$1169.19 \pm 9.41$	$456.88 \pm 74.73$	$0.25 \pm 0.15$
G010.3204–00.2328	$32.43 \pm 5$	$<28.78$	$48.94 \pm 2.56$	$-0.32 \pm 0.13$
G010.3204–00.2586	$18.2 \pm 2.26$	$47.09 \pm 3.28$	$38.2 \pm 1.97$	$-0.58 \pm 0.11$
G010.4724+00.0275	$38.43 \pm 4.38$	$92.82 \pm 1.35$	$20.69 \pm 3.36$	$0.49 \pm 0.16$
G010.4736+00.0274	$19.3 \pm 2.39$	$94.83 \pm 1.01$	$17.68 \pm 3.02$	$0.07 \pm 0.17$
G010.6218–00.3848	$37.06 \pm 4.04$	$1238.9 \pm 2.96$	$167.89 \pm 4.76$	$-1.19 \pm 0.09$
G010.6223–00.3788	$483.33 \pm 49.87$	$1039.47 \pm 7.42$	$518.5 \pm 15.91$	$-0.06 \pm 0.08$
G010.6234–00.3837	$1952.22 \pm 176.18$	$3921.35 \pm 6.97$	$747.85 \pm 14.52$	$0.75 \pm 0.07$
G010.6240–00.3813	$71.65 \pm 7.24$	$492.7 \pm 2.53$	$237.88 \pm 8.45$	$-0.94 \pm 0.08$
G010.6297–00.3380	$26.39 \pm 4.29$	$44.91 \pm 2.27$	$74.02 \pm 1.42$	$-0.81 \pm 0.13$
G010.8519–00.4407	$11.09 \pm 1.46$		$7.92 \pm 0.53$	$0.26 \pm 0.12$
G010.9584+00.0221	$195.97 \pm 18.33$	$326.65 \pm 1.39$	$43.71 \pm 1.19$	$1.18 \pm 0.08$
G010.9656+00.0089	$51.75 \pm 6.1$	$206.89 \pm 2.11$	$141.83 \pm 9.47$	$-0.79 \pm 0.11$
G011.0328+00.0274	$5.69 \pm 1.06$	$<4.14$	$4.06 \pm 1.07$	$0.26 \pm 0.25$
G011.1104–00.3985	$305.37 \pm 28.55$	$303.63 \pm 9.12$	$326.73 \pm 3.86$	$-0.05 \pm 0.07$
G011.1712–00.0662	$102.17 \pm 12.73$	$131.49 \pm 5.72$	$77.43 \pm 4.17$	$0.22 \pm 0.11$
G011.9032–00.1407	$25.57 \pm 3.3$	$83.07 \pm 1.68$	$30.46 \pm 0.89$	$-0.14 \pm 0.1$
G011.9039–00.1411	$16.81 \pm 1.88$	$69.77 \pm 1.08$	$25.13 \pm 0.56$	$-0.32 \pm 0.09$
G011.9368–00.6158	$1155.9 \pm 105.38$		$690.47 \pm 5.18$	$0.4 \pm 0.07$

Continued on next page

Table A.1 – continued from previous page

Name	$S_C$ (mJy)	$S_{M,6cm}$ (mJy)	$S_{M,20cm}$ (mJy)	$\alpha_{C6cm-M20cm}$
G011.9446–00.0369	943.58 ± 98.5	2036.45 ± 24.35	1116.9 ± 77	−0.13 ± 0.1
G011.9786–00.0973	4.46 ± 1.08	<6.82	<2.64	>0.41
G012.1988–00.0345	62.71 ± 5.92	102.95 ± 1.47	42.52 ± 1.34	0.31 ± 0.08
G012.2081–00.1019	207.87 ± 19.73	309.84 ± 3.25	115.09 ± 5.64	0.46 ± 0.08
G012.4294–00.0479	45.17 ± 4.35	103.16 ± 4.93	56.7 ± 3.79	−0.18 ± 0.09
G012.8050–00.2007	12616.4 ± 1120.83	26528.17 ± 88.83	6884.66 ± 10.35	0.48 ± 0.07
G012.8131–00.1976	1500.39 ± 147.3	593.9 ± 103.73	731.91 ± 4.37	0.56 ± 0.08
G012.9995–00.3583	20.14 ± 3.7	6.68 ± 0.62	4.28 ± 0.34	1.22 ± 0.16
G013.2099–00.1428	946.76 ± 87.46	1864.65 ± 10.02	818.4 ± 9.95	0.11 ± 0.07
G013.3850+00.0684	603.94 ± 60.83	1223.45 ± 21.43	953.46 ± 9.06	−0.36 ± 0.08
G013.8726+00.2818	1447.55 ± 129.84	4276.31 ± 22.89	2422 ± 16.98	−0.4 ± 0.07
G014.1046+00.0918	24.61 ± 3.11	83.46 ± 4.89	66.7 ± 1.56	−0.78 ± 0.1
G014.1741+00.0245	47.73 ± 7.42	139.51 ± 2.76	86.1 ± 1.69	−0.46 ± 0.12
G014.2460–00.0728	51.26 ± 6.18	87.89 ± 3.65	63.45 ± 1.29	−0.17 ± 0.1
G014.5988+00.0198	4.39 ± 1.09	<3.45	7.14 ± 1.92	−0.38 ± 0.29
G014.7785–00.3328	18.25 ± 2.47	39.47 ± 1.08	<12.66	>0.29
G016.1448+00.0088	14.76 ± 1.55	27.8 ± 1.15	6.87 ± 0.52	0.6 ± 0.1
G016.3913–00.1383	124.27 ± 15.43	43.18 ± 3.61	57.52 ± 5.18	0.61 ± 0.12
G016.9445–00.0738	519.34 ± 47.78	901.84 ± 5.5	242.3 ± 4.44	0.6 ± 0.07
G017.0299–00.0696	5.38 ± 1.06	<7.01	<4.75	>0.10
G017.1141–00.1124	17.21 ± 2.19	34.3 ± 1.93	21.07 ± 2.01	−0.16 ± 0.13
G017.5549+00.1654	7.13 ± 1.22	12.15 ± 1.65	7.9 ± 1.28	−0.08 ± 0.19
G017.9850+00.1266	10.42 ± 2.07	18.55 ± 2.7	10.11 ± 1.11	0.02 ± 0.18
G018.1460–00.2839	856.18 ± 82.85	546.59 ± 33.33	1084.54 ± 342.92	−0.19 ± 0.26
G018.3024–00.3910	1277.88 ± 114.83	2032.05 ± 23.59	1372.98 ± 26.86	−0.06 ± 0.07
G018.4433–00.0056	81.31 ± 7.3	116.98 ± 2.35	56.96 ± 4.46	0.28 ± 0.09
G018.4614–00.0038	342.12 ± 31.5	548.25 ± 2.21	117.05 ± 4.72	0.84 ± 0.08
G018.6654+00.0294	5.65 ± 0.85	7.57 ± 1.45	3.7 ± 0.42	0.33 ± 0.15
G018.7106+00.0002	107.46 ± 10.62	177.74 ± 1.71	36.6 ± 0.94	0.85 ± 0.08
G018.7612+00.2630	51.38 ± 4.67	31.23 ± 2.24	21.99 ± 0.61	0.67 ± 0.07
G018.8250–00.4675	11.41 ± 2.17		<7.83	>0.30
G018.8338–00.3002	131.38 ± 13.35	219.21 ± 3.86	103.4 ± 1.73	0.19 ± 0.08
G019.0035+00.1280	6.41 ± 1.52	<9.77	5.06 ± 0.56	0.19 ± 0.21
G019.0754–00.2874	380.69 ± 37.06	605.36 ± 7.04	472.33 ± 27.38	−0.17 ± 0.09
G019.0767–00.2882	129.48 ± 13.15	231.03 ± 1.95	123.2 ± 5.79	0.04 ± 0.09
G019.4752+00.1728	37.22 ± 4.56	58.72 ± 2.55	41.58 ± 0.89	−0.09 ± 0.1
G019.6087–00.2351	2900.88 ± 260.93	5170.32 ± 17.38	2170.95 ± 7.04	0.23 ± 0.07
G019.6090–00.2313	259.95 ± 26.87	1079.53 ± 3.43	512.96 ± 2.52	−0.53 ± 0.08
G019.7281–00.1135	26.23 ± 3.09	27.19 ± 1.41	29 ± 0.61	−0.08 ± 0.09

Continued on next page

Table A.1 – continued from previous page

Name	$S_C$ (mJy)	$S_{M,6cm}$ (mJy)	$S_{M,20cm}$ (mJy)	$\alpha_{C6cm-M20cm}$
G019.7549–00.1282	$36.52 \pm 3.29$	$46.08 \pm 0.73$	$8.91 \pm 0.3$	$1.11 \pm 0.08$
G020.0720–00.1421	$210.13 \pm 21.54$	$416.03 \pm 3.51$	$211.18 \pm 7.05$	$0 \pm 0.08$
G020.0797–00.1337	$14.09 \pm 1.91$	$89.89 \pm 1.23$	$45.64 \pm 0.77$	$-0.92 \pm 0.11$
G020.0809–00.1362	$498.19 \pm 45.06$	$857.54 \pm 1.3$	$135.56 \pm 0.9$	$1.02 \pm 0.07$
G020.3633–00.0136	$55.11 \pm 5.93$	$98.78 \pm 1.33$	$53.41 \pm 0.62$	$0.02 \pm 0.09$
G020.7619–00.0646	$10.03 \pm 2.08$	$20.82 \pm 6.97$	$13.62 \pm 2.06$	$-0.24 \pm 0.2$
G020.9636–00.0744	$11.28 \pm 1.84$	$16.75 \pm 1.8$	$14.24 \pm 0.57$	$-0.18 \pm 0.13$
G021.3571–00.1766	$24.93 \pm 2.34$	$44.61 \pm 2.46$	$16.13 \pm 0.49$	$0.34 \pm 0.08$
G021.3855–00.2541	$113.91 \pm 11.24$	$207.13 \pm 4.78$	$46.24 \pm 0.76$	$0.71 \pm 0.08$
G021.6034–00.1685	$19.84 \pm 3.45$	$46.78 \pm 1.32$	$29.12 \pm 0.81$	$-0.3 \pm 0.14$
G021.8751+00.0075	$566.73 \pm 54.14$	$1064.73 \pm 8.85$	$685.9 \pm 7.84$	$-0.15 \pm 0.08$
G023.1974–00.0006	$10.01 \pm 1.54$	$18.65 \pm 1.24$	$13.27 \pm 0.73$	$-0.22 \pm 0.13$
G023.2654+00.0765	$88.57 \pm 9.87$	$149.89 \pm 4.39$	$90.95 \pm 0.96$	$-0.02 \pm 0.09$
G023.4553–00.2010	$14.39 \pm 1.56$	$<3.16$	$<6.18$	$>0.66$
G023.4835+00.0964	$8.23 \pm 1.39$	$<7.96$	$7.35 \pm 0.55$	$0.09 \pm 0.15$
G023.7110+00.1705	$208.5 \pm 20.34$	$548.53 \pm 1.38$	$279.31 \pm 33.22$	$-0.23 \pm 0.12$
G023.8618–00.1250	$39.16 \pm 6.29$	$38.86 \pm 2.59$	$48.71 \pm 1.63$	$-0.17 \pm 0.13$
G023.8985+00.0647	$43.42 \pm 5.45$	$115.83 \pm 5.25$	$102.69 \pm 1.07$	$-0.68 \pm 0.1$
G023.9564+00.1493	$1161.18 \pm 104.78$	$2658.26 \pm 8.5$	$1319.94 \pm 13.31$	$-0.1 \pm 0.07$
G024.1839+00.1199	$3.79 \pm 0.79$	$<3.44$	$3.39 \pm 0.39$	$0.09 \pm 0.19$
G024.4698+00.4954	$29.5 \pm 4.53$		$<276.17$	$>-1.78$
G024.4721+00.4877	$55.19 \pm 7.73$		$257.36 \pm 20.99$	$-1.21 \pm 0.13$
G024.4736+00.4950	$99.43 \pm 12.24$		$<404.40$	$>-1.10$
G024.4921–00.0386	$140.12 \pm 13.5$	$332.61 \pm 2.12$	$173.02 \pm 1.82$	$-0.17 \pm 0.08$
G024.5065–00.2224	$205.57 \pm 19.72$	$458.99 \pm 9.78$	$266.55 \pm 34.34$	$-0.2 \pm 0.13$
G024.8497+00.0881	$19.93 \pm 3.82$	$20.98 \pm 6.23$	$91.44 \pm 18.7$	$-1.2 \pm 0.22$
G025.3809–00.1815	$460.83 \pm 42.66$	$1799.06 \pm 7.23$	$992.44 \pm 112.85$	$-0.6 \pm 0.12$
G025.3824–00.1812	$200.13 \pm 20.03$	$929.75 \pm 2.71$	$419.49 \pm 42.51$	$-0.58 \pm 0.11$
G025.3948+00.0332	$296.86 \pm 27.46$	$549.92 \pm 3.95$	$303.63 \pm 6.08$	$-0.02 \pm 0.07$
G025.3970+00.5614	$121.17 \pm 11.53$		$63.72 \pm 0.5$	$0.5 \pm 0.08$
G025.3981–00.1411	$2132.24 \pm 194.31$	$4590.88 \pm 10.91$	$1837.09 \pm 10.65$	$0.12 \pm 0.07$
G025.3983+00.5617	$51.93 \pm 4.82$		$71.21 \pm 0.59$	$-0.25 \pm 0.07$
G025.3991–00.1366	$29.38 \pm 6.41$		$197.73 \pm 1.92$	$-1.5 \pm 0.17$
G025.7157+00.0487	$20.79 \pm 2.96$	$<6.82$	$18.63 \pm 0.91$	$0.09 \pm 0.12$
G025.8011–00.1568	$31.95 \pm 2.96$	$56.84 \pm 1.25$	$17.07 \pm 0.53$	$0.49 \pm 0.08$
G026.0083+00.1369	$6.58 \pm 1.03$	$8.13 \pm 2$	$2.77 \pm 0.39$	$0.68 \pm 0.17$
G026.0916–00.0565	$11.59 \pm 2.13$	$110.38 \pm 4.56$	$80.36 \pm 6.89$	$-1.52 \pm 0.16$
G026.1094–00.0937	$4.72 \pm 0.84$	$<7.73$	$<8.57$	$>-0.47$
G026.5976–00.0236	$69.92 \pm 7.45$	$145.65 \pm 2.86$	$67.39 \pm 1.9$	$0.03 \pm 0.09$

Continued on next page

Table A.1 – continued from previous page

Name	$S_C$ (mJy)	$S_{M,6cm}$ (mJy)	$S_{M,20cm}$ (mJy)	$\alpha_{C6cm-M20cm}$
G026.6089–00.2121	201.41 ± 21.67	380.66 ± 6.04	207.49 ± 1.26	−0.02 ± 0.08
G026.8304–00.2067	12.31 ± 1.51	19.08 ± 2.28	12.92 ± 0.33	−0.04 ± 0.1
G027.1859–00.0816	19.78 ± 2.17	30.5 ± 1.63	27.48 ± 0.24	−0.26 ± 0.09
G027.2800+00.1447	428.04 ± 42.07	769.86 ± 3.98	390.46 ± 23.49	0.07 ± 0.09
G027.3644–00.1657	60.14 ± 6.13	98.6 ± 1.54	39.44 ± 0.85	0.33 ± 0.08
G027.5637+00.0845	162.53 ± 18.81	149.05 ± 7.96	153.85 ± 2.94	0.04 ± 0.09
G027.9352+00.2056	4.44 ± 1.04	20.34 ± 1.24	8.16 ± 0.66	−0.48 ± 0.19
G028.1985–00.0503	136.26 ± 12.94	395.1 ± 2.08	130.88 ± 1.17	0.03 ± 0.07
G028.2003–00.0494	161.66 ± 15.59	395.27 ± 2.07	91.59 ± 1.24	0.45 ± 0.08
G028.2879–00.3641	552.77 ± 51.9	939.64 ± 4.66	381.7 ± 1.56	0.29 ± 0.07
G028.4518+00.0027	33.75 ± 3.22	73.57 ± 2	50.21 ± 2.52	−0.31 ± 0.08
G028.5816+00.1447	40.03 ± 7.76	65.99 ± 2.2	44.2 ± 0.81	−0.08 ± 0.15
G028.6082+00.0185	210.15 ± 20.28	379.49 ± 3.61	171.16 ± 1.93	0.16 ± 0.08
G028.6523+00.0273	228.85 ± 22.02	439.25 ± 2.75	255.07 ± 3.97	−0.09 ± 0.08
G028.6869+00.1770	102.98 ± 11.05	145.12 ± 3.36	123.81 ± 1.14	−0.14 ± 0.08
G029.7704+00.2189	49.98 ± 8.84	36.37 ± 5.17	82.1 ± 1.63	−0.39 ± 0.14
G029.9559–00.0168	3116.2 ± 296.94	5643.42 ± 9.45	1935.82 ± 55.93	0.37 ± 0.08
G030.0096–00.2734	4.54 ± 0.94	5.1 ± 1.31	<1.32	>0.97
G030.2527+00.0540	96.79 ± 10.2	158.43 ± 5.97	127.15 ± 3.02	−0.21 ± 0.08
G030.5313+00.0205	85.54 ± 9.65	488.53 ± 2.75	243.43 ± 4.33	−0.82 ± 0.09
G030.5353+00.0204	710.36 ± 66.36	1385.62 ± 4.56	557.91 ± 19.1	0.19 ± 0.08
G030.5887–00.0428	92.37 ± 8.33	99.57 ± 2.56	5.93 ± 0.99	2.16 ± 0.15
G030.6881–00.0718	466.99 ± 45.69	992.36 ± 9.39	656.15 ± 75.69	−0.27 ± 0.12
G030.7197–00.0829	969.33 ± 96.01	873.67 ± 4.51	430.79 ± 15.79	0.64 ± 0.08
G030.7532–00.0511	301.66 ± 29.35	165.02 ± 4.59	<551.85	>−0.47
G030.7579+00.2042	26.23 ± 6.12	<4.78	38.8 ± 1.62	−0.31 ± 0.19
G030.7661–00.0348	87.53 ± 14.67	<19.92	<262.05	>−0.86
G030.8662+00.1143	325.47 ± 32.96	476.58 ± 3.15	133.59 ± 2.15	0.7 ± 0.08
G030.9581+00.0869	25.79 ± 4.68	18.13 ± 3.13	45.36 ± 0.8	−0.44 ± 0.14
G031.0495+00.4697	13.64 ± 1.49		9.29 ± 2.44	0.3 ± 0.22
G031.0595+00.0922	11.7 ± 1.51	16.49 ± 3.31	22.06 ± 3.74	−0.5 ± 0.17
G031.1590+00.0465	7.04 ± 1.26	8.65 ± 1.42	10.45 ± 0.87	−0.31 ± 0.15
G031.1596+00.0448	23.83 ± 2.28	19.34 ± 1.29	17.06 ± 0.95	0.26 ± 0.09
G031.2420–00.1106	296.24 ± 27.05	800.06 ± 4.23	476.69 ± 2.51	−0.37 ± 0.07
G031.2435–00.1103	353.06 ± 32.36	601.08 ± 2.7	279 ± 1.02	0.18 ± 0.07
G031.2448–00.1132	37.39 ± 4.2	46.07 ± 1.94	56.56 ± 1.27	−0.33 ± 0.09
G031.2801+00.0632	268.86 ± 25.67	593.67 ± 9.48	325.13 ± 3.15	−0.15 ± 0.08
G031.3959–00.2570	80.96 ± 10.38	195.56 ± 9.22	170.16 ± 22.76	−0.58 ± 0.15
G031.4130+00.3065	954.8 ± 87.99	1798.53 ± 14.61	927.3 ± 4.15	0.02 ± 0.07

Continued on next page

Table A.1 – continued from previous page

Name	$S_C$ (mJy)	$S_{M,6cm}$ (mJy)	$S_{M,20cm}$ (mJy)	$\alpha_{C6cm-M20cm}$
G031.5815+00.0744	14.48 ± 1.89	20.26 ± 3.03	17.83 ± 1.09	-0.16 ± 0.11
G032.0297+00.0491	26.68 ± 3.82	34.34 ± 2.6	29.25 ± 1.06	-0.07 ± 0.12
G032.1502+00.1329	533.63 ± 59.66	1207.3 ± 16.24	631.48 ± 9.29	-0.13 ± 0.09
G032.2730-00.2258	309.28 ± 34.38	735.13 ± 7.64	307.37 ± 3.27	0 ± 0.09
G032.4727+00.2036	97.38 ± 9.67	180.96 ± 2.05	48.75 ± 0.59	0.54 ± 0.08
G032.7398+00.1940	3.39 ± 0.78	3.23 ± 0.9	2.45 ± 0.73	0.26 ± 0.3
G032.7492-00.0643	13.12 ± 1.67	12.82 ± 2.5	14.42 ± 1	-0.07 ± 0.11
G032.7966+00.1909	3123.37 ± 281.38	3841.71 ± 10.04	1445.26 ± 6.98	0.61 ± 0.07
G032.7982+00.1937	17.22 ± 2		13.18 ± 2.22	0.21 ± 0.16
G032.9273+00.6060	285.57 ± 31.27		260.63 ± 4.14	0.07 ± 0.09
G033.1328-00.0923	378.59 ± 34.75	949.93 ± 5.99	192.26 ± 1.36	0.53 ± 0.07
G033.4163-00.0036	75.16 ± 9.16	173.65 ± 11.75	108.73 ± 4.87	-0.29 ± 0.1
G033.8100-00.1864	107.63 ± 10.51	152.81 ± 1.64	59.67 ± 1.2	0.46 ± 0.08
G033.9145+00.1105	842.22 ± 88.66	1661.36 ± 15.8	803.4 ± 7.5	0.04 ± 0.08
G034.0901+00.4365	9.62 ± 1.9		35.22 ± 4.34	-1.02 ± 0.18
G034.1978-00.5912	10.54 ± 2.42		13.14 ± 1.13	-0.17 ± 0.19
G034.2544+00.1460	352.37 ± 39.13	1625.53 ± 42.08	<1031.69	>-0.84
G034.2571+00.1466	47.8 ± 8.94	937.04 ± 59.69	<678.32	>-2.08
G034.2572+00.1535	1762.63 ± 163.28	2771.66 ± 11.59	655.95 ± 4	0.78 ± 0.07
G034.4032+00.2277	8.92 ± 1.24	14.97 ± 1.18	4.08 ± 0.74	0.61 ± 0.18
G034.5920+00.2434	20.23 ± 2.4	35.02 ± 2.23	18.19 ± 0.89	0.08 ± 0.1
G035.0242+00.3502	11.44 ± 1.23	22.25 ± 0.6	2.78 ± 0.63	1.11 ± 0.2
G035.0524-00.5177	67.75 ± 7.56		125.86 ± 1.7	-0.49 ± 0.09
G035.4570-00.1791	7.52 ± 1.07	12.75 ± 0.89	6.43 ± 0.7	0.12 ± 0.14
G035.4669+00.1394	317.6 ± 29.36	573.76 ± 5.67	249.89 ± 1.4	0.19 ± 0.07
G035.5781-00.0305	187.75 ± 18.44	252.49 ± 2.34	68.91 ± 1.39	0.79 ± 0.08
G036.4057+00.0226	22.34 ± 2.21	58.2 ± 2.01	20.9 ± 0.78	0.05 ± 0.08
G036.4062+00.0221	9.31 ± 1.15	52.18 ± 1.76	18.82 ± 0.7	-0.55 ± 0.1
G037.5457-00.1120	406.46 ± 41.28	913.02 ± 20.15	454.75 ± 8.67	-0.09 ± 0.08
G037.7347-00.1128	16.02 ± 1.63	<2.28	9.54 ± 1.04	0.41 ± 0.12
G037.7562+00.5605	35.68 ± 8.12		43.73 ± 2.4	-0.16 ± 0.18
G037.8197+00.4140	25.99 ± 4.33	81.53 ± 3.1	36.66 ± 1.22	-0.27 ± 0.13
G037.8209+00.4125	20.24 ± 2.72	51.89 ± 2.14	29.07 ± 0.9	-0.28 ± 0.11
G037.8683-00.6008	210.28 ± 21.72		237.48 ± 1.86	-0.1 ± 0.08
G037.8731-00.3996	2561.21 ± 234.04	5189.35 ± 23.38	1769.56 ± 6.57	0.29 ± 0.07
G037.9723-00.0965	20.89 ± 2.52	26.37 ± 2.96	19.41 ± 0.77	0.06 ± 0.1
G038.5493+00.1646	88.3 ± 11.26	248.94 ± 4.7	138.65 ± 1.73	-0.35 ± 0.1
G038.6465-00.2260	11.52 ± 1.98	35.13 ± 1.76	19.09 ± 0.91	-0.4 ± 0.14
G038.6529+00.0875	7.84 ± 1.04	36.01 ± 1.54	12.96 ± 0.57	-0.39 ± 0.11

Continued on next page

Table A.1 – continued from previous page

Name	$S_C$ (mJy)	$S_{M,6cm}$ (mJy)	$S_{M,20cm}$ (mJy)	$\alpha_{C6cm-M20cm}$
G038.6934–00.4524	$19.88 \pm 2.44$		$21.86 \pm 0.88$	$-0.07 \pm 0.1$
G038.8756+00.3080	$311.31 \pm 29.87$	$599.65 \pm 2.25$	$215.24 \pm 1.37$	$0.29 \pm 0.08$
G039.1956+00.2255	$62.27 \pm 6.41$	$100.08 \pm 1.72$	$27.91 \pm 0.74$	$0.63 \pm 0.08$
G039.8824–00.3460	$276.87 \pm 26.38$	$636.36 \pm 3.18$	$236.6 \pm 1.31$	$0.12 \pm 0.07$
G040.4251+00.7002	$11.1 \pm 2.42$		$25.95 \pm 0.99$	$-0.67 \pm 0.17$
G041.7419+00.0973	$227.4 \pm 23.95$	$584.48 \pm 8.18$	$289.36 \pm 2.11$	$-0.19 \pm 0.08$
G042.1090–00.4469	$14.8 \pm 1.53$		$19.72 \pm 0.54$	$-0.23 \pm 0.08$
G042.4345–00.2605	$83.65 \pm 9.25$		$127.2 \pm 8.07$	$-0.33 \pm 0.1$
G043.1460+00.0139	$694.6 \pm 69.66$		$924.55 \pm 4.97$	$-0.22 \pm 0.08$
G043.1489+00.0130	$44.13 \pm 6.07$		$266.28 \pm 5.85$	$-1.41 \pm 0.11$
G043.1520+00.0115	$306.63 \pm 34.78$		$462.01 \pm 49.65$	$-0.32 \pm 0.12$
G043.1651–00.0283	$2714.29 \pm 262.82$		$2011.44 \pm 89.31$	$0.24 \pm 0.08$
G043.1652+00.0129	$160.07 \pm 17.72$		$120.87 \pm 37.07$	$0.22 \pm 0.26$
G043.1657+00.0116	$98.25 \pm 10.44$		$374.41 \pm 30.64$	$-1.05 \pm 0.11$
G043.1665+00.0106	$1365.68 \pm 125.16$		$743.01 \pm 51.46$	$0.48 \pm 0.09$
G043.1674+00.0128	$74.54 \pm 9.28$		$199.37 \pm 29.72$	$-0.77 \pm 0.15$
G043.1677+00.0196	$115.47 \pm 17.88$		$478.89 \pm 39.85$	$-1.12 \pm 0.14$
G043.1684+00.0087	$185.25 \pm 21.98$		$633.19 \pm 67.95$	$-0.97 \pm 0.13$
G043.1684+00.0124	$63.6 \pm 6.86$		$185.7 \pm 47.2$	$-0.84 \pm 0.22$
G043.1699+00.0115	$43.79 \pm 7.45$		$248.48 \pm 68.98$	$-1.36 \pm 0.26$
G043.1701+00.0078	$1108.08 \pm 103.11$		$1863.27 \pm 630.08$	$-0.41 \pm 0.28$
G043.1706–00.0003	$170.72 \pm 16.13$		$349.99 \pm 77.45$	$-0.56 \pm 0.19$
G043.1716+00.0001	$51.74 \pm 11.17$		$466.43 \pm 137.69$	$-1.73 \pm 0.29$
G043.1720+00.0080	$98.59 \pm 12.52$		$<724.09$	$>-1.57$
G043.1763+00.0248	$159.42 \pm 21.7$		$610.27 \pm 27.29$	$-1.05 \pm 0.11$
G043.1778–00.5181	$181.65 \pm 23.04$		$206.16 \pm 3.51$	$-0.1 \pm 0.1$
G043.2371–00.0453	$178.78 \pm 20.41$		$383.53 \pm 3.41$	$-0.6 \pm 0.09$
G043.3064–00.2114	$20.08 \pm 3.25$		$<7.44$	$>0.78$
G043.7954–00.1274	$24.58 \pm 2.97$		$14.63 \pm 0.92$	$0.41 \pm 0.11$
G043.7960–00.1286	$9.78 \pm 1.94$		$19.24 \pm 0.84$	$-0.53 \pm 0.16$
G043.8894–00.7840	$528.18 \pm 48.82$		$367.2 \pm 2.91$	$0.29 \pm 0.07$
G044.3103+00.0410	$5.47 \pm 0.94$		$4.47 \pm 0.65$	$0.16 \pm 0.18$
G044.4228+00.5377	$4.27 \pm 0.87$		$4.27 \pm 1.1$	$0 \pm 0.26$
G045.0694+00.1323	$46.17 \pm 4.44$		$45.05 \pm 0.51$	$0.02 \pm 0.08$
G045.0712+00.1321	$146.67 \pm 14.65$		$38.72 \pm 0.55$	$1.05 \pm 0.08$
G045.1223+00.1321	$2984.27 \pm 274.33$		$1420.06 \pm 4.98$	$0.58 \pm 0.07$
G045.1242+00.1356	$62.55 \pm 11.86$		$220.37 \pm 57.06$	$-0.99 \pm 0.25$
G045.4545+00.0591	$1029.45 \pm 98.24$		$1447.75 \pm 233.21$	$-0.27 \pm 0.15$
G045.4559+00.0613	$51.59 \pm 7.58$		$493.27 \pm 104.52$	$-1.77 \pm 0.2$

Continued on next page

Table A.1 – continued from previous page

Name	$S_C$ (mJy)	$S_{M,6\text{cm}}$ (mJy)	$S_{M,20\text{cm}}$ (mJy)	$\alpha_{C6\text{cm}-M20\text{cm}}$
G045.4656+00.0452	$62.26 \pm 5.79$		$25.31 \pm 1.66$	$0.71 \pm 0.09$
G045.5431-00.0073	$49.16 \pm 7.8$		$79.92 \pm 2.24$	$-0.38 \pm 0.13$



## Appendix B

Distances, physical properties,  
morphologies

Table B.1 Heliocentric and galactocentric distances, physical properties, and morphologies of the 239 CORNISH UCHIIs. Heliocentric distances adopted from Cesaroni et al. [2015] are marked with † (the KDA is not resolved and the far distance is quoted); those from the RMS database are denoted by ‡, and the ones computed in this work – with ⋆. All remaining heliocentric distances (and the corresponding Lyman continuum flux values) were adopted from Urquhart et al. [2013]. Upper limits on the physical sizes are given for unresolved sources of known distance. The morphological classes reported here are based on the radio (5 GHz and 10 GHz), mid-IR, and joint classifications from Chapter 4, in accordance with the De Pree et al. [2005] morphological categories, marked as S – spherical, C – cometary, B – bipolar, SL – shell-like, I – irregular/multiply-peaked, and P denotes insufficiently resolved/point-like UCHIIs. In cases where a CORNISH UCHII was resolved into a multiple system in the JVLA maps, all component morphologies are listed. Over-resolved radio sources and saturated/confused mid-IR sources were not classified.

Name	$d_h$ (kpc)	$d_G$ (kpc)	$D$ (pc)	$\log N_i$ ( $s^{-1}$ )	$\log EM$ ( $cm^{-6}pc$ )	$\log n_e$ ( $cm^{-3}$ )	$\log T_b$ (K)	$\tau_{5GHz, 10^4K}$	$\log L_{bol}$ ( $L_\odot$ )	Radio morph	MIR morph	Joint morph
G010.3009–00.1477	2.4	6.15	0.061	47.5	7.03	4.2	$3.02 \pm 0.04$	0.11		I	C	I
G010.3204–00.2328	12.6†	4.5	0.18	47.7	6.19	3.54	$2.18 \pm 0.07$	0.015	4.51	C	C	C
G010.3204–00.2586	3.5	5.1	< 0.028	46.3	6.51	4.12	$2.5 \pm 0.06$	0.032	4.18	P	C	C
G010.4724+00.0275	11	3.06	0.091	47.6	6.58	3.84	$2.57 \pm 0.05$	0.038	5.84	P		P
G010.4736+00.0274	11	3.06	0.075	47.3	6.37	3.76	$2.36 \pm 0.05$	0.023		P		P
G010.6218–00.3848	2.4	6.16	0.02	46.3	6.55	4.15	$2.54 \pm 0.05$	0.035		P		P
G010.6223–00.3788	2.4	6.16	0.065	47.4	6.86	4.11	$2.85 \pm 0.04$	0.074		C		C
G010.6234–00.3837	2.4	6.16	0.051	48	7.66	4.55	$3.65 \pm 0.04$	0.59	4.95		C	C
G010.6240–00.3813	2.4	6.16	0.016	46.6	6.92	4.36	$2.91 \pm 0.04$	0.084		P		P
G010.6297–00.3380	4.95‡	3.75	0.074	46.8	6.05	3.65	$2.03 \pm 0.08$	0.011		B	C	C
G010.8519–00.4407							$2.21 \pm 0.061$	0.016		P	P	P

Continued on next page

Table B.1 – continued from previous page

Name	$d_h$ (kpc)	$d_G$ (kpc)	$D$ (pc)	$\log N_i$ ( $s^{-1}$ )	$\log EM$ ( $cm^{-6}pc$ )	$\log n_e$ ( $cm^{-3}$ )	$\log T_b$ (K)	$\tau_{5GHz, 10^4K}$	$\log L_{bol}$ ( $L_\odot$ )	Radio morph	MIR morph	Joint morph
G010.9584+00.0221	13.7	5.59	0.11	48.5	7.31	4.16	$3.3 \pm 0.04$	0.22	5.27	P	S	S
G010.9656+00.0089	2.7	5.87	0.06	46.5	6.04	3.7	$2.03 \pm 0.05$	0.011	3.39	C	C	C
G011.0328+00.0274	2.6	5.97	0.015	45.5	5.9	3.85	$1.89 \pm 0.09$	0.0078	2.87	P	C	C
G011.1104–00.3985	16.8	8.62	0.67	48.9	6.34	3.34	$2.33 \pm 0.04$	0.022	5.65	C	C	C
G011.1712–00.0662	12.8 <sup>†</sup>	4.76	0.66	48.2	5.65	3	$1.64 \pm 0.05$	0.0043	4.43		B	B
G011.9032–00.1407	4.1	4.57	0.056	46.6	6.1	3.73	$2.09 \pm 0.06$	0.012	4.11	C	C	C
G011.9039–00.1411	4.1	4.57	0.022	46.4	6.39	4	$2.38 \pm 0.05$	0.024		P	P	P
G011.9368–00.6158	4	4.66	0.11	48.2	7.22	4.17	$3.21 \pm 0.04$	0.18		B	B	B
G011.9446–00.0369	12.6	4.63	0.89	49.1	6.34	3.29	$2.33 \pm 0.04$	0.022	5.01	C	C	C
G011.9786–00.0973							$1.85 \pm 0.12$	0.0071		P	C	C
G012.1988–00.0345	11.9	4.02	0.13	47.9	6.64	3.82	$2.63 \pm 0.04$	0.044	5.3	P		P
G012.2081–00.1019	13.6	5.59	0.16	48.5	7.11	4.01	$3.1 \pm 0.04$	0.13	5.87	C		C
G012.4294–00.0479	13.9	5.89	0.15	47.9	6.49	3.7	$2.48 \pm 0.04$	0.03	4.83	C	S	C
G012.4317–01.1112	4.1	4.58	0.081	47	6.25	3.74	$2.24 \pm 0.06$	0.018		C	C	C
G012.8050–00.2007	2.1	6.47	0.16	48.7	7.38	4.17	$3.37 \pm 0.04$	0.27		B	B	B
G012.8131–00.1976	2.1	6.47	0.053	47.8	7.41	4.42	$3.4 \pm 0.04$	0.29		C	C	C
G012.9995–00.3583	1.9	6.66	0.025	45.8	6.03	3.88	$2.02 \pm 0.09$	0.01	3.39	S	C	C
G013.2099–00.1428	4.6	4.16	0.18	48.3	6.83	3.87	$2.82 \pm 0.04$	0.069	4.14	I	I	I
G013.3850+00.0684	1.9	6.67	0.18	47.3	5.92	3.42	$1.91 \pm 0.04$	0.0081	3.55	SL	SL	SL
G013.8726+00.2818	4.4	4.36	0.33	48.4	6.48	3.57	$2.47 \pm 0.04$	0.03	4.84	C		C
G014.1046+00.0918							$2.17 \pm 0.055$	0.015		C	C	C

Continued on next page

Table B.1 – continued from previous page

Name	$d_h$ (kpc)	$d_G$ (kpc)	$D$ (pc)	$\log N_i$ ( $s^{-1}$ )	$\log EM$ ( $cm^{-6}pc$ )	$\log n_e$ ( $cm^{-3}$ )	$\log T_b$ (K)	$\tau_{5GHz, 10^4K}$	$\log L_{bol}$ ( $L_\odot$ )	Radio morph	MIR morph	Joint morph
G014.1741+00.0245	14.7 <sup>†</sup>	6.79	0.48	48	5.7	3.09	$1.69 \pm 0.07$	0.0049	5.05		SL	SL
G014.2460–00.0728	11.6	3.96	0.2	47.8	6.22	3.53	$2.21 \pm 0.05$	0.016		B	B	B
G014.5988+00.0198	2.8	5.83	0.015	45.5	5.81	3.79	$1.8 \pm 0.12$	0.0063		P	P	P
G014.7785–00.3328	13.1	5.34	0.11	47.5	6.24	3.62	$2.23 \pm 0.06$	0.017	5.09	P	S	P
G016.1448+00.0088	12.4	4.85	< 0.096	47.3	6.46	3.83	$2.45 \pm 0.05$	0.029	4.52	C	C	C
G016.3913–00.1383	12.2 <sup>†</sup>	4.7	0.69	48.2	5.66	3	$1.64 \pm 0.05$	0.0044	4.25		SL	SL
G016.9445–00.0738	17	9.21	0.26	49.1	7.34	4.03	$3.33 \pm 0.04$	0.24	5.71	S	S	S
G017.0299–00.0696	10.4	3.37	0.096	46.7	5.68	3.39	$1.66 \pm 0.10$	0.0046	4.74	C	SL	C
G017.1141–00.1124	10.4	3.38	0.12	47.2	6.03	3.53	$2.02 \pm 0.06$	0.011	4.27	C	C	C
G017.5549+00.1654	14.1	6.52	0.11	47.1	5.87	3.43	$1.85 \pm 0.08$	0.0072	4.77	C	P	C
G017.9850+00.1266	13.7	6.2	0.21		5.62	3.21	$1.61 \pm 0.1$	0.01		I	C	C
G018.1460–00.2839	4.3	4.61	0.49	48.2	5.89	3.19	$1.88 \pm 0.04$	0.0077	4.1		I	I
G018.3024–00.3910	3	5.73	0.21	48	6.48	3.66	$2.47 \pm 0.04$	0.03	4.59	I	I	I
G018.4433–00.0056	12	4.77	0.11	48	6.85	3.94	$2.84 \pm 0.04$	0.071	4.89	I	P	I
G018.4614–00.0038	12.1	4.85	0.13	48.7	7.35	4.16	$3.34 \pm 0.04$	0.25	5.16	P	P	P
G018.6654+00.0294	10.9	3.94	< 0.092	46.8	5.97	3.59	$1.96 \pm 0.07$	0.0092		P+B	P	P+B
G018.7106+00.0002	2.6	6.09	0.018	46.8	7.11	4.44	$3.1 \pm 0.04$	0.13	3.6	C	P	C
G018.7612+00.2630	14	6.55	< 0.12	48	6.91	4	$2.89 \pm 0.04$	0.082	5.29	C	C	C
G018.8250–00.4675	4.5	4.48	0.044	46.3	5.95	3.69	$1.94 \pm 0.09$	0.0088	4.25	C	C	C
G018.8338–00.3002	12.6	5.32	0.4	48.3	6.16	3.36	$2.15 \pm 0.04$	0.014	5.42	C	C	C
G019.0035+00.1280	11.3	4.28	0.13	46.9	5.63	3.31	$1.62 \pm 0.12$	0.0042	4.72	P	P	P

Continued on next page

Table B.1 – continued from previous page

Name	$d_h$ (kpc)	$d_G$ (kpc)	$D$ (pc)	$\log N_i$ ( $s^{-1}$ )	$\log EM$ ( $cm^{-6}pc$ )	$\log n_e$ ( $cm^{-3}$ )	$\log T_b$ (K)	$\tau_{5GHz, 10^4K}$	$\log L_{bol}$ ( $L_\odot$ )	Radio morph	MIR morph	Joint morph
G019.0754–00.2874	4.6	4.42	0.19	47.9	6.42	3.66	$2.41 \pm 0.04$	0.026	5.08	C	C	C
G019.0767–00.2882	4.6	4.42	0.045	47.4	7.01	4.22	$3 \pm 0.04$	0.1		C	P	C
G019.4752+00.1728	14.1	6.71	0.23	47.8	6.12	3.45	$2.11 \pm 0.05$	0.013		C	C	C
G019.6087–00.2351	12.7	5.49	0.8	49.6	6.93	3.6	$2.92 \pm 0.04$	0.086	5.01	I	I	I
G019.6090–00.2313	12.7	5.49	0.22	48.6	6.95	3.88	$2.94 \pm 0.04$	0.09		C	C	C
G019.7281–00.1135	4.3	4.68	0.063	46.6	6.07	3.7	$2.05 \pm 0.05$	0.011	3.84	C	C	C
G019.7549–00.1282	9.3	3.15	$< 0.073$	47.5	6.84	4.07	$2.82 \pm 0.04$	0.069	5.47	C	P	C
G020.0720–00.1421	12.6	5.46	0.32	48.5	6.56	3.61	$2.55 \pm 0.04$	0.036		B	B	B
G020.0797–00.1337	12.6	5.46	0.098	47.3	6.18	3.62	$2.17 \pm 0.06$	0.015		C	P	C
G020.0809–00.1362	12.6	5.46	0.16	48.9	7.45	4.18	$3.44 \pm 0.04$	0.32	5.2	I	I	I
G020.3633–00.0136	3.9	5.03	0.047	46.9	6.51	3.97	$2.5 \pm 0.05$	0.032	3.47	C	C	C
G020.7619–00.0646	11.8	4.89	0.11	47.1	5.92	3.47	$1.91 \pm 0.1$	0.0081	4.65	C	P	C
G020.9636–00.0744	13.2	6.08	0.13	47.2	5.96	3.47	$1.95 \pm 0.08$	0.009	4.79	C+I	P	C+I
G021.3571–00.1766	10.3	3.91	0.06	47.4	6.53	3.87	$2.52 \pm 0.04$	0.034	5.45	C	P	C
G021.3855–00.2541	10.3	3.91	0.08	48	7.06	4.1	$3.05 \pm 0.04$	0.12	5.62	P	P	P
G021.6034–00.1685	16.2	8.87	0.27	47.7	5.85	3.28	$1.84 \pm 0.07$	0.007	4.41	I	C	C
G021.8751+00.0075	13.8	6.71	0.76	49	6.33	3.31	$2.32 \pm 0.04$	0.021	4.94	SL	SL	SL
G023.1974–00.0006	4.8	4.5	0.04	46.3	5.99	3.72	$1.98 \pm 0.07$	0.0095	3.95	P	C	C
G023.2654+00.0765	4.9	4.44	0.1	47.3	6.32	3.73	$2.31 \pm 0.05$	0.021	3.99	C	C	C
G023.4553–00.2010	5.8	3.93	$< 0.048$	46.6	6.39	3.94	$2.38 \pm 0.05$	0.024	4.24	P	P	P
G023.4835+00.0964	5.2	4.27	0.038	46.3	5.95	3.7	$1.94 \pm 0.08$	0.0088	4.04	C	C	C

Continued on next page

Table B.1 – continued from previous page

Name	$d_h$ (kpc)	$d_G$ (kpc)	$D$ (pc)	$\log N_i$ ( $s^{-1}$ )	$\log EM$ ( $cm^{-6}pc$ )	$\log n_e$ ( $cm^{-3}$ )	$\log T_b$ (K)	$\tau_{5GHz, 10^4K}$	$\log L_{bol}$ ( $L_\odot$ )	Radio morph	MIR morph	Joint morph
G023.7110+00.1705	6.5	3.65	0.14	47.9	6.68	3.84	$2.67 \pm 0.04$	0.048	5.05	C	C	C
G023.8618–00.1250	10.7	4.52	0.2	47.6	6.08	3.47	$2.07 \pm 0.07$	0.012	4.81	C	C	C
G023.8985+00.0647	12.6	5.93	0.23	47.8	6.11	3.45	$2.1 \pm 0.06$	0.013	5.2	C	C	C
G023.9564+00.1493	5	4.42	0.32	48.4	6.53	3.6	$2.52 \pm 0.04$	0.033	5.28	SL	SL	SL
G024.1839+00.1199	7.8	3.48	$< 0.064$	46.3	5.83	3.6	$1.81 \pm 0.10$	0.0065	4.14	C	B	C
G024.4698+00.4954	5.51*	4.17	0.064	46.9	6.26	3.78	$2.25 \pm 0.07$	0.018		P	P	P
G024.4721+00.4877	5.51*	4.17	0.096	47.2	6.27	3.72	$2.26 \pm 0.06$	0.018	4.87	B		B
G024.4736+00.4950	5.5*	4.17	0.14	47.4	6.2	3.6	$2.19 \pm 0.05$	0.016	4.32	I		I
G024.4921–00.0386	6.3	3.8	0.13	47.7	6.55	3.8	$2.54 \pm 0.04$	0.035	4.44	B		B
G024.5065–00.2224	5.8	4.02	0.17	47.8	6.43	3.68	$2.42 \pm 0.04$	0.027	4.39	C	C	C
G024.8497+00.0881	5.77*	4.07	0.092	46.8	5.87	3.52	$1.86 \pm 0.10$	0.0073	5.14	B	C	C
G025.3809–00.1815	2.7	6.17	0.11	47.5	6.51	3.82	$2.5 \pm 0.04$	0.032		C		C
G025.3824–00.1812	2.7	6.17	0.041	47.1	6.93	4.23	$2.92 \pm 0.04$	0.087	4.82	C	C	C
G025.3948+00.0332	17.1	10.1	0.36	48.9	6.84	3.72	$2.83 \pm 0.04$	0.07	5.78	S	S	S
G025.3970+00.5614	14	7.3	0.095	48.3	7.17	4.1	$3.16 \pm 0.04$	0.15	5.29	C	P	C
G025.3981–00.1411	5.6	4.2	0.23	48.8	7.16	3.99	$3.15 \pm 0.04$	0.15	5.1	C	I	C
G025.3983+00.5617	14	7.3	0.14	48	6.62	3.78	$2.61 \pm 0.04$	0.041		C	C	C
G025.3991–00.1366	5.6	4.2	0.081	46.9	6.12	3.67	$2.11 \pm 0.09$	0.013		S		P
G025.7157+00.0487	9.5	4.12	0.083	47.2	6.27	3.71	$2.26 \pm 0.06$	0.018	5.41	C	P	C
G025.8011–00.1568	5.6	4.23	$< 0.048$	47	6.7	4.1	$2.69 \pm 0.04$	0.05	4.13	C	P	C
G026.0083+00.1369	13.8*	7.17	0.073	47.1	5.99	3.54	$1.98 \pm 0.07$	0.0096	3.07	S	P	P

Continued on next page

Table B.1 – continued from previous page

Name	$d_h$ (kpc)	$d_G$ (kpc)	$D$ (pc)	$\log N_i$ ( $s^{-1}$ )	$\log EM$ ( $cm^{-6}pc$ )	$\log n_e$ ( $cm^{-3}$ )	$\log T_b$ (K)	$\tau_{5GHz, 10^4K}$	$\log L_{bol}$ ( $L_\odot$ )	Radio morph	MIR morph	Joint morph
G026.0916–00.0565	13.1	6.62	0.13	47.3	5.95	3.46	$1.94 \pm 0.09$	0.0087	5.09	C	P	C
G026.1094–00.0937	13.3	6.79	< 0.1	46.9	5.98	3.57	$1.97 \pm 0.08$	0.0093	4.93	C	C	C
G026.5976–00.0236	13.4	6.94	0.14	48.1	6.7	3.82	$2.69 \pm 0.05$	0.05	5.19	C	C	C
G026.6089–00.2121	7.6	3.81	0.24	48	6.38	3.59	$2.36 \pm 0.05$	0.023	4.02	I	I	I
G026.8304–00.2067	11.9*	5.77	0.075	47.2	6.2	3.66	$2.19 \pm 0.06$	0.015	4.19	I	P	C
G027.1859–00.0816	13.2	6.85	0.09	47.5	6.38	3.72	$2.37 \pm 0.05$	0.024	5.65	C	C	C
G027.2800+00.1447	12.8	6.53	0.34	48.8	6.81	3.72	$2.8 \pm 0.04$	0.066	5.1	I	C	I
G027.3644–00.1657	8	3.93	0.066	47.5	6.77	4	$2.76 \pm 0.04$	0.059	5.37	C	P	C
G027.5637+00.0845	9.9	4.59	0.59	48.2	5.73	3.07	$1.72 \pm 0.05$	0.0053	4.22	C	C	C
G027.9352+00.2056	12.1	6.08	< 0.094	46.8	5.94	3.57	$1.93 \pm 0.11$	0.0085	5.16	P	P	P
G028.1985–00.0503	5.8	4.36	0.076	47.6	6.87	4.06	$2.86 \pm 0.04$	0.075		C	P	C
G028.2003–00.0494	5.8	4.36	0.045	47.7	7.23	4.31	$3.22 \pm 0.04$	0.18	5.73	SL	P	SL
G028.2879–00.3641	11.6	5.76	0.25	48.8	7.12	3.94	$3.11 \pm 0.04$	0.14	5.68	I		I
G028.4518+00.0027	16.5	9.89	0.14	47.9	6.5	3.7	$2.49 \pm 0.04$	0.031	5.03	C		C
G028.5816+00.1447	16.5	9.91	0.41	48	5.85	3.2	$1.84 \pm 0.08$	0.007	4.38	I	S	I
G028.6082+00.0185	7.5	4.07	0.12	48	6.91	3.98	$2.89 \pm 0.04$	0.082	5.06	C	C	C
G028.6523+00.0273	7.5	4.08	0.2	48.1	6.55	3.71	$2.54 \pm 0.04$	0.036	5.02	C	C	C
G028.6869+00.1770	9.8	4.71	0.24	47.9	6.27	3.52	$2.26 \pm 0.05$	0.018	4.45	C	C	C
G029.7704+00.2189	9.84*	4.89	0.31	47.6	5.76	3.22	$1.75 \pm 0.08$	0.0057		S	S	S
G029.9559–00.0168	7.4	4.24	0.34	49.2	7.23	3.93	$3.22 \pm 0.04$	0.18	5.54	C	C	C
G030.0096–00.2734	7.4	4.25	< 0.058	46.3	5.94	3.68	$1.93 \pm 0.10$	0.0085	4.43	P	P	P

Continued on next page

Table B.1 – continued from previous page

Name	$d_h$ (kpc)	$d_G$ (kpc)	$D$ (pc)	$\log N_i$ ( $s^{-1}$ )	$\log EM$ ( $cm^{-6}pc$ )	$\log n_e$ ( $cm^{-3}$ )	$\log T_b$ (K)	$\tau_{5GHz, 10^4K}$	$\log L_{bol}$ ( $L_\odot$ )	Radio morph	MIR morph	Joint morph
G030.2527+00.0540	10.2	5.15	0.28	48	6.16	3.44	$2.15 \pm 0.05$	0.014	4.39	I	C	I
G030.5313+00.0205	11.4	5.94	0.29	48	6.15	3.42	$2.13 \pm 0.05$	0.014	4.36	C	C	C
G030.5353+00.0204	11.4	5.94	0.34	48.9	6.95	3.79	$2.94 \pm 0.04$	0.092	5.58	C	C	C
G030.5887–00.0428	11.8	6.23	< 0.1	48.1	7.16	4.17	$3.15 \pm 0.04$	0.15	5.4	C+P	P	C+P
G030.6881–00.0718	4.9 <sup>‡</sup>	4.96	0.25	48	6.3	3.54	$2.29 \pm 0.04$	0.02		C	C	C
G030.7197–00.0829	4.9	4.96	0.1	48.3	7.36	4.25	$3.35 \pm 0.04$	0.25		SL	S	SL
G030.7532–00.0511	4.9	4.97	0.069	47.8	7.15	4.22	$3.13 \pm 0.04$	0.15	4.85	C	P	C
G030.7579+00.2042	7.22*	4.35	0.14	47.1	5.88	3.45	$1.87 \pm 0.10$	0.0075	4.28	B	I	B
G030.7661–00.0348	7.22*	4.35	0.1	47.6	6.61	3.87	$2.6 \pm 0.08$	0.041		C	P	C
G030.8662+00.1143	11.9	6.34	0.16	48.6	7.23	4.08	$3.22 \pm 0.04$	0.18	5.61	C	P	C
G030.9581+00.0869	11.8	6.28	0.16	47.5	6.1	3.51	$2.09 \pm 0.08$	0.012	4.78	S	S	S
G031.0495+00.4697	12.2	6.59	< 0.1	47.3	6.33	3.74	$2.32 \pm 0.05$	0.021	4.23	I	P	C
G031.0595+00.0922	13.4	7.53	0.084	47.3	6.16	3.61	$2.15 \pm 0.06$	0.014	4.55	C	C	C
G031.1590+00.0465	2.7	6.35	0.018	45.7	5.94	3.85	$1.93 \pm 0.08$	0.0085		C	P	C
G031.1596+00.0448	2.7	6.35	< 0.022	46.2	6.62	4.23	$2.61 \pm 0.04$	0.042	3.73	C	P	C
G031.2420–00.1106	12.7*	7.03	0.48	48.6	6.39	3.44	$2.38 \pm 0.04$	0.024		C	C	C
G031.2435–00.1103	13	7.23	0.14	48.7	7.39	4.17	$3.38 \pm 0.04$	0.27	5.59	C	P	C
G031.2448–00.1132	13	7.23	0.18	47.8	6.28	3.58	$2.27 \pm 0.05$	0.019		C	C	C
G031.2801+00.0632	7.1	4.42	0.32	48.1	6.19	3.43	$2.18 \pm 0.04$	0.015	4.75	C	C	C
G031.3959–00.2570	9.1	4.8	0.44	47.8	5.61	3.07	$1.6 \pm 0.06$	0.0039	5.67		I	I
G031.4130+00.3065	5.6	4.73	0.25	48.4	6.74	3.75	$2.73 \pm 0.04$	0.055	5.25	C	C	C

Continued on next page

Table B.1 – continued from previous page

Name	$d_h$ (kpc)	$d_G$ (kpc)	$D$ (pc)	$\log N_i$ ( $s^{-1}$ )	$\log EM$ ( $cm^{-6}pc$ )	$\log n_e$ ( $cm^{-3}$ )	$\log T_b$ (K)	$\tau_{5GHz, 10^4K}$	$\log L_{bol}$ ( $L_\odot$ )	Radio morph	MIR morph	Joint morph
G031.5815+00.0744	7.2	4.45	0.066	46.8	6.1	3.68	$2.09 \pm 0.06$	0.012	5.22	C	C	C
G032.0297+00.0491	4.9 <sup>‡</sup>	5.06	0.095	46.8	5.87	3.52	$1.86 \pm 0.07$	0.0072	4.03	C	B	C
G032.1502+00.1329	7.2	4.52	0.43	48.4	6.24	3.39	$2.23 \pm 0.05$	0.017	4.79	C	C	C
G032.2730–00.2258	12.8	7.22	0.6	48.7	6.21	3.3	$2.19 \pm 0.05$	0.016	4.59	C	C	C
G032.4727+00.2036	11.1	6.02	0.091	48	6.98	4.04	$2.97 \pm 0.04$	0.098	5.6	I		I
G032.7398+00.1940	12.9	7.36	< 0.099	46.7	5.83	3.51	$1.82 \pm 0.11$	0.0066	4.08	C	P	C
G032.7492–00.0643	11.7	6.47	0.085	47.2	6.16	3.63	$2.15 \pm 0.06$	0.014	4.49	I	P	I
G032.7966+00.1909	13.3	7.69	0.64	49.7	7.19	3.78	$3.18 \pm 0.04$	0.17	5.05	2I+2C	I	2I+2C
G032.7982+00.1937	13.3	7.69	0.084	47.4	6.34	3.71	$2.33 \pm 0.05$	0.022		P	P	I
G032.9273+00.6060	18.6	12.4	0.6	48.9	6.49	3.44	$2.48 \pm 0.05$	0.031	5.54	I	I	I
G033.1328–00.0923	9.4	5.18	0.17	48.5	7.07	3.99	$3.06 \pm 0.04$	0.12	5.28	C	C	C
G033.4163–00.0036	9.4	5.22	0.39	47.8	5.69	3.13	$1.68 \pm 0.05$	0.0048	4.37	C	C	C
G033.8100–00.1864	11.1	6.22	0.086	48.1	7.05	4.08	$3.04 \pm 0.04$	0.12	5.71	C+P	P	C+P
G033.9145+00.1105	6.7	4.76	0.32	48.5	6.61	3.64	$2.6 \pm 0.05$	0.041	5.88	C	C	C
G034.0901+00.4365	11.4	6.46	0.11	47.1	5.92	3.49	$1.91 \pm 0.09$	0.0082	4.36	I	C	I
G034.1978–00.5912	10.3	5.79	0.14	47	5.7	3.33	$1.69 \pm 0.12$	0.0049	4.49	B	P	B
G034.2544+00.1460	3.58*	5.9	0.099	47.6	6.71	3.94	$2.7 \pm 0.05$	0.051		I	I	I
G034.2571+00.1466	3.58*	5.9	0.033	46.7	6.61	4.08	$2.6 \pm 0.09$	0.041		P		P
G034.2572+00.1535	2.1	6.87	0.057	47.8	7.43	4.42	$3.42 \pm 0.04$	0.3		C	C	C
G034.2573+00.1523	2.1	6.87	< 0.015	46.3	7.05	4.52	$3.04 \pm 0.05$	0.12		P		P
G034.2581+00.1533	2.1	6.87	< 0.015	46.2	6.9	4.45	$2.89 \pm 0.05$	0.081		P		P

Continued on next page

Table B.1 – continued from previous page

Name	$d_h$ (kpc)	$d_G$ (kpc)	$D$ (pc)	$\log N_i$ ( $s^{-1}$ )	$\log EM$ ( $cm^{-6}pc$ )	$\log n_e$ ( $cm^{-3}$ )	$\log T_b$ (K)	$\tau_{5GHz, 10^4K}$	$\log L_{bol}$ ( $L_\odot$ )	Radio morph	MIR morph	Joint morph
G034.4032+00.2277	2.1	6.87	< 0.018	45.5	6.17	4.05	$2.16 \pm 0.06$	0.014	3.82	S	C	C
G034.5920+00.2434	16.4	10.6	0.18	47.7	6.14	3.49	$2.13 \pm 0.05$	0.013	4.35	C	B	C
G035.0242+00.3502	10.4	5.97	< 0.078	47	6.38	3.83	$2.37 \pm 0.05$	0.024	5.6	P	P	P
G035.0524–00.5177	10.6 <sup>‡</sup>	6.07	0.17	47.8	6.4	3.65	$2.39 \pm 0.05$	0.025	4.97	C	C	C
G035.4570–00.1791	9.72*	5.67	< 0.079	46.8	6.13	3.7	$2.12 \pm 0.07$	0.013	4.31	C	P	C
G035.4669+00.1394	8.8	5.28	0.21	48.3	6.78	3.81	$2.77 \pm 0.04$	0.061	5.7	C	C	C
G035.5781–00.0305	10.4	6.05	0.1	48.3	7.17	4.12	$3.16 \pm 0.04$	0.15	5.59	C	C	C
G036.4057+00.0226	3.8	5.89	0.02	46.5	6.51	4.08	$2.5 \pm 0.04$	0.032	4.28	C		C
G036.4062+00.0221	3.8	5.89	< 0.03	46.1	6.25	3.98	$2.24 \pm 0.06$	0.017		C+P	P	C+P
G037.5457–00.1120	10	6.12	0.39	48.6	6.48	3.53	$2.47 \pm 0.04$	0.03	5.5	C	C	C
G037.7347–00.1128	10.3	6.31	< 0.088	47.2	6.42	3.83	$2.41 \pm 0.05$	0.026	5.01	C	P	C
G037.7562+00.5605	12.2*	7.55	0.41	47.7	5.56	3.06	$1.55 \pm 0.10$	0.0036	4.5	I		B
G037.8197+00.4140	12.2	7.57	0.24	47.5	5.86	3.32	$1.85 \pm 0.07$	0.007			I	I
G037.8209+00.4125	12.2	7.57	0.095	47.4	6.32	3.69	$2.3 \pm 0.06$	0.02	5.17	C	P	C
G037.8683–00.6008	10	6.17	0.24	48.3	6.59	3.69	$2.58 \pm 0.04$	0.039	5.76	C	C	C
G037.8731–00.3996	9.4	5.87	0.4	49.3	7.21	3.89	$3.2 \pm 0.04$	0.17	5.73	C	C	C
G037.9723–00.0965	9.74*	6.05	0.09	47.3	6.24	3.68	$2.23 \pm 0.06$	0.017	3.84	C	C	C
G038.5493+00.1646	2.07 <sup>‡</sup>	7	0.081	46.5	5.81	3.53	$1.8 \pm 0.06$	0.0063		I	C	C
G038.6465–00.2260	4.7	5.65	0.046	46.4	5.96	3.69	$1.95 \pm 0.08$	0.009	3.61	C	P	C
G038.6529+00.0875	17.1	11.7	< 0.13	47.3	6.19	3.62	$2.18 \pm 0.06$	0.015	4.9	P	P	C
G038.6934–00.4524	9.9	6.24	0.11	47.2	6.14	3.6	$2.13 \pm 0.06$	0.014	4.22	C	P	C

Continued on next page

Table B.1 – continued from previous page

Name	$d_h$ (kpc)	$d_G$ (kpc)	$D$ (pc)	$\log N_i$ ( $s^{-1}$ )	$\log EM$ ( $cm^{-6}pc$ )	$\log n_e$ ( $cm^{-3}$ )	$\log T_b$ (K)	$\tau_{5GHz, 10^4K}$	$\log L_{bol}$ ( $L_\odot$ )	Radio morph	MIR morph	Joint morph
G038.8756+00.3080	15.9	10.7	0.25	48.9	7.09	3.91	$3.08 \pm 0.04$	0.13	5.43	C	C	C
G039.1956+00.2255	15.9	10.8	0.093	48.2	6.92	3.96	$2.9 \pm 0.04$	0.084	5.49	C	P	C
G039.8824–00.3460	9.1	6.03	0.15	48.3	6.98	3.97	$2.97 \pm 0.04$	0.098	4.63	C	B	C
G040.4251+00.7002	12.1	7.88	0.15	47.2	5.81	3.37	$1.8 \pm 0.09$	0.0063	5.26	C	P	C
G041.7419+00.0973	11.8	7.86	0.31	48.5	6.56	3.62	$2.55 \pm 0.05$	0.036	4.79	SL	SL	SL
G042.1090–00.4469	8.8	6.22	0.047	47	6.34	3.81	$2.33 \pm 0.05$	0.022	4.37	C	P	C
G042.4345–00.2605	5.1	5.85	0.082	47.3	6.5	3.86	$2.49 \pm 0.05$	0.032	5.21	B	C	B
G043.1460+00.0139	11.1	7.6	0.32	48.9	6.95	3.8	$2.94 \pm 0.04$	0.092		I	C	I
G043.1489+00.0130	11.1	7.6	< 0.089	47.7	6.91	4.07	$2.9 \pm 0.06$	0.083	5.09	P	P	P
G043.1520+00.0115	11.1	7.6	0.11	48.5	7.36	4.19	$3.34 \pm 0.05$	0.25		I	P	C
G043.1651–00.0283	11.1	7.6	0.51	49.5	7.17	3.82	$3.16 \pm 0.04$	0.16	5.47	C	C	C
G043.1652+00.0129	11.1	7.6	0.075	48.2	7.27	4.2	$3.26 \pm 0.05$	0.2		P		B
G043.1657+00.0116	11.1	7.6	0.059	48	7.16	4.17	$3.15 \pm 0.05$	0.15		I	P	C
G043.1665+00.0106	11.1	7.6	0.18	49.2	7.7	4.29	$3.69 \pm 0.04$	0.68	5.68	I	P	I
G043.1674+00.0128	11.1	7.6	< 0.093	47.9	7.1	4.15	$3.09 \pm 0.05$	0.13		C	P	C
G043.1677+00.0196	11.1	7.6	0.21	48.1	6.53	3.68	$2.51 \pm 0.07$	0.033		B	C	C
G043.1684+00.0087	11.1	7.6	0.097	48.3	7.24	4.16	$3.23 \pm 0.05$	0.19		C	P	C
G043.1684+00.0124	11.1	7.6	< 0.081	47.8	7.15	4.21	$3.14 \pm 0.05$	0.15		C		C
G043.1699+00.0115	11.1	7.6	0.081	47.7	6.68	3.9	$2.67 \pm 0.08$	0.048		C	P	C
G043.1701+00.0078	11.1	7.61	0.4	49.1	6.99	3.78	$2.98 \pm 0.04$	0.1		C	SL	C
G043.1706–00.0003	11.1	7.61	0.054	48.3	7.41	4.3	$3.4 \pm 0.04$	0.29	5.84	C	P	C/B

Continued on next page

Table B.1 – continued from previous page

Name	$d_h$ (kpc)	$d_G$ (kpc)	$D$ (pc)	$\log N_i$ ( $s^{-1}$ )	$\log EM$ ( $cm^{-6}pc$ )	$\log n_e$ ( $cm^{-3}$ )	$\log T_b$ (K)	$\tau_{5GHz, 10^4K}$	$\log L_{bol}$ ( $L_\odot$ )	Radio morph	MIR morph	Joint morph
G043.1716+00.0001	11.1	7.61	0.12	47.8	6.56	3.79	$2.55 \pm 0.11$	0.036		I	P	C
G043.1720+00.0080	11.1	7.61	0.11	48	6.86	3.94	$2.85 \pm 0.05$	0.073		S	P	P
G043.1763+00.0248	11.1	7.61	0.23	48.2	6.59	3.69	$2.58 \pm 0.06$	0.039	5.24	I	S	I
G043.1778–00.5181	8.2	6.15	0.28	48	6.25	3.49	$2.24 \pm 0.05$	0.018	5.17	C	C	C
G043.2371–00.0453	11.9	8.15	0.2	48.4	6.8	3.82	$2.79 \pm 0.05$	0.063	5.49	I	C	I
G043.3064–00.2114	4.4	6.1	0.043	46.5	6.2	3.82	$2.19 \pm 0.07$	0.015	5.15	I	P	I
G043.7954–00.1274	9.2	6.63	0.045	47.3	6.57	3.92	$2.56 \pm 0.05$	0.037	5.51	C+C	P	C+C
G043.7960–00.1286	9.2	6.63	0.08	46.9	5.94	3.54	$1.93 \pm 0.09$	0.0085		P	P	P
G043.8894–00.7840	4.4	6.14	0.11	48	6.96	4.04	$2.95 \pm 0.04$	0.094	4.23	C	C	C
G043.9675+00.9939	14.1	9.93	$< 0.12$	47.9	6.85	3.98	$2.84 \pm 0.04$	0.072	5.28	C	P	C
G044.3103+00.0410	8	6.24	$< 0.065$	46.5	5.99	3.68	$1.98 \pm 0.08$	0.0096	5.42	C+P	P	C+P
G044.4228+00.5377	17.9	13.2	$< 0.14$	47.1	5.92	3.48	$1.91 \pm 0.09$	0.0082	4.51	C	P	C
G045.0694+00.1323	4.4	6.23	0.028	46.9	6.78	4.17	$2.77 \pm 0.04$	0.061		C		C
G045.0712+00.1321	4.4	6.23	0.026	47.4	7.31	4.44	$3.3 \pm 0.04$	0.22	5.64	S	P	C
G045.1223+00.1321	4.4	6.23	0.16	48.7	7.43	4.2	$3.42 \pm 0.04$	0.3	5.31	B	B	B
G045.1242+00.1356	4.4	6.23	0.098	47	6.13	3.65	$2.12 \pm 0.08$	0.013		B	B	B
G045.4545+00.0591	7.2	6.18	0.26	48.7	6.95	3.85	$2.94 \pm 0.04$	0.091	5.63	C	C	C
G045.4559+00.0613	7.2	6.18	0.1	47.4	6.36	3.73	$2.35 \pm 0.07$	0.022		C	P	C
G045.4656+00.0452	6	6.06	$< 0.049$	47.3	7.03	4.26	$3.02 \pm 0.04$	0.11	5.12	P	P	P
G045.5431–00.0073	5.89*	6.07	0.17	47.2	5.84	3.39	$1.83 \pm 0.07$	0.0068	3.96		C	C
G048.6099+00.0270	10.8 <sup>‡</sup>	8.18	0.36	48.1	6.12	3.37	$2.11 \pm 0.05$	0.013	5.09		C	C

Continued on next page

Table B.1 – continued from previous page

Name	$d_h$ (kpc)	$d_G$ (kpc)	$D$ (pc)	$\log N_i$ ( $s^{-1}$ )	$\log EM$ ( $cm^{-6}pc$ )	$\log n_e$ ( $cm^{-3}$ )	$\log T_b$ (K)	$\tau_{5GHz, 10^4K}$	$\log L_{bol}$ ( $L_\odot$ )	Radio morph	MIR morph	Joint morph
G048.9296–00.2793	5.4	6.41	0.16	47.7	6.39	3.68	$2.38 \pm 0.04$	0.024	4.36	I	I	I
G048.9901–00.2988	5.4	6.42	< 0.046	46.3	6.08	3.8	$2.07 \pm 0.10$	0.012	4.93	B	P	B
G049.2679–00.3374	5.4	6.44	0.16	47.4	6.12	3.55	$2.11 \pm 0.07$	0.013	4.18	C	C	C
G049.3666–00.3010	5.4	6.45	0.089	47.7	6.82	4.01	$2.81 \pm 0.11$	0.067		C	C	C
G049.4640–00.3511	5.46*	6.46	0.15	48.3	7.02	4.01	$3.01 \pm 0.06$	0.11		C	I	C
G049.4891–00.3763	5.46*	6.46	0.071	47.8	7.06	4.17	$3.05 \pm 0.07$	0.12	5.67	I	C	C
G049.4905–00.3688	5.4	6.46	0.15	49	7.76	4.38	$3.75 \pm 0.04$	0.83	5.36	B	S	B
G050.3152+00.6762	1.9	7.43	0.014	46.4	6.96	4.43	$2.95 \pm 0.04$	0.094	3.93	C	P	C
G050.3157+00.6747	8.58*	7.26	0.4	47.7	5.58	3.07	$1.57 \pm 0.05$	0.0037		C	C	C
G051.6785+00.7193	10.5	8.48	< 0.091	47.3	6.55	3.88	$2.54 \pm 0.04$	0.035	5.28	P	P	P
G052.7533+00.3340	9.3	7.94	0.38	48.5	6.41	3.5	$2.4 \pm 0.04$	0.026	4.54	C	C	C
G053.9589+00.0320	5	6.87	0.044	47	6.63	4.03	$2.62 \pm 0.04$	0.043	4.7	C	P	C
G058.7739+00.6457	4.4	7.27	0.049	45.9	5.51	3.46	$1.50 \pm 0.12$	0.0031	4.42	B	P	B
G059.6027+00.9118	4.2	7.33	< 0.034	47	7.08	4.36	$3.07 \pm 0.04$	0.12	4.21	P	P	P
G060.8842–00.1286	2.16 <sup>‡</sup>	7.68	< 0.016	45.9	6.62	4.3	$2.61 \pm 0.05$	0.041	4.23	C	C	C
G061.4763+00.0892	4.01*	7.47	0.12	48	6.93	4	$2.92 \pm 0.04$	0.086	5.49	C		C
G061.4770+00.0891	4.01*	7.47	< 0.03	47	7.16	4.43	$3.15 \pm 0.04$	0.15		P	P	P
G061.7207+00.8630	14.0 <sup>‡</sup>	12.5	0.13	48.3	6.94	3.95	$2.92 \pm 0.04$	0.088	5.59	SL	P	SL



# Appendix C

## Extended IR source fluxes

Table C.1 GLIMPSE fluxes and magnitudes of the sample of CORNISH UCHII regions, computed in this work. All flux values and their associated errors are in mJy. Missing values are due to missing data, unreliable data, and the exclusion of non-detections. The † symbol marks instances with possible saturation issues. Note that the magnitudes presented here are shown in the AB system, for consistency with our UKIDSS results.

Name	$S_{3.6\mu\text{m}}$ (mJy)	$S_{4.5\mu\text{m}}$ (mJy)	$S_{5.8\mu\text{m}}$ (mJy)	$S_{8.0\mu\text{m}}$ (mJy)	[3.6]	[4.5]	[5.8]	[8.0]
G010.3009–00.1477	191.81 ± 80.80	316.14 ± 99.64	1982.12 ± 712.14	5117.70 ± 2547.03	10.69 ± 0.45	10.15 ± 0.34	8.16 ± 0.39	7.13 ± 0.54
G010.3204–00.2328	107.48 ± 3.13	159.13 ± 4.36	812.79 ± 22.51	1646.41 ± 53.34	11.32 ± 0.03	10.90 ± 0.03	9.13 ± 0.03	8.36 ± 0.03
G010.3204–00.2586	8.68 ± 2.98	57.50 ± 4.64	213.39 ± 41.53	495.73 ± 136.43	14.05 ± 0.37	12.00 ± 0.09	10.58 ± 0.21	9.66 ± 0.30
G010.6218–00.3848	5.80 ± 3.48	26.34 ± 4.77			14.49 ± 0.65	12.85 ± 0.20		
G010.6223–00.3788		53.54 ± 23.54				12.08 ± 0.48		
G010.6234–00.3837	36.98 ± 15.23	147.58 ± 21.27	498.96 ± 259.22	1128.85 ± 700.78	12.48 ± 0.44	10.98 ± 0.16	9.65 ± 0.56	8.77 ± 0.67
G010.6240–00.3813			117.75 ± 61.52	522.44 ± 159.40			11.22 ± 0.57	9.60 ± 0.33
G010.6297–00.3380	106.73 ± 3.35	162.38 ± 3.85	1325.45 ± 29.06	3592.56 ± 83.78	11.33 ± 0.03	10.87 ± 0.03	8.59 ± 0.02	7.51 ± 0.03
G010.9584+00.0221	25.54 ± 2.71	85.09 ± 2.70	250.68 ± 22.46	522.95 ± 80.51	12.88 ± 0.11	11.58 ± 0.03	10.40 ± 0.10	9.60 ± 0.17
G010.9656+00.0089	47.99 ± 7.31	65.33 ± 7.72	378.14 ± 59.23	1163.15 ± 175.39	12.20 ± 0.16	11.86 ± 0.13	9.96 ± 0.17	8.74 ± 0.16
G011.0328+00.0274	15.93 ± 1.73	23.95 ± 1.64	201.82 ± 5.16	532.55 ± 10.22	13.39 ± 0.12	12.95 ± 0.07	10.64 ± 0.03	9.58 ± 0.02
G011.1104–00.3985	255.78 ± 14.95	391.37 ± 19.24	2148.49 ± 197.93	5957.55 ± 585.03	10.38 ± 0.06	9.92 ± 0.05	8.07 ± 0.10	6.96 ± 0.11
G011.1712–00.0662	119.78 ± 12.64	114.47 ± 11.19	691.14 ± 30.49	1766.80 ± 48.46	11.20 ± 0.11	11.25 ± 0.11	9.30 ± 0.05	8.28 ± 0.03
G011.9032–00.1407		40.18 ± 4.12	118.80 ± 12.85	248.42 ± 30.12		12.39 ± 0.11	11.21 ± 0.12	10.41 ± 0.13
G011.9368–00.6158	256.25 ± 8.38	609.17 ± 14.57	3641.50 ± 77.35	10277.65 ± 103.72	10.38 ± 0.04	9.44 ± 0.03	7.50 ± 0.02	6.37 ± 0.01
G011.9446–00.0369	820.14 ± 101.43	1048.06 ± 82.95	4647.68 ± 513.01	13816.60 ± 1300.61	9.12 ± 0.13	8.85 ± 0.09	7.23 ± 0.12	6.05 ± 0.10
G012.1988–00.0345	29.57 ± 2.53	177.31 ± 2.66	512.85 ± 7.35	811.23 ± 12.64	12.72 ± 0.09	10.78 ± 0.02	9.63 ± 0.02	9.13 ± 0.02
G012.2081–00.1019	60.29 ± 8.03	53.71 ± 7.44	218.63 ± 46.01	623.32 ± 129.21	11.95 ± 0.14	12.07 ± 0.15	10.55 ± 0.23	9.41 ± 0.22

Continued on next page

Table C.1 – continued from previous page

Name	$S_{3.6\mu\text{m}}$ (mJy)	$S_{4.5\mu\text{m}}$ (mJy)	$S_{5.8\mu\text{m}}$ (mJy)	$S_{8.0\mu\text{m}}$ (mJy)	[3.6]	[4.5]	[5.8]	[8.0]
G012.4294–00.0479		$15.77 \pm 5.48$	$149.58 \pm 59.20$	$498.99 \pm 180.38$		$13.41 \pm 0.37$	$10.96 \pm 0.43$	$9.65 \pm 0.39$
G012.4317–01.1112	$122.36 \pm 8.64$	$235.54 \pm 8.96$	$1969.68 \pm 83.09$	$5774.60 \pm 264.67$	$11.18 \pm 0.08$	$10.47 \pm 0.04$	$8.16 \pm 0.05$	$7.00 \pm 0.05$
G012.8050–00.2007	$914.06 \pm 90.47$	$2585.81 \pm 124.41$	$13458.14 \pm 1259.96$	$40822.39 \pm 3200.87$	$9.00 \pm 0.11$	$7.87 \pm 0.05$	$6.08 \pm 0.10$	$4.87 \pm 0.08$
G012.8131–00.1976	$101.42 \pm 14.56$	$380.61 \pm 21.59$	$2485.64 \pm 279.36$	$7721.11 \pm 700.72$	$11.38 \pm 0.16$	$9.95 \pm 0.06$	$7.91 \pm 0.12$	$6.68 \pm 0.10$
G012.9995–00.3583	$16.35 \pm 0.98$	$60.61 \pm 1.36$	$320.47 \pm 5.36$	$802.16 \pm 9.71$	$13.37 \pm 0.06$	$11.94 \pm 0.02$	$10.14 \pm 0.02$	$9.14 \pm 0.01$
G013.2099–00.1428	$44.47 \pm 18.40$	$193.80 \pm 25.50$	$1385.79 \pm 201.71$	$3876.50 \pm 669.53$	$12.28 \pm 0.44$	$10.68 \pm 0.14$	$8.55 \pm 0.16$	$7.43 \pm 0.19$
G013.3850+00.0684	$410.91 \pm 42.92$	$521.85 \pm 41.26$	$3639.65 \pm 245.02$	$9936.61 \pm 498.90$	$9.87 \pm 0.11$	$9.61 \pm 0.09$	$7.50 \pm 0.07$	$6.41 \pm 0.05$
G013.8726+00.2818		$900.18 \pm 419.46$	$6252.28 \pm 2905.30$	$21687.65 \pm 9209.99$		$9.01 \pm 0.50$	$6.91 \pm 0.50$	$5.56 \pm 0.46$
G014.1741+00.0245	$39.69 \pm 11.61$	$54.71 \pm 9.87$	$436.16 \pm 59.02$	$1309.20 \pm 160.70$	$12.40 \pm 0.32$	$12.05 \pm 0.19$	$9.80 \pm 0.15$	$8.61 \pm 0.13$
G014.2460–00.0728		$15.58 \pm 5.25$	$134.93 \pm 33.36$	$429.36 \pm 80.03$		$13.42 \pm 0.36$	$11.07 \pm 0.27$	$9.82 \pm 0.20$
G014.5988+00.0198	$17.98 \pm 1.94$	$65.09 \pm 2.38$	$186.92 \pm 8.35$	$338.53 \pm 29.88$	$13.26 \pm 0.12$	$11.87 \pm 0.04$	$10.72 \pm 0.05$	$10.08 \pm 0.10$
G014.7785–00.3328	$8.86 \pm 1.07$	$24.07 \pm 1.04$	$96.88 \pm 4.95$	$291.01 \pm 12.93$	$14.03 \pm 0.13$	$12.95 \pm 0.05$	$11.43 \pm 0.06$	$10.24 \pm 0.05$
G016.1448+00.0088	$16.55 \pm 2.29$	$29.86 \pm 1.99$	$235.40 \pm 7.96$	$635.54 \pm 14.93$	$13.35 \pm 0.15$	$12.71 \pm 0.07$	$10.47 \pm 0.04$	$9.39 \pm 0.03$
G016.3913–00.1383	$78.31 \pm 13.08$	$83.00 \pm 11.12$	$384.31 \pm 53.40$	$947.84 \pm 97.22$	$11.67 \pm 0.18$	$11.60 \pm 0.14$	$9.94 \pm 0.15$	$8.96 \pm 0.11$
G016.9445–00.0738	$91.62 \pm 5.62$	$188.82 \pm 6.22$	$1034.45 \pm 34.01$	$2645.22 \pm 91.93$	$11.50 \pm 0.07$	$10.71 \pm 0.04$	$8.86 \pm 0.04$	$7.84 \pm 0.04$
G017.0299–00.0696	$28.70 \pm 2.85$	$38.88 \pm 2.66$	$97.05 \pm 20.13$	$182.44 \pm 71.63$	$12.76 \pm 0.11$	$12.43 \pm 0.07$	$11.43 \pm 0.22$	$10.75 \pm 0.42$
G017.1141–00.1124	$63.88 \pm 4.15$	$80.79 \pm 3.55$	$637.16 \pm 14.37$	$1692.88 \pm 26.65$	$11.89 \pm 0.07$	$11.63 \pm 0.05$	$9.39 \pm 0.02$	$8.33 \pm 0.02$
G017.5549+00.1654	$21.75 \pm 2.53$	$26.90 \pm 2.59$	$182.66 \pm 35.80$	$485.29 \pm 139.22$	$13.06 \pm 0.13$	$12.83 \pm 0.10$	$10.75 \pm 0.21$	$9.68 \pm 0.31$
G017.9850+00.1266	$104.15 \pm 4.12$	$81.18 \pm 3.40$	$390.02 \pm 11.80$	$999.52 \pm 12.53$	$11.36 \pm 0.04$	$11.63 \pm 0.05$	$9.92 \pm 0.03$	$8.90 \pm 0.01$
G018.1460–00.2839	$1395.50 \pm 429.02$	$1693.76 \pm 402.28$	$7930.30 \pm 2666.90$	$24389.19 \pm 7411.47$	$8.54 \pm 0.33$	$8.33 \pm 0.26$	$6.65 \pm 0.36$	$5.43 \pm 0.33$
G018.3024–00.3910	$1898.17 \pm 57.13$	$2404.38 \pm 59.05$	$14926.67 \pm 460.53$	$39597.30 \pm 856.07$	$8.20 \pm 0.03$	$7.95 \pm 0.03$	$5.97 \pm 0.03$	$4.91 \pm 0.02$
G018.4433–00.0056	$9.92 \pm 2.22$	$19.13 \pm 2.68$	$126.12 \pm 11.92$	$393.09 \pm 27.58$	$13.91 \pm 0.24$	$13.20 \pm 0.15$	$11.15 \pm 0.10$	$9.91 \pm 0.08$

Continued on next page

Table C.1 – continued from previous page

Name	$S_{3.6\mu\text{m}}$ (mJy)	$S_{4.5\mu\text{m}}$ (mJy)	$S_{5.8\mu\text{m}}$ (mJy)	$S_{8.0\mu\text{m}}$ (mJy)	[3.6]	[4.5]	[5.8]	[8.0]
G018.4614–00.0038	31.09 ± 3.54	111.95 ± 3.01	358.18 ± 12.63	958.09 ± 23.80	12.67 ± 0.12	11.28 ± 0.03	10.01 ± 0.04	8.95 ± 0.03
G018.6654+00.0294	7.52 ± 2.38	16.02 ± 2.92	89.40 ± 7.87	232.82 ± 20.87	14.21 ± 0.34	13.39 ± 0.20	11.52 ± 0.10	10.48 ± 0.10
G018.7106+00.0002	49.17 ± 1.95	74.35 ± 1.91	285.55 ± 7.83	585.66 ± 19.86	12.17 ± 0.04	11.72 ± 0.03	10.26 ± 0.03	9.48 ± 0.04
G018.7612+00.2630	28.92 ± 6.59	45.43 ± 5.73	343.32 ± 27.21	903.15 ± 85.56	12.75 ± 0.25	12.26 ± 0.14	10.06 ± 0.09	9.01 ± 0.10
G018.8250–00.4675	53.07 ± 4.44	69.51 ± 2.92	601.06 ± 30.77	1433.97 ± 100.38	12.09 ± 0.09	11.79 ± 0.05	9.45 ± 0.06	8.51 ± 0.08
G019.0035+00.1280	13.53 ± 2.68	22.32 ± 3.12	106.10 ± 12.84	280.81 ± 17.05	13.57 ± 0.21	13.03 ± 0.15	11.34 ± 0.13	10.28 ± 0.07
G019.0754–00.2874	251.49 ± 74.31	375.62 ± 77.71	2487.01 ± 690.27	6920.80 ± 2186.79	10.40 ± 0.32	9.96 ± 0.22	7.91 ± 0.30	6.80 ± 0.34
G019.0767–00.2882	68.24 ± 6.47	100.86 ± 7.81	946.54 ± 90.19	3167.07 ± 296.65	11.81 ± 0.10	11.39 ± 0.08	8.96 ± 0.10	7.65 ± 0.10
G019.4752+00.1728	12.48 ± 3.03	27.45 ± 4.42	175.62 ± 27.95	483.39 ± 37.65	13.66 ± 0.26	12.80 ± 0.17	10.79 ± 0.17	9.69 ± 0.08
G019.6087–00.2351	760.05 ± 51.30	1310.98 ± 48.99	6499.63 ± 311.51	17921.26 ± 869.50	9.20 ± 0.07	8.61 ± 0.04	6.87 ± 0.05	5.77 ± 0.05
G019.6090–00.2313	56.47 ± 15.69	151.16 ± 15.49	652.04 ± 159.76	2260.90 ± 397.04	12.02 ± 0.30	10.95 ± 0.11	9.36 ± 0.26	8.01 ± 0.19
G019.7281–00.1135	34.63 ± 2.95	61.13 ± 2.29	546.84 ± 11.05	1412.71 ± 34.49	12.55 ± 0.09	11.93 ± 0.04	9.56 ± 0.02	8.52 ± 0.03
G020.0720–00.1421	115.94 ± 11.86	203.74 ± 11.73	846.74 ± 48.86	2385.06 ± 95.67	11.24 ± 0.11	10.63 ± 0.06	9.08 ± 0.06	7.96 ± 0.04
G020.0797–00.1337		10.10 ± 2.36	83.23 ± 9.37	330.94 ± 12.02		13.89 ± 0.25	11.60 ± 0.12	10.10 ± 0.04
G020.0809–00.1362	22.21 ± 8.21	86.98 ± 9.52	281.08 ± 47.21	742.47 ± 22.29	13.03 ± 0.40	11.55 ± 0.12	10.28 ± 0.18	9.22 ± 0.03
G020.3633–00.0136	4.54 ± 2.59	17.40 ± 2.32	86.49 ± 5.55	251.89 ± 8.53	14.76 ± 0.62	13.30 ± 0.14	11.56 ± 0.07	10.40 ± 0.04
G020.9636–00.0744	10.17 ± 2.93	20.53 ± 2.78	140.53 ± 10.63	390.77 ± 32.59	13.88 ± 0.31	13.12 ± 0.15	11.03 ± 0.08	9.92 ± 0.09
G021.3855–00.2541	53.14 ± 2.75	108.23 ± 2.37	504.32 ± 12.87	1600.15 ± 17.22	12.09 ± 0.06	11.31 ± 0.02	9.64 ± 0.03	8.39 ± 0.01
G021.6034–00.1685	27.22 ± 3.30	34.99 ± 2.71	282.22 ± 9.96	754.83 ± 19.23	12.81 ± 0.13	12.54 ± 0.08	10.27 ± 0.04	9.21 ± 0.03
G021.8751+00.0075	211.88 ± 43.15	314.86 ± 47.90	2194.29 ± 227.29	6067.15 ± 537.18	10.58 ± 0.22	10.15 ± 0.16	8.05 ± 0.11	6.94 ± 0.10
G023.1974–00.0006	70.96 ± 3.14	90.61 ± 2.80	695.26 ± 18.21	1881.53 ± 59.25	11.77 ± 0.05	11.51 ± 0.03	9.29 ± 0.03	8.21 ± 0.03
G023.2654+00.0765	68.81 ± 5.87	117.37 ± 5.71	853.94 ± 48.71	2236.12 ± 95.03	11.81 ± 0.09	11.23 ± 0.05	9.07 ± 0.06	8.03 ± 0.05

Continued on next page

Table C.1 – continued from previous page

Name	$S_{3.6\mu\text{m}}$ (mJy)	$S_{4.5\mu\text{m}}$ (mJy)	$S_{5.8\mu\text{m}}$ (mJy)	$S_{8.0\mu\text{m}}$ (mJy)	[3.6]	[4.5]	[5.8]	[8.0]
G023.4835+00.0964	42.91 ± 3.19	55.98 ± 3.67	178.26 ± 27.42	298.54 ± 64.71	12.32 ± 0.08	12.03 ± 0.07	10.77 ± 0.17	10.21 ± 0.23
G023.7110+00.1705	227.87 ± 13.88	324.14 ± 17.80	1738.13 ± 150.25	5138.15 ± 396.72	10.51 ± 0.07	10.12 ± 0.06	8.30 ± 0.09	7.12 ± 0.08
G023.8618–00.1250	37.45 ± 5.17	56.44 ± 5.20	417.85 ± 55.07	976.60 ± 175.64	12.47 ± 0.15	12.02 ± 0.10	9.85 ± 0.14	8.93 ± 0.19
G023.8985+00.0647	54.81 ± 9.43	89.85 ± 10.68	607.22 ± 67.15	1417.84 ± 154.64	12.05 ± 0.19	11.52 ± 0.13	9.44 ± 0.12	8.52 ± 0.12
G023.9564+00.1493	1775.59 ± 57.21	2305.34 ± 61.92	13569.53 ± 491.26	37519.12 ± 1406.80	8.28 ± 0.03	7.99 ± 0.03	6.07 ± 0.04	4.96 ± 0.04
G024.1839+00.1199	30.76 ± 1.32	61.75 ± 1.22	268.60 ± 6.60	667.40 ± 16.03	12.68 ± 0.05	11.92 ± 0.02	10.33 ± 0.03	9.34 ± 0.03
G024.4698+00.4954			524.66 ± 297.18				9.60 ± 0.61	
G024.4721+00.4877	150.30 ± 28.44	188.65 ± 26.00	941.01 ± 273.80	4025.91 ± 1574.29	10.96 ± 0.20	10.71 ± 0.15	8.97 ± 0.31	7.39 ± 0.42
G024.4736+00.4950	106.84 ± 45.20	139.24 ± 55.13	961.10 ± 548.22	3734.72 ± 2386.14	11.33 ± 0.46	11.04 ± 0.43	8.94 ± 0.62	7.47 ± 0.69
G024.5065–00.2224	290.25 ± 20.68	405.36 ± 22.98	2601.48 ± 241.89	7109.98 ± 767.93	10.24 ± 0.08	9.88 ± 0.06	7.86 ± 0.10	6.77 ± 0.12
G024.8497+00.0881	77.97 ± 8.87	110.89 ± 14.29	541.36 ± 58.58	1424.67 ± 240.40	11.67 ± 0.12	11.29 ± 0.14	9.57 ± 0.12	8.52 ± 0.18
G025.3948+00.0332	72.83 ± 6.46	260.66 ± 7.16	1129.20 ± 37.97	2389.80 ± 106.08	11.74 ± 0.10	10.36 ± 0.03	8.77 ± 0.04	7.95 ± 0.05
G025.3970+00.5614	24.32 ± 1.55	93.97 ± 1.42	381.40 ± 10.54	913.01 ± 35.13	12.94 ± 0.07	11.47 ± 0.02	9.95 ± 0.03	9.00 ± 0.04
G025.3981–00.1411	389.84 ± 110.58	1001.96 ± 120.32	5658.69 ± 1120.13	16138.67 ± 3107.68	9.92 ± 0.31	8.90 ± 0.13	7.02 ± 0.21	5.88 ± 0.21
G025.3983+00.5617	40.72 ± 1.85	105.87 ± 1.81	506.75 ± 11.99	1177.70 ± 34.80	12.38 ± 0.05	11.34 ± 0.02	9.64 ± 0.03	8.72 ± 0.03
G025.3991–00.1366	49.22 ± 15.25	94.48 ± 22.34	811.57 ± 308.98	2525.76 ± 1045.67	12.17 ± 0.33	11.46 ± 0.26	9.13 ± 0.41	7.89 ± 0.45
G025.7157+00.0487	119.78 ± 2.88	165.50 ± 3.60	818.64 ± 18.74	2358.09 ± 56.92	11.20 ± 0.03	10.85 ± 0.02	9.12 ± 0.02	7.97 ± 0.03
G026.0916–00.0565	23.51 ± 3.67	32.99 ± 3.56	277.79 ± 20.92	722.48 ± 55.99	12.97 ± 0.17	12.60 ± 0.12	10.29 ± 0.08	9.25 ± 0.08
G026.1094–00.0937	26.39 ± 2.19	47.37 ± 2.12	150.53 ± 12.19	342.55 ± 34.26	12.85 ± 0.09	12.21 ± 0.05	10.96 ± 0.09	10.06 ± 0.11
G026.5976–00.0236	59.31 ± 3.18	232.09 ± 3.27	849.86 ± 26.07	1416.62 ± 35.68	11.97 ± 0.06	10.49 ± 0.02	9.08 ± 0.03	8.52 ± 0.03
G026.6089–00.2121	130.91 ± 9.34	147.16 ± 7.69	611.47 ± 27.40	1534.05 ± 63.55	11.11 ± 0.08	10.98 ± 0.06	9.43 ± 0.05	8.44 ± 0.04
G026.8304–00.2067	18.09 ± 2.36	22.84 ± 1.98	231.67 ± 8.11	635.05 ± 19.28	13.26 ± 0.14	13.00 ± 0.09	10.49 ± 0.04	9.39 ± 0.03

Continued on next page

Table C.1 – continued from previous page

Name	$S_{3.6\mu\text{m}}$ (mJy)	$S_{4.5\mu\text{m}}$ (mJy)	$S_{5.8\mu\text{m}}$ (mJy)	$S_{8.0\mu\text{m}}$ (mJy)	[3.6]	[4.5]	[5.8]	[8.0]
G027.1859–00.0816	30.24 ± 6.31	66.50 ± 5.97	339.28 ± 50.65	921.01 ± 105.02	12.70 ± 0.23	11.84 ± 0.10	10.07 ± 0.16	8.99 ± 0.12
G027.2800+00.1447	66.41 ± 15.56	118.31 ± 14.43	711.42 ± 123.84	2160.30 ± 356.56	11.84 ± 0.25	11.22 ± 0.13	9.27 ± 0.19	8.06 ± 0.18
G027.3644–00.1657	31.39 ± 6.31	60.12 ± 5.52	409.05 ± 66.10	1311.50 ± 216.18	12.66 ± 0.22	11.95 ± 0.10	9.87 ± 0.17	8.61 ± 0.18
G027.5637+00.0845	113.44 ± 17.22	121.82 ± 14.81	620.61 ± 73.59	1633.34 ± 212.29	11.26 ± 0.16	11.19 ± 0.13	9.42 ± 0.13	8.37 ± 0.14
G028.4518+00.0027	7.35 ± 1.67	14.40 ± 1.59	157.58 ± 11.77	426.25 ± 39.14	14.23 ± 0.25	13.50 ± 0.12	10.91 ± 0.08	9.83 ± 0.10
G028.5816+00.1447	22.57 ± 3.24	35.81 ± 3.48	272.12 ± 15.05	688.78 ± 26.33	13.02 ± 0.16	12.51 ± 0.10	10.31 ± 0.06	9.30 ± 0.04
G028.6082+00.0185	108.13 ± 7.08	194.96 ± 7.79	1265.97 ± 78.57	3237.33 ± 218.20	11.32 ± 0.07	10.68 ± 0.04	8.64 ± 0.07	7.62 ± 0.07
G028.6523+00.0273	51.05 ± 4.75	113.25 ± 5.15	649.34 ± 28.60	1720.71 ± 73.23	12.13 ± 0.10	11.26 ± 0.05	9.37 ± 0.05	8.31 ± 0.05
G028.6869+00.1770	110.74 ± 6.41	147.02 ± 5.85	1280.73 ± 64.02	3364.81 ± 216.00	11.29 ± 0.06	10.98 ± 0.04	8.63 ± 0.05	7.58 ± 0.07
G029.7704+00.2189	26.98 ± 4.21	37.95 ± 3.52	180.00 ± 16.38	487.54 ± 32.77	12.82 ± 0.17	12.45 ± 0.10	10.76 ± 0.10	9.68 ± 0.07
G030.0096–00.2734		8.83 ± 1.04	23.89 ± 4.75	40.24 ± 11.39		14.03 ± 0.13	12.95 ± 0.21	12.39 ± 0.31
G030.2527+00.0540	42.90 ± 6.66	74.83 ± 6.14	647.62 ± 26.15	1848.75 ± 65.95	12.32 ± 0.17	11.71 ± 0.09	9.37 ± 0.04	8.23 ± 0.04
G030.5313+00.0205	221.93 ± 5.69	209.73 ± 6.48	1066.10 ± 82.44	3049.80 ± 220.26	10.53 ± 0.03	10.60 ± 0.03	8.83 ± 0.08	7.69 ± 0.08
G030.5353+00.0204	280.41 ± 13.63	403.72 ± 13.23	2221.58 ± 119.77	5625.50 ± 322.46	10.28 ± 0.05	9.88 ± 0.04	8.03 ± 0.06	7.02 ± 0.06
G030.5887–00.0428	101.76 ± 1.28	409.13 ± 1.52	1366.37 ± 11.89	1795.32 ± 30.59	11.38 ± 0.01	9.87 ± 0.00	8.56 ± 0.01	8.26 ± 0.02
G030.6881–00.0718	193.14 ± 16.70	360.17 ± 19.81	1842.89 ± 156.50	5928.66 ± 525.02	10.69 ± 0.09	10.01 ± 0.06	8.24 ± 0.09	6.97 ± 0.10
G030.7197–00.0829	103.00 ± 11.38	102.44 ± 9.37	422.69 ± 86.84	1044.04 ± 112.78	11.37 ± 0.12	11.37 ± 0.10	9.83 ± 0.22	8.85 ± 0.12
G030.7532–00.0511			894.17 ± 375.99				9.02 ± 0.45	
G030.7579+00.2042	21.78 ± 3.47	53.65 ± 3.73	494.34 ± 25.26	1557.61 ± 73.18	13.05 ± 0.17	12.08 ± 0.08	9.66 ± 0.06	8.42 ± 0.05
G030.7661–00.0348	821.01 ± 25.07	1030.24 ± 57.64	2357.18 ± 415.24	5130.34 ± 1666.61	9.11 ± 0.03	8.87 ± 0.06	7.97 ± 0.19	7.12 ± 0.35
G030.9581+00.0869	94.82 ± 2.69	338.15 ± 3.75	1289.53 ± 20.84	2303.79 ± 13.07	11.46 ± 0.03	10.08 ± 0.01	8.62 ± 0.02	7.99 ± 0.01
G031.0495+00.4697	15.35 ± 1.05	22.91 ± 1.33	179.98 ± 7.20	452.47 ± 15.55	13.43 ± 0.07	13.00 ± 0.06	10.76 ± 0.04	9.76 ± 0.04

Continued on next page

Table C.1 – continued from previous page

Name	$S_{3.6\mu\text{m}}$ (mJy)	$S_{4.5\mu\text{m}}$ (mJy)	$S_{5.8\mu\text{m}}$ (mJy)	$S_{8.0\mu\text{m}}$ (mJy)	[3.6]	[4.5]	[5.8]	[8.0]
G031.0595+00.0922	13.25 ± 2.00	21.25 ± 2.38	237.44 ± 8.74	652.68 ± 28.83	13.59 ± 0.16	13.08 ± 0.12	10.46 ± 0.04	9.36 ± 0.05
G031.1590+00.0465	12.23 ± 1.64	26.60 ± 1.62	163.52 ± 9.23	473.97 ± 22.71	13.68 ± 0.14	12.84 ± 0.07	10.87 ± 0.06	9.71 ± 0.05
G031.1596+00.0448	11.28 ± 1.54	24.03 ± 1.64	141.49 ± 9.89	386.67 ± 29.22	13.77 ± 0.15	12.95 ± 0.07	11.02 ± 0.08	9.93 ± 0.08
G031.2420–00.1106	102.54 ± 9.58	149.96 ± 7.36	894.50 ± 47.67	2332.76 ± 116.65	11.37 ± 0.10	10.96 ± 0.05	9.02 ± 0.06	7.98 ± 0.05
G031.2435–00.1103	297.10 ± 3.89	212.20 ± 3.94	513.08 ± 30.06	1265.34 ± 99.72	10.22 ± 0.01	10.58 ± 0.02	9.62 ± 0.06	8.64 ± 0.09
G031.2448–00.1132	30.57 ± 3.65	44.75 ± 3.57	305.07 ± 25.61	847.95 ± 73.93	12.69 ± 0.13	12.27 ± 0.09	10.19 ± 0.09	9.08 ± 0.09
G031.3959–00.2570	255.27 ± 33.12	399.77 ± 28.76	1789.22 ± 277.93	4898.04 ± 845.34	10.38 ± 0.14	9.90 ± 0.08	8.27 ± 0.17	7.17 ± 0.19
G031.4130+00.3065	40.42 ± 11.84	121.78 ± 13.66	1058.07 ± 59.31	3157.47 ± 103.40	12.38 ± 0.32	11.19 ± 0.12	8.84 ± 0.06	7.65 ± 0.04
G031.5815+00.0744	12.10 ± 2.51	38.12 ± 3.11	280.50 ± 12.78	781.33 ± 32.52	13.69 ± 0.22	12.45 ± 0.09	10.28 ± 0.05	9.17 ± 0.04
G032.0297+00.0491	195.53 ± 6.02	196.68 ± 5.18	1479.13 ± 25.79	3958.75 ± 77.25	10.67 ± 0.03	10.67 ± 0.03	8.47 ± 0.02	7.41 ± 0.02
G032.1502+00.1329	714.72 ± 85.40	718.35 ± 69.54	4660.34 ± 631.16	13715.66 ± 1894.70	9.26 ± 0.13	9.26 ± 0.10	7.23 ± 0.15	6.06 ± 0.15
G032.2730–00.2258	234.33 ± 21.21	227.17 ± 17.66	1293.33 ± 78.37	3634.94 ± 260.50	10.48 ± 0.10	10.51 ± 0.08	8.62 ± 0.07	7.50 ± 0.08
G032.4727+00.2036	205.35 ± 1.91	346.68 ± 1.96	784.93 ± 9.67	1495.90 ± 28.72	10.62 ± 0.01	10.05 ± 0.01	9.16 ± 0.01	8.46 ± 0.02
G032.7398+00.1940	9.64 ± 0.98	17.09 ± 0.92	126.21 ± 5.59	335.04 ± 15.87	13.94 ± 0.11	13.32 ± 0.06	11.15 ± 0.05	10.09 ± 0.05
G032.7492–00.0643 <sup>†</sup>	288.71 ± 1.33	537.69 ± 1.63	1380.26 ± 7.30	1616.34 ± 8.32	10.25 ± 0.00	9.57 ± 0.00	8.55 ± 0.01	8.38 ± 0.01
G032.9273+00.6060	146.00 ± 11.41	182.68 ± 8.58	936.85 ± 48.02	2626.01 ± 125.84	10.99 ± 0.08	10.75 ± 0.05	8.97 ± 0.06	7.85 ± 0.05
G033.1328–00.0923	19.10 ± 4.59	79.33 ± 4.52	265.90 ± 37.60	586.27 ± 128.20	13.20 ± 0.26	11.65 ± 0.06	10.34 ± 0.15	9.48 ± 0.24
G033.4163–00.0036	274.35 ± 9.22	259.63 ± 10.10	997.27 ± 103.59	2321.88 ± 261.59	10.30 ± 0.04	10.36 ± 0.04	8.90 ± 0.11	7.99 ± 0.12
G033.8100–00.1864	318.18 ± 4.74	394.98 ± 7.29	3830.11 ± 54.64	6988.93 ± 76.97	10.14 ± 0.02	9.91 ± 0.02	7.44 ± 0.02	6.79 ± 0.01
G033.9145+00.1105	711.40 ± 20.66	925.40 ± 18.30	5839.29 ± 124.65	17553.89 ± 276.96	9.27 ± 0.03	8.98 ± 0.02	6.98 ± 0.02	5.79 ± 0.02
G034.0901+00.4365	37.11 ± 1.92	40.69 ± 2.60	354.66 ± 21.97	1060.27 ± 72.87	12.48 ± 0.06	12.38 ± 0.07	10.03 ± 0.07	8.84 ± 0.07
G034.1978–00.5912	53.29 ± 2.72	76.23 ± 2.71	717.16 ± 22.77	2058.83 ± 69.59	12.08 ± 0.06	11.69 ± 0.04	9.26 ± 0.03	8.12 ± 0.04

Continued on next page

Table C.1 – continued from previous page

Name	$S_{3.6\mu\text{m}}$ (mJy)	$S_{4.5\mu\text{m}}$ (mJy)	$S_{5.8\mu\text{m}}$ (mJy)	$S_{8.0\mu\text{m}}$ (mJy)	[3.6]	[4.5]	[5.8]	[8.0]
G034.4032+00.2277	49.67 ± 0.79	130.38 ± 1.44	412.32 ± 7.94	931.48 ± 19.27	12.16 ± 0.02	11.11 ± 0.01	9.86 ± 0.02	8.98 ± 0.02
G034.5920+00.2434	14.42 ± 1.54	23.93 ± 1.52	182.79 ± 8.15	482.14 ± 25.29	13.50 ± 0.12	12.95 ± 0.07	10.75 ± 0.05	9.69 ± 0.06
G035.0242+00.3502	17.56 ± 1.21	116.41 ± 1.77	171.48 ± 10.37		13.29 ± 0.07	11.24 ± 0.02	10.81 ± 0.07	
G035.0524–00.5177	90.38 ± 6.22	127.87 ± 7.94	785.46 ± 60.15	2342.59 ± 202.82	11.51 ± 0.07	11.13 ± 0.07	9.16 ± 0.08	7.98 ± 0.09
G035.4570–00.1791	1.65 ± 0.96	3.02 ± 0.90	20.94 ± 3.35	56.69 ± 6.23	15.86 ± 0.63	15.20 ± 0.32	13.10 ± 0.17	12.02 ± 0.12
G035.4669+00.1394	484.27 ± 3.12	668.88 ± 5.42	4448.55 ± 41.55	13779.98 ± 108.29	9.69 ± 0.01	9.34 ± 0.01	7.28 ± 0.01	6.05 ± 0.01
G035.5781–00.0305	63.64 ± 5.65	142.12 ± 5.79	506.18 ± 74.32	1380.06 ± 238.34	11.89 ± 0.10	11.02 ± 0.04	9.64 ± 0.16	8.55 ± 0.19
G036.4057+00.0226	75.91 ± 1.86	124.39 ± 1.75	561.88 ± 12.78	1345.25 ± 6.63	11.70 ± 0.03	11.16 ± 0.02	9.53 ± 0.02	8.58 ± 0.01
G036.4062+00.0221	55.10 ± 1.49	110.72 ± 1.64	501.24 ± 7.75	1244.41 ± 5.90	12.05 ± 0.03	11.29 ± 0.02	9.65 ± 0.02	8.66 ± 0.01
G037.5457–00.1120	355.43 ± 28.74	517.81 ± 25.57	2548.83 ± 542.22	6332.31 ± 1325.82	10.02 ± 0.09	9.61 ± 0.05	7.88 ± 0.23	6.90 ± 0.23
G037.7347–00.1128	6.36 ± 0.96	25.45 ± 1.11	79.50 ± 7.11	134.37 ± 15.19	14.39 ± 0.16	12.89 ± 0.05	11.65 ± 0.10	11.08 ± 0.12
G037.7562+00.5605	43.19 ± 3.20	53.63 ± 3.39	511.81 ± 24.83	1453.70 ± 74.01	12.31 ± 0.08	12.08 ± 0.07	9.63 ± 0.05	8.49 ± 0.05
G037.8197+00.4140	10.55 ± 1.60	18.52 ± 2.14	148.25 ± 7.57	470.25 ± 17.94	13.84 ± 0.16	13.23 ± 0.12	10.97 ± 0.06	9.72 ± 0.04
G037.8209+00.4125	8.08 ± 1.26	15.24 ± 1.56	116.91 ± 5.58	346.93 ± 17.94	14.13 ± 0.17	13.44 ± 0.11	11.23 ± 0.05	10.05 ± 0.06
G037.8683–00.6008	141.33 ± 2.80	212.42 ± 2.49	1104.76 ± 12.86	3111.53 ± 20.62	11.02 ± 0.02	10.58 ± 0.01	8.79 ± 0.01	7.67 ± 0.01
G037.9723–00.0965	8.41 ± 0.96	16.18 ± 0.97	117.41 ± 4.89	329.87 ± 12.67	14.09 ± 0.12	13.38 ± 0.06	11.23 ± 0.04	10.10 ± 0.04
G038.5493+00.1646	95.57 ± 5.16	104.48 ± 4.53	677.19 ± 27.61	2060.49 ± 37.39	11.45 ± 0.06	11.35 ± 0.05	9.32 ± 0.04	8.12 ± 0.02
G038.6465–00.2260	24.02 ± 2.10	38.61 ± 2.42	341.05 ± 16.30	891.27 ± 44.66	12.95 ± 0.09	12.43 ± 0.07	10.07 ± 0.05	9.02 ± 0.05
G038.6529+00.0875	2.44 ± 0.52	6.81 ± 0.67	56.82 ± 2.97	173.26 ± 5.79	15.43 ± 0.23	14.32 ± 0.11	12.01 ± 0.06	10.80 ± 0.04
G038.6934–00.4524	16.84 ± 1.13	30.05 ± 1.30	234.87 ± 5.29	648.54 ± 8.02	13.33 ± 0.07	12.71 ± 0.05	10.47 ± 0.02	9.37 ± 0.01
G038.8756+00.3080	48.16 ± 2.84	66.43 ± 3.90	396.82 ± 15.07	1100.65 ± 30.97	12.19 ± 0.06	11.84 ± 0.06	9.90 ± 0.04	8.80 ± 0.03
G039.1956+00.2255	27.49 ± 0.96	48.95 ± 1.14	220.85 ± 4.14	630.23 ± 9.07	12.80 ± 0.04	12.18 ± 0.03	10.54 ± 0.02	9.40 ± 0.02

Continued on next page

Table C.1 – continued from previous page

Name	$S_{3.6\mu\text{m}}$ (mJy)	$S_{4.5\mu\text{m}}$ (mJy)	$S_{5.8\mu\text{m}}$ (mJy)	$S_{8.0\mu\text{m}}$ (mJy)	[3.6]	[4.5]	[5.8]	[8.0]
G039.8824–00.3460	56.13 ± 2.88	115.25 ± 2.77	700.94 ± 21.96	1888.43 ± 63.74	12.03 ± 0.06	11.25 ± 0.03	9.29 ± 0.03	8.21 ± 0.04
G040.4251+00.7002	18.42 ± 1.68	57.91 ± 1.61	231.50 ± 16.84	605.19 ± 55.68	13.24 ± 0.10	11.99 ± 0.03	10.49 ± 0.08	9.45 ± 0.10
G041.7419+00.0973	135.80 ± 7.49	201.40 ± 7.00	1125.66 ± 61.24	3197.17 ± 144.94	11.07 ± 0.06	10.64 ± 0.04	8.77 ± 0.06	7.64 ± 0.05
G042.1090–00.4469	102.82 ± 3.74	139.53 ± 5.59	693.42 ± 20.68	1759.70 ± 64.85	11.37 ± 0.04	11.04 ± 0.04	9.30 ± 0.03	8.29 ± 0.04
G042.4345–00.2605	673.00 ± 3.59	884.65 ± 5.20	1998.88 ± 45.48	4439.75 ± 147.80	9.33 ± 0.01	9.03 ± 0.01	8.15 ± 0.02	7.28 ± 0.04
G043.1489+00.0130	340.70 ± 10.94	925.01 ± 16.48	4357.36 ± 159.72	6808.83 ± 475.75	10.07 ± 0.03	8.98 ± 0.02	7.30 ± 0.04	6.82 ± 0.08
G043.1520+00.0115	198.77 ± 10.16	406.81 ± 17.23	1666.28 ± 115.88	5187.89 ± 425.47	10.65 ± 0.06	9.88 ± 0.05	8.35 ± 0.08	7.11 ± 0.09
G043.1657+00.0116		140.18 ± 9.94	1391.33 ± 155.20	2510.54 ± 642.52		11.03 ± 0.08	8.54 ± 0.12	7.90 ± 0.28
G043.1665+00.0106		182.69 ± 30.73	1663.19 ± 338.49	3472.96 ± 1164.28		10.75 ± 0.18	8.35 ± 0.22	7.55 ± 0.36
G043.1674+00.0128	43.36 ± 3.71	134.68 ± 4.65	861.46 ± 70.11	2752.10 ± 326.89	12.31 ± 0.09	11.08 ± 0.04	9.06 ± 0.09	7.80 ± 0.13
G043.1677+00.0196	62.04 ± 7.91	141.54 ± 7.32	751.87 ± 126.99	2375.49 ± 389.76	11.92 ± 0.14	11.02 ± 0.06	9.21 ± 0.18	7.96 ± 0.18
G043.1684+00.0124	182.89 ± 4.47	342.97 ± 5.12	900.96 ± 74.74	2483.86 ± 305.79	10.74 ± 0.03	10.06 ± 0.02	9.01 ± 0.09	7.91 ± 0.13
G043.1699+00.0115	40.44 ± 8.92	105.66 ± 9.37	647.46 ± 102.37	1682.22 ± 327.76	12.38 ± 0.24	11.34 ± 0.10	9.37 ± 0.17	8.34 ± 0.21
G043.1701+00.0078			1189.51 ± 770.12				8.71 ± 0.70	
G043.1706–00.0003	23.93 ± 12.87	47.47 ± 24.79	447.07 ± 165.84		12.95 ± 0.58	12.21 ± 0.57	9.77 ± 0.40	
G043.1716+00.0001	55.98 ± 18.44	103.09 ± 34.48	790.68 ± 219.15	2386.61 ± 1215.33	12.03 ± 0.36	11.37 ± 0.36	9.15 ± 0.30	7.96 ± 0.55
G043.1763+00.0248	133.77 ± 11.47	263.68 ± 21.63	935.86 ± 219.71	3289.25 ± 719.00	11.08 ± 0.09	10.35 ± 0.09	8.97 ± 0.25	7.61 ± 0.24
G043.1778–00.5181	160.36 ± 8.79	233.12 ± 7.11	1549.17 ± 91.66	4098.20 ± 282.81	10.89 ± 0.06	10.48 ± 0.03	8.42 ± 0.06	7.37 ± 0.07
G043.2371–00.0453	25.99 ± 2.27	78.06 ± 2.75	479.57 ± 16.91	1437.11 ± 68.83	12.86 ± 0.09	11.67 ± 0.04	9.70 ± 0.04	8.51 ± 0.05
G043.3064–00.2114	29.58 ± 0.51	68.73 ± 0.67	322.74 ± 2.92	807.95 ± 5.25	12.72 ± 0.02	11.81 ± 0.01	10.13 ± 0.01	9.13 ± 0.01
G043.7954–00.1274	55.90 ± 1.00	293.62 ± 1.81	939.12 ± 14.85	1831.11 ± 34.62	12.03 ± 0.02	10.23 ± 0.01	8.97 ± 0.02	8.24 ± 0.02
G043.7960–00.1286	59.29 ± 1.08	134.84 ± 1.47	798.18 ± 15.71	1934.54 ± 41.03	11.97 ± 0.02	11.08 ± 0.01	9.14 ± 0.02	8.18 ± 0.02

Continued on next page

Table C.1 – continued from previous page

Name	$S_{3.6\mu\text{m}}$ (mJy)	$S_{4.5\mu\text{m}}$ (mJy)	$S_{5.8\mu\text{m}}$ (mJy)	$S_{8.0\mu\text{m}}$ (mJy)	[3.6]	[4.5]	[5.8]	[8.0]
G043.8894–00.7840	235.66 ± 6.39	375.67 ± 7.02	1818.43 ± 54.14	5420.25 ± 168.60	10.47 ± 0.03	9.96 ± 0.02	8.25 ± 0.03	7.06 ± 0.03
G043.9675+00.9939	32.88 ± 0.84	46.75 ± 0.78	202.65 ± 4.89	613.68 ± 8.63	12.61 ± 0.03	12.23 ± 0.02	10.63 ± 0.03	9.43 ± 0.02
G044.3103+00.0410	31.50 ± 0.58	41.65 ± 0.63	265.33 ± 3.55	653.53 ± 12.17	12.65 ± 0.02	12.35 ± 0.02	10.34 ± 0.01	9.36 ± 0.02
G044.4228+00.5377	4.97 ± 1.25	6.76 ± 1.27	77.43 ± 9.20	272.30 ± 23.22	14.66 ± 0.27	14.32 ± 0.20	11.68 ± 0.13	10.31 ± 0.09
G045.1242+00.1356	166.07 ± 32.99	260.89 ± 35.53	4049.91 ± 202.54	8943.36 ± 752.21	10.85 ± 0.21	10.36 ± 0.15	7.38 ± 0.05	6.52 ± 0.09
G045.4545+00.0591	704.08 ± 70.16	1487.07 ± 69.14	5402.69 ± 541.82	16875.34 ± 1621.34	9.28 ± 0.11	8.47 ± 0.05	7.07 ± 0.11	5.83 ± 0.10
G045.4559+00.0613	187.57 ± 32.14	393.95 ± 36.92	2661.24 ± 297.80	8733.53 ± 942.49	10.72 ± 0.18	9.91 ± 0.10	7.84 ± 0.12	6.55 ± 0.12
G045.4656+00.0452	32.56 ± 1.46	103.05 ± 3.25	98.79 ± 29.93		12.62 ± 0.05	11.37 ± 0.03	11.41 ± 0.33	
G045.5431–00.0073	52.16 ± 5.67	74.41 ± 6.75	726.58 ± 44.00	2139.10 ± 126.27	12.11 ± 0.12	11.72 ± 0.10	9.25 ± 0.07	8.07 ± 0.06
G048.6099+00.0270	476.67 ± 12.12	427.73 ± 13.26	910.97 ± 153.20	2074.39 ± 506.61	9.70 ± 0.03	9.82 ± 0.03	9.00 ± 0.18	8.11 ± 0.26
G048.9296–00.2793	72.36 ± 37.48	120.43 ± 28.84			11.75 ± 0.56	11.20 ± 0.26		
G048.9901–00.2988	40.73 ± 2.64	98.80 ± 3.89	181.77 ± 18.48	667.17 ± 82.06	12.38 ± 0.07	11.41 ± 0.04	10.75 ± 0.11	9.34 ± 0.13
G049.3666–00.3010	44.28 ± 27.27	116.96 ± 58.43			12.28 ± 0.67	11.23 ± 0.54		
G049.4640–00.3511	46.41 ± 13.98	115.48 ± 19.44	734.54 ± 177.15	3201.85 ± 556.14	12.23 ± 0.33	11.24 ± 0.18	9.23 ± 0.26	7.64 ± 0.19
G050.3152+00.6762	79.77 ± 3.10	106.53 ± 3.07	858.95 ± 32.26	2480.15 ± 122.16	11.65 ± 0.04	11.33 ± 0.03	9.07 ± 0.04	7.91 ± 0.05
G050.3157+00.6747	191.53 ± 8.60	178.21 ± 8.04	1536.99 ± 67.06	4672.83 ± 195.93	10.69 ± 0.05	10.77 ± 0.05	8.43 ± 0.05	7.23 ± 0.05
G052.7533+00.3340	246.92 ± 9.27	275.77 ± 10.00	1925.19 ± 62.50	5219.79 ± 141.53	10.42 ± 0.04	10.30 ± 0.04	8.19 ± 0.04	7.11 ± 0.03
G053.9589+00.0320	72.29 ± 2.08	97.01 ± 1.67	674.40 ± 28.03	1980.35 ± 104.89	11.75 ± 0.03	11.43 ± 0.02	9.33 ± 0.04	8.16 ± 0.06
G058.7739+00.6457	108.24 ± 12.26	160.66 ± 9.43	1232.48 ± 101.73	3168.97 ± 343.44	11.31 ± 0.12	10.89 ± 0.06	8.67 ± 0.09	7.65 ± 0.12
G059.6027+00.9118	12.03 ± 2.75	39.88 ± 2.74	99.68 ± 8.52	244.34 ± 10.79	13.70 ± 0.25	12.40 ± 0.07	11.40 ± 0.09	10.43 ± 0.05
G061.4763+00.0892		752.61 ± 76.83	5192.64 ± 1661.68	15695.08 ± 3054.71		9.21 ± 0.11	7.11 ± 0.35	5.91 ± 0.21
G061.4770+00.0891		198.75 ± 55.98				10.65 ± 0.30		

Continued on next page

**Table C.1 – continued from previous page**

Name	$S_{3.6\mu\text{m}}$ (mJy)	$S_{4.5\mu\text{m}}$ (mJy)	$S_{5.8\mu\text{m}}$ (mJy)	$S_{8.0\mu\text{m}}$ (mJy)	[3.6]	[4.5]	[5.8]	[8.0]
G061.7207+00.8630	$82.01 \pm 1.02$	$87.55 \pm 0.96$	$520.03 \pm 6.93$	$1465.15 \pm 16.38$	$11.62 \pm 0.01$	$11.54 \pm 0.01$	$9.61 \pm 0.01$	$8.49 \pm 0.01$

Table C.2 UKIDSS fluxes, AB magnitudes and colours of the CORNISH UCHII regions with a visible counterpart in at least the K band. All flux values and their associated errors are in mJy. Missing values are due to missing or unreliable data. All values without a quoted error are limits (upper flux limits and their corresponding lower magnitude limits).

Name	$S_J$ (mJy)	$S_H$ (mJy)	$S_K$ (mJy)	$J$	$H$	$K$	$J - H$	$H - K$
G010.3009-00.1477	1.47	3.54	$4.64 \pm 1.81$	15.05	13.65	$12.83 \pm 0.42$	1.40	0.81
G010.6297-00.3380	0.89	2.18	$1.38 \pm 0.58$	15.59	14.17	$14.15 \pm 0.45$	1.41	0.02
G010.9584+00.0221	0.66	1.86	$1.63 \pm 0.77$	15.92	14.35	$13.97 \pm 0.51$	1.57	0.38
G011.1104-00.3985	2.68	4.51	$26.25 \pm 1.53$	14.39	13.39	$10.95 \pm 0.06$	1.01	2.43
G011.9368-00.6158	1.94	3.90	$6.65 \pm 1.79$	14.74	13.54	$12.44 \pm 0.29$	1.20	1.10
G011.9446-00.0369	20.54	$33.35 \pm 18.56$	$43.24 \pm 15.87$	12.18	$11.21 \pm 0.60$	$10.41 \pm 0.40$	0.97	$0.8 \pm 0.72$
G012.4317-01.1112		4.48	$5.24 \pm 1.27$		13.39	$12.70 \pm 0.26$		0.69
G012.8050-00.2007	5.61	$7.15 \pm 4.35$	$30.26 \pm 5.86$	13.59	$12.88 \pm 0.66$	$10.80 \pm 0.21$	0.70	$2.09 \pm 0.69$
G012.8131-00.1976	0.99	2.08	$2.11 \pm 0.86$	15.47	14.22	$13.69 \pm 0.44$	1.25	0.54
G014.1046+00.0918	0.76	2.43	$2.17 \pm 0.96$	15.77	14.06	$13.66 \pm 0.48$	1.71	0.40
G017.1141-00.1124	0.66	1.93	$3.25 \pm 0.85$	15.91	14.31	$13.22 \pm 0.28$	1.60	1.09
G018.1460-00.2839	$10.90 \pm 0.31$	$69.19 \pm 11.81$	$91.95 \pm 12.47$	$12.87 \pm 0.03$	$10.42 \pm 0.18$	$9.59 \pm 0.15$	$2.45 \pm 0.19$	$0.83 \pm 0.24$
G018.3024-00.3910	$2.07 \pm 0.10$	$17.23 \pm 4.71$	$66.23 \pm 4.80$	$14.67 \pm 0.05$	$11.93 \pm 0.29$	$9.95 \pm 0.08$	$2.74 \pm 0.30$	$1.98 \pm 0.31$
G018.8250-00.4675	0.53	1.30	$1.17 \pm 0.60$	16.16	14.74	$14.33 \pm 0.56$	1.42	0.41
G019.0754-00.2874	2.09	5.29	$27.71 \pm 2.33$	14.66	13.21	$10.89 \pm 0.09$	1.45	2.32
G019.6087-00.2351	10.36	31.23	$33.87 \pm 8.43$	12.92	11.28	$10.68 \pm 0.27$	1.64	0.61
G019.6090-00.2313	2.19	6.61	$8.26 \pm 2.05$	14.61	12.97	$12.21 \pm 0.27$	1.64	0.76
G020.0720-00.1421	2.46	7.08	$14.25 \pm 2.46$	14.49	12.90	$11.62 \pm 0.19$	1.59	1.28
G021.3571-00.1766	0.55	1.87	$2.87 \pm 0.70$	16.12	14.34	$13.35 \pm 0.26$	1.78	0.99

Continued on next page

Table C.2 – continued from previous page

Name	$S_J$ (mJy)	$S_H$ (mJy)	$S_K$ (mJy)	$J$	$H$	$K$	$J - H$	$H - K$
G021.3855–00.2541	0.75	2.27	$3.32 \pm 0.81$	15.78	14.13	$13.20 \pm 0.26$	1.65	0.93
G023.1974–00.0006	0.65	$2.09 \pm 0.51$	$3.95 \pm 0.53$	15.93	$14.22 \pm 0.26$	$13.01 \pm 0.14$	1.71	$1.21 \pm 0.30$
G023.2654+00.0765	1.13	2.45	$2.66 \pm 0.89$	15.33	14.05	$13.44 \pm 0.36$	1.29	0.61
G023.7110+00.1705	0.87	$6.19 \pm 0.84$	$8.85 \pm 0.92$	15.62	$13.04 \pm 0.15$	$12.13 \pm 0.11$	2.57	$0.91 \pm 0.18$
G024.4698+00.4954	$0.94 \pm 0.22$	$2.41 \pm 0.57$	$3.60 \pm 0.77$	$15.53 \pm 0.26$	$14.06 \pm 0.25$	$13.11 \pm 0.23$	$1.47 \pm 0.36$	$0.95 \pm 0.34$
G024.4721+00.4877	$4.71 \pm 0.31$	$12.92 \pm 0.92$	$14.20 \pm 1.34$	$13.78 \pm 0.07$	$12.24 \pm 0.08$	$11.62 \pm 0.10$	$1.54 \pm 0.11$	$0.62 \pm 0.13$
G024.4736+00.4950	1.23	2.55	$4.74 \pm 1.12$	15.24	14.00	$12.81 \pm 0.26$	1.23	1.19
G024.5065–00.2224	1.23	2.63	$10.76 \pm 1.36$	15.23	13.97	$11.92 \pm 0.14$	1.26	2.05
G025.3809–00.1815	$17.74 \pm 1.51$	$76.01 \pm 8.15$	$93.97 \pm 5.22$	$12.34 \pm 0.09$	$10.32 \pm 0.12$	$9.57 \pm 0.06$	$2.02 \pm 0.15$	$0.75 \pm 0.13$
G025.3824–00.1812	$8.49 \pm 0.41$	$51.78 \pm 3.33$	$80.95 \pm 2.67$	$13.14 \pm 0.05$	$10.74 \pm 0.07$	$9.73 \pm 0.04$	$2.4 \pm 0.09$	$1.01 \pm 0.08$
G025.3981–00.1411	2.60	6.13	$4.92 \pm 2.38$	14.43	13.05	$12.77 \pm 0.52$	1.37	0.28
G025.8011–00.1568	0.40	$3.56 \pm 0.31$	$8.45 \pm 0.39$	16.47	$13.64 \pm 0.09$	$12.18 \pm 0.05$	2.83	$1.46 \pm 0.11$
G027.2800+00.1447	3.45	9.12	$8.15 \pm 2.60$	14.12	12.62	$12.22 \pm 0.34$	1.50	0.40
G028.2879–00.3641	$9.16 \pm 0.44$	$40.46 \pm 1.35$	$57.53 \pm 2.95$	$13.06 \pm 0.05$	$11.00 \pm 0.04$	$10.10 \pm 0.06$	$2.05 \pm 0.06$	$0.9 \pm 0.07$
G028.6082+00.0185	0.34	$0.79 \pm 0.25$	$9.50 \pm 0.66$	16.63	$15.28 \pm 0.34$	$12.06 \pm 0.07$	1.35	$3.22 \pm 0.35$
G028.6869+00.1770	0.51	1.35	$8.65 \pm 0.99$	16.19	14.70	$12.16 \pm 0.12$	1.49	2.54
G029.9559–00.0168	$8.11 \pm 1.34$	$50.68 \pm 2.69$	$109.83 \pm 3.11$	$13.19 \pm 0.18$	$10.76 \pm 0.06$	$9.40 \pm 0.03$	$2.43 \pm 0.19$	$1.36 \pm 0.06$
G030.5353+00.0204	1.98	3.66	$28.94 \pm 1.32$	14.72	13.61	$10.85 \pm 0.05$	1.11	2.76
G030.6881–00.0718	0.99	1.80	$7.67 \pm 1.25$	15.48	14.39	$12.29 \pm 0.18$	1.09	2.10
G030.7532–00.0511	0.39	0.89	2.92	16.49	15.15	13.33	1.34	1.81
G030.7661–00.0348	0.41	$5.30 \pm 0.46$	$36.20 \pm 2.10$	16.44	$13.21 \pm 0.09$	$10.60 \pm 0.06$	3.23	$2.61 \pm 0.11$
G030.8662+00.1143	0.48	0.88	1.95	16.26	15.16	13.77	1.10	1.39

Continued on next page

Table C.2 – continued from previous page

Name	$S_J$ (mJy)	$S_H$ (mJy)	$S_K$ (mJy)	$J$	$H$	$K$	$J - H$	$H - K$
G031.0495+00.4697	0.17	0.32	0.97	17.37	16.25	14.53	1.12	1.72
G031.2435−00.1103	$0.59 \pm 0.15$	$3.09 \pm 0.46$	$6.20 \pm 0.86$	$16.03 \pm 0.28$	$13.80 \pm 0.16$	$12.52 \pm 0.15$	$2.23 \pm 0.32$	$1.28 \pm 0.22$
G031.3959−00.2570			$12.52 \pm 0.14$			$11.76 \pm 0.01$		−11.76
G032.0297+00.0491	0.77	$1.00 \pm 0.43$	$5.16 \pm 1.00$	15.74	$15.02 \pm 0.46$	$12.72 \pm 0.21$	0.72	$2.31 \pm 0.51$
G032.1502+00.1329	$6.45 \pm 1.07$	$21.64 \pm 2.28$	$45.80 \pm 4.71$	$13.44 \pm 0.18$	$11.68 \pm 0.11$	$10.35 \pm 0.11$	$1.75 \pm 0.21$	$1.34 \pm 0.16$
G032.4727+00.2036	0.30	$4.54 \pm 0.25$	$17.25 \pm 0.65$	16.76	$13.38 \pm 0.06$	$11.41 \pm 0.04$	3.38	$1.97 \pm 0.07$
G032.7492−00.0643	0.76	2.06	$8.73 \pm 0.71$	15.76	14.23	$12.15 \pm 0.09$	1.52	2.09
G032.7966+00.1909	4.94	10.02	$33.71 \pm 4.00$	13.73	12.52	$10.68 \pm 0.13$	1.21	1.84
G034.2544+00.1460	1.06	2.22	$9.73 \pm 1.31$	15.40	14.15	$12.03 \pm 0.15$	1.24	2.13
G034.2571+00.1466	0.55	1.17	$6.18 \pm 0.78$	16.12	14.85	$12.52 \pm 0.14$	1.26	2.33
G034.4032+00.2277	0.40	0.75	$3.00 \pm 0.30$	16.47	15.33	$13.31 \pm 0.11$	1.14	2.02
G035.0524−00.5177	0.77	$1.56 \pm 0.53$	$4.34 \pm 0.68$	15.74	$14.54 \pm 0.37$	$12.91 \pm 0.17$	1.20	$1.63 \pm 0.40$
G035.5781−00.0305	0.63	1.71	$3.23 \pm 0.66$	15.96	14.44	$13.23 \pm 0.22$	1.52	1.21
G036.4057+00.0226	0.36	0.79	$3.06 \pm 0.35$	16.58	15.27	$13.29 \pm 0.12$	1.31	1.99
G037.5457−00.1120	2.57	$8.69 \pm 1.71$	$11.62 \pm 2.00$	14.44	$12.67 \pm 0.21$	$11.84 \pm 0.19$	1.76	$0.84 \pm 0.28$
G037.8683−00.6008	1.26	$1.68 \pm 1.09$	$5.26 \pm 1.13$	15.21	$14.46 \pm 0.70$	$12.70 \pm 0.23$	0.76	$1.76 \pm 0.74$
G039.8824−00.3460	1.08	2.09	$1.46 \pm 0.81$	15.38	14.22	$14.09 \pm 0.60$	1.16	0.13
G042.1090−00.4469	0.39	$1.15 \pm 0.31$	$4.35 \pm 0.45$	16.50	$14.87 \pm 0.29$	$12.90 \pm 0.11$	1.63	$1.97 \pm 0.31$
G042.4345−00.2605	0.57	1.76	$10.87 \pm 0.74$	16.06	14.41	$11.91 \pm 0.07$	1.66	2.50
G043.1651−00.0283		$2.62 \pm 0.07$	$12.81 \pm 0.25$		$13.98 \pm 0.03$	$11.73 \pm 0.02$		$2.25 \pm 0.04$
G043.1677+00.0196	0.75	1.83	$1.46 \pm 0.72$	15.78	14.37	$14.09 \pm 0.54$	1.41	0.28
G043.1763+00.0248	0.85	$3.35 \pm 0.67$	$7.96 \pm 0.77$	15.64	$13.71 \pm 0.22$	$12.25 \pm 0.10$	1.94	$1.46 \pm 0.24$

Continued on next page

Table C.2 – continued from previous page

Name	$S_J$ (mJy)	$S_H$ (mJy)	$S_K$ (mJy)	$J$	$H$	$K$	$J - H$	$H - K$
G043.7960–00.1286		0.92	$2.02 \pm 0.30$		15.12	$13.74 \pm 0.16$		1.38
G043.8894–00.7840	1.58	$3.74 \pm 1.01$	$11.72 \pm 0.93$	14.97	$13.59 \pm 0.29$	$11.83 \pm 0.09$	1.38	$1.76 \pm 0.30$
G043.9675+00.9939	0.25	0.55	$2.30 \pm 0.40$	16.96	15.67	$13.60 \pm 0.19$	1.29	2.07
G044.3103+00.0410	0.31	0.71	$1.60 \pm 0.27$	16.74	15.40	$13.99 \pm 0.18$	1.34	1.40
G045.0694+00.1323			$1.55 \pm 0.05$			$14.02 \pm 0.04$		–14.02
G045.1223+00.1321	$15.09 \pm 1.19$	$32.43 \pm 2.74$	$149.19 \pm 2.81$	$12.52 \pm 0.08$	$11.24 \pm 0.09$	$9.07 \pm 0.02$	$1.27 \pm 0.12$	$2.18 \pm 0.09$
G045.1242+00.1356	1.07	8.22	$8.20 \pm 1.06$	15.39	12.73	$12.22 \pm 0.14$	2.65	0.52
G045.4545+00.0591	$17.78 \pm 0.94$	$32.43 \pm 2.14$	$40.46 \pm 3.23$	$12.34 \pm 0.06$	$11.24 \pm 0.07$	$10.48 \pm 0.09$	$1.09 \pm 0.09$	$0.76 \pm 0.11$
G045.4559+00.0613	0.95	2.16	$8.90 \pm 1.20$	15.52	14.18	$12.13 \pm 0.15$	1.34	2.06
G045.4656+00.0452	0.37	0.81	$3.10 \pm 0.39$	16.53	15.24	$13.27 \pm 0.14$	1.29	1.97
G048.6099+00.0270	1.15	4.02	$5.67 \pm 3.93$	15.31	13.51	$12.62 \pm 0.75$	1.80	0.89
G049.3666–00.3010	0.83	1.65	$1.74 \pm 0.66$	15.67	14.48	$13.90 \pm 0.41$	1.19	0.58
G049.4905–00.3688	$5.44 \pm 0.41$	$47.46 \pm 1.21$	$134.25 \pm 1.77$	$13.62 \pm 0.08$	$10.83 \pm 0.03$	$9.18 \pm 0.01$	$2.79 \pm 0.09$	$1.65 \pm 0.03$
G050.3152+00.6762	0.51	3.62	$3.17 \pm 0.56$	16.18	13.63	$13.25 \pm 0.19$	2.56	0.38
G050.3157+00.6747	$1.68 \pm 0.68$	$7.27 \pm 1.41$	$11.06 \pm 1.47$	$14.90 \pm 0.44$	$12.87 \pm 0.21$	$11.89 \pm 0.14$	$2.03 \pm 0.49$	$0.98 \pm 0.25$
G052.7533+00.3340	2.42	5.06	$8.61 \pm 1.77$	14.50	13.26	$12.16 \pm 0.22$	1.24	1.10
G053.9589+00.0320	0.44	0.87	$2.84 \pm 0.42$	16.35	15.17	$13.37 \pm 0.16$	1.18	1.80
G058.7739+00.6457	0.67	$2.86 \pm 0.62$	$5.15 \pm 0.52$	15.89	$13.88 \pm 0.23$	$12.72 \pm 0.11$	2.01	$1.16 \pm 0.26$
G060.8842–00.1286		0.95	$4.89 \pm 0.64$		15.08	$12.78 \pm 0.14$		2.30
G061.7207+00.8630	0.47	0.93	$8.55 \pm 0.35$	16.27	15.10	$12.17 \pm 0.04$	1.17	2.93

Table C.3 Extinctions towards the CORNISH UCHII with visible near-IR nebulae (at least in the K band), computed from the measured near-IR fluxes using four different methods.  $A_\lambda/A_V$  ratios were computed following Cardelli et al. [1989]: those are  $\sim 0.28$ ,  $0.18$ , and  $0.11$ , for UKIDSS  $\lambda = J, H, K$ , respectively, assuming  $R_V = 3.1$ . Missing values in the table are due to missing or unreliable data. All values without a quoted error are lower limits.

Name	$A_H$	$A_K$	$A_V(H)$	$A_V(K)$	$A_V(J-H)$	$A_V(H-K)$
G010.3009-00.1477	4.16	$4.03 \pm 0.44$	36.71	$35.49 \pm 3.85$	19.60	9.37
G010.6297-00.3380	1.24	$1.9 \pm 0.46$	10.97	$16.74 \pm 4.08$	19.74	-1.89
G010.9584+00.0221	3.59	$3.89 \pm 0.52$	31.69	$34.31 \pm 4.6$	21.31	3.17
G011.1104-00.3985	3.11	$1.36 \pm 0.07$	27.45	$11.96 \pm 0.65$	15.63	32.41
G011.9368-00.6158	4.72	$4.29 \pm 0.31$	41.57	$37.84 \pm 2.77$	17.57	13.43
G011.9446-00.0369	$2.17 \pm 0.60$	$2.04 \pm 0.40$	$19.1 \pm 5.33$	$17.98 \pm 3.54$	$15.24 \pm 6.07$	$9.21 \pm 10.24$
G012.4317-01.1112	1.51	$1.49 \pm 0.27$	13.29	$13.15 \pm 2.38$		7.64
G012.8050-00.2007	$6.65 \pm 0.68$	$5.24 \pm 0.25$	$58.65 \pm 6.00$	$46.22 \pm 2.22$	$12.58 \pm 6.65$	$27.48 \pm 9.81$
G012.8131-00.1976	5.68	$5.82 \pm 0.47$	50.08	$51.32 \pm 4.18$	18.09	5.41
G014.1046+00.0918	1.05	$1.33 \pm 0.48$	9.27	$11.72 \pm 4.22$	22.74	3.45
G017.1141-00.1124	0.91	$0.5 \pm 0.28$	8.06	$4.44 \pm 2.5$	21.63	13.26
G018.1460-00.2839	$1.27 \pm 0.19$	$1.12 \pm 0.15$	$11.18 \pm 1.66$	$9.83 \pm 1.32$	$30.2 \pm 1.89$	$9.59 \pm 3.35$
G018.3024-00.3910	$3.21 \pm 0.31$	$1.91 \pm 0.09$	$28.32 \pm 2.71$	$16.81 \pm 0.83$	$33.18 \pm 3.03$	$26 \pm 4.34$
G018.8250-00.4675	0.90	$1.17 \pm 0.56$	7.90	$10.28 \pm 4.95$	19.81	3.56
G019.0754-00.2874	3.18	$1.54 \pm 0.10$	28.03	$13.55 \pm 0.89$	20.15	30.77
G019.6087-00.2351	3.46	$3.52 \pm 0.29$	30.48	$31.07 \pm 2.51$	22.03	6.45
G019.6090-00.2313	2.52	$2.44 \pm 0.28$	22.26	$21.48 \pm 2.45$	22.06	8.66
G020.0720-00.1421	2.22	$1.61 \pm 0.19$	19.56	$14.23 \pm 1.7$	21.53	16.02

Continued on next page

Table C.3 – continued from previous page

Name	$A_H$	$A_K$	$A_V(H)$	$A_V(K)$	$A_V(J - H)$	$A_V(H - K)$
G021.3571-00.1766	1.35	$1.04 \pm 0.26$	11.91	$9.16 \pm 2.33$	23.41	11.85
G021.3855-00.2541	2.79	$2.53 \pm 0.28$	24.57	$22.32 \pm 2.43$	22.12	11.05
G023.1974-00.0006	$0.24 \pm 0.26$	$-0.3 \pm 0.15$	$2.09 \pm 2.30$	$-2.63 \pm 1.28$	$22.76 \pm 2.64$	$15.03 \pm 4.25$
G023.2654+00.0765	2.43	$2.5 \pm 0.37$	21.43	$22.02 \pm 3.27$	18.47	6.46
G023.7110+00.1705	$2.36 \pm 0.16$	$2.12 \pm 0.13$	$20.77 \pm 1.43$	$18.72 \pm 1.13$	$31.47 \pm 1.49$	$10.72 \pm 2.63$
G024.4698+00.4954	$1.25 \pm 0.26$	$0.98 \pm 0.24$	$11.06 \pm 2.29$	$8.62 \pm 2.08$	$20.32 \pm 3.64$	$11.35 \pm 4.87$
G024.4721+00.4877	$0.11 \pm 0.08$	$0.17 \pm 0.10$	$1.01 \pm 0.68$	$1.47 \pm 0.9$	$20.99 \pm 1.06$	$6.66 \pm 1.81$
G024.4736+00.4950	2.51	$2 \pm 0.27$	22.16	$17.6 \pm 2.34$	17.94	14.76
G024.5065-00.2224	3.27	$1.9 \pm 0.15$	28.82	$16.71 \pm 1.29$	18.22	26.96
G025.3809-00.1815	$0.49 \pm 0.12$	$0.42 \pm 0.06$	$4.36 \pm 1.03$	$3.69 \pm 0.54$	$25.89 \pm 1.49$	$8.48 \pm 1.85$
G025.3824-00.1812	$0.01 \pm 0.07$	$-0.32 \pm 0.04$	$0.05 \pm 0.61$	$-2.86 \pm 0.33$	$29.76 \pm 0.88$	$12.1 \pm 1.11$
G025.3981-00.1411	4.89	$5.29 \pm 0.54$	43.12	$46.6 \pm 4.77$	19.35	1.80
G025.8011-00.1568	$0.92 \pm 0.10$	$0.14 \pm 0.05$	$8.1 \pm 0.85$	$1.21 \pm 0.44$	$34.03 \pm 0.94$	$18.54 \pm 1.49$
G027.2800+00.1447	2.72	$2.99 \pm 0.36$	23.95	$26.39 \pm 3.14$	20.59	3.47
G028.2879-00.3641	$1.38 \pm 0.05$	$1.15 \pm 0.06$	$12.13 \pm 0.47$	$10.13 \pm 0.57$	$26.22 \pm 0.64$	$10.64 \pm 0.94$
G028.6082+00.0185	$4.6 \pm 0.36$	$2.05 \pm 0.10$	$40.53 \pm 3.21$	$18.11 \pm 0.84$	$19.12 \pm 3.42$	$43.6 \pm 4.93$
G028.6869+00.1770	3.25	$1.38 \pm 0.13$	28.62	$12.18 \pm 1.16$	20.57	33.93
G029.9559-00.0168	$3.01 \pm 0.10$	$2.33 \pm 0.07$	$26.53 \pm 0.91$	$20.5 \pm 0.65$	$30.02 \pm 1.90$	$17.15 \pm 0.92$
G030.5353+00.0204	4.26	$2.17 \pm 0.08$	37.52	$19.11 \pm 0.69$	16.70	37.12
G030.6881-00.0718	4.57	$3.15 \pm 0.20$	40.33	$27.81 \pm 1.75$	16.48	27.62
G030.7532-00.0511	4.86	3.73	42.87	32.85	19.04	23.57
G030.7661-00.0348	$1.58 \pm 0.12$	$-0.35 \pm 0.06$	$13.95 \pm 1.09$	$-3.07 \pm 0.57$	$38.11 \pm 0.96$	$34.88 \pm 1.61$

Continued on next page

Table C.3 – continued from previous page

Name	$A_H$	$A_K$	$A_V(H)$	$A_V(K)$	$A_V(J - H)$	$A_V(H - K)$
G030.8662+00.1143	4.96	4.25	43.71	37.45	16.61	17.52
G031.0495+00.4697	2.61	1.56	22.98	13.76	16.77	22.29
G031.2435−00.1103	$3.68 \pm 0.19$	$3.08 \pm 0.17$	$32.45 \pm 1.68$	$27.17 \pm 1.51$	$28.05 \pm 3.27$	$15.94 \pm 3.13$
G031.3959−00.2570	−11.71	$0.72 \pm 0.03$		$6.34 \pm 0.26$		
G032.0297+00.0491	$2.11 \pm 0.47$	$0.48 \pm 0.21$	$18.57 \pm 4.14$	$4.21 \pm 1.86$	$12.72 \pm 4.66$	$30.58 \pm 7.21$
G032.1502+00.1329	$2.02 \pm 0.13$	$1.36 \pm 0.12$	$17.78 \pm 1.17$	$11.98 \pm 1.06$	$23.2 \pm 2.15$	$16.78 \pm 2.26$
G032.4727+00.2036	$1.87 \pm 0.08$	$0.57 \pm 0.04$	$16.46 \pm 0.72$	$5.04 \pm 0.39$	$39.61 \pm 0.61$	$25.83 \pm 1.03$
G032.7492−00.0643	0.55	$−0.86 \pm 0.09$	4.81	$−7.62 \pm 0.82$	20.85	27.47
G032.7966+00.1909	4.77	$3.61 \pm 0.16$	42.07	$31.82 \pm 1.42$	17.68	23.94
G034.2544+00.1460	4.04	$2.59 \pm 0.17$	35.60	$22.83 \pm 1.49$	18.03	28.02
G034.2571+00.1466	2.57	$0.91 \pm 0.15$	22.65	$8.06 \pm 1.29$	18.23	30.96
G034.4032+00.2277	1.22	$−0.12 \pm 0.11$	10.76	$−1.08 \pm 0.96$	17.00	26.51
G035.0524−00.5177	$2.63 \pm 0.38$	$1.68 \pm 0.18$	$23.21 \pm 3.33$	$14.77 \pm 1.56$	$17.6 \pm 3.71$	$21.03 \pm 5.74$
G035.5781−00.0305	3.64	$3.1 \pm 0.24$	32.09	$27.36 \pm 2.1$	20.87	15.04
G036.4057+00.0226	2.16	$0.85 \pm 0.13$	19.05	$7.5 \pm 1.11$	18.69	26.05
G037.5457−00.1120	$2.71 \pm 0.23$	$2.55 \pm 0.20$	$23.91 \pm 2.02$	$22.5 \pm 1.77$	$23.29 \pm 2.15$	$9.69 \pm 4.02$
G037.8683−00.6008	$3.78 \pm 0.71$	$2.7 \pm 0.25$	$33.31 \pm 6.25$	$23.78 \pm 2.18$	$13.12 \pm 7.07$	$22.8 \pm 10.48$
G039.8824−00.3460	3.84	$4.39 \pm 0.61$	33.87	$38.69 \pm 5.4$	17.17	−0.37
G042.1090−00.4469	$1.31 \pm 0.29$	$0.02 \pm 0.11$	$11.55 \pm 2.59$	$0.19 \pm 0.99$	$21.92 \pm 2.94$	$25.75 \pm 4.44$
G042.4345−00.2605	2.73	$0.91 \pm 0.08$	24.07	$8.01 \pm 0.7$	22.20	33.33
G043.1651−00.0283	$6.08 \pm 0.18$	$4.51 \pm 0.13$	$53.57 \pm 1.58$	$39.74 \pm 1.17$		$29.73 \pm 0.5$
G043.1677+00.0196	3.04	$3.44 \pm 0.56$	26.78	$30.31 \pm 4.92$	19.75	1.72

Continued on next page

Table C.3 – continued from previous page

Name	$A_H$	$A_K$	$A_V(H)$	$A_V(K)$	$A_V(J - H)$	$A_V(H - K)$
G043.1763+00.0248	$2.73 \pm 0.24$	$1.95 \pm 0.13$	$24.07 \pm 2.15$	$17.16 \pm 1.16$	$25.03 \pm 2.19$	$18.57 \pm 3.42$
G043.7960-00.1286	1.11	$0.4 \pm 0.16$	9.78	$3.57 \pm 1.43$		17.43
G043.8894-00.7840	$3.91 \pm 0.31$	$2.83 \pm 0.12$	$34.49 \pm 2.75$	$24.92 \pm 1.02$	$19.41 \pm 2.95$	$22.85 \pm 4.33$
G043.9675+00.9939	3.23	$1.83 \pm 0.20$	28.44	$16.14 \pm 1.73$	18.49	27.25
G044.3103+00.0410	0.76	$0.03 \pm 0.18$	6.68	$0.27 \pm 1.59$	19.04	17.76
G045.0694+00.1323	-12.32	$2.38 \pm 0.08$		$20.94 \pm 0.68$		
G045.1223+00.1321	$3.45 \pm 0.13$	$1.95 \pm 0.06$	$30.39 \pm 1.16$	$17.15 \pm 0.51$	$18.32 \pm 1.26$	$28.77 \pm 1.33$
G045.1242+00.1356	0.74	$0.9 \pm 0.15$	6.53	$7.93 \pm 1.31$	32.30	5.15
G045.4545+00.0591	$2.29 \pm 0.10$	$2.21 \pm 0.11$	$20.2 \pm 0.85$	$19.45 \pm 0.94$	$16.52 \pm 0.92$	$8.62 \pm 1.59$
G045.4559+00.0613	1.98	$0.6 \pm 0.15$	17.47	$5.3 \pm 1.3$	18.99	27.05
G045.4656+00.0452	3.25	$1.95 \pm 0.15$	28.62	$17.2 \pm 1.31$	18.49	25.83
G048.6099+00.0270	2.32	$2.1 \pm 0.75$	20.47	$18.54 \pm 6.64$	23.69	10.51
G049.3666-00.3010	3.64	$3.73 \pm 0.48$	32.05	$32.92 \pm 4.21$	17.54	6.01
G049.4905-00.3688	$3.3 \pm 0.10$	$2.33 \pm 0.07$	$29.11 \pm 0.87$	$20.53 \pm 0.6$	$33.7 \pm 0.88$	$21.26 \pm 0.44$
G050.3152+00.6762	1.92	$2.22 \pm 0.20$	16.90	$19.53 \pm 1.78$	31.33	3.17
G050.3157+00.6747	$1.05 \pm 0.21$	$0.75 \pm 0.15$	$9.22 \pm 1.87$	$6.57 \pm 1.29$	$25.98 \pm 4.91$	$11.69 \pm 3.62$
G052.7533+00.3340	3.24	$2.82 \pm 0.24$	28.59	$24.88 \pm 2.08$	18.04	13.40
G053.9589+00.0320	2.84	$1.72 \pm 0.17$	25.05	$15.12 \pm 1.48$	17.40	23.43
G058.7739+00.6457	$-0.91 \pm 0.24$	$-1.39 \pm 0.15$	$-8.03 \pm 2.14$	$-12.28 \pm 1.33$	$25.82 \pm 2.36$	$14.27 \pm 3.67$
G060.8842-00.1286	1.77	$0.15 \pm 0.14$	15.64	$1.29 \pm 1.24$		30.56
G061.7207+00.8630	3.64	$1.38 \pm 0.06$	32.04	$12.14 \pm 0.53$	17.26	39.48



# Appendix D

## JVLA follow-up – photometric results

Table D.1 Photometric results for the higher-resolution data targets. New components of CORNISH sources that were previously merged into single unresolved sources have been measured as individual sources, where appropriate, and assigned a letter for distinction of the name. The measured source coordinates, clean beam axes, deconvolved source axes and position angles, average source diameters, integrated and peak fluxes are presented, in this order.

Name	$\alpha$ (J2000) (hh:mm:ss)	$\delta$ (J2000) (dd:mm:ss)	$\theta_{\text{Maj beam}}$ (")	$\theta_{\text{min beam}}$ (")	$\theta_{\text{M}}$ (")	$\theta_{\text{m}}$ (")	$\theta_{\text{PA}}$ ( $^{\circ}$ )	$\theta_{\text{source}}$ (")	$F_{\text{int}}$ (mJy)	$F_{\text{peak}}$ (mJy beam $^{-1}$ )
G016.1448+00.0088	18:20:04.58	-14:53:25.43	0.29	0.17	$0.70 \pm 0.03$	$0.43 \pm 0.02$	$53.6 \pm 3.5$	$0.55 \pm 0.02$	$12.82 \pm 0.45$	$1.64 \pm 0.05$
G017.0299-00.0696	18:22:05.08	-14:08:48.90	0.28	0.17	$0.61 \pm 0.04$	$0.45 \pm 0.03$	$164.7 \pm 8.4$	$0.52 \pm 0.02$	$2.03 \pm 0.11$	$0.30 \pm 0.01$
G017.5549+00.1654	18:22:14.79	-13:34:22.10	0.28	0.17	$1.58 \pm 0.06$	$1.42 \pm 0.06$	$156 \pm 20$	$1.50 \pm 0.04$	$5.98 \pm 0.23$	$0.12 \pm 0.00$
G018.4433-00.0056	18:24:34.65	-12:52:05.58	0.28	0.17	$2.34 \pm 0.06$	$2.21 \pm 0.06$	$121 \pm 26$	$2.27 \pm 0.04$	$97.1 \pm 2.4$	$0.88 \pm 0.02$
G018.6654+00.0294a	18:24:52.60	-12:39:20.51	0.27	0.17	$0.55 \pm 0.04$	$0.29 \pm 0.03$	$16.2 \pm 5.3$	$0.40 \pm 0.02$	$3.21 \pm 0.2$	$0.69 \pm 0.04$
G018.6654+00.0294b	18:24:52.57	-12:39:20.55	0.27	0.17	$0.23 \pm 0.03$	$0.19 \pm 0.03$	$119 \pm 41$	$0.21 \pm 0.02$	$0.75 \pm 0.04$	$0.37 \pm 0.02$
G018.7106+00.0002	18:25:04.15	-12:37:45.82	0.28	0.17	$0.89 \pm 0.03$	$0.78 \pm 0.02$	$114 \pm 12$	$0.83 \pm 0.02$	$101.2 \pm 2.5$	$6.43 \pm 0.15$
G018.7612+00.2630	18:24:12.88	-12:27:41.73	0.28	0.17	$0.87 \pm 0.02$	$0.76 \pm 0.02$	$12.8 \pm 9.6$	$0.81 \pm 0.01$	$44.71 \pm 0.97$	$2.93 \pm 0.06$
G018.8250-00.4675	18:26:59.04	-12:44:46.54	0.27	0.17	$1.68 \pm 0.08$	$1.39 \pm 0.07$	$105 \pm 11$	$1.53 \pm 0.05$	$7.85 \pm 0.38$	$0.15 \pm 0.01$
G019.0767-00.2882	18:26:48.87	-12:26:23.79	0.28	0.17	$1.21 \pm 0.05$	$1.12 \pm 0.04$	$84 \pm 25$	$1.16 \pm 0.03$	$91 \pm 3$	$3.03 \pm 0.10$
G019.7549-00.1282	18:27:31.60	-11:45:55.16	0.26	0.17	$0.45 \pm 0.02$	$0.40 \pm 0.01$	$156 \pm 16$	$0.42 \pm 0.01$	$37.2 \pm 1.1$	$7.28 \pm 0.19$
G020.0797-00.1337	18:28:09.79	-11:28:48.53	0.27	0.17	$0.96 \pm 0.07$	$0.92 \pm 0.07$	$79 \pm 84$	$0.94 \pm 0.05$	$14.07 \pm 0.65$	$0.69 \pm 0.03$
G020.7619-00.0646	18:29:12.35	-10:50:38.47	0.26	0.17	$1.98 \pm 0.09$	$1.29 \pm 0.06$	$82.6 \pm 4$	$1.59 \pm 0.05$	$5.89 \pm 0.25$	$0.10 \pm 0.00$
G020.9636-00.0744a	18:29:37.31	-10:40:10.76	0.26	0.18	$3.15 \pm 0.09$	$2.15 \pm 0.06$	$98.1 \pm 3$	$2.60 \pm 0.05$	$19.21 \pm 0.55$	$0.13 \pm 0.00$
G020.9636-00.0744b	18:29:37.32	-10:40:12.56	0.26	0.18	$0.65 \pm 0.06$	$0.56 \pm 0.05$	$116 \pm 30$	$0.60 \pm 0.04$	$2.59 \pm 0.18$	$0.28 \pm 0.02$
G021.3571-00.1766	18:30:43.92	-10:22:06.86	0.25	0.17	$0.71 \pm 0.07$	$0.45 \pm 0.05$	$139.2 \pm 9.1$	$0.57 \pm 0.04$	$10.83 \pm 0.92$	$1.28 \pm 0.10$
G023.4835+00.0964	18:33:44.05	-08:21:23.43	0.24	0.17	$0.82 \pm 0.05$	$0.56 \pm 0.04$	$171.2 \pm 7.2$	$0.68 \pm 0.03$	$3.2 \pm 0.2$	$0.27 \pm 0.02$

Continued on next page

Table D.1 – continued from previous page

Name	$\alpha$ (J2000) (hh:mm:ss)	$\delta$ (J2000) (dd:mm:ss)	$\theta_{\text{Maj beam}}$ (")	$\theta_{\text{min beam}}$ (")	$\theta_{\text{M}}$ (")	$\theta_{\text{m}}$ (")	$\theta_{\text{PA}}$ (°)	$\theta_{\text{source}}$ (")	$F_{\text{int}}$ (mJy)	$F_{\text{peak}}$ (mJy beam <sup>-1</sup> )
G024.1839+00.1199	18:34:57.19	-07:43:26.16	0.24	0.17	0.85 ± 0.04	0.65 ± 0.03	91.8 ± 7.6	0.74 ± 0.03	4.32 ± 0.2	0.30 ± 0.01
G025.3970+00.5614	18:35:37.44	-06:26:38.34	0.24	0.17	0.78 ± 0.04	0.67 ± 0.03	155 ± 18	0.72 ± 0.03	119.3 ± 5.5	8.76 ± 0.38
G025.7157+00.0487	18:38:02.78	-06:23:47.42	0.24	0.17	1.25 ± 0.06	0.87 ± 0.04	153.8 ± 5.7	1.04 ± 0.04	14.51 ± 0.72	0.54 ± 0.03
G025.8011-00.1568	18:38:56.37	-06:24:53.42	0.24	0.18	0.98 ± 0.10	0.92 ± 0.09	125 ± 73	0.95 ± 0.07	30.8 ± 2.7	1.39 ± 0.12
G026.0083+00.1369	18:38:16.28	-06:05:45.46	0.24	0.17	0.31 ± 0.01	0.28 ± 0.01	17 ± 30	0.30 ± 0.01	4.91 ± 0.14	1.55 ± 0.04
G026.0916-00.0565	18:39:06.98	-06:06:38.26	0.24	0.17	1.18 ± 0.09	0.86 ± 0.07	158 ± 10	1.01 ± 0.05	6.85 ± 0.5	0.27 ± 0.02
G026.1094-00.0937	18:39:16.92	-06:06:43.39	0.34	0.17	0.33 ± 0.03	0.22 ± 0.02	115 ± 10	0.27 ± 0.02	2.19 ± 0.09	0.92 ± 0.03
G026.5976-00.0236	18:39:55.89	-05:38:45.32	0.33	0.17	1.44 ± 0.04	0.79 ± 0.02	149.9 ± 1.8	1.07 ± 0.02	39.3 ± 1.1	1.91 ± 0.05
G026.8304-00.2067	18:41:00.84	-05:31:22.37	0.33	0.17	1.36 ± 0.05	1.18 ± 0.04	143 ± 13	1.27 ± 0.03	10.59 ± 0.39	0.37 ± 0.01
G027.1859-00.0816	18:41:13.26	-05:08:58.10	0.33	0.17	1.54 ± 0.07	1.39 ± 0.06	84 ± 22	1.46 ± 0.04	18.35 ± 0.71	0.47 ± 0.02
G027.3644-00.1657	18:41:50.96	-05:01:45.12	0.32	0.17	0.89 ± 0.03	0.81 ± 0.03	150 ± 22	0.85 ± 0.02	36.2 ± 1.1	2.61 ± 0.07
G027.9352+00.2056	18:41:34.35	-04:21:06.78	0.34	0.17	0.33 ± 0.01	0.23 ± 0.01	139.4 ± 2.5	0.28 ± 0.01	4.83 ± 0.21	3.77 ± 0.10
G028.2003-00.0494	18:42:58.11	-04:13:57.59	0.34	0.17	0.93 ± 0.04	0.57 ± 0.03	148.9 ± 3.6	0.73 ± 0.02	222.3 ± 9.3	22.18 ± 0.84
G028.4518+00.0027	18:43:14.60	-03:59:06.59	0.34	0.17	1.83 ± 0.06	1.63 ± 0.05	72 ± 12	1.73 ± 0.04	25.23 ± 0.73	0.49 ± 0.01
G030.0096-00.2734	18:47:04.72	-02:43:31.23	0.33	0.17	0.26 ± 0.04	0.17 ± 0.07	15 ± 21	0.21 ± 0.04	4.11 ± 0.28	2.09 ± 0.10
G030.5887-00.0428a	18:47:18.90	-02:06:16.72	0.32	0.17	0.22 ± 0.10	0.17 ± 0.13	107 ± 75	0.19 ± 0.09	25.6 ± 4.8	14.80 ± 1.90
G030.5887-00.0428b	18:47:18.88	-02:06:17.18	0.32	0.17	1.09 ± 0.19	0.33 ± 0.07	163.6 ± 5.2	0.60 ± 0.08	97 ± 16	12.10 ± 1.70
G031.0495+00.4697	18:46:19.86	-01:27:39.54	0.24	0.18	1.43 ± 0.08	0.85 ± 0.05	15.4 ± 4.3	1.10 ± 0.04	16.27 ± 0.91	0.55 ± 0.03
G031.0595+00.0922	18:47:41.61	-01:37:27.35	0.24	0.18	0.76 ± 0.03	0.56 ± 0.02	17.3 ± 4.9	0.65 ± 0.02	6.94 ± 0.23	0.62 ± 0.02
G031.1590+00.0465	18:48:02.27	-01:33:23.65	0.24	0.18	0.79 ± 0.06	0.56 ± 0.05	117 ± 10	0.67 ± 0.04	2.96 ± 0.22	0.26 ± 0.02
G031.2435-00.1103	18:48:45.04	-01:33:10.49	0.24	0.18	1.84 ± 0.07	1.81 ± 0.07	62 ± 112	1.83 ± 0.05	383 ± 13	4.87 ± 0.17

Continued on next page

Table D.1 – continued from previous page

Name	$\alpha$ (J2000) (hh:mm:ss)	$\delta$ (J2000) (dd:mm:ss)	$\theta_{\text{Maj beam}}$ (")	$\theta_{\text{min beam}}$ (")	$\theta_{\text{M}}$ (")	$\theta_{\text{m}}$ (")	$\theta_{\text{PA}}$ ( $^{\circ}$ )	$\theta_{\text{source}}$ (")	$F_{\text{int}}$ (mJy)	$F_{\text{peak}}$ (mJy beam $^{-1}$ )
G031.5815+00.0744	18:48:42.56	-01:10:04.43	0.24	0.18	2.67 $\pm$ 0.07	1.54 $\pm$ 0.04	111.8 $\pm$ 1.9	2.03 $\pm$ 0.04	15.3 $\pm$ 0.4	0.16 $\pm$ 0.00
G032.4727+00.2036	18:49:52.55	+00:18:56.63	0.25	0.18	1.07 $\pm$ 0.05	0.58 $\pm$ 0.03	92.5 $\pm$ 3	0.78 $\pm$ 0.03	56.3 $\pm$ 2.6	3.68 $\pm$ 0.16
G032.7398+00.1940	18:50:23.83	+00:04:57.30	0.24	0.17	0.44 $\pm$ 0.03	0.41 $\pm$ 0.03	150 $\pm$ 85	0.42 $\pm$ 0.02	4.54 $\pm$ 0.25	0.84 $\pm$ 0.04
G032.7492-00.0643	18:51:20.02	+00:11:30.89	0.24	0.18	2.09 $\pm$ 0.07	2.04 $\pm$ 0.07	20 $\pm$ 70	2.07 $\pm$ 0.05	22.72 $\pm$ 0.75	0.23 $\pm$ 0.01
G032.7982+00.1937	18:50:30.27	-00:01:49.76	0.24	0.18	2.21 $\pm$ 0.21	0.80 $\pm$ 0.08	23.2 $\pm$ 3.2	1.33 $\pm$ 0.14	16.8 $\pm$ 1.6	0.39 $\pm$ 0.04
G033.8100-00.1864a	18:53:42.23	+00:41:47.32	0.24	0.18	0.68 $\pm$ 0.05	0.26 $\pm$ 0.03	179.4 $\pm$ 3	0.42 $\pm$ 0.03	39.3 $\pm$ 2.9	7.28 $\pm$ 0.45
G033.8100-00.1864b	18:53:42.27	+00:41:45.71	0.24	0.18	0.70 $\pm$ 0.05	0.42 $\pm$ 0.03	134.4 $\pm$ 5.8	0.54 $\pm$ 0.03	9.02 $\pm$ 0.62	1.15 $\pm$ 0.07
G034.0901+00.4365	18:51:59.74	+01:13:47.63	0.24	0.18	2.34 $\pm$ 0.12	1.36 $\pm$ 0.07	92.9 $\pm$ 3.6	1.79 $\pm$ 0.06	6.95 $\pm$ 0.35	0.09 $\pm$ 0.00
G034.4032+00.2277	18:53:18.67	+01:24:47.64	0.22	0.18	0.45 $\pm$ 0.02	0.35 $\pm$ 0.01	53.2 $\pm$ 6.4	0.40 $\pm$ 0.01	6.62 $\pm$ 0.19	1.32 $\pm$ 0.03
G035.4570-00.1791	18:56:41.03	+02:09:55.33	0.22	0.18	0.96 $\pm$ 0.05	0.83 $\pm$ 0.04	126 $\pm$ 14	0.89 $\pm$ 0.03	7.48 $\pm$ 0.37	0.36 $\pm$ 0.02
G036.4057+00.0226	18:57:41.98	+03:06:05.18	0.22	0.18	1.25 $\pm$ 0.04	1.17 $\pm$ 0.04	119 $\pm$ 20	1.21 $\pm$ 0.03	25.14 $\pm$ 0.75	0.65 $\pm$ 0.02
G037.7347-00.1128	19:00:36.99	+04:13:18.56	0.22	0.18	0.85 $\pm$ 0.04	0.84 $\pm$ 0.04	116 $\pm$ 161	0.85 $\pm$ 0.03	17.79 $\pm$ 0.73	0.91 $\pm$ 0.04
G037.8209+00.4125	18:58:54.03	+04:32:18.89	0.22	0.18	1.57 $\pm$ 0.06	1.23 $\pm$ 0.05	17.2 $\pm$ 6.1	1.39 $\pm$ 0.04	17.37 $\pm$ 0.63	0.35 $\pm$ 0.01
G037.9723-00.0965	19:00:59.67	+04:26:26.59	0.22	0.18	1.63 $\pm$ 0.06	1.22 $\pm$ 0.04	116.8 $\pm$ 4.8	1.41 $\pm$ 0.03	15.39 $\pm$ 0.53	0.30 $\pm$ 0.01
G038.6465-00.2260	19:02:41.75	+04:58:49.87	0.22	0.18	3.84 $\pm$ 0.12	2.76 $\pm$ 0.08	124.2 $\pm$ 3.7	3.26 $\pm$ 0.07	41.9 $\pm$ 1.3	0.15 $\pm$ 0.00
G038.6529+00.0875	19:01:35.25	+05:07:47.30	0.22	0.18	0.24 $\pm$ 0.01	0.20 $\pm$ 0.01	9.1 $\pm$ 13.9	0.22 $\pm$ 0.01	8.7 $\pm$ 0.29	3.84 $\pm$ 0.09
G038.6934-00.4524	19:03:35.35	+04:55:06.22	0.21	0.17	1.40 $\pm$ 0.05	1.26 $\pm$ 0.05	124 $\pm$ 15	1.33 $\pm$ 0.03	19.27 $\pm$ 0.69	0.37 $\pm$ 0.01
G039.1956+00.2255	19:02:05.58	+05:40:31.63	0.21	0.17	0.84 $\pm$ 0.03	0.82 $\pm$ 0.03	29 $\pm$ 50	0.83 $\pm$ 0.02	58.7 $\pm$ 1.7	2.82 $\pm$ 0.08
G042.1090-00.4469	19:09:53.56	+07:57:15.18	0.2	0.17	0.74 $\pm$ 0.04	0.50 $\pm$ 0.03	114.1 $\pm$ 5.7	0.61 $\pm$ 0.02	8.54 $\pm$ 0.44	0.71 $\pm$ 0.03
G043.1489+00.0130	19:10:11.05	+09:05:20.15	0.47	0.43	0.47 $\pm$ 0.01	0.26 $\pm$ 0.01	120 $\pm$ 1.5	0.35 $\pm$ 0.01	69.03 $\pm$ 0.76	41.46 $\pm$ 0.31
G043.1520+00.0115	19:10:11.72	+09:05:27.79	0.47	0.43	2.16 $\pm$ 0.17	1.11 $\pm$ 0.09	80.4 $\pm$ 4.4	1.55 $\pm$ 0.09	255 $\pm$ 20	19.80 $\pm$ 1.40

Continued on next page

Table D.1 – continued from previous page

Name	$\alpha$ (J2000) (hh:mm:ss)	$\delta$ (J2000) (dd:mm:ss)	$\theta_{\text{Maj beam}}$ (")	$\theta_{\text{min beam}}$ (")	$\theta_{\text{M}}$ (")	$\theta_{\text{m}}$ (")	$\theta_{\text{PA}}$ (°)	$\theta_{\text{source}}$ (")	$F_{\text{int}}$ (mJy)	$F_{\text{peak}}$ (mJy beam <sup>-1</sup> )
G043.1706–00.0003	19:10:16.36	+09:06:06.98	0.47	0.43	$0.95 \pm 0.05$	$0.68 \pm 0.04$	$47.8 \pm 6.5$	$0.80 \pm 0.03$	$385 \pm 17$	$91.70 \pm 3.40$
G043.1720+00.0080	19:10:14.75	+09:06:25.66	0.47	0.43	$1.16 \pm 0.04$	$1.08 \pm 0.04$	$174 \pm 24$	$1.12 \pm 0.03$	$62.8 \pm 1.9$	$8.75 \pm 0.23$
G043.7954–00.1274a	19:11:53.99	+09:35:50.30	0.2	0.17	$0.31 \pm 0.01$	$0.20 \pm 0.01$	$103.3 \pm 2.8$	$0.25 \pm 0.01$	$54.6 \pm 1.3$	$18.53 \pm 0.33$
G043.7954–00.1274b	19:11:54.06	+09:35:49.77	0.2	0.17	$0.46 \pm 0.06$	$0.40 \pm 0.05$	$178 \pm 40$	$0.43 \pm 0.04$	$6.91 \pm 0.81$	$1.06 \pm 0.11$
G043.9675+00.9939	19:08:11.01	+10:16:03.12	0.24	0.15	$0.76 \pm 0.06$	$0.46 \pm 0.04$	$1.5 \pm 6.5$	$0.59 \pm 0.03$	$30.7 \pm 2.2$	$2.84 \pm 0.18$
G044.3103+00.0410a	19:12:15.73	+10:07:53.54	0.24	0.15	$0.80 \pm 0.06$	$0.70 \pm 0.06$	$156 \pm 26$	$0.75 \pm 0.04$	$3.66 \pm 0.25$	$0.22 \pm 0.01$
G044.3103+00.0410b	19:12:15.78	+10:07:52.58	0.24	0.15	$0.17 \pm 0.02$	$0.03 \pm 0.02$	$31.7 \pm 4.2$	$0.07 \pm 0.02$	$0.70 \pm 0.03$	$0.56 \pm 0.02$
G044.4228+00.5377	19:10:40.99	+10:27:40.69	0.22	0.18	$0.90 \pm 0.05$	$0.73 \pm 0.04$	$160 \pm 11$	$0.81 \pm 0.03$	$6.36 \pm 0.32$	$0.36 \pm 0.02$
G045.0694+00.1323	19:13:21.81	+10:50:48.44	0.22	0.18	$1.33 \pm 0.11$	$0.67 \pm 0.06$	$67.6 \pm 4.4$	$0.94 \pm 0.06$	$24.1 \pm 2$	$1.01 \pm 0.08$
G048.9901–00.2988	19:22:26.13	+14:06:39.72	0.21	0.18	$0.57 \pm 0.02$	$0.16 \pm 0.01$	$61.9 \pm 1.1$	$0.30 \pm 0.01$	$7.45 \pm 0.29$	$1.92 \pm 0.06$
G050.3152+00.6762	19:21:27.52	+15:44:20.78	0.21	0.18	$1.13 \pm 0.04$	$0.98 \pm 0.04$	$46 \pm 11$	$1.05 \pm 0.03$	$50.3 \pm 2$	$1.68 \pm 0.06$
G053.9589+00.0320	19:31:05.23	+18:38:16.91	0.2	0.18	$1.79 \pm 0.06$	$1.12 \pm 0.04$	$122.1 \pm 2.9$	$1.42 \pm 0.03$	$31.3 \pm 1.1$	$0.56 \pm 0.02$
G060.8842–00.1286	19:46:20.14	+00:35:29.31	0.23	0.14	$0.75 \pm 0.04$	$0.69 \pm 0.04$	$144 \pm 28$	$0.72 \pm 0.03$	$26.5 \pm 1.1$	$1.57 \pm 0.06$
G061.7207+00.8630	19:44:23.64	+01:48:43.35	0.23	0.14	$2.25 \pm 0.06$	$2.23 \pm 0.06$	$127 \pm 122$	$2.24 \pm 0.04$	$112.7 \pm 2.8$	$0.74 \pm 0.02$

Table D.2 Photometric results for CORNISH UCHII found within the same fields as the targets of the JVLA follow-up (referred to as the neighbour set in the text). All columns are defined as for the previous table.

Name	$\alpha$ (J2000) (hh:mm:ss)	$\delta$ (J2000) (dd:mm:ss)	$\theta_{\text{Maj beam}}$ (")	$\theta_{\text{min beam}}$ (")	$\theta_{\text{M}}$ (")	$\theta_{\text{m}}$ (")	$\theta_{\text{PA}}$ ( $^{\circ}$ )	$\theta_{\text{source}}$ (")	$F_{\text{int}}$ (mJy)	$F_{\text{peak}}$ (mJy beam $^{-1}$ )
G020.0809–00.1362	18:28:10.38	–11:28:48.45	0.27	0.17	$4.11 \pm 0.29$	$1.40 \pm 0.10$	$113.9 \pm 2.2$	$2.40 \pm 0.12$	$597 \pm 41$	$4.69 \pm 0.32$
G025.3983+00.5617	18:35:37.55	–06:26:33.51	0.24	0.17	$2.68 \pm 0.08$	$2.43 \pm 0.07$	$42 \pm 13$	$2.55 \pm 0.05$	$96.6 \pm 2.8$	$0.61 \pm 0.02$
G031.1596+00.0448	18:48:02.71	–01:33:24.73	0.24	0.18	$0.99 \pm 0.04$	$0.89 \pm 0.04$	$175 \pm 24$	$0.94 \pm 0.03$	$24.19 \pm 0.95$	$1.14 \pm 0.04$
G032.7966+00.1909a	18:50:31.00	+00:01:56.90	0.24	0.18	$1.07 \pm 0.06$	$0.96 \pm 0.05$	$173 \pm 53$	$1.02 \pm 0.04$	$267 \pm 14$	$10.65 \pm 0.52$
G032.7966+00.1909b	18:50:30.80	+00:01:53.81	0.24	0.18	$3.96 \pm 0.41$	$1.48 \pm 0.15$	$15.3 \pm 3.7$	$2.42 \pm 0.18$	$301 \pm 31$	$2.18 \pm 0.22$
G032.7966+00.1909c	18:50:30.73	+00:01:57.91	0.24	0.18	$1.34 \pm 0.11$	$0.75 \pm 0.07$	$43 \pm 5.6$	$1.00 \pm 0.06$	$145 \pm 12$	$5.88 \pm 0.47$
G032.7966+00.1909d	18:50:30.68	+00:02:00.39	0.24	0.18	$2.02 \pm 0.07$	$1.32 \pm 0.04$	$50.2 \pm 3$	$1.63 \pm 0.04$	$1121 \pm 36$	$17.64 \pm 0.56$
G036.4062+00.0221a	18:57:42.14	+03:06:06.22	0.22	0.18	$0.34 \pm 0.01$	$0.32 \pm 0.01$	$167 \pm 34$	$0.33 \pm 0.01$	$10.71 \pm 0.21$	$2.88 \pm 0.05$
G036.4062+00.0221b	18:57:42.23	+03:06:05.25	0.22	0.18	$0.26 \pm 0.04$	$0.19 \pm 0.03$	$19 \pm 48$	$0.22 \pm 0.03$	$0.82 \pm 0.10$	$0.37 \pm 0.03$
G043.1651–00.0283	19:10:21.78	+09:05:02.64	0.47	0.43	$3.79 \pm 0.13$	$1.31 \pm 0.05$	$170.9 \pm 1$	$2.23 \pm 0.05$	$1075 \pm 36$	$41.20 \pm 1.30$
G043.1652+00.0129	19:10:12.89	+09:06:11.77	0.47	0.43	$0.67 \pm 0.05$	$0.47 \pm 0.05$	$132 \pm 12$	$0.56 \pm 0.04$	$228 \pm 14$	$88.20 \pm 4.10$
G043.1657+00.0116	19:10:13.22	+09:06:11.19	0.23	0.14	$0.83 \pm 0.06$	$0.75 \pm 0.06$	$91 \pm 33$	$0.79 \pm 0.04$	$308 \pm 20$	$14.46 \pm 0.89$
G043.1665+00.0106	19:10:13.55	+09:06:12.43	0.47	0.43	$4.89 \pm 0.30$	$2.93 \pm 0.18$	$95.7 \pm 4.5$	$3.79 \pm 0.16$	$3570 \pm 220$	$49.80 \pm 3.00$
G043.1674+00.0128	19:10:13.16	+09:06:18.61	0.47	0.43	$0.85 \pm 0.07$	$0.78 \pm 0.07$	$84 \pm 61$	$0.81 \pm 0.05$	$295 \pm 20$	$69.20 \pm 3.90$
G043.1684+00.0087	19:10:14.16	+09:06:15.82	0.47	0.43	$2.03 \pm 0.17$	$1.67 \pm 0.14$	$130 \pm 19$	$1.84 \pm 0.11$	$308 \pm 25$	$17.40 \pm 1.30$
G043.1699+00.0115	19:10:13.76	+09:06:24.91	0.47	0.43	$1.64 \pm 0.13$	$1.16 \pm 0.10$	$156.5 \pm 9.4$	$1.38 \pm 0.08$	$71.9 \pm 5.7$	$6.91 \pm 0.50$
G043.1701+00.0078	19:10:14.54	+09:06:19.48	0.47	0.43	$5.37 \pm 0.26$	$1.39 \pm 0.07$	$153.1 \pm 1$	$2.73 \pm 0.09$	$331 \pm 15$	$8.51 \pm 0.39$
G043.1716+00.0001	19:10:16.41	+09:06:10.26	0.23	0.14	$2.92 \pm 0.18$	$1.06 \pm 0.07$	$57.9 \pm 2.1$	$1.76 \pm 0.08$	$67.8 \pm 4.1$	$0.66 \pm 0.04$
G045.0712+00.1321	19:13:22.08	+10:50:53.25	0.22	0.18	$0.78 \pm 0.03$	$0.57 \pm 0.03$	$106.6 \pm 5.6$	$0.66 \pm 0.02$	$331 \pm 14$	$26.60 \pm 1.00$